Basics of Magnetic Resonance Imaging and Magnetic Resonance Spectroscopy

2

2.1 Overview

In this chapter, the basic principles of magnetic resonance imaging (MRI) and magnetic resonance spectroscopy (MRS) (Sects. 2.2, 2.3, and 2.4), the technical components of the MRI scanner (Sect. 2.5), and the basics of contrast agents and the application thereof (Sect. 2.6) are described. Furthermore, flow phenomena and MR angiography (Sect. 2.7) as well as diffusion and tensor imaging (Sect. 2.7) are elucidated.

The basic physical principles of the nuclear magnetic resonance (NMR in medical literature: magnetic resonance [MR]) can be understood in depth and in detail based on quantum mechanics. In Sect. 2.2, however, another description is attempted that is almost physically exact and uses only a few simple arguments of quantum mechanics. In turn, the presentation will be more complex, but still can be understood with only basic knowledge in physics. For this reason, this synopsis should precede the detailed description in the following sections to guide the reader.

MR examinations are possible if atomic nuclei of tissue of interest possess a nuclear magnetic moment μ. Atomic nuclei with odd numbers of nucleons (here: protons, neutrons) do possess such magnetic moments. The nucleus of the hydrogen atom consisting of only one proton is the simplest atomic nucleus with an odd number of nucleons and thus has the biggest magnetic moment of all nuclei. Its natural abundance of almost 100% and its ubiquitous occurrence and the high mobility of water protons in living matter are further prepositions for using low-sensitivity NMR method for imaging in human subjects. This low sensitivity compared with other imaging methods—e.g., positron emission tomography—cannot be emphasized enough. The sensitivity difference of this both methods is several orders of magnitude ($\sim 10^5$–10^6). This fact has to be taken into account when magnetic resonance imaging is envisioned for specific probe imaging, nowadays known as molecular imaging.

In spite of the abovementioned low sensitivity of MR, proton imaging is possible in humans because of the high magnetic moment, ~100% abundance, high concentration, and high mobility of protons in tissue. The following consideration will be restricted to the hydrogen nuclei only.

The basis of the magnetic resonance imaging is a simple resonance phenomenon. In a magnetic field, free environmental magnetic moments of a specimen are not oriented at all; however, in an external magnetic field the magnetic moments are no longer randomly oriented. The application of an external magnetic field B_0 forces the magnetic moments μ to align along the magnetic field. Due to basic physics principles, the orientation has two quantum states with respect to the external magnetic field: first the parallel, and second the antiparallel state, both of which have different magnetic energies E_m, and its energy difference being $\Delta E_m = \gamma \cdot \hbar \cdot B_0$, and γ, $\hbar$ being the gyromagnetic ratio and Planck's constant, respectively. In thermal equilibrium, both states possess different occupation numbers, with the low-energy parallel state having higher probability of occupation than does the low-energy antiparallel state, resulting in a macroscopic and therefore measurable net magnetization parallel to the orientation of the external magnetic field. This thermal equilibrium state can be distorted by irradiation with alternating electromagnetic field having a radiation energy E_{RF} identically to the energy-splitting ΔE_m caused by the magnetic field, and the radiation energy being $E_{RF} = \hbar \cdot \omega_0$, and ω_0 being the resonance frequency of the spin system—the so-called Larmor frequency. Due to the resonant irradiation, the spin system takes up additional energy that can be dissipated only if the system is coupled to its microenvironment. This coupling strength is described by the so-called T_1 relaxation time (also known as longitudinal or spin-lattice relaxation time). An equivalent for the coupling of the spins to each other is the T_2 relaxation time (also known as transversal or spin-spin relaxation time). For tissues, typical T_1 relaxation times for tissues are between 100 and 2,000 ms and T_2 relaxation times between 10 and 1,000 ms.

MR imaging utilizing pulsed NMR—this means the alternating electromagnetic field, the so-called radiofrequency (RF) field—is applied only for a short period of time (in general, pulses are some milliseconds). The short RF pulse excites the spin system via a transmitter coil. After irradiation of the nuclear spin system, a receiver coil can detect a damped time-dependent signal with a frequency of ω_0. This signal is called the free induction decay (FID). The damping of the signal is ruled by the T_2 relaxation times, and the period by the strength of the external magnetic field (constant magnetic moment assumed). In practical terms, not only does the T_2 relaxation time influence the damping of the signal, but also the technically related inhomogeneity of the external magnetic field. The signal damping caused by the inhomogeneity is called T_2* relaxation time, and is in general much stronger than that caused by T_2 relaxation times. Only special pulse sequences (e.g., spin-echo sequences) can eliminate the influence of the inhomogeneity of the external magnetic field and thus allow the measurement of the T_2 relaxation times specific to the substance/tissue. The influence of T_2 relaxation times is mainly limited to the amplitude of the signal.

Preposition for the image reconstruction (Sect. 2.3) is the exact information about the MR signal's origin. This spatial information can be generated by space-dependent magnetic fields additionally applied along the three space coordinates. These space-dependent magnetic fields—called magnetic field gradients—are small as compared with the main external field and are generated by special coils mounted in the bore of the magnet. Due to these additional magnetic field gradients, the total magnetic field is slightly different in each volume element (voxel) and in turn, so is the resonance frequency of the spin system in each voxel. As a result, irradiation with a RF pulse of defined frequency ω' excites only those nuclei in such voxels where the Larmor frequency ω_0 given by the field strength matches the resonance condition. Suitable changes of the field gradients allow moving a volume element in space, fulfilling this condition. Keeping in mind that the signal intensity of a volume element is given by the number of the spins in the volume element, the relaxation times of the tissue and the specific measurement parameters (e.g., pulse repetition time, echo time etc.), this signal intensity is assigned to the corresponding picture element (pixel). In this manner, the region of interest can be sampled by moving the volume element through space, and successively, an image with respect to pixels can be constructed. This method requires a long time to acquire images, assuming every experiment needs about 1 s to measure a voxel and a pixel, respectively. Thus, the measurement of an image 128 × 128 pixels will require more than 16,000 s to complete. Nowadays, 2D-, 3D-, and/or phase encoding methods as well as half-Fourier methods are applied, allowing data acquisition times of minutes or even less. Special fast imaging techniques (e.g., FLASH, RARE, EPI sequences) allow further reduction of the acquisition time (cf. Sect. 2.4).

In contrast to X-ray computed tomography, where the attenuation is governed purely by the electron density, as mentioned above, in MRI the signal intensity is a complex function of the proton density and the T_1, T_2, and T_2* relaxation times. Additionally, the signal intensity—and hence the image contrast—can be influenced by the measurement parameters (e.g., echo time, repetition time) set at the scanner. The knowledge of these interrelations of the different parameters influencing the signal intensity and hence the image contrast is mandatory in interpreting MR images correctly.

The MR scanner is a complex system (Sect. 2.5). Its main components are the magnet, the RF system, and the gradient coils. The entire system is controlled and supervised by a computer. The development of MR imaging was only possible after the development of Fourier transform NMR as well as fast computers calculating fast Fourier transformations within minutes. The development of large-bore superconducting magnets of ≥ 0.3–1.5 T in the 1980s accelerated the development and the application of MRI in clinical practice. Nowadays, 3-T scanners are in routine clinical use. Scanners with ≥ 7 T are installed and will further accelerate the development of MRI and MRS. Most of the magnets are made of solenoid coils. Other magnet types, like scanners with Helmholtz coils configuration, give better access to the patients; however, are installed mostly for special purposes, e.g., in an operation suite. MR scanners with conventional resistivity magnets and fields smaller than 0.5 T are rarely used, except in countries with short supplies of helium or other restrictions that may not allow installation of a superconducting system.

The risk of side effects is assumed low if the magnetic fields are ≤ 1.5 T, except for the danger caused by ferromagnetic subjects accelerated into the magnet. Nevertheless, at fields of 1.5 T and even ≥ 3 T, the knowledge about side effects is rare, especially the long-term exposure due to high static magnetic fields, gradient fields, and RF fields to organisms. The problems concerning safety are extensively discussed in Sect. 2.9.

In the early days of MRI, the simplicity and wide range with which to manipulate contrasts in MRI by changing the imaging parameters led to the conclusion that development of MR contrast agents is dispensable. However, experience taught that contrast media significantly improve MR diagnostics, not only in the central nervous system, but also in other diagnostic procedures. In contrary to X-ray contrast agents, where absorption is the dominating physical effect producing the contrast, MR contrast media are based on other principles. The paramagnetic and/or super-paramagnetic properties of the contrast media influence the relaxation times of tissue, or change contrast by obliterating the signal of protons and thus increase contrast. Whereas in X-ray the contrast is proportional to the concentration of the contrast medium, in MR the dependency on the concentration is in general much stronger than linear —most often exponential. MR-contrast media are described in Sect. 2.6.

The intrinsic sensitivity of NMR to motion was already observed early in the 1950s. In MR imaging, motion, in particular flow, is often recognized as artifacts. However, these phenomena can be used to measure flow and/or represent the vascular system. Two effects are used for these kinds of measurements, the time-of-flight phenomenon (or the wash-in/wash-out effect) or the spin-phase phenomenon. In time-of-flight measurements, moving spins are excited at one location (in the vessel), and detection of the spins is performed downstream at another known location (slice). The delay time between excitation and detection can be used to calculate the flow velocity. Several modifications of the method exist (e.g., presaturation, bolus tracking), and are used depending on the setup of the measurement and sequences used. The spin-phase phenomenon can be used for angiographic imaging as well. The phase of the transverse magnetization of moving spins along a field gradient changes according to the Larmor equation. These phase-shift effects are observed for flow in all directions. The phase changes are prone to different flow parameters (e.g., velocity, turbulences, acceleration, etc.) and on the pulse sequences used. The signal variations produced by the two effects can be used to produce images of the vascular structures. Using phase-sensitive effects, magnitude subtraction is a common procedure: dephased and rephrased image are acquired sequentially and are subtracted. Using time-of-flight effects, mostly maximum-intensity projection is used to construct images of the vasculature. The angiographic techniques are described in detail Sect. 2.7.

Diffusion-weighted and -tensor imaging is a method applied first for clinical problems in brain, e.g. stroke, characterization of brain tumors, multiple sclerosis, etc. Molecules in gases and fluids undergo microscopic random motions due to the thermal energy proportional to the temperature of the gas or fluid. If the molecules—in this context only water molecules are considered—are imbedded in a structure, for instance in tissues, the random walk motion may be restricted by the cellular tissue structure and hence reduce diffusion constants. If the structure of tissue has a preferred direction, diffusion will no longer isotropic; the diffusion will have higher components in the preferred direction of tissue. This kind of diffusion is called anisotropic diffusion. In mathematical terms, the anisotropic diffusion can be represented by a tensor. The so-called apparent diffusion coefficient can be measured, and the anisotropy of the diffusion can be determined and contains information about the structure of tissue. The basics of diffusion imaging are elucidated in Sect. 2.8.

2.2 Physical Basics

G. Brix

2.2.1 Nuclear Spin and Magnetic Moment

All nuclei with an odd number of protons and/or neutrons possess in their ground state a non-zero angular momentum or nuclear spin $\boldsymbol{I}$, which results from the intrinsic angular momentums and the orbital angular momentums of the constituent protons and neutrons.

As with any other angular momentum at the atomic and nuclear level, the angular momentum vector $\boldsymbol{I}$ is quantized. This quantization is described by the following fundamental postulates of quantum physics:

- Quantization of the magnitude: The magnitude (length) $|\boldsymbol{I}|$ of the angular momentum vector can only take the discrete values $|\boldsymbol{I}| = \hbar\sqrt{I(I+1)}$, with $\hbar$ being the Planck's constant ($\hbar = 1.05 \times 10^{-34}$ Js) and I the spin quantum number, which is either integer or half-integer.
- Quantization of the direction: The component I_z of the angular momentum vector $\boldsymbol{I}$ along the direction of an external magnetic field is quantized. For a given value of I, only the discrete values of $I_z = m\hbar$ are admitted, where m is the magnetic quantum number which is limited to the values $-I, -I+1, \ldots, I-1, I$. In total, there are thus only $2I + 1$ orientations of the angular momentum vector $\boldsymbol{I}$ allowed.

Example: Figure 2.2.1 illustrates spin quantization in form of a vector diagram for a nucleus with the spin quantum number $I = 3/2$. In this case, there are $2I + 1 = 2 \cdot 3/2 + 1 = 4$ orientations of the spin vector $\boldsymbol{I}$ with the magnitude (length) $|\boldsymbol{I}| = \hbar\sqrt{I(I+1)} = \hbar\sqrt{3/2 \cdot (3/2+1)} = \hbar\sqrt{15/4}$ allowed.

Remark: The spin quantum number I is frequently referred to as "nuclear spin," which means that the maximum (minimum) component of the vector $\boldsymbol{I}$ along the chosen axes is $\hbar I$ ($-\hbar I$).

The angular momentum $\boldsymbol{I}$ of an atomic nucleus is always related with a magnetic moment $\boldsymbol{\mu}$. This nuclear magnetism forms the basis of magnetic resonance.

Remark: An atomic nucleus can be imagined as a rotating, positively charged sphere (Fig. 2.2.2). The rotation of the charge results in a circular electric current, inducing a magnetic dipolar field. Both the direction and magnitude of the magnetic field are characterized by the magnetic moment $\boldsymbol{\mu}$. In the simple model considered, the vector $\boldsymbol{\mu}$ is collinear with the mechanical angular momentum of the sphere. Surprisingly, in quantum physics this simple relationship is even valid when the angular momentum is an inherent property of a particle (e.g., an electron or a nucleus) which is not associated with a mechanic rotation.

As shown by a large number of experiments, there is a linear relationship between the nuclear magnetic moment and the nuclear spin

$$\boldsymbol{\mu} = \gamma \boldsymbol{I}. \tag{2.2.1}$$

The proportionality constant γ is denoted as gyromagnetic ratio and is a characteristic property of a nuclide. Whereas all nuclei with $I \neq 0$ can be used in principle for spectroscopic MR examinations, the nucleus of the hy-

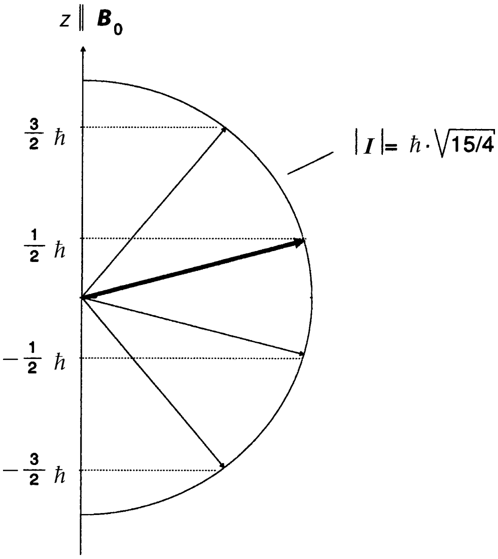

Fig 2.2.1 Quantization of the nuclear spin. Vector diagram for a nucleus with the quantum numbers $I = 3/2$ and $m = 1/2$. The three other possible orientations of the spin vector $\boldsymbol{I}$ are drawn thinly

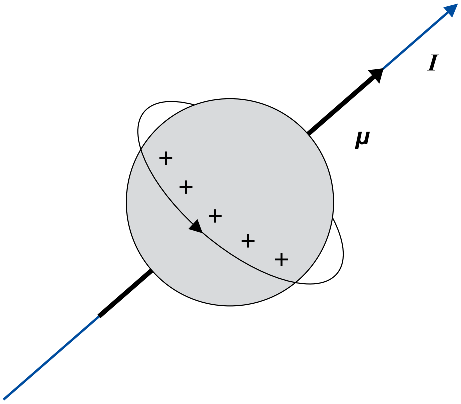

Fig 2.2.2 Magnetic moment of a charged sphere. In the classical model, the rotation of a charged particle, described by its angular momentum $\boldsymbol{I}$, results in an electric current, which induces a magnetic dipolar field. Direction and magnitude of this field are described by the magnetic moment $\boldsymbol{\mu}$. The vector $\boldsymbol{\mu}$ is directed collinear to the angular momentum $\boldsymbol{I}$ of the sphere (magnetomechanic parallelism)

Table 2.2.1 MR-relevant properties of nuclei which are important for biological MR examinations (Harris 1986 [3])

Isotope	Spin quantum number I	Gyromagnetic ratio $\gamma/10^7$ (rad T^{-1} s^{-1})	Resonance frequency $\upsilon = \omega/2\pi$ at $B_0 = 1T$ (MHz)	Natural abundance (%)	Relative MR sensitivity compared to ^1H (%)
^1H	1/2	26.752	42.577	99.985	100.0
^2H	1	4.1066	6.536	0.015	0.96
^{12}C	0	–	–	98.89	–
^{13}C	1/2	6.7283	10.708	1.11	1.59
^{14}N	1	1.9338	3.078	99.63	0.10
^{15}N	1/2	– 2.7120	4.316	0.37	0.10
^{16}O	0	–	99.76	–	–
^{17}O	5/2	– 3.6279	5.774	0.04	2.91
^{18}O	0	–	–	0.20	–
^{19}F	1/2	25.181	40.077	100.0	83.34
^{23}Na	3/2	7.0801	11.268	100.0	9.25
^{31}P	1/2	10.841	17.254	100.0	6.63

drogen atom, which has a spin quantum number of $I = 1/2$, is almost exclusively used in MRI due to two reasons:

- It is the most abundant nucleus in biological systems.
- It has the largest gyromagnetic ratio of all stable nuclei.

Table 2.2.1 summarizes MR-relevant properties of the most important nuclei in biological tissue.

2.2.2 Nucleus in a Magnetic Field

2.2.2.1 Quantum Mechanical Description

In the absence of a magnetic field, all allowed orientations of the magnetic moment $\boldsymbol{\mu} = \gamma \boldsymbol{I}$ are energetically equal. This corresponds to the well-known fact that a bar magnet can be positioned arbitrarily within the field-free space; its potential energy is independent of its orientation. However, if the nucleus is located in a homogenous static magnetic field with the magnetic flux density $\boldsymbol{B}_0$ (magnitude, $B_0 = |\boldsymbol{B}_0|$) directed along the z-axis of a coordinate system, the nucleus has the additional potential energy

$$E = -\mu_z B_0, \qquad (2.2.2)$$

where μ_z is the z-component of the magnetic moment, which can only take the discrete values $\mu_z = \gamma\hbar m$ (with $m = -I, -I+1, \ldots, I-1, I$). Consequently, there are $2I+1$ equidistant energy levels, which are denoted as nuclear Zeeman levels (Fig. 2.2.3)

$$E_m = -\gamma\hbar m B_0. \qquad (2.2.3)$$

Remark: Numerous books use the magnetic field strength $\boldsymbol{H}$ instead of the magnetic flux density $\boldsymbol{B}$. Within matter, however,

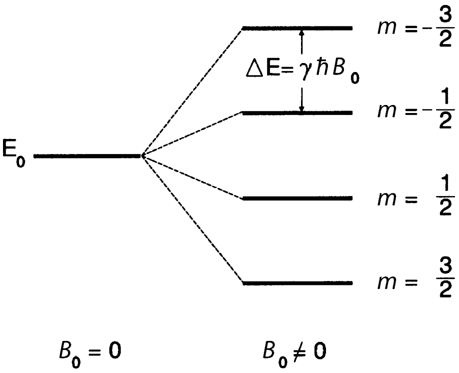

Fig. 2.2.3 Nuclear Zeeman levels. Splitting of the energy levels of a nucleus with the spin quantum number $I = 3/2$ in an external magnetic field with the flux density $\boldsymbol{B}_0$. The energy difference between the four equidistant nuclear Zeeman levels is $\Delta E = \hbar\omega_0 = \gamma\hbar B_0$

the $\boldsymbol{B}$ field represents the "real" magnetic field that interacts with the magnetic moments of the nuclei. The relation between the two magnetic field quantities is explained in Sect. 2.2.8.1.

When considering an isolated magnetic moment within a static magnetic field, one will find that transitions between the different energy levels are prohibited due to the law of energy conservation. Transitions can exclusively be induced by an additional time-dependent electromagnetic RF field that interacts with the magnetic moment, the effect is known as magnetic resonance (MR).

In MR, transitions are induced by a magnetic RF field $\boldsymbol{B}_1(t)$ with the angular frequency ω_{RF}, which is irradiated perpendicular to the direction of the static magnetic field $\boldsymbol{B}_0$. Such a time-dependent magnetic field, however, can only induce transitions fulfilling the selection rule $\Delta m = \pm 1$, i.e., transitions between neighboring energy levels. As a consequence, the energy $E_{\mathrm{RF}} = \hbar\omega_{\mathrm{RF}}$ of a photon of the RF field must be identical with the energy difference $\Delta E = \hbar\omega_0 = \gamma\hbar B_0$ between two neighbored energy levels, which yields the resonance condition

$$\omega_{\mathrm{RF}} = \omega_0 = \gamma B_0. \tag{2.2.4}$$

Remarkably, Planck's constant $\hbar$ does not occur in this fundamental equation of magnetic resonance. This indicates that the basic principles of magnetic resonance cannot only be described by quantum physics, but also by a classical approach, which is mediated by the intuitive semi-classical model described in the next section.

2.2.2.2 Semiclassical Description

In an external magnetic field, a cylindrical permanent magnet—characterized by a magnetic moment $\boldsymbol{\mu}$—experiences a mechanical torque that tends to align the permanent magnet parallel to the external magnetic field and thus minimize the potential energy of the system. However, in the case that the permanent magnet rotates around its longitudinal axis and thus possesses an angular momentum ("magnetic gyroscope"), it cannot align parallel to the external field due to the conservation of the angular momentum. In this situation, it experiences a torque perpendicular to both the direction of the magnetic field and the angular momentum, which results in a rotation (precession) of the magnet on a cone about the direction of the external $\boldsymbol{B}_0$ field (see Fig. 2.2.4b). The frequency of this precession, the Larmor frequency, corresponds to the resonance frequency ω_0 given by Eq. 2.2.4.

Remark: The precession of a magnetic gyroscope in an external magnetic field can be illustrated by a mechanic analog. When a child's spinning top is deflected so that its axis is not parallel to

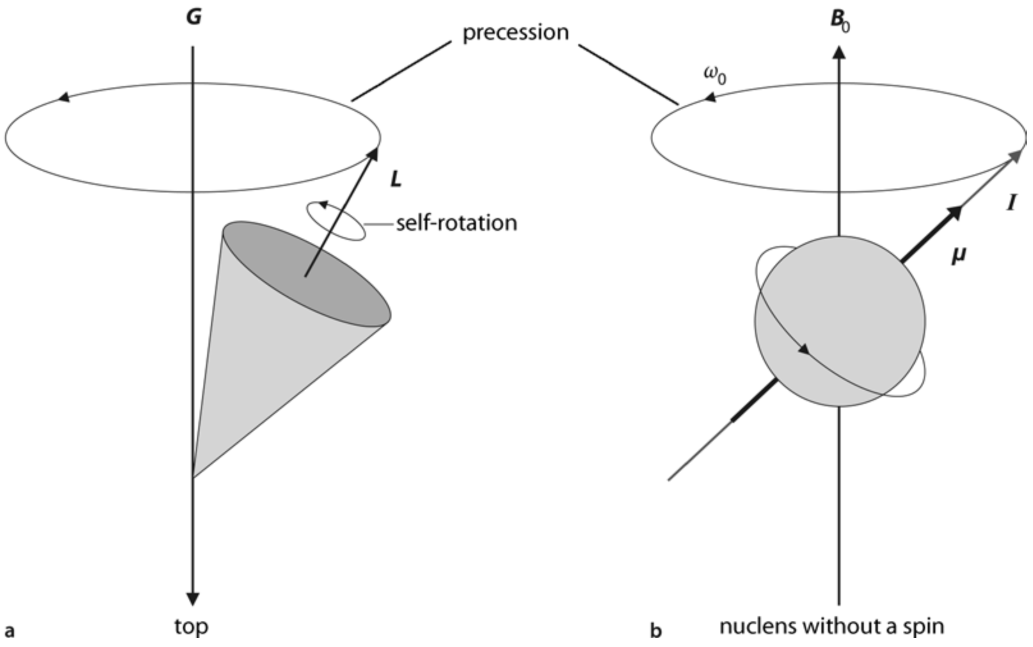

Fig 2.2.4 Analogy between an atomic nucleus and a top. **a** Precession of a rotating top in the gravitational field $\boldsymbol{G}$ of the earth. **b** Precession of a magnetic moment $\boldsymbol{\mu}$ around the direction of a static magnetic field $\boldsymbol{B}_0$. The fundamental difference between the top and the nucleus is that the nucleus possesses an intrinsic angular momentum $\boldsymbol{I}$, whereas the angular momentum $\boldsymbol{L}$ of the top has to be initiated mechanically

the direction of the gravitational field, it will continue rotating around its axis, but the axis itself will start rotating—the top precesses on a cone around the direction of the gravitational field (Fig. 2.2.4a). It should be mentioned, however, that the child's top and the nucleus differ with regard to the fact that the child's top has to be spun, whereas the nucleus possesses an intrinsic angular momentum.

The quantization of direction of the nuclear magnetic moment $\boldsymbol{\mu}$ can be integrated into this classical description by limiting the angle between the field axis and the precession cone to the discrete values which relate to the $2I + 1$ orientations of the angular momentum $\boldsymbol{I}$ permitted. For a spin-1/2 nucleus, this results in a double-precession cone as shown in Fig. 2.2.5.

However, this semiclassical model is rendered questionable, because the classical concept of a continuous trajectory in space is hardly compatible with the quantization of physical quantities. For instance, what would the trajectory of the vector $\boldsymbol{\mu}$ look like when transitions between the various precession cones, reflecting discrete energy levels, are induced by an RF field, such as for a spin-1/2 nucleus, the transition from the lower to the upper precession cone (cf. Fig. 2.2.5)? Is it possible to assign to the vector $\boldsymbol{\mu}$ a well-defined direction in space at any point in time, and would this direction change over time? If so, then this negates the postulate of discrete energy and angular momentum levels. This aporime can only be solved by a rigorous quantum mechanical treatment of the system. However, when considering only the mean values of physical quantities averaged over a large ensemble of nuclei—which can only be measured in a real MR experiment—it becomes obvious that the models and laws of classical physics are valid.

2.2.3 Macroscopic Magnetization

In field-free space, the magnetic moments of nuclei in a macroscopic sample are randomly oriented due to their thermal motion and thus mutually compensate each other. In a homogeneous static magnetic field $\boldsymbol{B}_0$, however, only $2I + 1$ discrete orientations of the magnetic moments with respect to the direction of the external field are permitted, the energy levels of which differ according Eq. 2.2.3. In thermal equilibrium, the population of the $2I + 1$ levels (spin states) is described by the Boltzmann statistic: The lower the energy $E_m = -\gamma\hbar B_0 m$ of a state with the magnetic moment $\mu_z = \gamma\hbar m$ in the z-direction, the greater is the occupation number.

Example: Let us consider an ensemble of hydrogen nuclei in a static magnetic field of the flux density $B_0 = 1$ T. According to the Boltzmann statistic, more nuclei will occupy the state of the lower energy ($m = +1/2$, μ_z parallel to $\boldsymbol{B}_0$) than the state of the higher energy ($m = -1/2$, μ_z antiparallel to $\boldsymbol{B}_0$) (Fig. 2.2.6). However, as compared with the thermal energy, the difference between the two energy levels is extremely small, so that the difference in the occupation numbers of the two levels is very small. At body temperature of 37°C, the difference in the occupation numbers with respect to the total number of spins is as low as 0.000003!

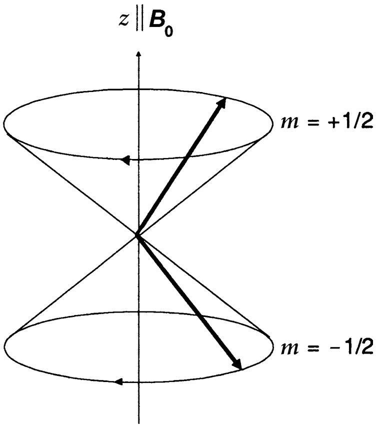

Fig 2.2.5 Double-precession cone for a nucleus with the nuclear spin quantum number $I = 1/2$. The two permitted spin states (precession cones) are characterized by the magnetic quantum numbers $m = \pm 1/2$

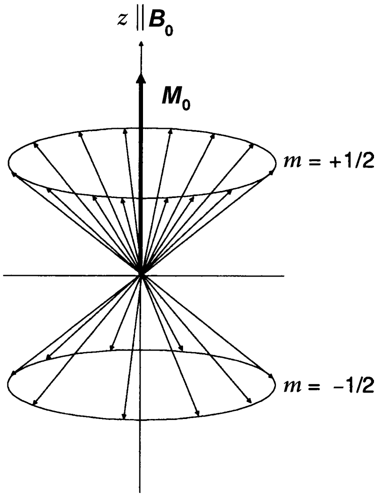

Fig 2.2.6 Origin of the nuclear magnetization. In thermal equilibrium, the distribution of an ensemble of spin-1/2 nuclei on the two allowed precession cones is described by the Boltzmann statistic. The occupation number of the state of the lower energy ($m = +1/2$, μ_z parallel to $\boldsymbol{B}_0$) is somewhat higher than that of the state of the higher energy ($m = -1/2$, μ_z antiparallel to $\boldsymbol{B}_0$) which leads to macroscopic (bulk) magnetization $\boldsymbol{M}_0$

Although the difference in the occupation numbers is extremely small, it results in a measurable bulk magnetic moment along the direction of the $\boldsymbol{B}_0$ field due to the large number of nuclei in a macroscopic sample ("nuclear paramagnetism"). The macroscopic magnetization in thermal equilibrium is described by the magnetization vector $\boldsymbol{M}_0$, which is defined as the vector sum of the nuclear magnetic moments per unit volume V. The magnitude of the equilibrium magnetization $\boldsymbol{M}_0$ is given by

$$M_0 = |\boldsymbol{M}_0| = \frac{1}{V}\sum_{i=1}^{N}(\mu_z)_i = \frac{N}{V}\cdot\frac{I(I+1)\gamma^2\hbar^2 B_0}{3kT}, \qquad (2.2.5)$$

where N is the total number of nuclei in the sample, T the absolute temperature of the sample, and k Boltzmann's constant ($k = 1.38 \cdot 10^{-23}$ J/K). The ratio $\rho = N/V$ is called spin density. As both the body temperature and the spin density cannot be altered in living beings, the equilibrium magnetization M_0 can only be increased according to Eq. 2.2.5 by increasing the magnetic flux density B_0.

2.2.4 Dynamic of Magnetization I: Resonance Excitation

The equilibrium state of a spin system can be disturbed by a magnetic RF field $\boldsymbol{B}_1(t)$ with a frequency ω_{RF} equal to the Larmor frequency ω_0, which tilts the magnetization $\boldsymbol{M}$. Whereas a nuclear magnetic moment $\boldsymbol{\mu}$ can only take $2I + 1$ discrete orientations relative to the static magnetic field $\boldsymbol{B}_0$ (quantization of direction), the macroscopic magnetization $\boldsymbol{M}$ can take any direction in space and change it steadily.

The action of a magnetic RF field $\boldsymbol{B}_1(t)$, which rotates with the Larmor frequency ω_0 around the direction of the static $\boldsymbol{B}_0$ field, can be analyzed most effectively in a rotating frame, i.e., a coordinate system that rotates with the Larmor frequency around the z-axis (Fig. 2.2.7). The change to a rotating frame with the axes (x', y', z) has two advantages:

- As the x'–y'-plane of the rotating frame is synchronized with the RF field, the $\boldsymbol{B}_1$ vector remains stationary in this frame. In the following analysis, we will assume that the static $\boldsymbol{B}_1$ field points along the x'-axis (Fig. 2.2.7).
- As shown in Sect. 2.2.2.2, a nuclear magnetic moment $\boldsymbol{\mu}$ precesses with the Larmor frequency ω_0 around the direction of the $\boldsymbol{B}_0$ field (see Fig. 2.2.5). Of course, this holds equally for the sum of the nuclear magnetic moments, i.e., for the macroscopic magnetization $\boldsymbol{M}$. Therefore, an observer observing the precession of the magnetization $\boldsymbol{M}$ from the rotating frame will come to conclude that the position of the magnetization does not change. From his point of view, the magnetization behaves as if the $\boldsymbol{B}_0$ field is absent (Larmor's theorem).

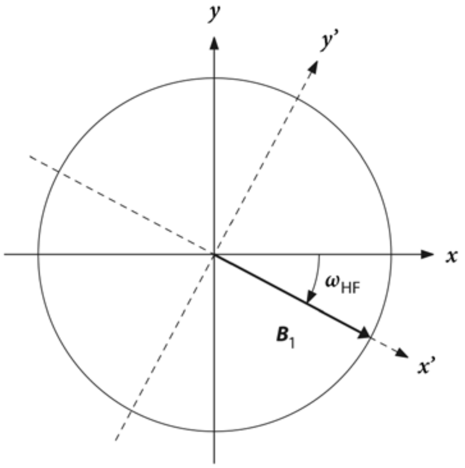

Fig 2.2.7 Radiofrequency field in a stationary and in a rotating frame of reference. In the stationary frame (x, y, z) the magnetic RF field $\boldsymbol{B}_1(t)$ rotates with the angular frequency ω_{RF} in the x–y-plane around the z-axis. If one observes this rotation from a rotating frame (x', y', z), which rotates with the angular frequency ω_{RF} around the z-axis, the vector is stationary. Typically, the rotating frame is chosen in such a way that the $\boldsymbol{B}_1$ field points in the x'-direction

Summarizing both reflections, it can be concluded that the dynamics of the magnetization $\boldsymbol{M}$ in the rotating frame is determined only by the static $\boldsymbol{B}_1$ field. If it points toward the x'-axis, then the magnetization $\boldsymbol{M}$ will precess around the x'-axis (Fig. 2.2.8a). Analogous to Eq. 2.2.4, the frequency ω_1 of this precession is given by

$$\omega_1 = \gamma B_1. \qquad (2.2.6)$$

When looking at this simple rotation of the magnetization $\boldsymbol{M}$ in the y'–z-plane of the rotating frame from a laboratory frame of reference (x, y, z), the movement is superimposed by a markedly faster rotation ($B_0 > B_1$) around the z-axis. Thus, within the laboratory frame of reference, the tip of the vector $\boldsymbol{M}$ moves in a helical manner on the surface of a sphere around the $\boldsymbol{B}_0$ field; the length of the vector $\boldsymbol{M}$ remains constant (Fig. 2.2.8b).

If the magnetization $\boldsymbol{M}$ points toward the static field $\boldsymbol{B}_0$ before the RF field $\boldsymbol{B}_1(t)$ is switched on, the magnetization $\boldsymbol{M}$ is rotated from the equilibrium position under the influence of the RF field during the duration t_{p} by the flip angle:

$$\alpha = \omega_1 t_{\mathrm{p}} = \gamma B_1 t_{\mathrm{p}}. \qquad (2.2.7)$$

If the duration t_{p} of the RF field is chosen to rotate the magnetization in the rotating frame by 90°, then this pulse is denoted as 90° or $\pi/2$ pulse (Fig. 2.2.9a). Accordingly, the magnetization $\boldsymbol{M}$ is rotated by 180° when the duration of the RF pulse is doubled at the same flux density B_1. This pulse, which inverts the magnetization from the positive to the negative z-direction, is called 180° or π pulse (Fig. 2.2.9b).

Remark: Precisely speaking, a short RF pulse with the carrier frequency ω_{RF} will excite not only the nuclei that exactly fulfill the resonance condition $\omega_{\mathrm{RF}} = \omega_0$, but also nuclei whose resonance frequency slightly differs from ω_{RF}. This is because the frequency spectrum of an RF pulse of finite duration consists of a continuous frequency band around the nominal frequency ω_{RF} (Fig. 2.2.10). The width of the frequency distribution is inversely proportional to the duration t_{p} of the pulse: the shorter the pulse, the broader the frequency spectrum is be distributed around ω_{RF}. If the RF field is irradiated over a very long period ($t_{\mathrm{p}} \rightarrow \infty$), the spectrum will be quasi-monochromatic.

To simplify the following analysis, the magnetization $\boldsymbol{M}$ is separated into two components: the longitudinal magnetization M_z, which is parallel to the direction of the static magnetic field $\boldsymbol{B}_0$, and the transverse magnetization M_{xy}, which is perpendicular to it (Fig. 2.2.11). In the laboratory frame the transverse magnetization M_{xy} precesses with the Larmor frequency ω_0; in the rotating frame it remains stationary.

It is instructive to describe the effect of a 90°/180° pulse on an ensemble of spin-1/2 nuclei within the semiclassical model described in Sect. 2.2.2.2. As can be shown, the magnetic RF field induces transitions between the two permitted spin states (precession cones) until the occupation numbers are either identical (90° pulse) or inverted (180° pulse). Furthermore, irradiation of a 90° pulse results in a phase synchronization of the nuclear magnetic moments of the sample, which yields a macroscopic transverse magnetization M_{xy}, the magnitude of which is equal to that of the equilibrium magnetization M_0. Figuratively speaking, this means that the precession of the transverse magnetization M_{xy} can be described as a common (phase coherent) precession of a "spin package" (Fig. 2.2.12).

2.2.5 Dynamic of Magnetization II: Relaxation

Up to this point, we have assumed that interactions of nuclear spins between one another and with their environment can be neglected. However, this assumption is not valid for real spin systems, as the magnetization returns to its equilibrium ($M_{xy} = 0$, $M_z = M_0$) after RF excitation. This process is called relaxation. Two different relaxation processes have to be distinguished:

- The relaxation of the longitudinal magnetization M_z characterized by the longitudinal or spin-lattice relaxation time T_1
- The relaxation of the transverse magnetization M_{xy} characterized by the transverse or spin-spin relaxation time T_2.

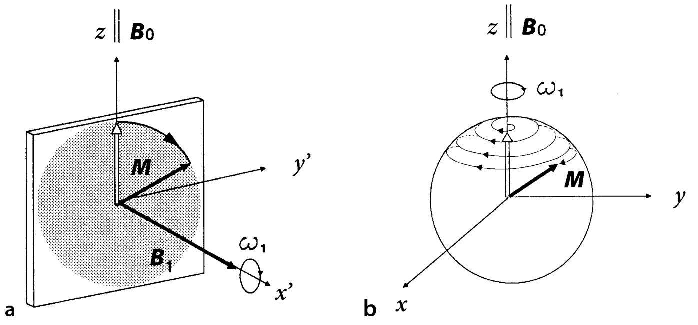

Fig 2.2.8 Resonance excitation. **a** In a rotating frame of reference, which rotates with the Larmor frequency ω_0 around the direction of the $\boldsymbol{B}_0$ field, the magnetization $\boldsymbol{M}$ precesses with the frequency ω_1 around the stationary $\boldsymbol{B}_1$ field. **b** In the stationary frame this simple rotation is superimposed by the markedly faster rotation around the z-axis. Therefore, the tip of the vector $\boldsymbol{M}$ moves in a helical manner on the surface of a sphere

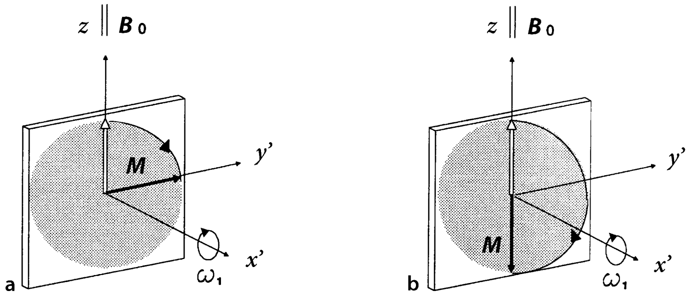

Fig. 2.2.9 90° and 180° pulse. If one chooses the rotating frame so that the RF pulse is irradiated along the x'-axis, the magnetization $\boldsymbol{M}$ will be rotated (**a**) by a 90° pulse along the y'-direction and (**b**) by a 180° pulse to the negative z-direction

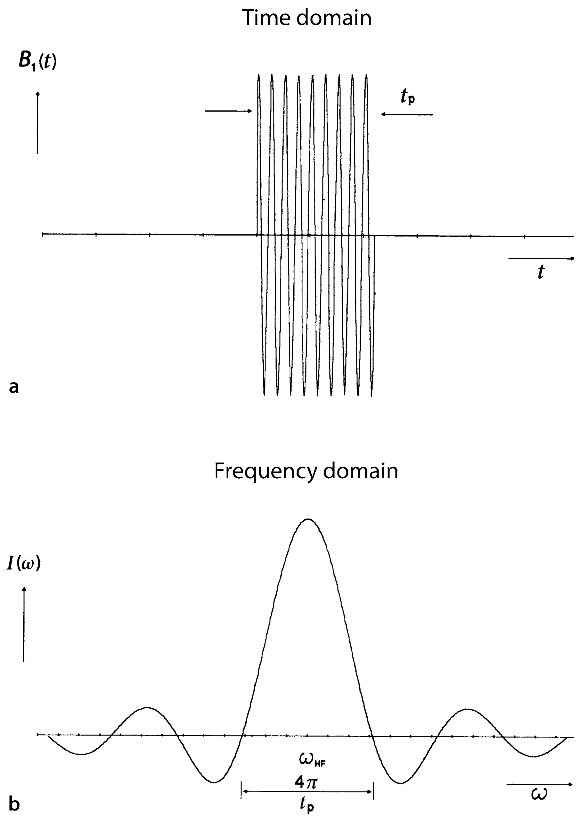

Fig. 2.2.10 RF pulse in the time and frequency domain. **a** RF pulse with carrier frequency ω_{RF} and duration t_{p}. **b** Fourier transformation of the RF pulse. Due to its finite duration, the frequency spectrum of the pulse is not monochromatic, but contains an entire frequency band, which is distributed around the nominal frequency ω_{RF}

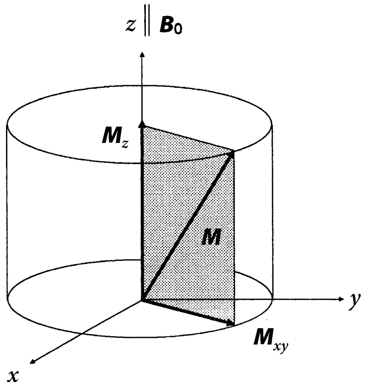

Fig. 2.2.11 Definition of the longitudinal and transverse magnetization. As the macroscopic magnetization $\boldsymbol{M}$ precesses in the stationary frame around the z-axis, it is beneficial to split it into two components: the rotating transverse magnetization M_{xy} and the longitudinal magnetization M_z

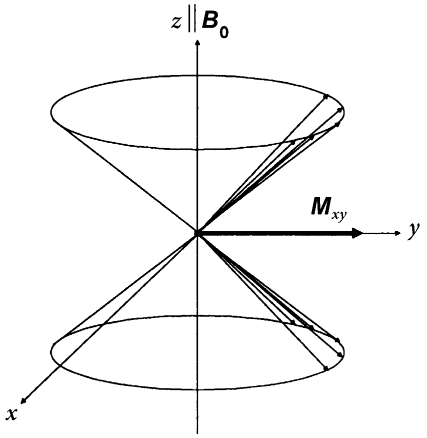

Fig. 2.2.12 Phase synchronization by a 90° pulse. The 90° pulse leads to a synchronization of the phases of the magnetic moments $\boldsymbol{\mu}$ of the nuclei in the sample (spin packet), which results in a macroscopic transverse magnetization M_{xy}, the magnitude of which corresponds to that of the longitudinal magnetization before irradiation of the 90° pulse. In the figure, only the part of the magnetic moments of the sample which are distributed in an anisotropic manner on the precession cone is shown

2.2.5.1 Physical Model of Relaxation Processes

In real spin systems, every nucleus is surrounded by other intra- and intermolecular magnetic moments, which are in motion due to rotations, translations, and vibrations of molecules as well as exchange processes. These processes induce an additional fluctuating magnetic field $\boldsymbol{B}_{\mathrm{lok}}(t)$ at the position of a given nucleus, which has to be added to the external field. As the movements and exchange processes are random, the fluctuating fields differ in time from nucleus to nucleus—in contrast to the coherent RF field $\boldsymbol{B}_{\mathrm{lok}}(t)$ irradiated from the outside.

As any other temporal process, the locally fluctuating magnetic fields $\boldsymbol{B}_{\mathrm{lok}}(t)$ can be decomposed into its frequency components.

Remark: The decomposition of a function into harmonic (i.e., sinusoidal) basis functions is denoted as Fourier analysis, the mathematical operation that gives the intensity (amplitude) of the harmonic basis functions as Fourier transformation. If the given function is periodic with period T, it can be decomposed into a sum of sinus and/or cosine functions with the discrete frequencies $\omega, 2\omega, 3\omega \ldots (\omega = 2\pi/T)$. In contrast, a nonperiodic function has a continuous spectrum of frequencies.

The contribution of the different frequency components to the fluctuating local field $\boldsymbol{B}_{\mathrm{lok}}(t)$ is described by the spectral density function $J(\omega)$. A general feature of this function is that the more rapidly the molecular motion is, the broader the frequency spectrum (Fig. 2.2.13).

In order to understand the effect of the fluctuating local magnetic fields $\boldsymbol{B}_{\mathrm{lok}}(t)$ on a spin system, the components parallel and perpendicular to $\boldsymbol{B}_0$ have to be discussed separately. Whereas the parallel component exclusively contributes to T_2 relaxation, the perpendicular component influences both T_1 and T_2 relaxation:

- The field component perpendicular to the $\boldsymbol{B}_0$ field induces—in analogy to the external RF field $\boldsymbol{B}_1(t)$ —transitions between the energy levels (precession cones) of an individual spin. The probability of these transitions depends on the intensity of the frequency component of the fluctuating fields that oscillates at the Larmor frequency ω_0: the higher the spectral density $J(\omega_0)$, the more transitions are induced. As Fig. 2.2.13 shows, $J(\omega_0)$ assumes a maximum when the limiting frequency ω_G of the spectral density function is comparable to the Larmor frequency ω_0. The described relaxation process allows the excited spin system to emit and absorb photons of energy $\hbar\omega_0$ until the Boltzmann distribution of the energy levels is reached. The energy difference between the excited and the equilibrium state is dissipated to the surrounding medium or "lattice." Since the change in the occupational numbers of the spin states (precession cones) is related with a change in the macroscopic longitudinal magnetization M_z, the described mechanism contributes to longitudinal relaxation. Moreover, it contributes to T_2 relaxation, as the locally induced transitions between the precession cones destroy the phase coherence between those spins which form, as a spin-package, the macroscopic transverse magnetization (cf. Fig. 2.2.12).
- The component of the fluctuating field $\boldsymbol{B}_{\mathrm{lok}}(t)$ oriented parallel to the z-axis locally modulates the static field $\boldsymbol{B}_0$ at the position of a nucleus and thereby changes the precession frequency ω_0 of its nuclear magnetic moment $\boldsymbol{\mu}$. Since the local fluctuations seen by the nuclei are spatially uncorrelated, the precessing magnetic moments within a sample lose their phase coherence, which causes the transverse magnetization to decay (see Fig. 2.2.12). Given the fact that the effect of the high-frequency components of the fluctuating field vanishes when averaged over time, only the quasi-static frequency components, the intensity of which is approximately given by $J(\omega = 0)$, have a measurable effect on the transversal magnetization (see Fig. 2.2.13). As no transitions between the energy levels (precession cones) are induced by the described relaxation mechanism, the longitudinal magnetization M_z remains unchanged, which means that the mechanism solely contributes to transversal relaxation.

The qualitative discussion of the relaxation mechanisms reveals that their effectiveness depends on two different factors, namely on the magnitude and the temporal characteristics of the field fluctuations. The dependence from the magnitude is utilized when using paramagnetic contrast agents (see Sect. 2.6), which possess unpaired electron spins and consequently a magnetic moment. When considering the fact that the magnetic moment of an electron amounts to 658 times the magnetic moment of a proton, one can easily understand why even the slightest amounts of paramagnetic substances can lower the relaxation times considerably.

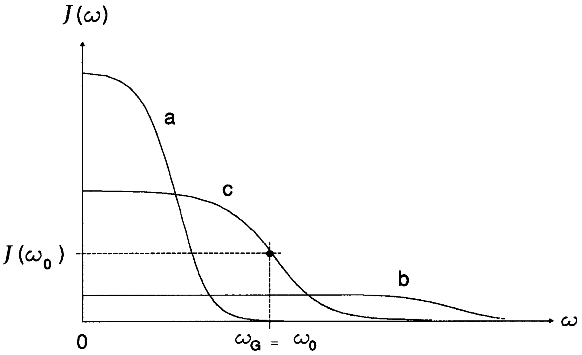

Fig. 2.2.13 Schematic representation of the density function $J(\omega)$ for three substances with a different thermal mobility of the constituting atoms or molecules. **a** If the atoms or molecules move very slowly (such as in solids), the intensity of high-frequency components is very low. **b** This is different in fluids. In this case, the atoms or molecules move very rapidly, so that the spectral density function contains high-frequency components to a significant degree. **c** At a given frequency ω_0 the intensity $J(\omega_0)$ will attain a maximum if the cut-off frequency ω_G of the spectral density function approximately corresponds to the given frequency ω_0. At low frequencies, $J(\omega)$ is nearly independent on the frequency, so that the density of the quasi-static frequency components can be approximated by $J(\omega = 0)$

2.2.5.2 Phenomenological Description of Relaxation Processes

For spin systems with a sufficiently high molecular mobility, relaxation processes can be described by exponential functions with the time constant T_1 or T_2. The longitudinal magnetization increases exponentially toward its equilibrium value $M_z = M_0$, the transverse magnetization decreases exponentially toward $M_{xy} = 0$. Figure 2.2.14 shows the exponential relaxation of both magnetization components after excitation of the spin system by a 90° pulse and gives a simple interpretation of the relaxation times T_1 and T_2:

- The longitudinal relaxation time T_1 gives the time required for the longitudinal magnetization after a 90° pulse to grow again to 63% of its equilibrium value M_0.
- The transverse relaxation time T_2 gives the time required for the transverse magnetization after a 90° pulse do drop to 37% of its original magnitude.

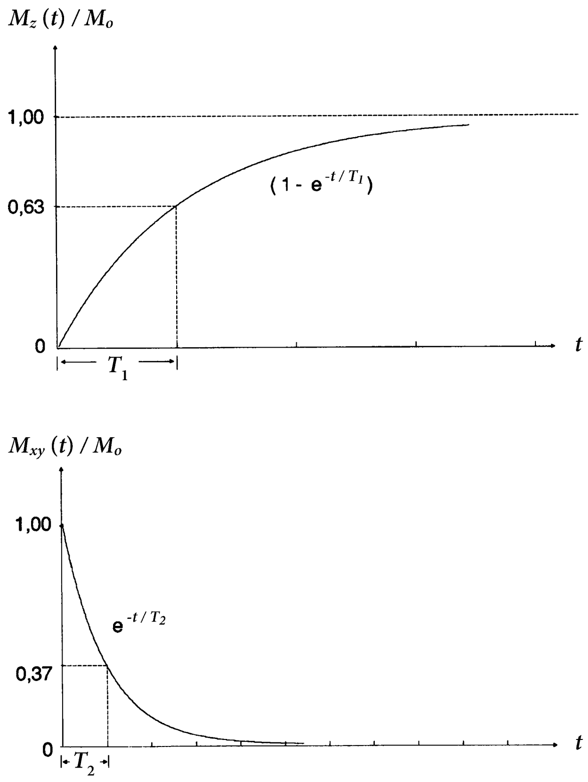

Fig. 2.2.14 Relaxation of the longitudinal and transverse magnetization. After excitation by a 90° pulse, the longitudinal magnetization M_z relaxes toward the equilibrium magnetization $M_z = M_0$, and the transverse magnetization toward $M_{xy} = 0$. The temporal evolution is defined by the relaxation times T_1 and T_2, respectively ($e^{-1} \cong 0.37$)

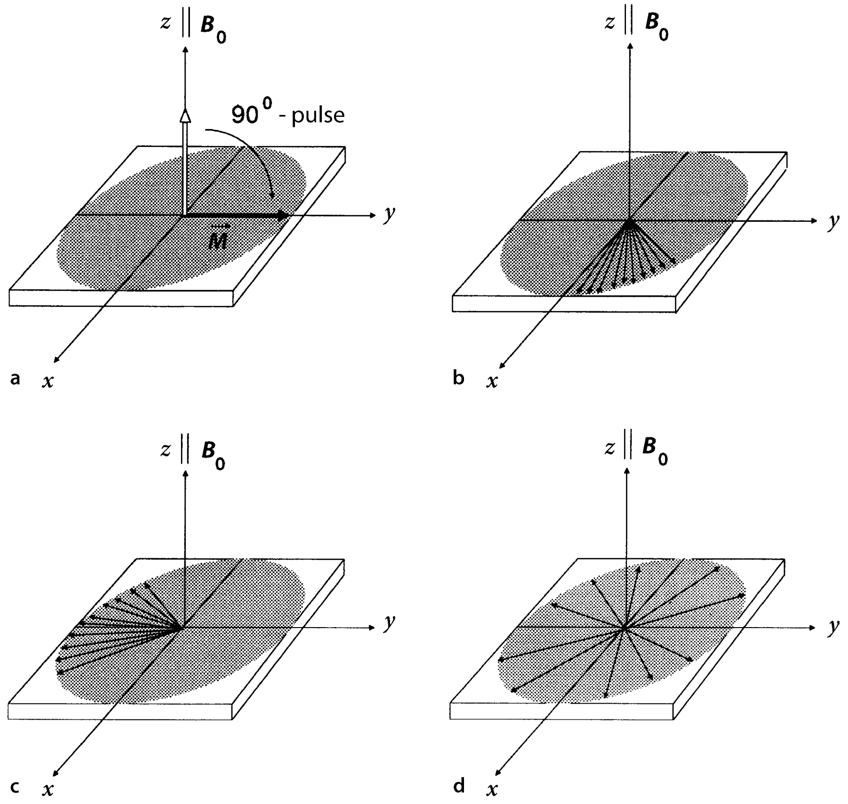

Fig. 2.2.15 Dephasing of the transverse magnetization. The transverse magnetization M_{xy} of the sample is split up into several magnetization components, which precess with slightly differing Larmor frequencies around the direction of the B_0 field. **a** Immediately after the 90° pulse, all magnetization components are aligned parallel. **b**–**d** Afterward, the components dephase due to their different Larmor frequencies, and thus the macroscopic transverse magnetization decays

The process of transverse relaxation can be described intuitively on the macroscopic level. To this end, the transversal magnetization M_{xy} is split into different magnetization components, or spin packets. Whereas the spins of each spin packet precess with the same Larmor frequency, the spins in different packets slightly differ in their Lamor frequencies. Right after excitation, all components of the magnetization point toward the same direction; shortly afterward, however, some parts precess more quickly than others around the direction of the $\boldsymbol{B}_0$ field. Due to this fact, the components fan out (dephasing), and the resulting transverse magnetization decreases (Fig. 2.2.15).

In real MR experiments always macroscopic samples are examined, so that not only the fluctuating local magnetic fields, but also spatial field inhomogeneities of the external field $\boldsymbol{B}_0$, introduced by technical imperfections, contribute to the transverse relaxation. As both effects superpose on one another, the resulting effective relaxation time T_2^* is always shorter than the real, substance-specific transverse relaxation time T_2.

2.2.5.3 Proton Relaxation Times of Biological Tissues

Relaxation times in solids and fluids differ markedly (Fig. 2.2.16). Whereas the longitudinal relaxation in solids can take hours or even days, in pure fluids it only takes some seconds. This difference is because the spectral density function $J(\omega_0)$ at the Larmor frequency is much larger in fluids than it is in solids, in which the low-frequency components dominate (see Fig. 2.2.13). For the same physical reason, the T_2 relaxation time in solids usually only amounts to some microseconds, whereas in fluids it is only slightly shorter than the longitudinal relaxation time T_1.

Soft tissues range, based on their consistency, between solids and pure fluids: with regard to their relaxation behavior, they can in general be treated as viscose fluids. Table 2.2.2 summarizes representative proton relaxation times for different biological tissues. Due to the considerable differences in the tissue relaxation times, it is possible to acquire MR images with an excellent tissue contrast even when the proton densities of the tissues or organs only slightly differ from one another. When interpreting the relaxation times, two aspects have to be taken into account:

- The relaxation time T_1 of biological tissues strongly depends on the Larmor frequency, whereas the relaxation time T_2 is nearly independent of the frequency. When comparing T_1 values, one therefore needs to

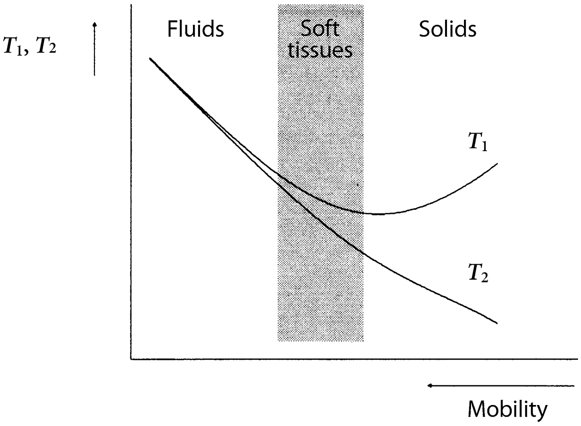

Fig. 2.2.16 Relaxation in fluids and solids. The relaxation behavior of a substance depends strongly on the thermal mobility of the constituting atoms and molecules. For fluids with a high thermal mobility the relation $T_1 \cong T_2$ holds, for solids $T_1 >> T_2$. The relaxation time T_1 is minimal, when the cut-off frequency of the spectral density function $J(\omega)$ of the substance approximately corresponds to the Larmor frequency (see Fig. 2.2.13)

Table 2.2.2 ^{1}H relaxation times of biological tissues at different magnetic flux densities B_0 (Bottomley et al. 1984 [2])

Tissue	T_2 (ms)	T_1 (s) at 0.5 T	T_1 (s) at 1.0 T	T_1 (s) at 1.5 T
Skeletal muscle	47±13	0.55±0.10	0.73±0.13	0.87±0.16
Heart muscle	57±16	0.58±0.09	0.75±0.12	0.87±0.14
Liver	43±14	0.33±0.07	0.43±0.09	0.50±0.11
Kidney	58±24	0.50±0.13	0.59±0.16	0.65±0.18
Spleen	62±27	0.54±0.10	0.68±0.13	0.78±0.15
Fatty tissue[a]	84±36	0.21±0.06	0.24±0.07	0.26±0.07
Grey brain matter	101±13	0.66±0.11	0.81±0.14	0.92±0.16
White brain matter	92±22	0.54±0.09	0.68±0.12	0.79±0.13

[a] In fatty tissue, the single component relaxation times have to be considered as rough estimations

consider the magnetic flux density B_0 at which the T_1 measurement was done.

- Relaxation processes often consist of multiple components, so that the description by a mono-exponential function is only a rough approximation. The relaxation times given in Table 2.2.2 therefore only represent weighted mean values of an entire spectrum of exponential functions, characterizing the relaxation behavior of protons in different cell and tissue compartments between which the water exchange is slow. However, at the timescale relevant for MRI, relaxation processes of most tissues can be approximated rather well by a single exponential function. An exception is fat-containing tissue (such as subcutaneous fatty tissue or bone marrow), which demands at least two exponential functions to be considered for the parameterization of the relaxation processes observed.

2.2.6 The MR Experiment

Figure 2.2.17 shows the general setup of an MR experiment; technical details will be presented in Sect. 2.5. The sample to be examined is located within a very homogeneous static magnetic field $\boldsymbol{B}_0$, which is created either by a permanent magnet or by a (superconducting) coil. The RF field required for the excitation of the spin system is generated by a transmit coil connected to the RF transmit system. This RF coil is positioned in such a way that the radiofrequency field $\boldsymbol{B}_1(t)$ is irradiated perpendicular to the $\boldsymbol{B}_0$ field into the sample volume.

Remark: Whereas atomic nuclei with a nuclear spin quantum number of $I \geq 1$ can interact with both the electric and the magnetic component of the electromagnetic RF field, spin-1/2 nuclei are only affected by the magnetic component $\boldsymbol{B}_1(t)$ of the RF field.

After excitation of the spin system by an RF pulse, the precessing transverse magnetization M_{xy} in turn induces a weak alternating voltage in a receiver coil, which in general is identical to the transmit coil (Fig. 2.2.18a). The measured voltage is amplified, filtered, digitalized, and fed to the computer of the MR system.

The measured MR signal $S(t)$ has the form of a damped oscillation (Fig. 2.2.18b), which is denoted as the free induction decay (FID). The FID signal has the following characteristic features:

- It oscillates with the Larmor frequency ω_0 of the stimulated nuclei.
- It decays in time with the time constant T_2^*.
- Its initial amplitude is proportional to the number N of the excited spins in the sample ($N = \rho V \propto M_0 V$; cf. Eq. 2.2.5).

If the sample contains nuclei of a certain type whose resonance frequency slightly differs due to intramolecular interactions (see Sect. 2.2.8), the MR signal induced in the receiver coil will consist of several interfering decay curves. However, such a curve is rather complicated to analyze and interpret. Therefore, the detected curve is usually spit up into its frequency components (Fourier analysis, see Sect. 2.2.5.1) and presented as frequency spectrum. Both types of description are merely different representations of the same data, which can be transformed into one another mathematically by a Fourier transformation.

Example: Figure 2.2.18b,c illustrates the relation between the description of the MR signal in the time or frequency domain by the example of a substance whose MR spectrum only shows one resonance line.

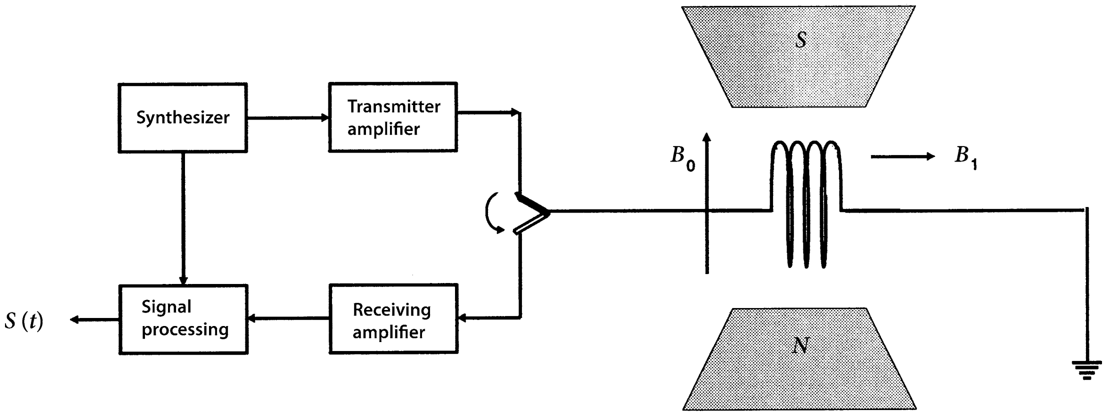

Fig. 2.2.17 Principle setup of an MR experiment. The object to be measured is placed within a homogeneous static magnetic field $\boldsymbol{B}_0$. Excitation of the spin system is performed by an RF field $\boldsymbol{B}_1(t)$ irradiated perpendicularly to $\boldsymbol{B}_0$ by an RF coil. After excitation, the MR signal of the sample is detected by an RF coil and transferred via a receiver channel to the computer of the MR system. (For details, see Sect. 2.5)

For quantitative analysis of an MR spectrum, the following features are important:

- The center of the resonance curve is at the Larmor frequency ω_0.
- The full width $\Delta\omega$ at half maximum of the curve is related with the characteristic time constant T_2^* of the FID by the relation $\Delta\omega = 2/T_2^*$.
- The area under the curve is approximately proportional to the number of excited nuclei in the sample.

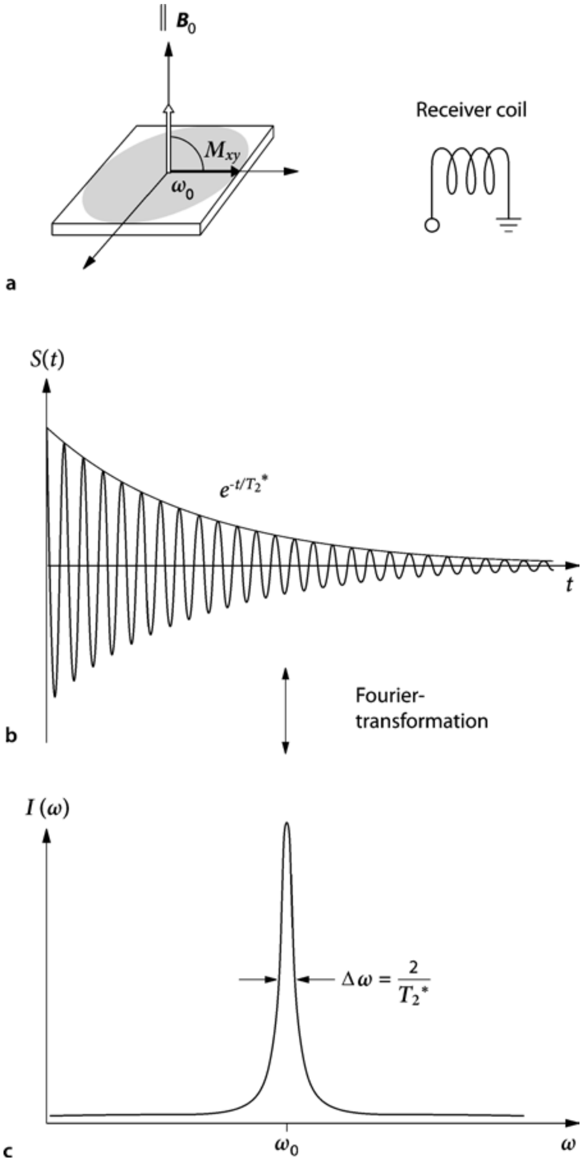

Fig. 2.2.18 Free induction decay (FID) and frequency spectrum. **a** After excitation of the spin system by a 90° pulse the magnetization M_{xy} precesses with the Larmor frequency ω_0 around the direction of the $\boldsymbol{B}_0$ field and induces an electric voltage in the receiver coil. **b** The measured FID signal $S(t)$ has the form of a damped oscillation, the frequency of which is given by the Larmor frequency ω_0. The decay of the signal is defined by the time constant T_2*. **c** A Fourier transformation of the FID signal gives the frequency spectrum of the MR signal. The resonance curve has its center at the Larmor frequency ω_0; its full width at half maximum (FWHM) is related with the characteristic time constant T_2* of the FID by the relation $\Delta\omega = 2/T_2^*$

2.2.7 Standard Pulse Sequences

In an MR experiment, only the RF signal can be determined by measurement, which is induced by the rotating transverse magnetization M_{xy} in the receiver coil (cf. Sect. 2.2.6). Nevertheless, a large variety of MR experiments can be realized that differ in the way by which the spin system is excited and prepared by means of RF pulses before the signal is acquired. A defined sequence of RF pulses, which is usually repeated several times, is called a pulse sequence. In the following, three "classical" pulse sequences are described that are frequently used for MR experiments (imaging sequences are described in Sect. 2.4):

- The saturation recovery sequence
- The inversion recovery sequence
- The spin-echo sequence.

2.2.7.1 Saturation Recovery Sequence

The saturation recovery (SR) sequence consists of only a single 90° pulse, which rotates the longitudinal magnetization M_z into the x–y-plane. The FID signal is acquired immediately after the RF excitation of the spin system. After a delay time, the repetition time T_R, the sequence is repeated. The SR sequence is described schematically by the pulse scheme (90°–AQ– T_R) (AQ = signal acquisition period; Fig. 2.2.19a).

If the repetition time T_R is long compared to T_1, the magnetization $\boldsymbol{M}$ relaxes back to its equilibrium state (see Fig. 2.2.14). In this case, the initial amplitude of the FID, even after repeated excitations, does only depend on the equilibrium magnetization M_0 and does not show any T_1 dependency. However, if the repetition time T_R is shortened to a value that is comparable to T_1, the longitudinal magnetization M_z will not fully relax after excitation, and the following 90° pulse will rotate the reduced longitudinal magnetization $M_z(T_R) = M_0[1-\exp(-T_R/T_1)]$ into the x–y-plane (Fig. 2.2.19b, c). Under the assumption that the transverse magnetization after the repetition time T_R has been decreased to zero ($T_R >> T_2$*), the following expression is obtained for the initial amplitude S_{SR} of the FID signal:

$$S_{SR} \propto N\,(1-e^{-T_R/T_1}), \qquad (2.2.8)$$

which exclusively depends on the relaxation time T_1 and the number N of the excited spins in the sample.

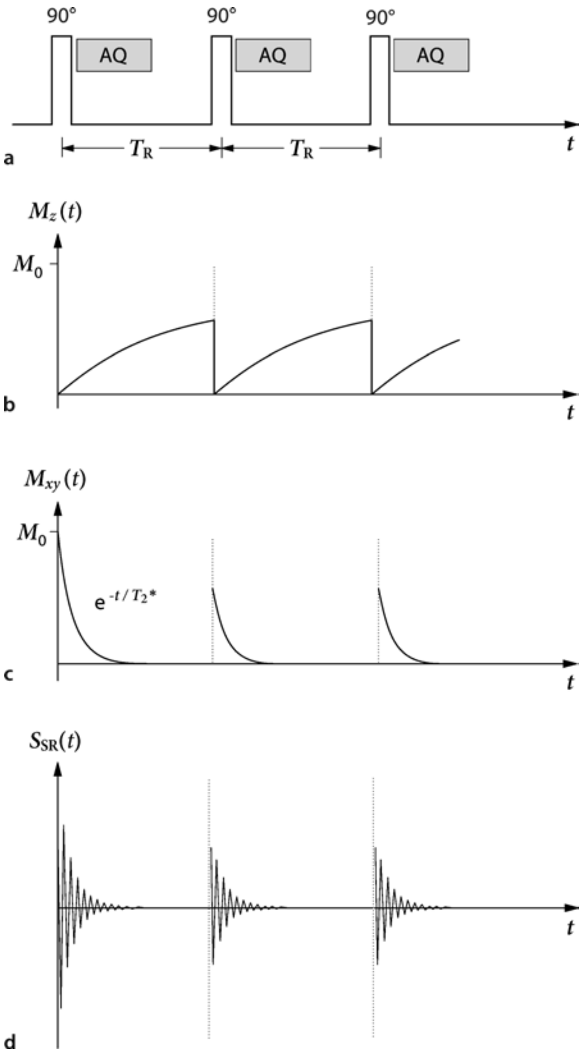

Fig. 2.2.19 Saturation recovery sequence. **a** Pulse scheme of the SR sequence (*AQ*: signal acquisition). **b** The 90° pulse rotates the actual longitudinal magnetization into the x–y-plane. During the repetition time T_R, the longitudinal magnetization relaxes toward the equilibrium magnetization M_0. The speed of this process is described by the longitudinal relaxation time T_1. Note that by the first 90° pulse, the equilibrium magnetization M_0 is rotated into the x–y-plane, whereas the subsequent 90° pulses rotate the reduced longitudinal magnetization $M_z(T_R) = M_0[1 - \exp(-T_R/T_1)]$. **c** Temporal evolution of the transverse magnetization M_{xy} in the rotating frame. **d** Induced MR signal $S_{SR}(t)$

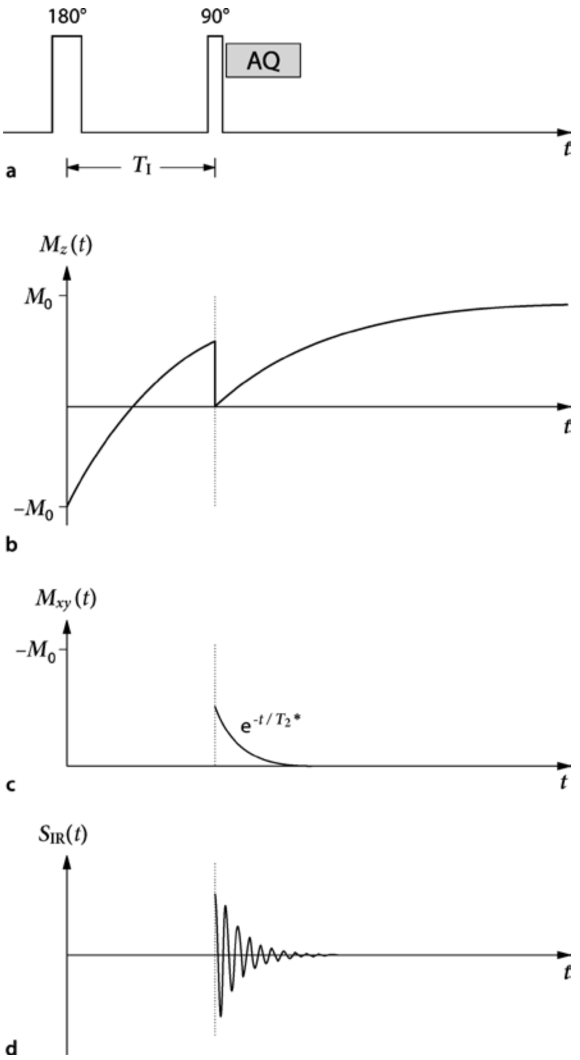

Fig. 2.2.20 Inversion recovery sequence. **a** Pulse scheme of the IR sequence (*AQ*: signal acquisition). **b** Initially, the longitudinal magnetization is inverted by the 180° pulse (inversion pulse), which is followed after an inversion time T_I by a 90° pulse (readout pulse), which rotates the existing longitudinal magnetization $M_z(T_I)$ into the x–y-plane. After the 90° pulse, the longitudinal magnetization relaxes toward the equilibrium magnetization M_0. **c** Temporal evolution of the transverse magnetization M_{xy} in the rotating frame. **d** Induced MR signal $S_{IR}(t)$

2.2.7.2 Inversion Recovery Sequence

In the inversion recovery (IR) method, the longitudinal magnetization is inverted by a 180° pulse (inversion pulse), which is followed after an inversion time T_I by a 90° pulse (readout pulse). Immediately after the 90° pulse, which rotates the partially relaxed longitudinal magnetization $M_z(T_I)$ into the x–y-plane, the FID signal is acquired (Fig. 2.2.20).

The IR sequence is described by the pulse scheme (180°– T_I – 90° – AQ). The initial amplitude S_{IR} of the FID signal is directly proportional to the longitudinal magnetization immediately before irradiation of the read-out pulse, just as is the case in the SR method. In contrast to the SR sequence, however, the change in the longitudinal magnetization is twice as high and thus—in analogy to Eq. 2.2.8—the following expression is obtained (compare Figs. 2.2.19b and 2.2.20)

$$S_{\mathrm{SR}} \propto N\,(1-2e^{-T_I/T_1}). \tag{2.2.9}$$

The derivation of this relation is based on the assumption that the spin system is in its equilibrium state before it is excited by the inversion pulse. When repeating the IR sequence, one has therefore to make sure that the repetition time T_R is markedly longer than the relaxation time T_1.

Remark: If the IR sequence is repeated several times with different inversion times T_I, it is possible to sample the temporal course of the longitudinal magnetization step by step, since the initial amplitude of the FID signal is directly proportional to the longitudinal magnetization at time T_I (see Fig. 2.2.20). This procedure is applied frequently in order to determine the relaxation time T_1 of a sample according to Eq. 2.2.9.

2.2.7.3 Spin-Echo Sequence

As explained in Sect. 2.2.5.2 the temporal decay of the transverse magnetization M_{xy} is caused by two effects: fluctuating local magnetic fields and spatial inhomogeneities of the magnetic field $\boldsymbol{B}_0$. The transverse magnetization M_{xy} therefore relaxes not with the substance-specific relaxation time T_2 but rather with the effective time constant T_2^* ($T_2^* < T_2$). When determining the relaxation time T_2, it is therefore important to compensate the effect of the field inhomogeneities. This can be done, as E. Hahn has already shown in 1950, by using the so-called spin-echo (SE) sequence. This sequence utilizes the fact that the dephasing of the transverse magnetization caused by $\boldsymbol{B}_0$ inhomogeneities is reversible since they do not vary in time, whereas the influence of the fluctuating local magnetic fields is irreversible.

In order to understand the principle of the SE sequence with the pulse scheme (90° – τ – 180° – τ – AQ; see Fig. 2.2.22a), we initially neglect the influence of the

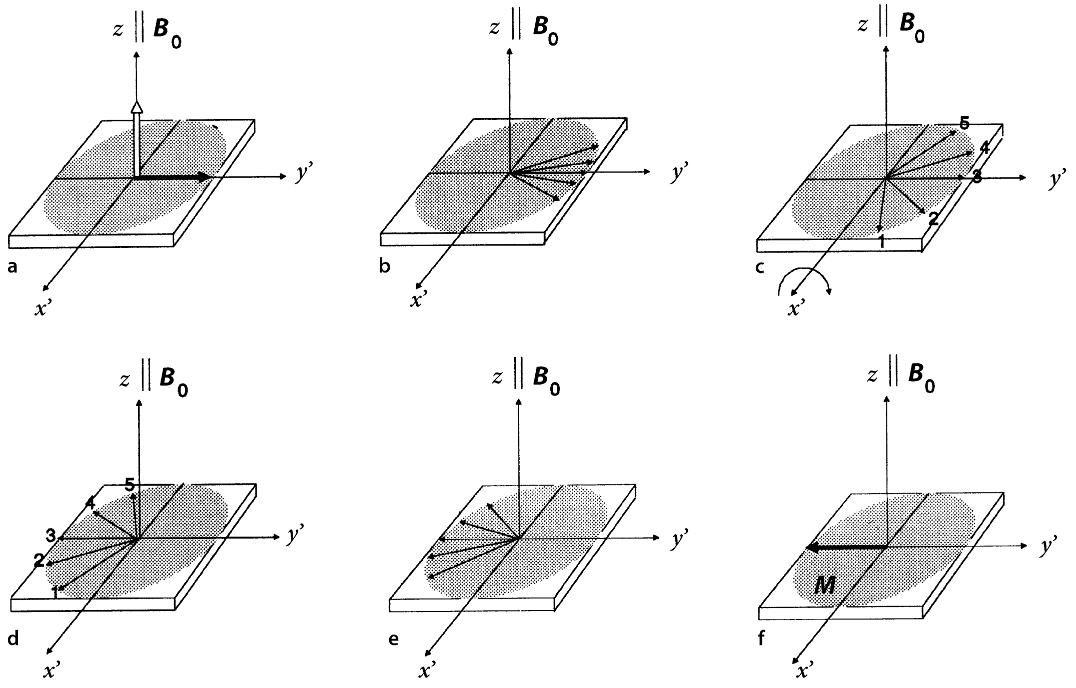

Fig. 2.2.21 Explanation of the spin-echo experiment in the rotating frame. For the sake of simplicity, the substance-specific transverse relaxation is not been considered in this figure. **a** The 90° pulse rotates the longitudinal magnetization into the x'–y'-plane. **b,c** In the course of time, the magnetization components, which form together the transverse magnetization M_{xy}, dephase so that the transverse magnetization decays with the characteristic time constant T_2^* (see Fig. 2.2.15). **d,e** Irradiation of the 180° pulse along the x'-axis mirrors the dephased magnetization vectors at the x'-axis. As neither the precession direction nor the precession velocity of the magnetization components are altered by the 180° pulse, the components rephase and thus the transverse magnetization increases. The regeneration of the transverse magnetization is called a spin echo. **f** At the time $T_E = 2\tau$, all magnetization components point into the same direction again. Due to the rephrasing effect of the 180° pulse, the amplitude $M_z(T_E = 2\tau)$ of the spin echo is independent of the static inhomogeneities of the $\boldsymbol{B}_0$ field

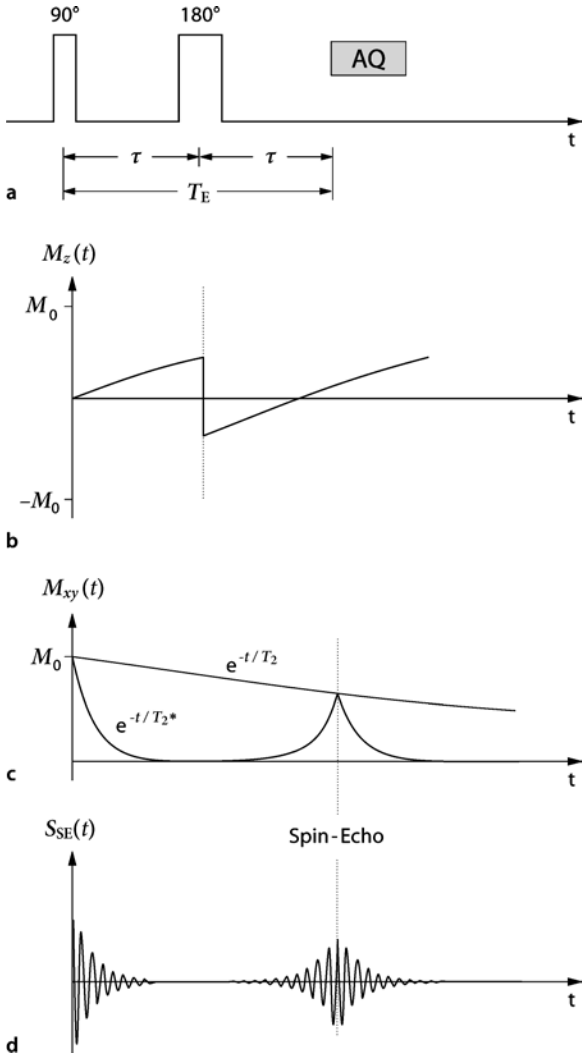

Fig. 2.2.22 Spin-echo sequence. **a** Pulse scheme of the SE sequence (*AQ*: signal acquisition). **b** Temporal evolution of the longitudinal magnetization M_z. Note that the 180° pulse at the time $t = \tau$ inverts the longitudinal magnetization. **c** Temporal evolution of the transverse magnetization M_{xy} in the rotating frame. After excitation of the spin system by the 90° pulse, the transverse magnetization decays with the characteristic time constant T_2*. The 180° pulse results in a regeneration of the transverse magnetization denoted as spin-echo. **d** Induced MR signal $S_{SE}(t)$

fluctuating local magnetic fields and solely consider the static magnetic field inhomogeneities. Immediately after the 90° pulse, all magnetization components composing the transverse magnetization M_{xy} point along the y'-axis (Fig. 2.2.21a). Shortly afterward, some components precess faster, others more slowly around the direction of the $\boldsymbol{B}_0$ field, so that the initial phase coherence is lost (see Fig. 2.2.15). When looking at this situation from a rotating frame, one observes a fanning out of the magnetization components around the y'-axis (Fig. 2.2.21.b,c). If a 180° pulse is applied after a time delay τ along the x'-axis, the magnetization components will be mirrored with respect to this axis (Fig. 2.2.21d). However, the 180° pulse does not change the rotational direction of the magnetization components, but merely inverts the distribution of the components: the faster components now follow the slower ones (Fig. 2.2.21e). After the time $t = 2\tau$, all magnetization components again point to the same direction, and the signal comes to a maximum (Fig. 2.2.21f). The 180° pulse thus induces a rephasing of the dephased transverse magnetization, which causes the MR signal to increase and to generate a spin echo (Fig. 2.2.22). After the spin-echo time $T_E = 2\tau$, the echo decays again—as the original FID does—with the time constant T_2*.

Due to the rephasing effect of the 180° pulse, the spin-echo signal $S_{SE}(T_E)$ is independent from the inhomogeneities of the static magnetic field: the loss of signal at the time $t = T_E$ as compared to the initial signal $S_{SE}(0)$ is determined exclusively via the substance-specific relaxation time T_2. If one irradiates a sequence of K 180° pulses at the times $\tau, 3\tau, 5\tau, \ldots, (2K\text{–}1)\tau$, one can detect a spin echo in between the subsequent 180° pulses (Fig. 2.2.23). The envelope of the echo signals $S_{SE}(2\tau k)$ ($k = 1, 2, 3, \ldots, K$) decays exponentially with the relaxation time T_2.

$$S_{SE} \propto N\, e^{-2\tau k/T_2}. \tag{2.2.10}$$

The major advantage of this multi echo sequence consists in the fact that the T_2 decay can very effectively be detected by a single measurement (Fig. 2.2.23).

2.2.8 Influence of the Electron Shell on the Local Magnetic Field

All the considerations so far have been based on the assumption that the external magnetic field $\boldsymbol{B}_0$ created by the RF coil is not altered by the electrons surrounding a nucleus. However, this is not the case as the electrons interact with the applied external magnetic field. In biological tissues in which atoms are covalently bound, two related effects need to be considered, the diamagnetism and the chemical shift.

2.2.8.1 Macroscopic Effect: Diamagnetism

Diamagnetism is a general feature of matter and is because electrons attempt to shield the interior of the sample against the external magnetic field. In electrodynamics, this effect is described by Lenz's law. It states that the current induced in a circuit by the change of a magnetic field is directed in such a way that the secondary magnetic field induced by the electric current weakens the

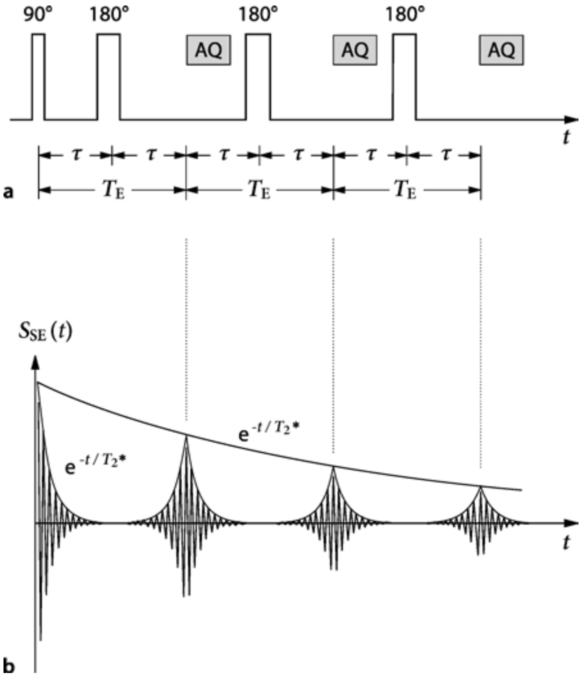

Fig. 2.2.23 Multi echo sequence. **a** Pulse scheme (*AQ:* signal acquisition). **b** Decay of the echo amplitudes as a function of time. The signal decay is determined exclusively by the substance-specific transverse relaxation time T_2, whereas the decay and the regeneration of the FID are essentially determined by technically conditioned field inhomogeneities

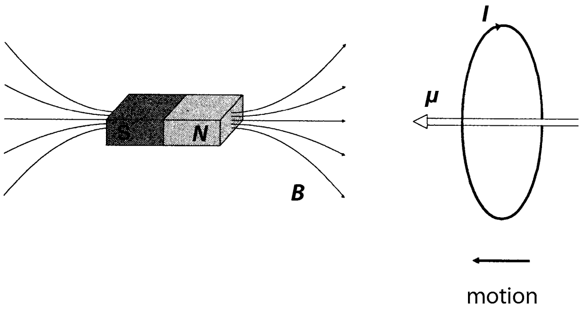

Fig. 2.2.24 Lenz's law. When a circuit is approached to a bar magnet with the magnetic flux density $\boldsymbol{B}$, a current $\boldsymbol{I}$ is induced in the circuit. This current induces a magnetic dipolar field, which is directed in such a way that it weakens the primary magnetic field. Magnitude and orientation of the dipolar field are described by the magnetic moment $\boldsymbol{\mu}$

primary magnetic field (Fig. 2.2.24). If a sample is positioned in an external magnetic field, a current is induced in the electron shell of the atoms and molecules, whose magnetic moment is directed against the external magnetic field, following Lenz's law. However, in contrast to the electrons within a macroscopic circuit, the electrons in the electron shell are "frictionless," which means that an induced electron current remains constant until the external magnetic field changes or until the sample is removed from the magnetic field.

The sum of the induced magnetic moments of the electrons per volume is—similar to the nuclear magnetization $\boldsymbol{M}$—denoted as electron magnetization $\boldsymbol{M}_e$. For averaging, the volume has to be chosen in such a way that, on the one hand, a great number of atoms and molecules is contained, and, on the other hand, that it is small compared to the volume of the sample (for example, 1 μm^3 water contains about $3.3 \cdot 10^{10}$ water molecules). The magnetization $\boldsymbol{M}_e$ thus represents a macroscopic quantity *per definitionem*.

Remark: Due to practical reasons, distinction is made in electrodynamics between free and bound currents: Free currents are experimentally controllable and are linked to macroscopic circuits, whereas bound currents are linked to atomic and molecular magnetic moments in matter. The field related to free currents is denoted as magnetic field $\boldsymbol{H}$ (unit: ampere/meter), the field created by the total current, i.e. by both the free and the bound current, as magnetic flux density $\boldsymbol{B}$ (unit: Tesla). At every point in space, the vector quantities $\boldsymbol{H}$, $\boldsymbol{B}$, and $\boldsymbol{M}_e$ are related by

$$\boldsymbol{B} = \mu_0(\boldsymbol{H} + \boldsymbol{M}_e), \tag{2.2.11}$$

with $\boldsymbol{M}_e \neq 0$ only inside the sample. In free space, Eq. 2.2.11 reduces to $\boldsymbol{B} = \mu_0\boldsymbol{H}$. The constant $\mu_0 = 1.257 \cdot 10^{-6}$ Vs/Am is known as the magnetic permeability of vacuum.

For most (non-ferromagnetic) substances, the electron magnetization $\boldsymbol{M}_e$ is proportional to the magnetic field strength $\boldsymbol{H}$:

$$\boldsymbol{M}_e = \chi\boldsymbol{H}. \tag{2.2.12}$$

The dimensionless proportionality constant χ is called the magnetic susceptibility. For diamagnetic substances, χ is, according to Lenz's law, always negative and has a very small absolute value (e.g. water: $\chi = -0.72 \cdot 10^{-6}$).

When putting a diamagnetic sample into an originally homogeneous magnetic field, a magnetization $\boldsymbol{M}_e$ is induced according to Eq. 2.2.12, which itself creates a magnetic field that counters the primary field. Therefore, the field distribution of the magnetic flux density $\boldsymbol{B}$ differs both inside and outside of the sample from the original field distribution.

Example: Figure 2.2.25 shows the field distribution of the magnetic flux density $\boldsymbol{B}$ inside and outside of a homogeneously magnetized sphere (χ = constant), which has been brought into an originally homogeneous field $\boldsymbol{B}_0$. Inside the sphere, the magnetic flux density $\boldsymbol{B}$ is given by $\boldsymbol{B} = (1{+}2\chi/3)\boldsymbol{B}_0$. It should be noted, however, that the homogeneously magnetized sphere represents an ideal case in which the $\boldsymbol{B}$ field is homogeneous on

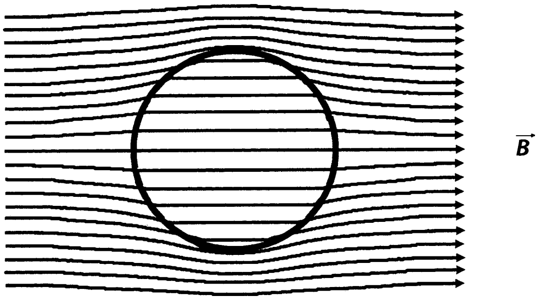

Fig. 2.2.25 Variation of the magnetic field by a diamagnetic sphere. Distribution of the ***B*** field inside and outside a homogeneously magnetized sphere, which was positioned in an originally homogeneous magnetic field. It should be noted, however, that field variations caused by biological tissue are markedly weaker than illustrated here

its inside, whereas in general, the ***B*** field is also inhomogeneous inside the object.

The discussion provides three important aspects with respect to MR examinations of humans:

- The distribution of the magnetic flux density ***B*** in the human body depends on the position, size, form, and magnetic susceptibility of all tissues and organs of the body.
- At the interface between tissues with different magnetic susceptibilities, there are local field inhomogeneities.
- The distortion of the external magnetic field caused by the body adds to the technical imperfections of the external field $\boldsymbol{B}_0$.

In MRI, susceptibility-related inhomogeneities of the static magnetic field inside the body are obviously unavoidable and can result in image artifacts. In spectroscopic examinations, however, this problem can be reduced by acquiring only MR signals from small, morphologically homogeneous tissues regions. Furthermore, one has the possibility to locally adjust the ***B*** field by means of external shim coils generating a weak additional magnetic field, so the homogeneity within the examined region fulfils the demands.

When speaking of the homogeneity of the ***B*** field within a given region of the body, this relates to the average macroscopic field; on the microscopic scale, the magnetic field is always inhomogeneous.

2.2.8.2 Microscopic Effect: Chemical Shift

The Larmor frequency of a nucleus is determined by the local magnetic field $\boldsymbol{B}_{\text{lok}}$ at the position of the nucleus, not by the macroscopic field ***B***, which has been averaged over a small but microscopically large volume surrounding the nucleus. Denoting the perturbation of the mean field ***B*** at the position of a nucleus caused by the surrounding electrons of the molecule by $\Delta\boldsymbol{B}$, we get the relation

$$\boldsymbol{B}_{\text{lok}} = \boldsymbol{B} + \Delta\boldsymbol{B}. \qquad (2.2.13)$$

As experimental and theoretical investigations have shown, the small local field perturbation $\Delta\boldsymbol{B}$ is proportional to the macroscopic field

$$\Delta\boldsymbol{B} = -\sigma\boldsymbol{B}, \qquad (2.2.14)$$

which yields the following expression for the resonance frequency of the nucleus, considered

$$\omega = \gamma\, B_{\text{lok}} = \gamma(1-\sigma)B. \qquad (2.2.15)$$

The dimensionless "shielding constant" σ gives the relative resonance frequency shift that is independent of the magnitude of the magnetic field. This shift depends on the distribution of the electrons around the nucleus and thus has different values in different molecules.

Remark: The magnitude of the additional field $\Delta\boldsymbol{B}$ at the position of a nucleus generally depends on the orientation of the molecule relative to the macroscopic field ***B***. In molecules that rotate rapidly, such as in fluids and soft tissues, the chemical shift anisotropy vanishes, so the quantity σ in Eq. 2.2.14 could be defined as a direction-independent constant. This quantity describes the shielding effect of the electron shell averaged over all spatial directions.

As the absolute value of the frequency shift cannot easily by measured, it is usually determined relative to the resonance frequency ω_R of a reference substance. The difference $(\omega - \omega_R)$ of the resonance frequencies is expressed as dimensionless constant

$$\delta = \frac{\omega - \omega_R}{\omega_0} \cdot 10^6 \cong (\sigma_R - \sigma) \cdot 10^6 \qquad (2.2.16)$$

relative to the frequency $\omega_0 = \gamma B_0$ of the MR system in parts per million (ppm). The chemical shift δ provides information about how the atom with the nucleus under study is bonded in the molecule and thus makes MR spectroscopy a powerful tool for the determination of the structure of molecules as well as for the investigation of biochemical processes. For the ^{1}H nucleus, which is surrounded by only one electron, the chemical shift is about 10 ppm; for atoms with several electrons (e.g., ^{13}C, ^{19}F, and ^{31}P) it can amount to several hundreds of ppm. To resolve these small differences in frequency it is necessary to use a strong and homogeneous static magnetic field ($B_0 \geq 1.5\,$T, $\Delta B/B_0 < 0.1$–0.5 ppm depending on the nucleus).

Example: Figure 2.2.26 shows the ^{1}H spectrum of ethanol (CH_3–CH_2–OH). Due to the different chemical surroundings of the protons in the hydroxyl, methylene, and methyl group, the spectrum shows three different resonance lines. The ratio of the areas under the resonance lines is 1 : 2 : 3 and thereby corresponds to the number of protons in the three groups.

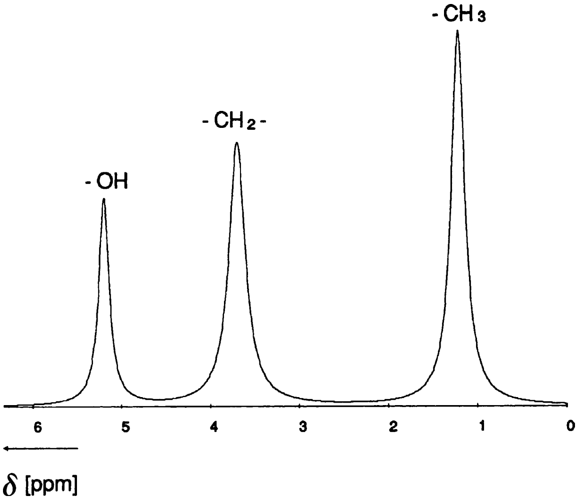

Fig. 2.2.26 Proton MR spectrum of ethanol (CH_3–CH_2–OH). The three resonances can be assigned to the protons of the hydroxyl, methylene and methyl groups. The ratio of the area under the resonance curves is 1:2:3 and thereby corresponds to the number of protons in the three groups

References

1. Bottomley PA, Foster TH, Argersinger RE, Pfeifer LM (1984) A review of normal tissue NMR relaxation times and relaxation mechanisms from 1 to 100 MHz: dependence on tissue type, NMR frequency, temperature, species, excision, and age. Med Phys 11:425–448
2. Harris RK (1986) Nuclear magnetic resonance spectroscopy. Longman Scientific Technical, Harlow

Suggested Reading

1. Abragam A (1986) Principles of nuclear magnetism. Oxford University Press, London
2. Becker ED (1980) High-resolution NMR. Academic, New York
3. Harris RK (1986) Nuclear magnetic resonance spectroscopy. Longman Scientific Technical, Harlow
4. Hauser KH, Kalbitzer KR (1991) NMR in medicine and biology. Springer, Berlin Heidelberg New York
5. Levitt MH (2001) Spin dynamics: basics of nuclear magnetic resonance. Wiley, New York
6. Slichter CP (2006) Principles of magnetic resonance, 3rd edn. Springer, Berlin Heidelberg New York Tokyo

2.3 Image Reconstruction

G. Brix

If the object to be imaged, such as the human body, is divided into small cuboidal volume elements (i.e., voxels), the task in MR imaging is to distinguish the signal contributions of the voxels to the detected summation signal from one another and to present them in form of sectional images (tomograms). This can be achieved by superimposing the homogeneous magnetic field $\boldsymbol{B}_0$ by an additional magnetic field with a well-defined dependence on the spatial position, so the Larmor frequency of the MR signal becomes a function of space.

2.3.1 Magnetic Gradient Fields

In practice, image reconstruction is achieved almost exclusively by means of magnetic gradient fields. These are three additional magnetic fields $\boldsymbol{B}^x$, $\boldsymbol{B}^y$, and $\boldsymbol{B}^z$, whose field vectors point toward the z-direction and whose field strengths depend linearly on the spatial position x, y, or z, respectively (Fig. 2.3.1). If the z-components of the three magnetic gradient fields are denoted by B^x, B^y, and B^z, the fields can be expressed as

$$B^x = G^x x,\ B^y = G^y y, \text{ and } B^z = G^z z, \tag{2.3.1}$$

where the proportionality constants G^x, G^y, and G^z describe the magnitude or steepness of the orthogonal gradient fields.

Remark: The magnetic gradient fields are shortly denoted as x-, y-, or z-gradients. What is meant are magnetic fields $\boldsymbol{B}^x$, $\boldsymbol{B}^y$, and $\boldsymbol{B}^z$, the magnitude of which varies linearly along the x-, y-, or z-axis, respectively (see Fig. 2.3.1).

In order to avoid image distortions, the magnitude of the gradients has to be chosen in such a way that the local field variations are markedly greater than the local inhomogeneities of the main magnetic field $\boldsymbol{B}_0$; typical values are between 1 and 50 mT/m. Technically, the gradient fields $\boldsymbol{B}^x$, $\boldsymbol{B}^y$, and $\boldsymbol{B}^z$ are produced by three coil systems (gradient coils), which can be operated independently from one another.

Example: Assuming a patient diameter in the x-direction of $X = 30$ cm, a magnetic flux density of the static field of $B_0 = 1$ T, and a gradient strength of $G^x = 10$ mT/m, the magnetic field $B = B_0 + G^x x$ will increase within the patient $(-X/2 \leq x \leq +X/2)$ linearly from 0.9985 to 1.0015 T.

In MR imaging, the magnetic gradient fields are used in two different ways:

- For selective excitation of the nuclear spins in a partial body region (e.g., a slice).
- For position encoding within an excited partial body region (e.g., a slice).

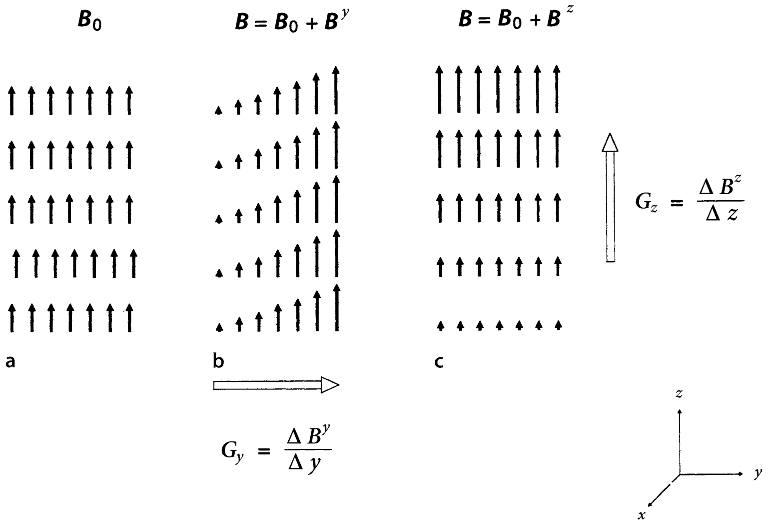

Fig. 2.3.1 Gradient fields. For image reconstruction, the homogeneous magnetic field $\boldsymbol{B}_0$ shown in **a** is superimposed by additional magnetic fields $\boldsymbol{B}^x$, $\boldsymbol{B}^y$, and $\boldsymbol{B}^z$, so-called gradient fields, the field vector of which points into the z-direction and the magnitude of which (length of the *black arrows*) depends linearly on the spatial coordinate x, y, and z, respectively. **b** and **c** show the field distributions in case the field $\boldsymbol{B}_0$ is superimposed by a gradient field $\boldsymbol{B}^y$ and $\boldsymbol{B}^z$, respectively. The open arrows indicate the direction of the field variation, whereas the constants G^y and G^z represent the magnitude of the field variation per unit of length. If the z-components of the two magnetic gradient fields are given by B^y and B^z, then the gradient strengths are defined by $G^y = \Delta B^y/\Delta y$ and $G^z = \Delta B^z/\Delta z$, respectively

2.3.2 Slice-Selective Excitation

An MR signal can principally only be detected from the volume in which the nuclei have been excited before by an RF pulse. This fact is used in planar imaging methods, in order to reduce the primarily 3D reconstruction problem to a 2D one by selectively exciting only nuclei in a thin slice of the body.

Remark: Depending on the type of the selectively excited partial body volume, one distinguishes between single-point, line, planar, and volume sampling strategies (Fig. 2.3.2). As the intensity of the detected MR signal is proportional to the number of nuclei within the excited volume, the different strategies markedly differ in the time required for the acquisition of qualitatively comparable MR images. Due to the long measurement time, single-point and line scanning techniques have not been successful in clinical practice.

In order to excite a distinct slice of the body selectively, the homogeneous static magnetic field $\boldsymbol{B}_0$ is superimposed with a gradient field (slice-selection gradient) that varies perpendicular to the slice, i.e., for an axial slice a gradient field in longitudinal direction of the body. Due to this superposition, the Larmor frequency ω of the nuclei varies along the direction of the gradient. If we consider, for instance, a z-gradient with magnitude G^z, the Larmor frequency is given by (see Fig. 2.3.1c):

$$\omega(z) = \gamma(B_0 + G^z z). \qquad (2.3.2)$$

Consequently, an object slice $z_1 \leq z \leq z_2$ is characterized by a narrow frequency interval $\gamma(B_0 + G^z z_1) \leq \omega \leq \gamma(B_0 + G^z z_2)$. If one irradiates an RF pulse, the frequency spectrum of which coincides with this frequency range, only the nuclei within the chosen slice will be excited (Fig. 2.3.3).

For the definition of a body slice, this has two implications:

- The width $d = z_2 - z_1$ of the slice can be varied by changing either the bandwidth of the RF pulse, i.e. the width of the frequency distribution, or the gradient strength G^z.
- The position of the slice can be altered by shifting the frequency spectrum of the RF pulse.

The practical realization of the concept of slice-selective excitation requires not only the shape of the RF pulse but also the switching mode of the slice-selection gradient to be carefully optimized:

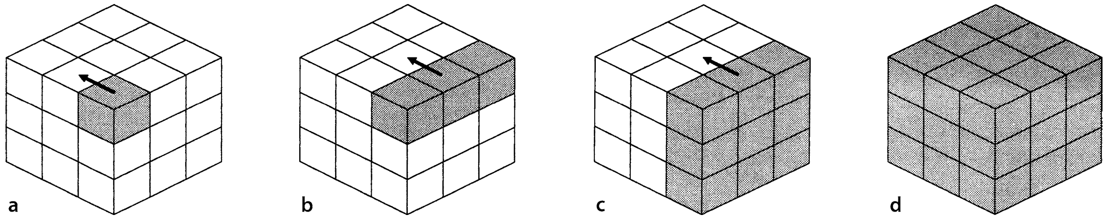

Fig. 2.3.2 Imaging strategies. **a** Single-point, **b** line, **c** planar, and **d** volume scanning of a sampling object. In each case the excited partial volumes are marked in *gray*

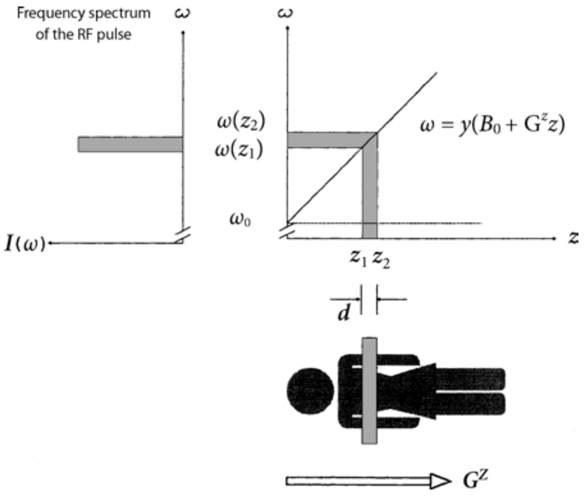

Fig. 2.3.3 Principle of slice-selective excitation. The main magnetic field $\boldsymbol{B}_0$ is superimposed with a magnetic gradient field $B^z = G^z z$ in z-direction (slice-selection gradient), so the Larmor frequency $\omega(z) = \gamma(B_0 + G^z z)$ of the nuclei depends linearly from the spatial coordinate z. The slice $z_1 \leq z \leq z_2$ within the object is thus unambiguously described by the frequency interval $\omega(z_1) \leq \omega(z) \leq \omega(z_2)$. If one irradiates an RF pulse with a frequency spectrum that corresponds to this frequency interval, only the nuclei within the chosen slice will be excited

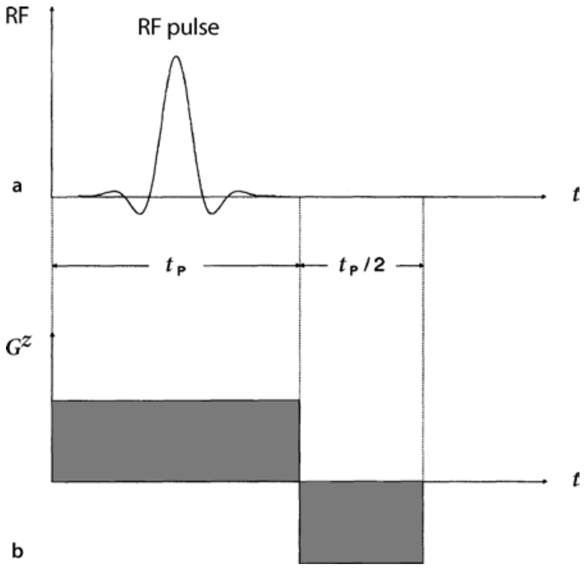

Fig. 2.3.4 Pulse modulation and gradient refocusing. **a** In order to obtain an approximately rectangular slice profile, one uses an RF pulse, the envelope of which is not rectangular but modulated in time. **b** If one dissects a thicker slice of the object into several thin subslices, an optimized RF pulse will deflect the magnetization of each subslice by the same angle from the *z*-direction, but the magnetization components are dephased after RF excitation, because the Larmor frequencies in the subslices differ. If a 90° pulse with duration t_P is used for slice-selective excitation, then the dephasing effect can be compensated in good approximation by inverting the gradient field after excitation for the duration $t_P/2$

- ***Pulse modulation:*** As shown in Fig. 2.2.10, the frequency spectrum of a rectangular RF pulse consists of several frequency bands with varying intensities. If such a pulse is used for the RF excitation, the profile of the excited slice is defined insufficiently. In order to obtain a uniform distribution of the transverse magnetization over the slice width, the shape of the selective RF pulse is modulated so that the frequency spectrum becomes as rectangular as possible ("sinc pulse," see Fig. 2.2.23a).
- ***Compensation gradients:*** If one imaginatively dissects an object slice into several thin subslices, then the magnetization components of all subslices will be deflected by the same angle from the *z*-direction when an optimized RF pulse is used for slice-selective excitation. However, the magnetization components will be dephased at the end of the excitation period t_P, since the Larmor frequencies of the distinct subslices differ from one another as the slice-selection gradient is switched on. This effect can be compensated by reversing the polarity of the gradient field for a well-defined period after RF excitation (Fig. 2.3.4b).

2.3.3 Principle of Spatial Encoding within a Partial Volume: Projections

After selective excitation of a partial body region, the MR signal from each voxel within this volume, e.g., a slice, needs to be spatially encoded. This can be achieved by two techniques: frequency and phase encoding of the MR signal. The principle of both encoding techniques will be explained in the following by the example of an axial slice parallel to the *x*–*y*-plane. For the sake of simplicity, relaxation effects are neglected in this connection.

2.3.3.1 Frequency Encoding

If the body to be imaged is placed in a homogenous magnetic field with the flux density B_0, the magnetization components of all voxels in the excited slice will precess with the same frequency around the direction of the $\boldsymbol{B}_0$ field. Thus, the frequency spectrum consist of only a single resonance line at the Larmor frequency $\omega_0 = \gamma B_0$—it does not contain any spatial information. However, if a magnetic gradient field, e.g., $B^x = G^x x$, is switched on during the acquisition phase of the MR signal (Fig. 2.3.5),

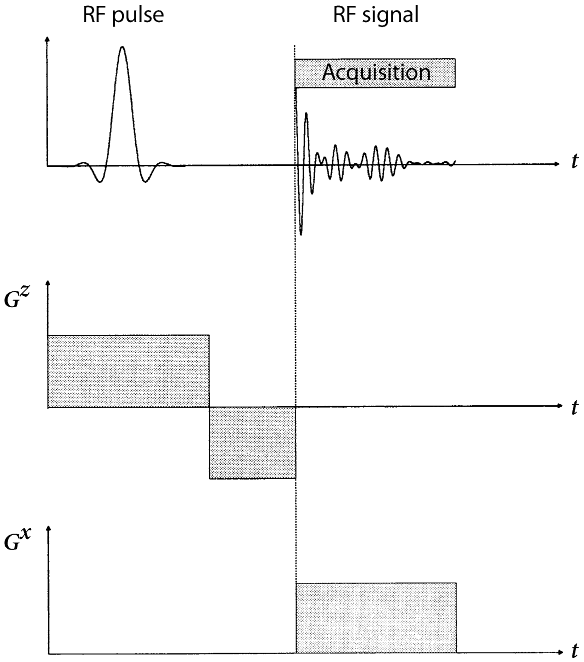

Fig. 2.3.5 Readout or frequency-encoding gradient. In frequency encoding, the main magnetic field $\boldsymbol{B}_0$ is superimposed with a gradient field (here $B^x + G^x x$) during the acquisition of the RF signal, so the precession frequency of the transverse magnetization in the selectively excited slice becomes a function of the coordinate *x*

the Larmor frequency is related to the position x (see Fig. 2.3.1) by the resonance condition

$$\omega(x) = \gamma(B_0 + G^x x). \tag{2.3.3}$$

Or in other words, nuclei in parallel strips oriented perpendicular to the direction of the readout (or frequency-encoding) gradient will experience a different magnetic field and thus contribute with different Larmor frequencies $\omega(x)$ to the detected MR signal of the excited slice—the spatial information is encoded in the resonance frequency.

In order to determine the contribution of the distinct frequency components to the summation signal, a Fourier transformation of the measured FID has to be performed (cf. Sect. 2.2.6). The intensity $I(\omega)$ of the resulting spectrum at the frequency ω is proportional to the number of nuclei precessing with this frequency, i.e., to the number of nuclei that are according to Eq. 2.3.3 at the position $x = (\omega - \gamma B_0) / \gamma G^x$. The frequency spectrum of the FID signal therefore gives the projection of the spin density distribution in the excited slice onto the direction of the readout gradient (Fig. 2.3.6).

Remark: When explaining the concept of frequency encoding, we assumed that there is only one resonance line in the frequency spectrum of the excited body region in the absence of the readout gradient. If this assumption is not fulfilled, i.e., if the spectrum contains several resonance lines due to chemical shift effects described in Sect. 2.2.8.2, then these frequency shifts will be interpreted by the decoding procedure (i.e., the Fourier analysis) of the FID signal as position information. Consequently, the spin density projections of molecules with different chemical shifts are shifted in space against one another. In ^{1}H imaging, the situation is rather easy, as only two dominant proton components contribute to the MR signal of the organism, the protons of the water molecules and those of the CH_2 group of fatty acids. As the resonance frequencies of the two components differ by about 3.5 ppm (Fig. 2.3.7), fat- and water-containing structures of the body are slightly shifted against one another in readout direction. This chemical-shift artifact becomes apparent predominantly at the interfaces between fat- and water-containing tissue.

From a technical point of view, the FID signal $S(t)$ can only be sampled and stored in discrete steps over a limited period of time t_{AQ}. Consequently, there is only a limited number $N = t_{AQ} / \Delta t$ of data points

$$S(\Delta t), S(2\Delta t), S(3\Delta t), \ldots, S(N\Delta t) \tag{2.3.4}$$

that can be used for Fourier transformation. Due to this reason, the spatial sampling interval Δx of the spin density projection is limited too. The following relations hold between the number N of data points, the maximum object size X, the spatial sampling interval Δx, the temporal

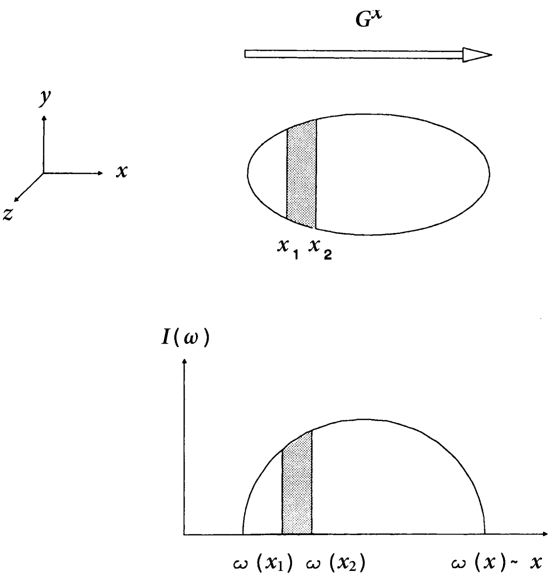

Fig. 2.3.6 Principle of frequency encoding. If the FID signal from a slice is measured in the presence of a gradient field $B^x = G^x x$ (see Fig. 2.3.5), then nuclei in strips oriented perpendicular to the direction of the gradient contribute with different Larmor frequencies $\omega(x) = \gamma(B_0 = G^x x)$ to the measured MR signal. The contribution $I(\omega)$ of the distinct frequency components to the summation signal can be calculated by a Fourier transformation of the FID signal. As the intensity $I(\omega)$ of the resulting spectrum at the frequency ω is, on the one hand, proportional to the number of nuclei precessing with this frequency, and, on the other hand, the spatial information is encoded in the frequency, the Fourier transformation yields the projection of the spin density distribution within the considered object slice on the direction of the readout gradient

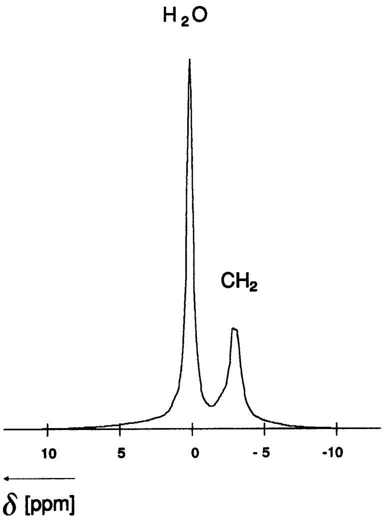

Fig. 2.3.7 In vivo ^{1}H spectrum of a human thigh at 1.5 T. The two resonance lines can be attributed to protons in water and in the CH_2 groups of fatty acids

sampling interval Δt, and the gradient strength G^x (sampling theorem):

$$\Delta x = X/N = 2\pi/\gamma G^x N\Delta t. \tag{2.3.5}$$

Example: If the FID signal is sampled 256 times at $\Delta t = 30\,\mu s$ in the presence of a magnetic gradient field of the strength $G^x = 1.566$ mT/m, then the resolution along the x-axis is $\Delta x = 1.953$ mm, and the maximum object size that can be imaged is $X = N\Delta x = 50$ cm.

With frequency encoding, the MR signal is sampled at discrete points in time $t_n = n\Delta t$ $(1 \le n \le N)$. According to Eq. 2.3.3, the transverse magnetization at the position x precesses under the influence of the readout gradient until the time t_n by the angle

$$\varphi_n(x) = (\gamma G^x x)t_n. \tag{2.3.6}$$

The spatial information is therefore encoded via the frequency $\omega(x)$ in the phase angles $\varphi_n(x)$ $(1 \le n \le N)$. However, the same phase angles can be realized by increasing the gradient strength $G_n^x = n\Delta G^x$ in equidistant steps ΔG^x at a fixed switch-on time of the gradient. This equivalent approach is called phase encoding.

2.3.3.2 Phase Encoding

The concept of phase encoding can easily be realized by applying a magnetic gradient field, e.g., $B^x = G^x x$, for a fixed time t_x before the FID signal is detected (Fig. 2.3.8). Under the effect of this phase-encoding gradient, the magnetization at the position x precesses by the phase angle

$$\varphi_n(x) = (\gamma\, G_n^x t_x)x = k_n x. \tag{2.3.7}$$

The parameter $k_n = \gamma G_n^x t_x = \gamma n \Delta G^x t_x$ is named spatial frequency. After switching off the phase-encoding gradient, the magnetization components of the voxels in the slice precess again with the original, position-independent Larmor frequency $\omega_0 = \gamma B_0$ around the direction of the $\boldsymbol{B}_0$ field—now, however, with position-dependent phase angles $\varphi_n(x)$. This is to say, in phase-encoding, all magnetization components of the excited voxels contribute to the detected MR signal with the same frequency ω_0, but with differing phases $\varphi_n(x)$.

In order to calculate the projection of the spin density distribution in the slice onto the direction of the phase-encoding gradient, the chosen sequence is repeated N times with different spatial frequencies $k_n = n(\gamma \Delta G^x t_x) = n\Delta k$ $(1 \le n \le N)$ (Fig. 2.3.9). However, in contrast to frequency encoding, during phase encoding not the entire FID is sampled, but only the MR signal $S(k_n, t_0)$ at a definitive time t_0. After N measurements (sequence cycles), the spin density projection can be calculated by a Fourier transformation of the acquired data set

$$S(\Delta k, t_0),\ S(2\Delta k, t_0),\ S(3\Delta k, t_0),\ \ldots,\ S(N\Delta k, t_0). \tag{2.3.8}$$

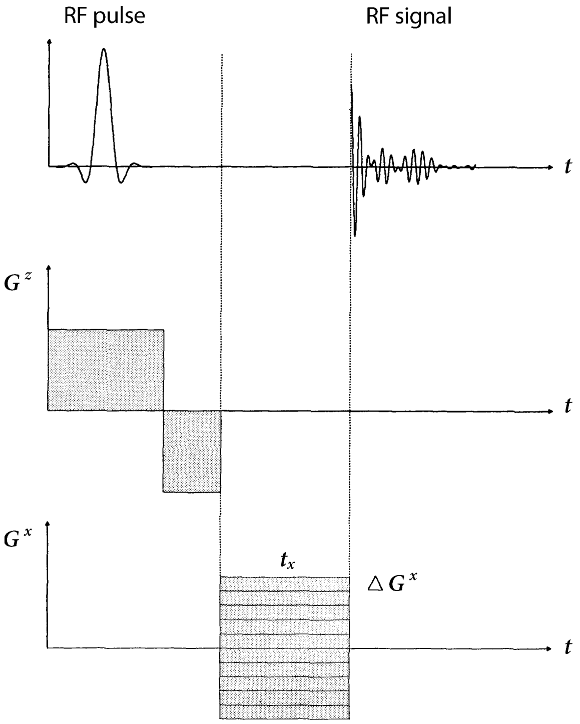

Fig. 2.3.8 Phase-encoding gradient. In phase encoding, a gradient field (here $B^x = G^x x$), the magnitude of which is increased in equidistant steps ΔG^x at each sequence cycle, is switched on for a fixed time t_x before the FID signal is acquired.

Even though both encoding-techniques described are absolutely equivalent from a mathematical point of view (see Fig. 2.3.10), they differ considerably with regard to the time needed to acquire the data sets given in Eqs. 2.3.4 and 2.3.8 for the calculation of the spin density projection: whereas frequency encoding only requires one single sequence cycle, phase-encoding needs to repeat the sequence N times.

Remark: In practice, this difference in the measurement times renders the phase-encoding technique especially vulnerable to movements (of the patient, blood flow, liquor pulsation, etc.). On the other hand, however, phase encoding does not show any chemical shift artifacts.

2.3.4 Methods of Image Reconstruction in MRI

In practical MRI, techniques of image reconstruction have prevailed that merely differ only in the way the aforementioned techniques of selective excitation and spatial encoding are combined.

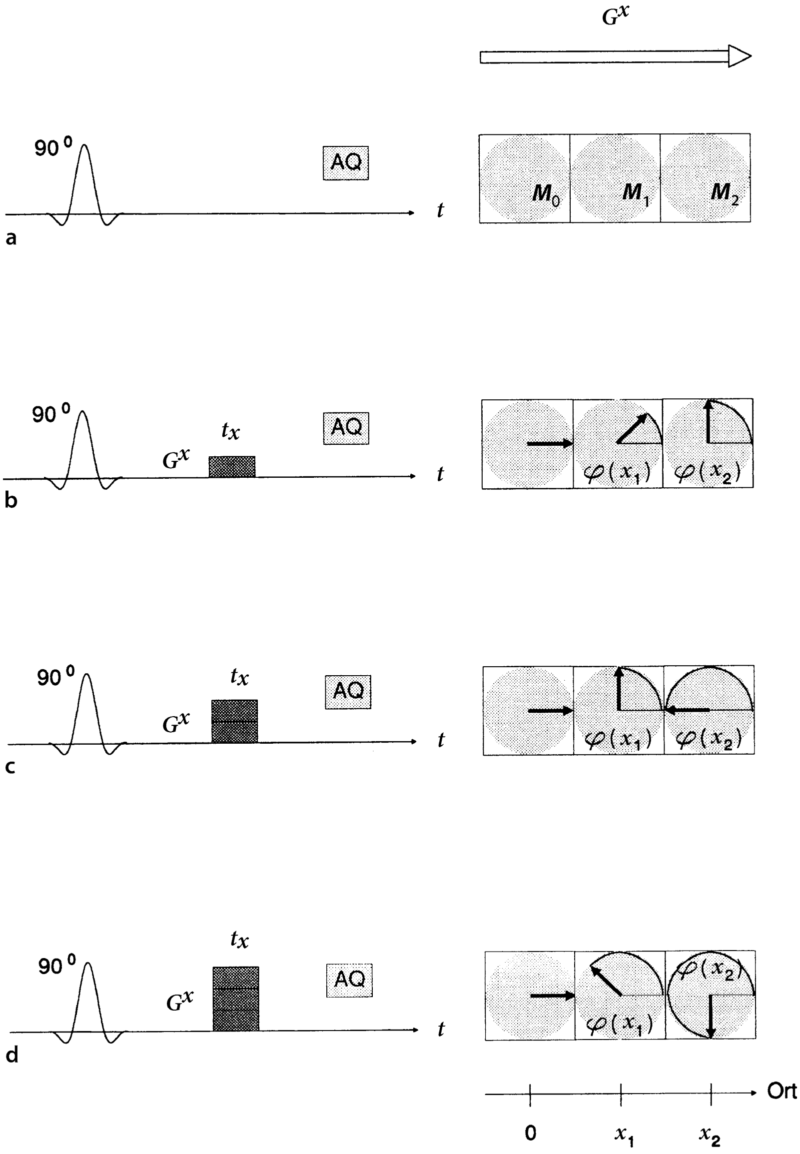

Fig. 2.3.9 Principle of phase encoding (displayed in the *rotating frame*). As shown in Fig. 2.3.8, a phase-encoding gradient G^x is switched on for a fixed time t_x before the FID signal is acquired (*AQ*). **a–d** The sequence is repeated several times at equidistantly increasing gradient strengths. Under the influence of the gradient field $B^x = G^x x$, the magnetization components of the different voxels in the slice precess with different Larmor frequencies. If the gradient is switched off after the time t_x, all components rotate again with the original, position-independent frequency $\omega_0 = \gamma B_0$ around the direction of the $\boldsymbol{B}_0$ field. However, magnetization components which precess more quickly during the operating time t_x of the gradient field, will maintain their advance compared with the slower ones. This advance is described by the phase angle $\varphi(x) = \gamma G^x x t_x$ of the different magnetization components. The figure shows the dependence of the phase angle $\varphi(x)$ on the gradient strength G^x and the spatial coordinate x schematically for four different gradient strengths ($G^x = 0$, ΔG^x, $2\,\Delta G^x$, and $3\Delta G^x$) and three adjacent voxels (with the magnetization vectors $\boldsymbol{M}_0$, $\boldsymbol{M}_1$, and $\boldsymbol{M}_2$). As shown in **b**, the magnetization $\boldsymbol{M}_1$ will rotate at the position x_1 under the influence of the gradient field by the phase angle $\varphi(x_1) = 45°$ and the magnetization $\boldsymbol{M}_2$ at the position x_2 by the phase angle $\varphi(x_2) = 90°$

2.3.4.1 Projection Reconstruction Method

This method, which P. Lauterbur used in 1973 to generate the first MR image, is based on a technique of image reconstruction used in computed tomography. Its basic idea is easy to understand: if projections of the spin density distribution of an object slice are available for various viewing angels Φ_n ($1 \le n \le N$), the spin density distribution in the slice can be reconstructed by "smearing back" the (filtered) profiles over the image plane along their viewing directions (Fig. 2.3.11).

This approach can be implemented easily by making use of the frequency-encoding technique by repeating the sequence shown in Fig. 2.3.5 several times while rotating step by step the direction of the readout gradient in the slice plane. In order to reconstruct a planar image of $N \times N$ picture elements (pixel), a minimum of N projections with N data points each is needed. The stepwise rotation of the readout gradient by the angle $\Delta\Phi = 180°/N$ is performed electronically by a weighted superposition of two orthogonal gradient fields.

The projection reconstruction method is easy to understand, but both mathematical description and data processing are rather complex. Furthermore, it carries the disadvantage that magnetic field inhomogeneities and patient movements result in considerable image artifacts. Due to these reasons, the Fourier techniques described in the following sections are preferred for the reconstruction of MR images.

a Frequency encoding

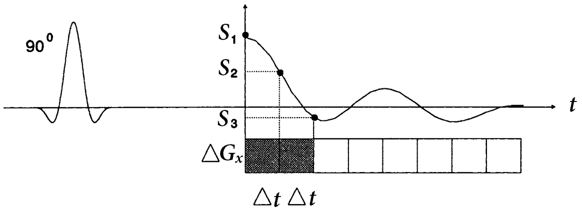

b Phase encoding

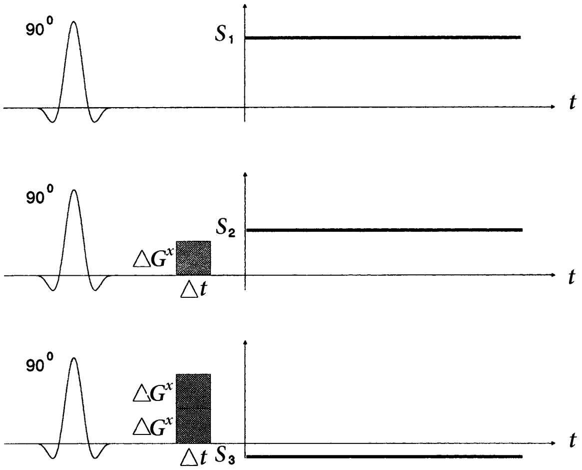

Fig. 2.3.10 Comparison between frequency and phase encoding. With both encoding techniques, the transverse magnetizations of all voxels within the excited slice contribute to the detected MR signal; the spatial information is encoded in both cases by the different phase of the magnetization components, which was formed by the influence of a magnetic gradient field (here $B^x = G^x x$) up to the moment of signal detection. In order to calculate the projection of an object onto the direction of the gradient, the MR signal S has to be measured N times (e.g., $N = 128$ or 256), with the phase difference between the magnetization components of the different voxels varying in a well-defined way form measurement to measurement. The difference between the two encoding techniques merely consists in the technique with which the data set $\{S_1, S_2, \ldots, S_N\}$ is acquired. **a** With frequency encoding, the MR signal is sampled at equidistant time steps Δt in presence of a constant gradient field (in the figure ΔG^x). As the magnetization components of the voxels within the excited slice steadily dephase under the influence of the gradient field, there is a different phase difference between them at every point in time $t_n = n\Delta t$ ($1 \leq n \leq N$), so the whole data set $\{S_1, S_2, \ldots, S_N\}$ can be detected by a single application of the sequence. The figure shows the first three values of the signal. It should be noted that only the temporal change of the MR signal caused by the gradient field is shown here, whereas the rapid oscillation of the signal with the Larmor frequency $\omega_0 = \gamma B_0$ as well as the T_2^* decay of the signal is neglected. **b** With phase encoding, a phase-encoding gradient is switched on for a fixed duration t_x before the FID signal is acquired. The magnitude of this gradient is increased at each sequence repetition by ΔG^x. During the switch-on period of the gradient field, the magnetization components of the different voxels precess with different frequencies so that a phase difference is established between them which is proportional to the magnitude of the gradient applied (see Fig. 2.3.9). After switching off the gradient, all components rotate again with the original, position-independent frequency $\omega_0 = \gamma B_0$ around the direction of the $\boldsymbol{B}_0$ field. In the chosen description, one therefore observes an MR signal S_n that is constant over time. In order to acquire the entire data set $\{S_1, S_2, \ldots, S_N\}$, the sequence needs to be repeated N times with different gradient strengths $G^x = n\Delta G^x$. The figure shows the dependence of the MR signal from the gradient strength schematically for three different gradient strengths ($G^x = 0, \Delta G^x, 2\Delta G^x$). If the product of the gradient strength and the switch-on time of the gradient up to the time of signal detection is equal in both encoding techniques, the phase difference between the various magnetization components at the time of signal detection is also identical and thus the same MR signal is measured. The product of the two quantities is indicated in the figure by the *dark areas*

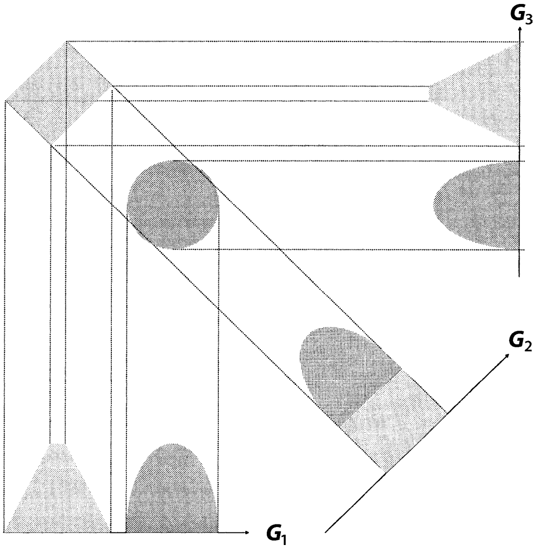

Fig. 2.3.11 Reconstruction by back projection. The figure shows three different projections of two objects in the field of view. If many projections are acquired at different viewing angles, an image can be reconstructed by (filtered) back projection of the profiles. For the measurement of the various projections, the frequency-encoding technique is used, with the readout gradient rotating step by step

2.3.4.2 2D Fourier Method

In the planar version of Fourier imaging, just as in projection reconstruction, the spins in a slice are selectively excited by an RF pulse in the first step. Afterwards, however, spatial encoding of the spins in the slice is not done by a successive rotation of a readout gradient, but by a combination of frequency and phase encoding using two orthogonal gradient fields. If we consider an axial slice parallel to the x–y-plane, then these gradients are G^x and G^y (Fig. 2.3.12). The sequence is repeated N times for different values of the phase-encoding gradient $G^x_n = n\Delta G^x$ $(1 \le n \le N)$, with the MR signal being measured M times during each sequence cycle at the times $t_m = m\Delta t$ $(1 \le m \le M)$ in the presence of the readout gradient G^y. Thus, one obtains a measurement value for each combination (k_n, t_m) of the parameters $k_n = \gamma n \Delta G^x t_x$ and $t_m = m\Delta t$, i.e., a matrix of $N \times M$ data points. A 2D Fourier transformation of this data set, the so-called hologram or k-space matrix (see Fig. 2.4.26), yields the MR image of the slice with a resolution of $N \times M$ pixels.

2.3.4.3 3D Fourier Method

In order to extend the 2D Fourier method to a 3D one, the slice-selection gradient is replaced by a second phase-encoding gradient as shown in Fig. 2.3.13. This means that the RF pulse excites all spins in the sensitive volume of the RF coil and that the spatial information is encoded exclusively by orthogonal gradients—by two phase-encoding gradients and one frequency-encoding gradient. The spatial resolution in the third dimension is defined by the strength of the related phase-encoding gradient and the number K of the phase-encoding steps. Depending

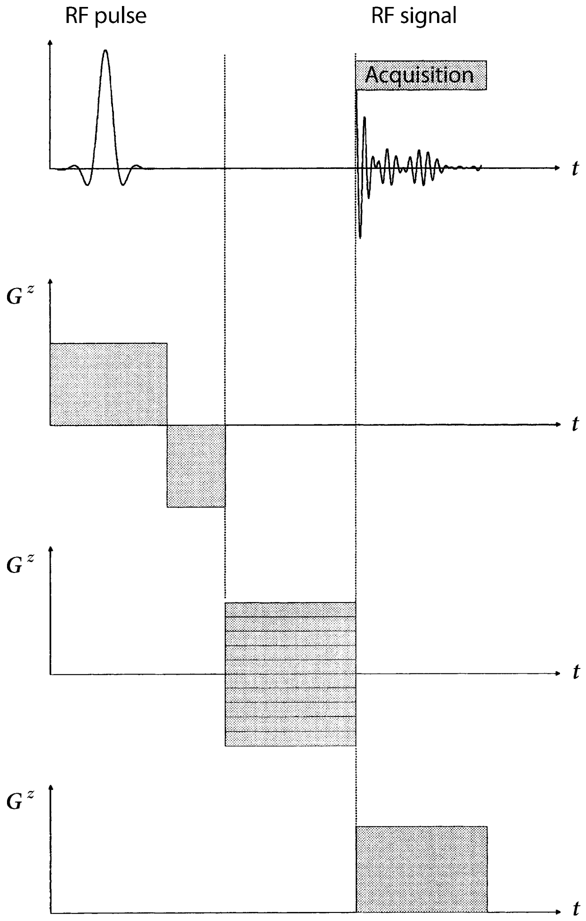

Fig. 2.3.12 Typical pulse and gradient sequence in 2D Fourier imaging. G^z is the slice-selection gradient, G^x the phase-encoding gradient, and G^y the readout gradient

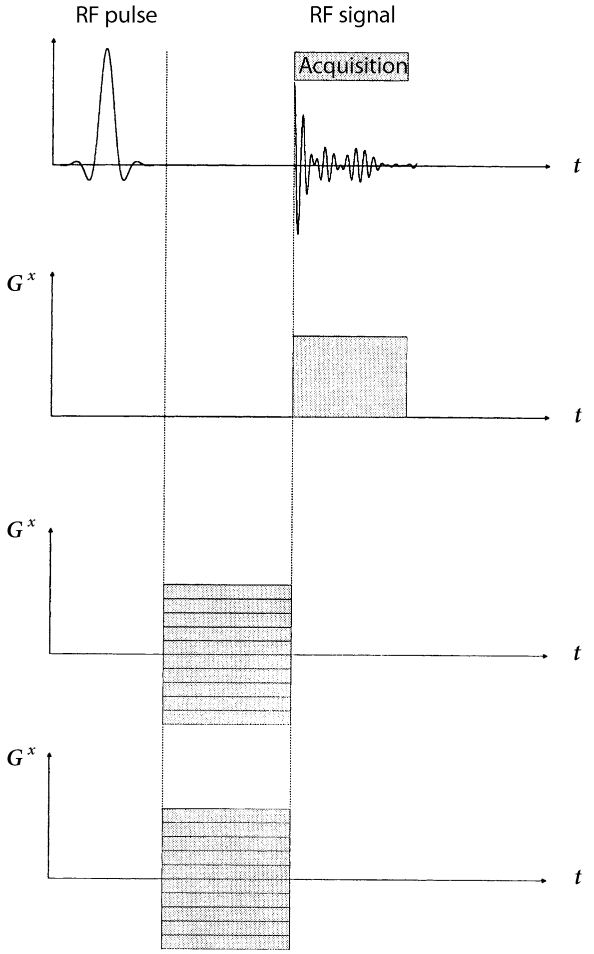

Fig. 2.3.13 Typical pulse and gradient sequence in 3D Fourier imaging. G^x and G^y are the phase-encoding gradients and G^z the readout gradient

on the choice of these parameters, the voxels have a cubic or cuboidal shape (isotropic or anisotropic resolution). In order to acquire a 3D k-space matrix with $N \times M \times K$ independent measurement values, the imaging sequence needs to be repeated $N \times K$ times.

Example: Using a standard sequence, the repetition time T_R is typically of the order of the spin-lattice relaxation time T_1, to allow the longitudinal magnetization to relax at least partially before the next RF pulse is irradiated. For instance, if one assumes $T_R = 500$ ms and an image resolution of 256 × 256 × 64 voxels, one obtains a measurement time of 136 min. 3D imaging is thus only feasible with fast imaging sequences (see Sect. 2.4.3).

A 3D Fourier transformation of the acquired 3D k-space matrix yields the 3D image data set of the partial body region excited by the RF pulse. Based on this image data set, multiplanar images in any orientation can be reformatted, which offers—among others—the possibility to look at an organ or a body structure from various viewing directions.

2.3.4.4 Alternative *k*-Space Sampling

In addition to the described conventional fashion of filling the k-space in Fourier imaging, there are a number of alternative strategies.

- ***Spiral acquisition.*** As will be described later, the EPI sequence is commonly using an oscillating frequency–encoding gradient. If both, the phase encoding as well as the frequency-encoding gradient are oscillating with increasing gradient amplitudes, the acquired data points will be along a spiral trajectory through k-space. That is why such an acquisition is called spiral EPI.
- ***Radial acquisition.*** If the direction of the frequency-encoding gradient is rotated as described in Sect. 2.3.4.1, the k-space trajectories will present a star.
- ***Blade, propeller, multivane.*** These hybrid techniques sample k-space data in blocks (so-called blades) each of which consists of some parallel k-space lines. In order to successively cover the entire k-space, the direction of the blades is rotated with a fixed radial increment. This sampling strategy offers some advantages. Since each blade contains data points close to the center of the k-space, patient movements can, for example, be easily detected and corrected.

To reconstruct MR images from alternative k-space trajectories by means of a conventional 2D or 3D Fourier transformation, it is necessary to re-grid the sampled k-space data to a rectangular grid.

2.3.5 Multiple-Slice Technique

Data acquisition by 2D imaging techniques can be carried out very efficiently when considering the fact that the time required for slice-selective excitation, spatial encoding, and acquisition of the MR signal is much shorter than the time needed by the spin system to relax at least partially after RF excitation, before it can be excited once again. The long waiting periods can be used to excite—in a temporally shifted manner—adjacent slices and to detect the spatially encoded MR signal from these slices. Thus, MR images from different parallel slices can be acquired simultaneously without prolongation of the total acquisition time (Fig. 2.3.14).

Example: Let us consider that 50 ms are needed for excitation, spatial encoding, and data acquisition per sequence cycle and that the sequence is repeated after $T_R = 1{,}000$ ms. Then MR data from 20 adjacent slices can be acquired simultaneously without prolonging the measurement time.

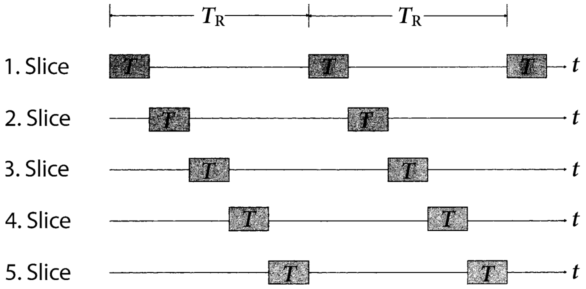

Fig. 2.3.14 Principle of the multiple-slice technique. In most 2D imaging sequences, the time T required for slice-selective excitation, spatial encoding, and detection of the MR signal is markedly shorter than the repetition time T_R. The long waiting periods can be used to subsequently excite spins in parallel slices and to detect the spatially encoded signals from these slices

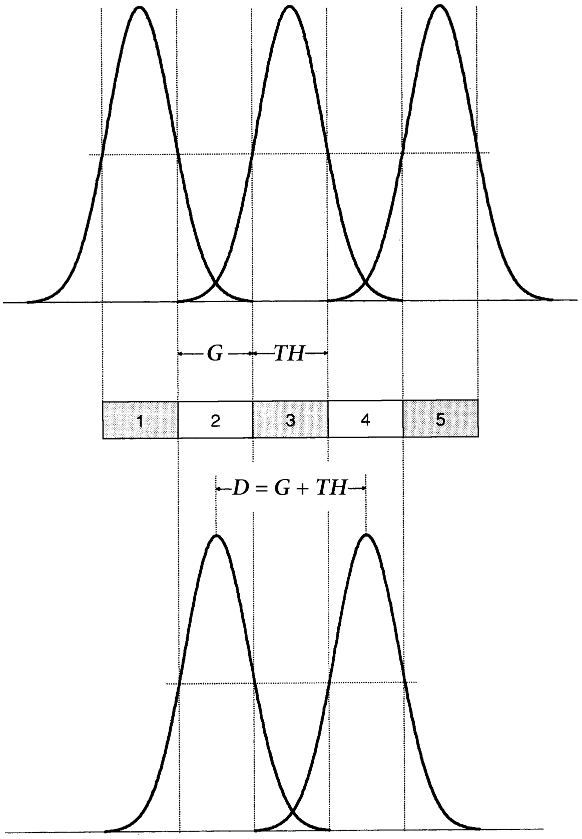

Fig. 2.3.15 Consideration of the slice profile by the multiple–slice technique. The profile of a slice is generally not rectangular but rather bell shaped. The thickness (*TH*) of the slice is therefore usually defined by the full-width at half-maximum. In order to prevent overlapping of adjacent slices in the multiple-slice technique, a sufficient gap (*G*) between the two adjacent slices has to be chosen ($G \geq TH$). Often the distance ($D = G + TH$) between the slices is indicated instead of the gap *G*. Images from adjacent slices can be detected without overlap by using in a first step a sequence that acquires data from the even slices and in a second step a sequence that acquires data from the odd slices. In both measurements, the gap *G* should be identical with the slice thickness *TH* ($D = G + TH = 2TH$)

However, when using the multiple-slice technique, one has to consider that the distance between slices may not be too small, as the slice profile usually is not rectangular, but bell shaped. In order to avoid repeated excitation of spins in overlapping slice regions, the gap between adjacent slices should correspond approximately to the width of the slice itself. Images from adjacent slices can be obtained in an interleaved manner by applying the sequence twice: in the first measurement, data are acquired from the odd slices and in the second from the even slices (Fig. 2.3.15).

Suggested Reading

1. Barrett HH, Myers K (2004) Foundations of image science. Wiley, New Jersey
2. Haacke EM, Brown RW, Thompson MR, Venkatesan R (1999) Magnetic resonance imaging: physical principles and sequence design. Wiley, New York
3. Oppelt A (2005) (ed) Imaging systems for medical diagnostics. Publicis MCD, Erlangen
4. Vlaardingerbroek MT, den Boer JA (2004) Magnetic resonance imaging: theory and practice. Springer, Berlin Heidelberg New York

2.4 Image Contrasts and Imaging Sequences

G. Brix, H. Kolem, and W.R. Nitz

2.4.1 Image Contrasts

2.4.1.1 Contrast Determinants and Optimization in MRI

The main advantage of MR imaging, apart from the flexibility in slice orientation, is the excellent soft-tissue contrast in the reconstructed MR images. It is based on the different relaxation times T_1 and T_2 of the tissues, which depend on the complex interaction between the hydrogen nuclei and their surroundings. Compared to that, differences in proton densities (*PD*) are only of minor relevance, at least when considering soft tissues.

Remark: The term proton density in MR imaging designates only those hydrogen nuclei whose magnetization contributes to the detectable image signal. Essentially, this refers to hydrogen nuclei in the ubiquitous water molecules and in the methylene groups of the mobile fatty acids (see Sect. 2.3.3.1 and Fig. 2.3.7). Hydrogen atoms, which are included in cellular membranes, proteins, or other relatively immobile macromolecular structures, usually do not contribute to the MR signal; their FID signal has already decayed to zero at the time of data acquisition ($T_2 << T_E$) (Brix 1990).

Another important contrast factor is the collective flow of the nuclei. The influence of flowing blood on the image signal will be discussed in Sect. 2.7 separately, in the context of MR angiography.

Whereas the image contrast of a CT scan only depends on the electron density of the tissues considered (as well as on the tube voltage and beam filtering), the MR signal and thus the character of an MR image is determined by the intrinsic tissue parameter *PD*, T_1, and T_2 as well as by the type of the sequence used and by the selected acquisition parameters. This variability offers the opportunity to enhance the image contrast between distinct tissues by cleverly selecting the type of sequence and the corresponding acquisition parameters, and thus to optimize the differentiation between these tissue structures. However, the subtle interplay of the many parameters bears the danger of misinterpretations. In order to prevent these, several MR images are always acquired in clinical routine, with different sequence parameters that are selected in such a way that the tissue contrast of the various images is determined mainly by a single tissue parameter; in this context, one uses the term T_1-, T_2-, or *PD*-weighted images.

Sometimes, one even goes one step further to calculate "pure" T_1, T_2, and *PD* parameter maps on the basis of several MR images that were acquired with different acquisition parameters. The advantage in doing this consists of the fact that the image contrast on the calculated parameter maps is usually more accentuated than in the weighted images. The calculated tissue parameters can furthermore be used to characterize various normal and pathological tissues. However, experience has shown that a characterization or typing of tissues by means of calculated MR tissue parameters is only possible with reservations (Bottomley et al. 1987; Higer and Bielke 1986; Pfannenstiel et al. 1987). This may be due not only to the insufficient measurement and analysis techniques used, but also to the fact that morphological information of the MR images as well as the clinical expertise of the radiologist have been left aside in many cases.

These considerations indicate that each MR practitioners should be aware of the dependence of the image contrast on the selected type of imaging sequence as well as on the sequence and tissue parameters in order to fully benefit from the potential of MRI and to avoid misinterpretations.

Remark: The term imaging sequence designates the temporal sequence of RF pulses and magnetic gradient fields, which are used to determine the image contrast and for image reconstruction, respectively.

2.4.1.2 Definition of Image Contrast

The foregone section has made intuitive use of the term image contrast in order to describe the possibility to distinguish between adjacent tissue structures in an MR image. We will now define this term. If one describes the signal intensities of two adjacent tissues structures *A* and *B* with S_A and S_B, the image contrast between the two tissues can be expressed by the absolute value of the signal difference

$$C_{AB} = |S_A - S_B| \tag{2.4.1}$$

or by the normalized difference

$$c_{AB} = \left|\frac{S_A - S_B}{S_A + S_B}\right|. \tag{2.4.2}$$

Remark: The delineation of a tissue structure depends, of course, also on the signal-to-noise ratio (*S/N*) as tiny, weakly contrasted structures can be masked by image noise. Some authors therefore proposed to use the contrast-to-noise ratio for evaluating the detectability of a detail. However, the explanatory power of this quantity can hardly be objectified since the contrast–detail detectability strongly depends on the signal detection in the human retina as well as on the signal processing in the central visual system of the observer. In the following, we will therefore use the absolute contrast defined in Eq. 2.4.1.

Example: In order to analyze the influence of the tissue and acquisition parameters on the image contrast by an example, we will consider in the following the contrast between white and

Table 2.4.1 Tissue parameters for gray and white brain matter at 1.5 T

Tissue	T_1 (ms)	T_2 (ms)	ρ (a.u.)
Gray brain matter	972 ± 124	109 ± 17	100 ± 7
White brain matter	599 ± 90	87 ± 7	96 ± 5

a.u. arbitrary units

gray brain matter. Representative tissues parameters, which have been measured for a patient collective at 1.5 T, are summarized Table 2.4.1.

2.4.2 Classical Imaging Sequences

2.4.2.1 Spin-Echo Sequence

In clinical routine, the spin-echo (SE) sequence is still a frequently applied imaging sequence, due to two reasons:

- It is rather insensitive to static field inhomogeneities and other inaccuracies of the MR system.
- It allows for the acquisition of T_1-, T_2-, and *PD*-weighted images by an appropriate choice of the acquisition parameters T_R and T_E.

The basic principle of the SE technique has already been described in Sect. 2.2.7.3. For image reconstruction, in general the 2D Fourier method is used. One of the possible combinations of the SE pulse sequence $\{90° - T_E/2 - 180° - T_E/2 - AQ - T_D\}$ (T_E, echo time; T_D, delay time; AQ, acquisition period), and the gradient sequence is shown in Fig. 2.4.1.

The signal intensity S_{SE} of a voxel with the tissue parameters *PD*, T_1, and T_2 can be described in good approximation by the equation ($T_R = T_E + T_D$, repetition time)

$$S_{SE} = PD \cdot \underbrace{[1-e^{-T_R/T_1}]}_{T_1 \text{ factor}} \cdot \underbrace{e^{-T_E/T_2}}_{T_2 \text{ factor}}. \qquad (2.4.3)$$

According to this equation, the signal intensity of a voxel is determined by three independent factors, each of which depends on only one of the three tissue parameters. This leads to a clear dependence of the image signal on the tissue and acquisition parameters:

- ***PD* dependence:** The signal intensity is directly proportional to the *PD* of the considered tissue, i.e., to the number of excited nuclei which contribute per unit volume to the signal of the MR image. The influence of the proton density on the image contrast is constant and cannot be varied.
- ***T_1* dependence:** after RF excitation, the longitudinal magnetization M_z relaxes with the time constant T_1 against the equilibrium magnetization M_0 (see Fig. 2.2.22); the equilibrium state is reached after a period of about $3T_1$. Usually, however, the sequence is repeated much earlier, so that the longitudinal magnetization will be reduced at the beginning of the next sequence cycle compared to the equilibrium magnetization by the T_1 factor $[1 - \exp(-T_R/T_1)]$. Accordingly, the T_1 contrast of an SE image can be varied by the choice of the repetition time T_R. In Fig. 2.4.2a, the T_1 factor is plotted for white and gray brain matter. As this example shows, the T_1 contrast reaches a maximum if the repetition time T_R is between the T_1 relaxation times of the two tissues considered. If T_R is markedly longer than the longer T_1 time, then the T_1 contrast vanishes.
- ***T_2* dependence:** The influence of the T_2 relaxation process on the signal intensity is described by the T_2 factor $\exp(-T_E/T_2)$ in the signal equation. For a given T_2 time the signal loss is the bigger, the longer the echo time T_E becomes. In Fig. 2.4.2b, the T_2 factor is plotted for white and gray brain matter versus the echo time T_E. The contrast will reach a maximum when the echo time T_E ranges between the T_2 relaxation times of the two tissues considered. For small T_E values ($T_E << T_2$), the contrast approximates zero, as the signal intensities in this case are independent of T_2.

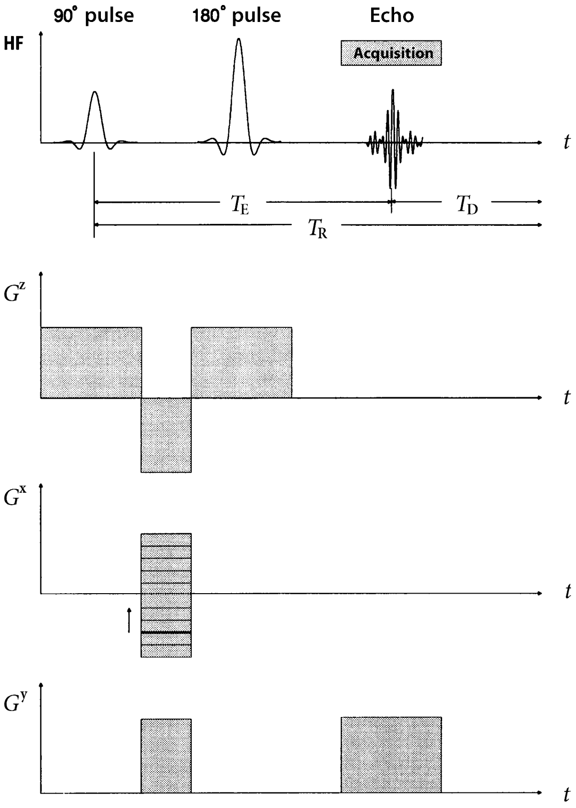

Fig. 2.4.1 Pulse and gradient scheme of the SE sequence. G^z slice-selection gradient, G^x phase-encoding gradient, G^y readout gradient. (The effect of the first gradient pulse in readout direction is explained in Fig. 2.4.16)

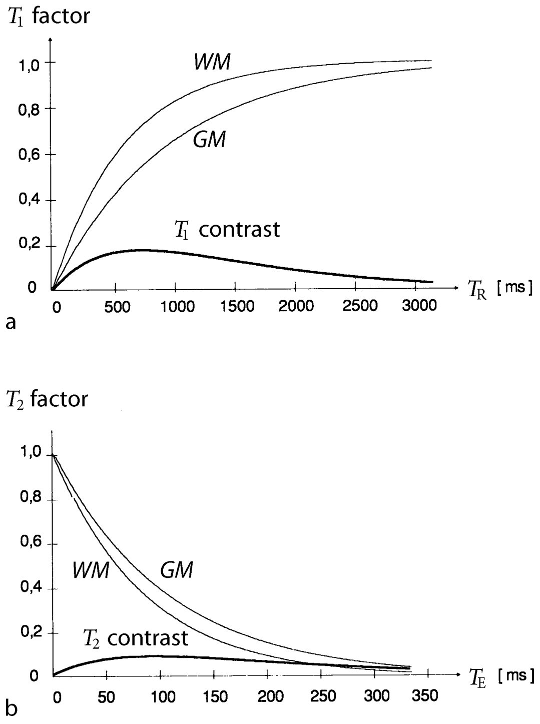

Fig. 2.4.2 T_1 and T_2 dependence of the SE signal intensity. **a** Plotted is the T_1 factor $[1 - \exp(-T_R/T_1)]$ of the SE signal equation as a function of the repetition time T_R for the white (*WM*) and gray (*GM*) brain matter. As can be seen, the T_1 contrast between the two tissues approaches 0 for very long as well as for very short repetition times. The highest T_1 contrast is obtained for $T_R \sim 750$ ms, i.e. for a repetition time in between the T_1 times of the two tissues considered (see Table 2.4.1). **b** The same considerations hold for the T_2 factor $\exp(-T_E/T_2)$. The T_2 contrast maximum is at $T_E \sim 100$ ms

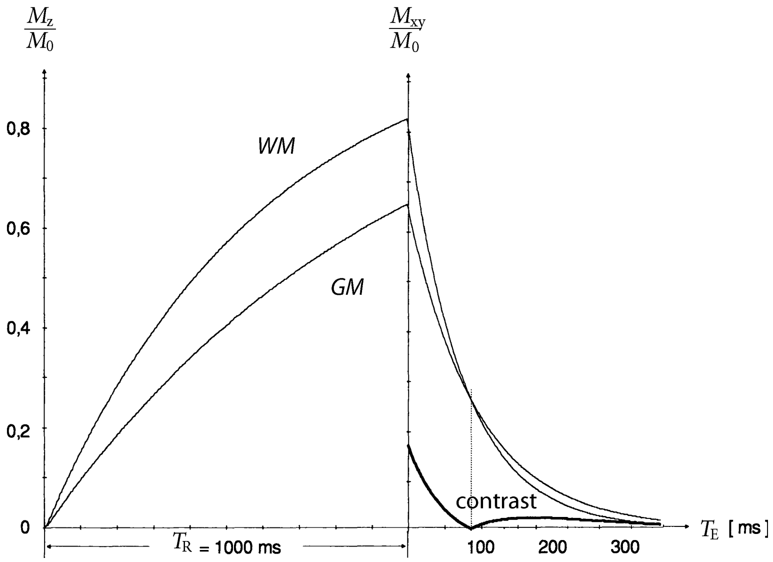

Fig. 2.4.3 Influence of the acquisition parameters T_R and T_E on the contrast behavior of an SE image. The figure shows the interplay of the longitudinal and transversal relaxation for this sequence at the example of white (*WM*) and gray brain matter (*GM*) for a fixed repetition time of T_R = 1.000 ms. In the *left* part, the temporal evolution of the longitudinal magnetization M_z during the recovery period ($0 \le t \le T_R$) is depicted. At $t = T_R$, the partially relaxed longitudinal magnetization is flipped into the x–y-plane by the 90° excitation pulse. The T_2 relaxation of the resulting transversal magnetization M_{xy} is plotted in the *right* part as a function of the echo time T_E. As can be seen, there is a reversal behavior of the T_1 and T_2 contrast. For T_E = 83 ms, the contrast is 0, so that the two types of brain matter cannot be differentiated in the relating SE image in spite of differing tissue parameters (see Fig. 2.4.5d). Note that the detected MR signal is directly proportional to the transversal magnetization M_{xy}

In general, adjacent tissues differ in all three tissue parameters *PD*, T_1 and T_2, so the different factors of the SE signal equation, which can partially compensate one another, need to be considered altogether. This holds even more as the relaxation times are usually positively correlated, i.e., the tissues with longer T_1 times usually also have longer T_2 times. In order to illustrate this statement, Fig. 2.4.3 shows the course of the longitudinal and transverse magnetization for both white and gray brain matter for a repetition time of T_R = 1,000 ms. As can be seen, the transverse magnetization of both substances—and therefore the signal intensities ($S_{SE} \propto M_{xy}$)—are identical at an echo time of T_E = 83 ms, so the tissues cannot be distinguished on the related SE image in spite of different tissue parameters. Fig. 2.4.4 shows the contrast between white and gray matter as a function of both the repetition and echo time. As expected, there are two regions with a high tissue contrast, which are separated by a low contrast region (cf. Fig. 2.4.3): For $T_E << T_2$ and $T_R \sim T_1$, the T_1 contrast is dominant (T_1-weighted image), for $T_R >> T_1$ and $T_E \sim T_2$, the T_2 contrast (T_2-weighted image). For $T_R >> T_1$ and $T_E << T_2$, the contrast vanishes, as the signal intensities in this case are nearly independent from the relaxation times (*PD*-weighted image).

Example: For T_E = 15 ms, the contrast maximum between white and gray brain matter is at $T_R \sim$ 640 ms, for T_R = 2,400 ms at $T_E \sim$110 ms. In order to illustrate the dependence of the image contrast on the acquisition parameters T_E and T_R, Fig. 2.4.5 shows four SE images of a transversal head section: a T_1-weighted image (T_R/T_E = 600/15), a T_2-weighted image (2,400/120), a *PD*-weighted image (2,400/22 ms), and a mixed T_1/T_2-weighted image with disappearing contrast between white and gray matter (1,000/85 ms).

Table 2.4.2 Influence of the sequence parameters T_R and T_E on the contrast of an SE image

Weighting	Condition	
PD	$T_R >> T_1$	$T_E << T_2$
T_1	$T_R \approx T_1$	$T_E << T_2$
T_2	$T_R >> T_1$	$T_E \approx T_2$

Remark: *PD*-weighted and T_2-weighted SE images can be acquired with one single measurement, if a double echo sequence (e.g., $T_R/T_{E1}/T_{E2}$ = 2,400/22/120) is used (cf. Fig. 2.2.23).

The influence of the acquisition parameters T_E and T_R on the contrast of an SE image is summarized in Table 2.4.2.

2.4.2.2 Inversion Recovery Sequence

In order to adapt the inversion recovery technique explained in Sect. 2.2.7.2 for MR imaging, one has to extend the conventional IR pulse sequence {180° – T_I – 90° – AQ – T_D} by a 180° pulse {180° – T_I – 90° – T_E/2 – 180° – T_E/2 – AQ – T_D} (T_I, inversion time; T_E, echo time; T_D, delay time; AQ, signal acquisition). In this imaging technique, the FID is not acquired directly after the readout pulse, but rather the SE signal, which is created by the additional rephasing 180° pulse. This modification is necessary to integrate the gradient fields required for image reconstruction into the sequence (Fig. 2.4.6).

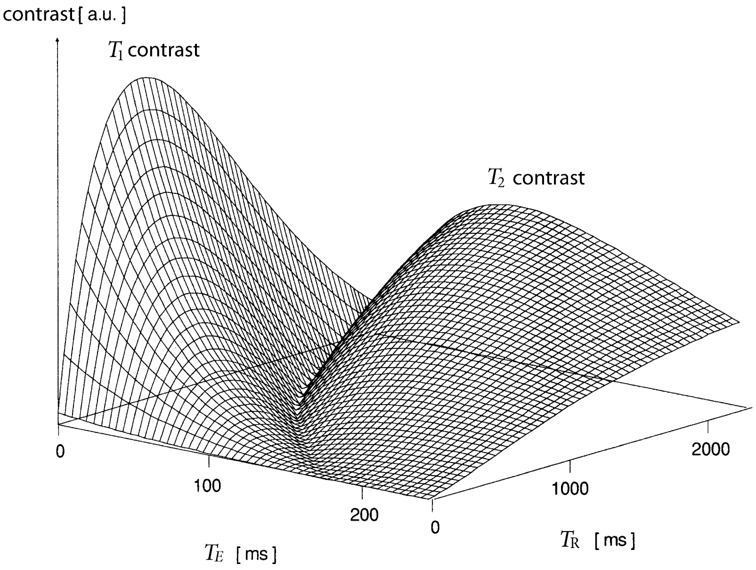

Fig. 2.4.4 Parameter weighting in SE imaging. The figure shows the image contrast between white and gray brain matter in dependence of the repetition time T_R and the echo time T_E. There are two regions with a high tissue contrast that are separated by a low contrast region (Fig. 2.4.3): For $T_E << T_2$ and $T_R \sim T_1$, the T_1 contrast is dominant (T_1-weighted image), for $T_R >> T_1$ and $T_E \sim T_2$ the T_2 contrast. For $T_R >> T_1$ and $T_E << T_2$, the contrast is only determined by the differences in the proton densities (*PD*-weighted image)

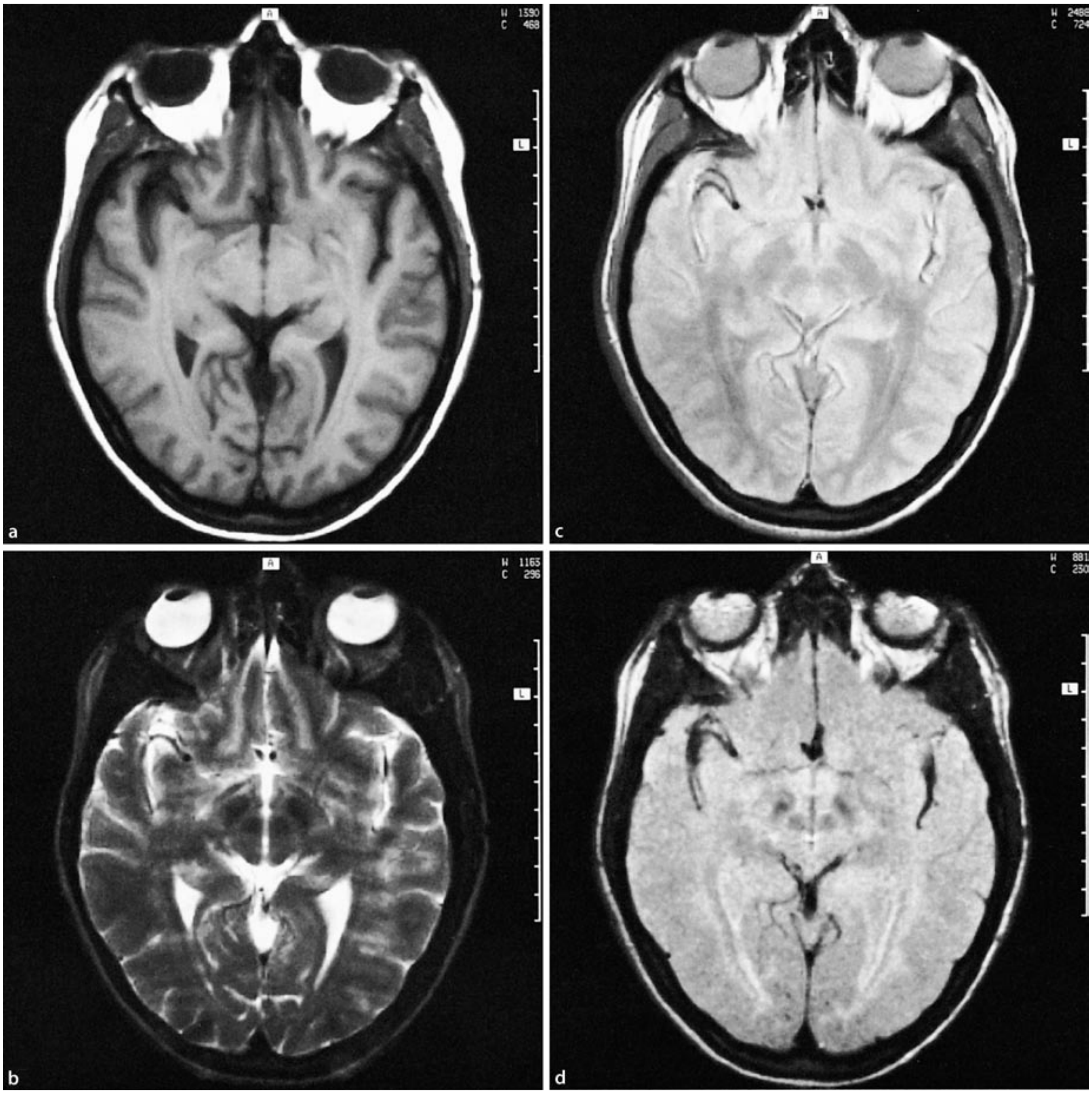

Fig. 2.4.5 SE images of a transversal head section with a thickness of 5 mm. **a** T_1-weighted image ($T_R/T_E/N_{AQ}$ = 600/15/4), **b** T_2-weighted image (2,400/120/1), **c** *PD*-weighted image (2,400/22/1), and **d** mixed T_1/T_2-weighted image (1,000/85/1) with disappearing contrast between white and gray matter (cf. Fig. 2.4.3)

The signal intensity S_{IR} of a tissue with the intrinsic parameters *PD*, T_1, and T_2 can be described approximately with the expression

$$S_{\mathrm{IR}} = PD \cdot \underbrace{[1 - 2e^{-T_I/T_1} + e^{-T_R/T_1}]}_{T_1 \text{ factor}} \cdot \underbrace{e^{-T_E/T_2}}_{T_2 \text{ factor}}. \qquad (2.4.4)$$

The image contrast of an IR image can therefore be varied via three acquisition parameters, at principally: via the inversion time T_I, the echo time T_E, and the repetition time $T_R = T_I + T_E + T_D$. Due to the pronounced T_1 dependence, the IR sequence is especially apt for acquiring T_1-weighted images:

- ***PD* dependence:** see Sect. 2.4.2.1
- ***T_1* dependence:** The longitudinal magnetization $M_z(t)$ at the time $t = 0$ is inverted by the 180° pulse of the IR sequence (the inversion pulse), so the longitudinal magnetization will relax strictly monotonously from negative values toward the equilibrium magnetization M_0 (inversion recovery). This is described by the T_1 factor of the IR signal Eq. 2.4.4, which depends on the

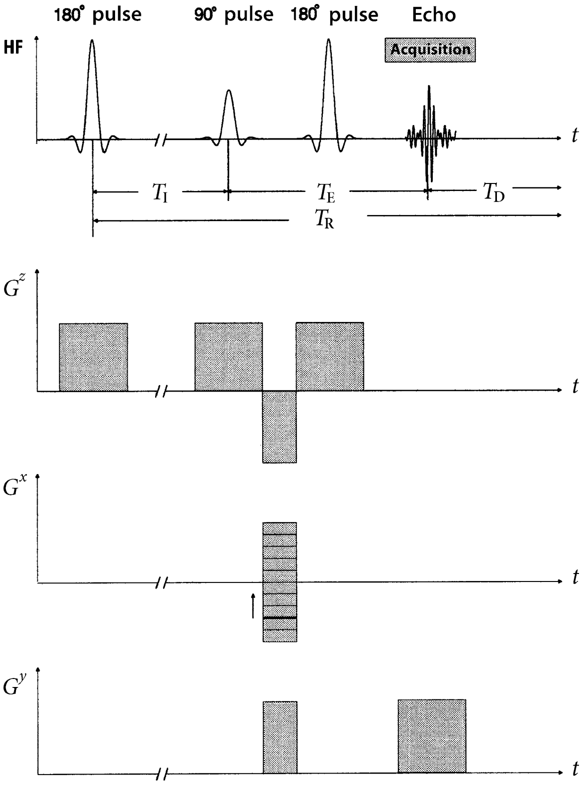

Fig. 2.4.6 Pulse and gradient scheme of the IR sequence. G^z slice-selection gradient, G^x phase-encoding gradient, G^y readout gradient. (The effect of the first gradient pulse in readout direction is explained in Fig. 2.4.16)

inversion time T_I as well as a on the repetition time T_R. In order to optimize the T_1 contrast, the inversion time T_I is usually varied, whereas with the parameter T_D, respectively T_R is chosen as high as possible ($T_D >> T_1$), to allow the recovery of a considerable longitudinal magnetization after RF excitation. The maximum range of values of the T_1 factor is between −1 and +1, thus being double the range of values of the SE sequence. There are two types of IR sequences depending on signal interpretation: If only the absolute values of the signal are considered (magnitude reconstruction, IRM), the range of values is limited de facto to the interval between 0 and 1, as in the SE sequence. If this mode of data representation is chosen, then the T_1 factor will initially decrease to 0 and then converges toward the equilibrium magnetization M_0. Figure 2.4.7 shows the dependence of the T_1 factor from the inversion time T_I for both possible modes of data representation for white and gray brain matter (T_R = 3,000 ms). As this example reveals, the neglect of the sign of the T_1 factors in the absolute value representation leads to a destructive T_1 contrast behavior in the region between the zeros of both T_1 functions considered. An IR sequence differentiating between parallel or antiparallel alignment of the longitudinal magnetization at the time of the excitation pulse is called phase sensitive.

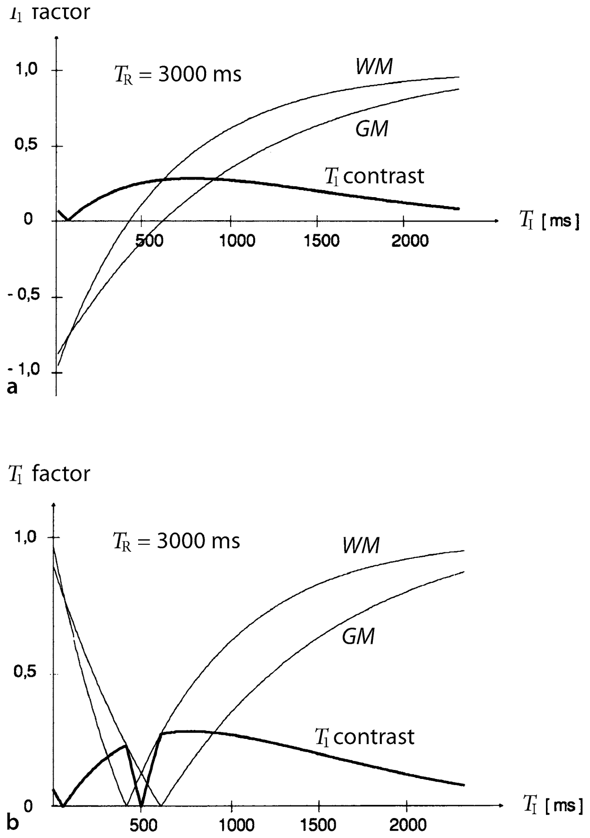

Fig. 2.4.7 T_1 dependence on the IR signal intensity. Plotted is the T_1 factor $[1 - 2\exp(-T_I/T_1) + \exp(-T_R/T_1)]$ of the IR signal equation for white (*WM*) and gray (*GM*) brain matter as a function of the inversion time T_I for a fixed repetition time of T_R = 3,000 ms for two different modes of data representation: **a** by considering and **b** by neglecting the sign of the longitudinal magnetization M_z. If the last-mentioned mode of data representation is used, there will be a destructive T_1 contrast behavior in the region between the zeros of the two tissue curves. The T_1 contrast maximum in the considered case is at $T_I \sim$ 760 ms, i.e., in between the T_1 times of the two tissues considered (see Table 2.4.1)

For evaluation of the tissue contrast, the *PD* and T_2 dependence of the image signal S_{IR} needs to be included in the considerations, too. Figure 2.4.8 demonstrates this with an example. In this figure, the tissue contrast between white and gray brain matter is plotted as a function of the echo time T_E for T_I = 800 ms and T_R = 2,400 ms. For the chosen T_I value, there is a reversal behavior of the T_1 and T_2 contrast, as the relaxation times of the two tissues

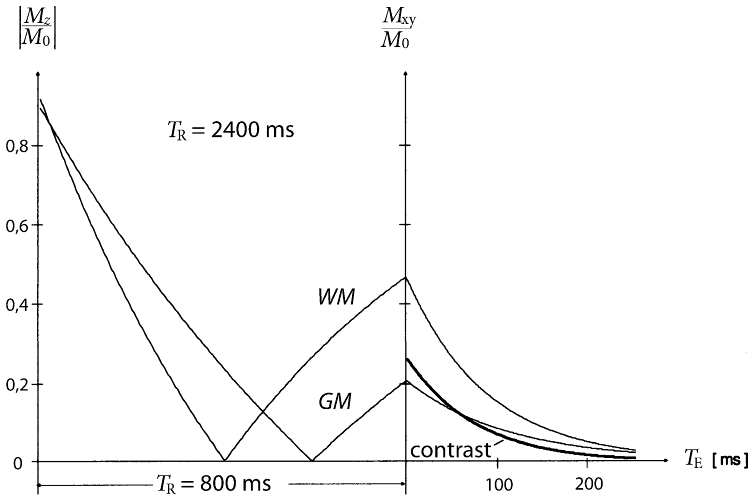

Fig. 2.4.8 Influence of the acquisition parameters T_I and T_E on the contrast behavior of the IR sequence (absolute value representation). The figure shows the interplay of the longitudinal and transversal relaxation for this sequence at the example of white (*WM*) and gray brain matter (*GM*) for a fixed inversion time $T_I = 800$ ms and a fixed repetition time $T_R = 2{,}400$ ms. The *left* part shows the temporal evolution of the longitudinal magnetization M_z during the inversion phase ($0 \leq t \leq T_I$). At $t = T_I$, the partially relaxed longitudinal magnetization is flipped into the x–y-plane by the 90° excitation pulse. The T_2 relaxation of the resulting transversal magnetization M_{xy} is plotted in the *right* part as a function of the echo time T_E. In the case considered, there is a reversal behavior of the T_1 and T_2 contrast, so that the contrast between the two brain tissues rapidly reduces with prolonged echo time. Note that the detected MR signal is directly proportional to the transversal magnetization M_{xy}

examined are positively correlated, i.e., the substance with the longer T_1 time also has a longer T_2 time. In order to fully grasp the complex interplay between the different tissue and acquisition parameters as a whole, the image contrast between white and gray brain matter is plotted in Fig. 2.4.9 as a function of both the inversion time T_I and the echo time T_E.

Example: In the case considered, the T_1 contrast assumes a maximum for $T_E = 20$ ms at $T_I = 620$ ms. Figure 2.4.10a shows the corresponding T_1-weighted IR image ($T_R/T_I/T_E = 2{,}400/600/20$). Compare this image with the T_1-weighted SE image shown in Fig. 2.4.5. The two images differ mainly in that the gray matter is not represented in the IR image as the T_1 factor of gray matter is approximately 0 for $T_I = 600$ ms (see Fig. 2.4.7).

The influence of the acquisition parameters T_E, T_I, and T_D on the contrast of an IR image is summarized in Table 2.4.3. In order to maximize the T_1 contrast (T_1-weighted image), the T_I time should be between the T_1 times of the two tissues considered, and the echo time T_E should be chosen as short as possible. As even for the acquisition of T_1-weighted images, relatively long repetition times are needed ($T_D >> T_1$), the IR sequence requires much more time than the SE sequence. Advantages occur mainly when the image signal of a given tissue structure shall be suppressed, e.g., the retrobulbar fatty tissue for the evaluation of the optic nerve. In this case, the acquisition parameter T_I needs to be chosen so that the T_1 factor of the tissue to be suppressed is approximately 0 (Fig. 2.4.7). For $T_R > 3T_1$, the corresponding T_I value can be estimated by $T_I = T_1 \cdot \ln 2$.

Example: At a magnetic flux density of 1.5 T, the T_1 time of fatty tissue is about 260 ms (see Table 2.2.2), so fatty tissue structures are not displayed in the IR image at a T_I value of 180 ms (Fig. 2.4.10b). At lower flux densities, the corresponding T_I value is somewhat lower.

Remark: An IR sequence with a very short T_I time is called STIR (short-tau inversion recovery) sequence. If the T_I time is selected to suppress the signal from liquor, the sequence is called FLAIR (fluid-attenuated inversion recovery).

Table 2.4.3 Influence of the sequence parameters T_E, T_I, and T_D on the contrast of an IR image ($T_R = T_I + T_E + T_D$)

Weighting	Condition		
PD	$T_I >> T_1$	T_D arbitrary	$T_E << T_2$
	$T_I << T_1$	$T_D >> T_1$	$T_E << T_2$
T_1	$T_I \approx T_1$	$T_D >> T_1$	$T_E << T_2$
T_2	$T_I >> T_1$	T_D arbitrary	$T_E \approx T_2$
	$T_I << T_1$	$T_D >> T_1$	$T_E \approx T_2$

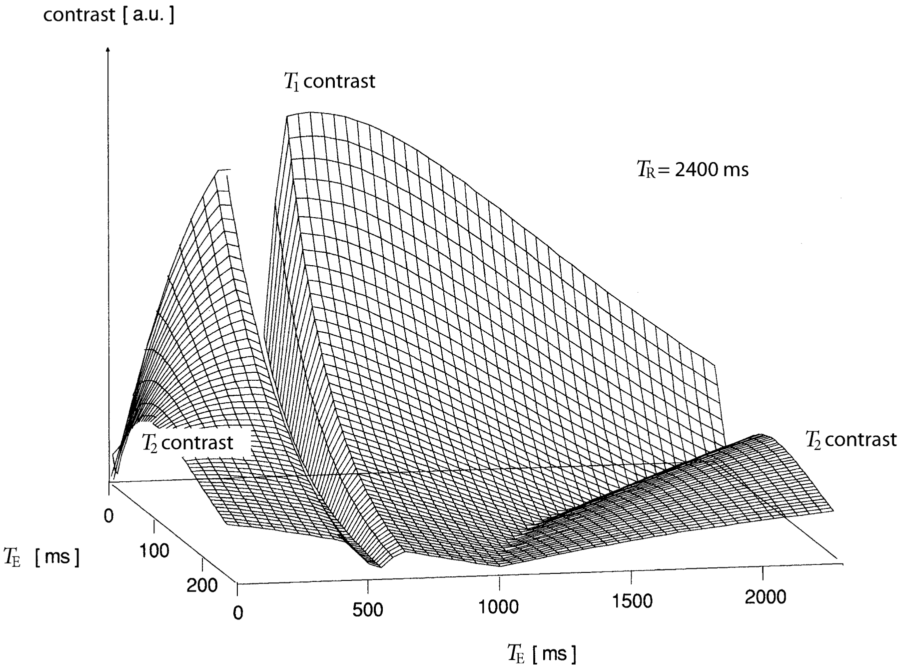

Fig. 2.4.9 Parameter weighting in IR imaging (absolute value representation). Plotted is the image contrast between white and gray brain matter in dependence of the inversion time T_I and the echo time T_E for a fixed repetition time of T_R = 2,400 ms. For $T_E << T_2$ and $T_I \sim T_1$, the T_1 contrast is dominant (T_1-weighted image), for $T_I >> T_1$ and $T_E \sim T_2$, the T_2 contrast (T_2-weighted image). Note the breakdown of the image contrast at short T_I times (see Fig. 2.4.7b)

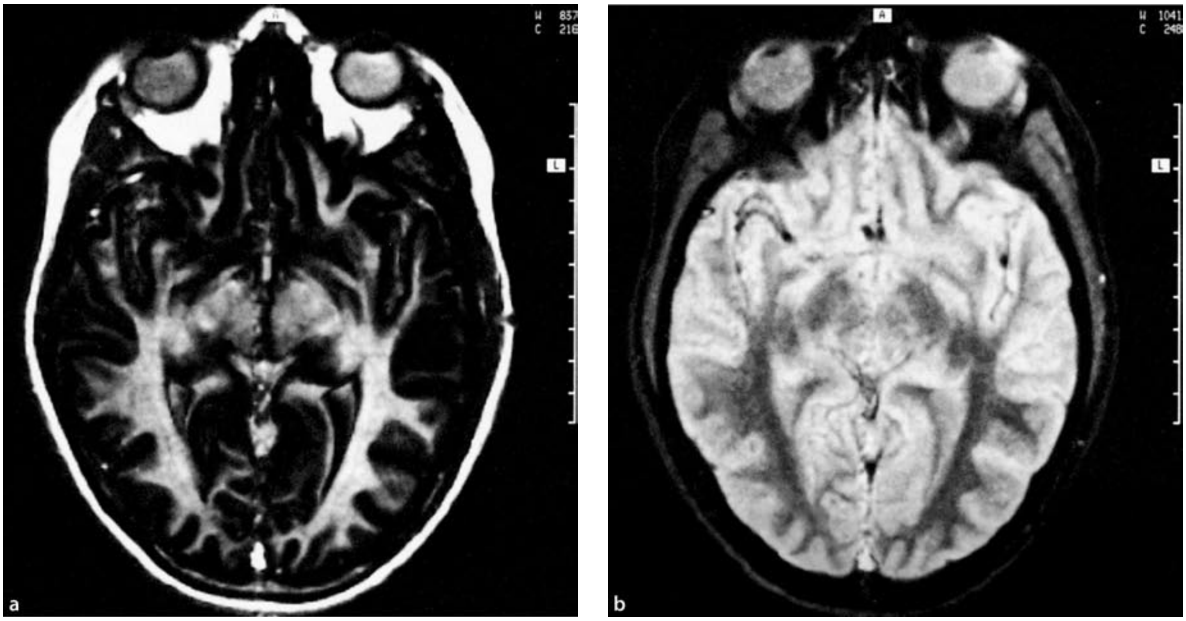

Fig. 2.4.10 IR images of a transversal head section with a thickness of 5 mm. **a** T_1-weighted image ($T_R/T_I/T_E/N_{AQ}$ = 2,400/600/20/1). Gray brain matter is depicted with very little signal in this image, as the corresponding T_1 factor for T_I = 600 ms is about 0 (see Fig. 2.4.7). **b** STIR image (1,500/180/20/1). In this case, the inversion time T_I has been chosen in such a way that the T_1 factor of fatty tissues is about 0. Consequently, fatty tissue in the retrobulbar and temple regions is not depicted

2.4.2.3 Limiting Factor: Acquisition Time

The numerous advantages of conventional imaging techniques are opposed by the long acquisition time as a limiting factor. The time T required for the acquisition of an MR image using the 2D Fourier method (see Sect. 2.3.4.2.) is given by the product of the repetition time T_R, the number of the sequence cycles needed for phase encoding N_{PH}, and the number of acquisitions N_{AQ} (or averages):

$$T = T_R N_{PH} N_{AQ}. \qquad (2.4.5)$$

- The number N_{PH} of sequence cycles needed for phase encoding is determined by the desired resolution of the image matrix. For the reconstruction of an MR image with a resolution of 256 × 256 pixels, for instance, 256 sequence cycles are required.
- The repetition time T_R is determined by the selected type of weighting. Typical values are $T_R = 500–600$ ms for T_1-weighted and $T_R \geq 3{,}000$ ms for T_2-weighted or *PD*-weighted SE images.
- In some cases, the imaging sequence is repeated several times (e.g., $N_{AQ} = 2$ or 4), in order to improve the signal-to-noise ratio ($S/N \propto \sqrt{N_{AQ}}$). This is especially valid for T_1-weighted SE images, which have a relatively low *S/N* ratio due to the short repetition time.

Example: Based on these considerations, the following representative acquisition times are obtained for SE images: $T = 2.1$ min for a T_1-weighted image ($T_R = 500$ ms, $N_{PH} = 256$, $N_{AQ} = 1$) and $T = 10.2$ min for a T_2-weighted and/or a *PD*-weighted image ($T_R = 2{,}400$ ms, $N_{PH} = 256$, $N_{AQ} = 1$).

By using the multiple slice technique described in Sect. 2.3.5, one can simultaneously acquire MR images from multiple parallel slices within the given acquisition times, but the overall acquisition time required for the acquisition of the images will not be reduced. In clinical practice, this basic limitation of conventional imaging sequences leads to the following problems:

- Depending on the clinical question, the time needed for a patient examination ranges between 15 and 45 min.
- This demands high cooperation from the patient, as the patient will be asked to remain motionless during the examination in order to assure the comparability of differently weighted MR images.
- Critically ill patients may not be examined full scale or might not fit for examination at all.
- The image quality is impaired by motion artifacts (such as heart beat, blood flow, breathing, or peristaltic movement). This problem is especially acute in patients with thorax and abdominal diseases, as MR images in general cannot be acquired completely during breath hold, as is the case in CT.
- Dynamic imaging studies are limited.

To overcome these limitations, several methods aiming to shorten the acquisition examination times have been developed. They can be categorized into two groups, depending on whether the repetition time T_R or the number of sequence cycles N_{PH} needed for phase encoding is reduced (see Eq. 2.4.5). The two strategies will be discussed in the following sections at the example of some selected imaging sequences. An almost complete overview of the clinically used fast imaging sequences will be provided in Sect. 2.4.6.

2.4.3 Gradient-Echo Techniques

2.4.3.1 Low–Flip Angle Excitation and Gradient Echoes

The long scan times of conventional imaging sequences are due to the fact that the 90° excitation pulse rotates the entire longitudinal magnetization into the x–y-plane, so the pulse sequence can only be repeated when the longitudinal magnetization has been—at least partially—recovered by T_1 relaxation processes. To acquire MR images with an acceptable *S/N*, the sequence repetition time T_R has to be of the order of the T_1 relaxation time. This basic problem in conventional imaging can be prevented, however, by using an RF pulse with a flip angle of $\alpha < 90°$ to excite the spin system, so that only a part of the longitudinal magnetization M_z will be rotated to the x–y-plane, Nevertheless, one obtains a relatively large transverse magnetization.

Example: If, for instance, a flip angle of $\alpha = 20°$ is used, then the longitudinal magnetization M_z will be reduced by 6%, whereas the transverse magnetization M_{xy} amounts to 34% of the maximum value (Fig. 2.4.11).

In order to discuss the principle of low–flip angle excitation, we will initially neglect the gradient fields needed for spatial encoding and consider the simple sequence shown in Fig. 2.4.12a. It consists of a single RF pulse with a flip angle $\alpha < 90°$ and a spoiler gradient, which destroys the remaining transverse magnetization after the acquisition of the FID.

Remark: As an alternative to spoiler gradients, the phase of the RF excitation pulse may be varied with every sequence cycle, in order to prevent the buildup of a steady state for the transverse magnetization (RF spoiling).

If the considered sequence is repeated several times, then the spin system already reaches a dynamic equilibrium after a few sequence cycles. Figure 2.4.13 shows the transient behavior of the longitudinal magnetization in white

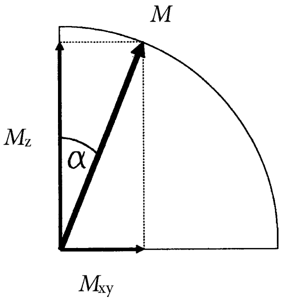

Fig. 2.4.11 Principle of low-flip angle excitation. In contrast to a conventional 90° excitation, the magnetization ***M*** in low-flip angle excitation is only rotated by a flip angle $\alpha < 90°$, so that the longitudinal magnetization M_z is only slightly reduced by the pulse. Nevertheless, this results in a relatively high transversal magnetization M_{xy}

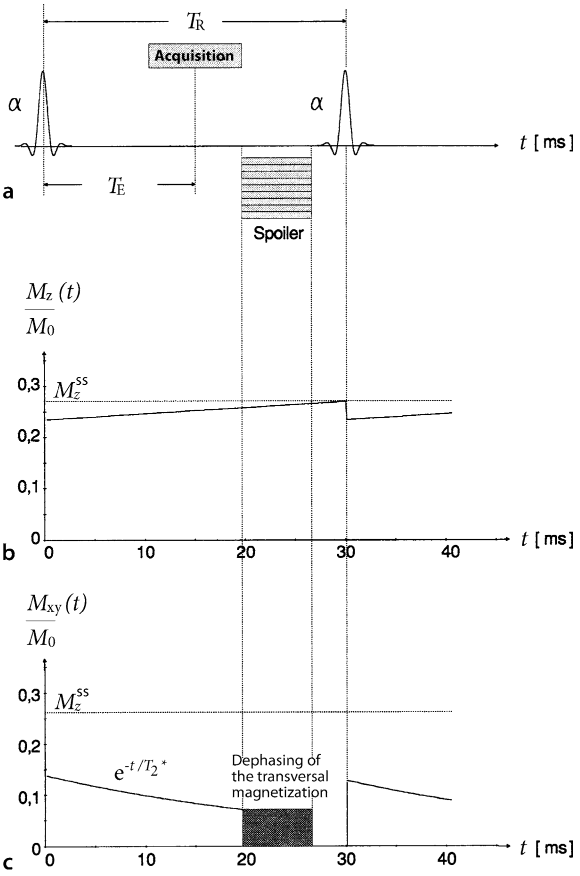

► **Fig. 2.4.12** Excitation scheme of the FLASH sequence. **a** This sequence consists of a single RF pulse with a flip angle $\alpha < 90°$ and a spoiler gradient that destroys the transversal magnetization after data acquisition. **b** Temporal evolution of the longitudinal magnetization M_z in the steady state. The steady-state magnetization is denoted by M_z^{SS}. **c** Temporal evolution of the transversal magnetization M_{xy} in the rotating frame

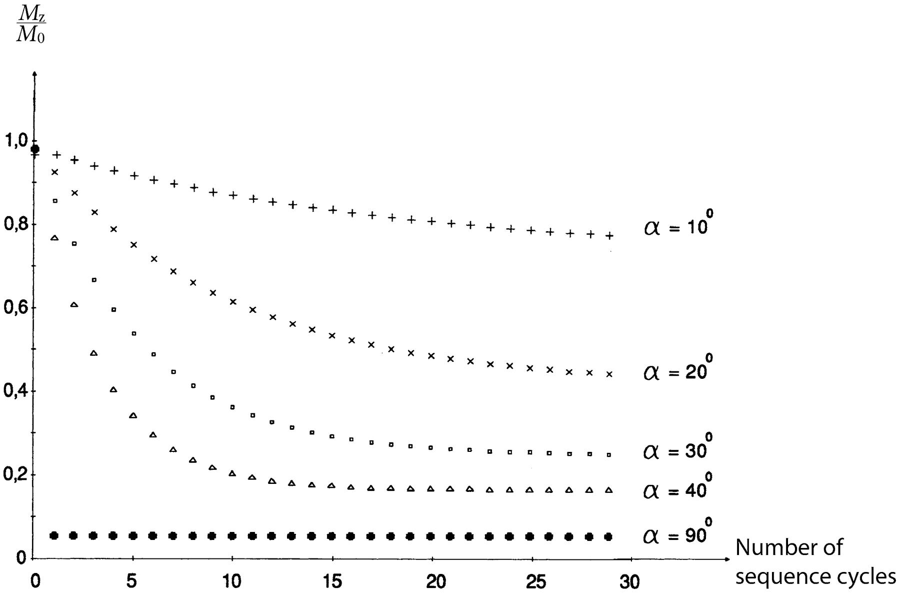

Fig. 2.4.13 Transient behavior of the longitudinal magnetization when using a FLASH sequence ($T_R = 25$ms, $T_1 = 600$ ms). If the sequence shown in Fig. 2.4.12 is repeated several times, then the longitudinal magnetization reaches a steady-state value M_z^{SS} after several repetitions. For $\alpha = 90°$, the steady state is reached already after the first excitation

brain matter ($T_1 \cong 600\,\text{ms}$) for different flip angles α. The equilibrium value of the longitudinal magnetization, the so-called steady-state magnetization M_z^{SS}, is given by the equation

$$M_z^{\text{SS}} = M_0 \frac{1-e^{-T_R/T_1}}{1-e^{-T_R/T_1}\cos\alpha}. \qquad (2.4.6)$$

The value of the steady-state longitudinal magnetization depends not only on the flip angle α of the excitation pulse, but also on the repetition time T_R and the longitudinal relaxation time T_1. It will be smaller when α becomes bigger. For $\alpha = 90°$, the longitudinal magnetization reaches the steady-state value $M_z^{\text{SS}} = M_0\,[1-e^{-T_R/T_1}]$ after the first excitation, as expected.

However, the MR signal is not given by the longitudinal magnetization but by the transverse magnetization M_{xy} at the time of data acquisition. By using Eq. 2.4.6 the amplitude S of the MR signal can be described by

$$S \propto M_{xy} = M_z^{\text{SS}} \sin\alpha \cdot e^{-T_E/T_2^*}. \qquad (2.4.7)$$

Whereas the factor $\exp(-T_E/T_2^*)$ describes the decay of the FID signal during the delay time T_E, the factor $\sin\alpha$ gives the fraction of the steady state magnetization M_z^{SS}, which is rotated in the x–y-plane (see Fig. 2.4.12b,c). To illustrate this relation, Fig. 2.4.14 shows the signal intensity S as a function of the ratio T_R/T_1. From this plot, two important statements can be derived:

- As compared with conventional 90° excitation, low–flip angle excitation yields considerably higher signal values for short repetition times.
- When using low–flip angle excitation, the signal is already independent of T_1 for $T_R < T_1$.

The signal increase realized by low–flip angle excitation in combination with short repetition times is obtained, however, by omitting the 180° pulse generating a spin-echo, as the 180° pulse not only inverts the phase of the transverse magnetization, but also the longitudinal magnetization (see Fig. 2.2.22b). This means that the dephasing of the spins due to static field inhomogeneities as well as to chemical shift effects cannot be compensated, when the concept of low–flip angle excitation is applied (see Sects. 2.4.3.4 and 2.4.3.5). In the following, several advantages and disadvantages of low flip angle excitation are summarized.

- Advantages:
  - Signal increase at short T_R times
  - Shorter T_E times, as the 180° pulse is omitted
  - Reduced energy deposition in the body by choosing an appropriate sequence
- Disadvantage:
  - Image artifacts due to local magnetic field inhomogeneities and chemical shift effects

In order to benefit from the advantages of low flip angel excitation for fast MR imaging, the sequence shown in Fig. 2.4.12a needs to be completed with the gradient fields required for slice selective excitation and spatial encoding. The pulse and gradient scheme of a typical 2D fast imaging sequence is shown schematically in Fig. 2.4.15. As is the case in the conventional imaging sequences, there is an additional rephasing gradient in slice-selection direction and a pre-dephasing gradient in readout direction. With this gradient scheme, the dephasing of the transversal magnetization caused by the three magnetic gradient fields is compensated (cf. Sect. 2.3.2), so there will be an echo signal called the gradient echo (GRE). Figure 2.4.16 shows the de- and rephasing behavior of the transverse magnetization for the three gradients in detail. Fast imaging sequences generating an echo by switching a pair of dephasing and rephasing

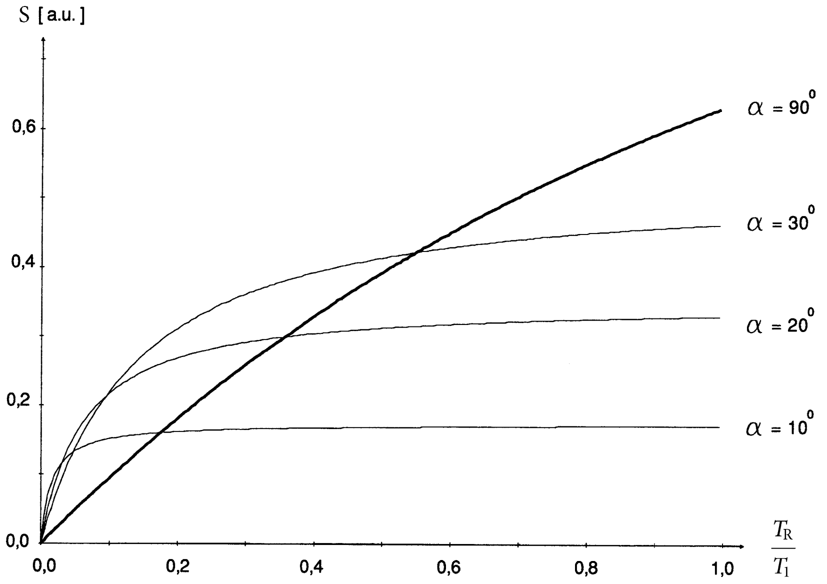

Fig. 2.4.14 Signal intensity of the FLASH sequence plotted as a function of T_R/T_1 for four different flip angles α. For short repetition times ($T_R << T_1$), the detectable MR signal is markedly higher when RF pulses with low flip angles are used instead of a conventional 90° pulse

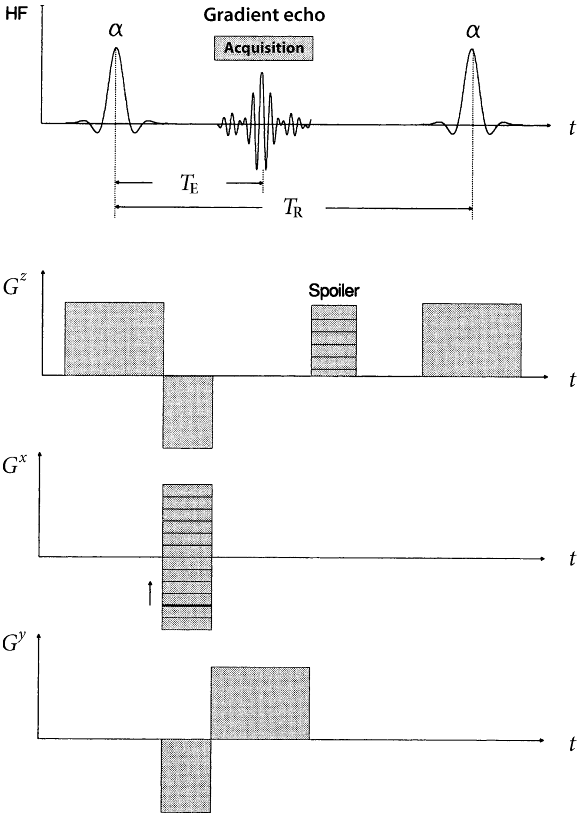

Fig. 2.4.15 Pulse and gradient scheme of the FLASH sequence. α flip angle of the excitation pulse, G^z slice selection-gradient, G^x phase-encoding gradient, G^y readout gradient

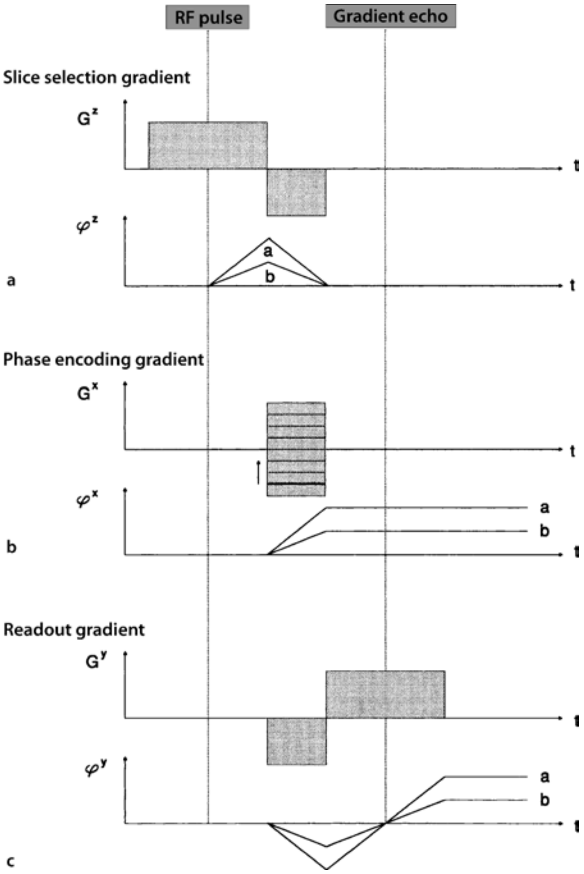

Fig. 2.4.16 Gradient refocusing of the FLASH sequence. Dephasing of the transversal magnetization caused by the slice selection and the readout gradient is compensated by two additional inverted gradients, so that a gradient-echo occurs. The figure shows the de- and rephasing process of two magnetization components (**a**,**b**), which are at different positions and therefore precess under the influence of the gradient-fields with different Larmor frequencies. φ_x, φ_y, and φ_z are the corresponding phase angles

gradients without a rephasing 180° RF pulse as with the spin-echo technique are called gradient-echo sequences (GRE sequences).

Remark: This term, however, may not conceal the fact that in conventional imaging sequences, there is always a gradient-echo created (see Figs. 2.4.1 and 2.4.6). The difference consists only in the fact that the 180° pulse of the SE technique creates an additional spin-echo, which temporally coincides with the gradient echo.

In contrast to the conventional imaging sequences, the nomenclature of the GRE sequences is not unified, but is handled differently by different manufacturers. In the following, the fundamentals of GRE imaging will be discussed in detail at the example of two representative sequences denoted by the acronyms FLASH and trueFISP. The excitation of the spin system and position encoding are identical in both sequences; they differ only in that the transverse magnetization is destroyed after acquisition of the MR signal in the FLASH sequence (spoiled GRE sequence), whereas it is maximized in the trueFISP sequence (refocused GRE sequence). This difference, however, leads to an entirely different contrast behavior.

Table 2.4.4 Recommendation of acquisition parameters for the measurement of weighted FLASH images

Weighting	α	T_R (ms)	T_E (ms)
PD	10–20°	50–500	$T_E << T_2^*$
T_1	40–80°	20–300	$T_E << T_2^*$
T_2^*	10–20°	50–500	15–40

2.4.3.2 Example FLASH

The spoiled GRE sequence shown in Fig 2.4.15 was introduced in 1985 by A. Haase et al. (1986) under the acronym FLASH (fast low-angle shot); its essential characteristics have already been outlined in the previous section. The signal intensity of a FLASH image can be described by the equation (cf. Sect. 2.4.3.1)

$$S_{\mathrm{FLASH}} = PD \cdot \underbrace{\frac{(1-e^{-T_R/T_1})\sin\alpha}{1-e^{-T_R/T_1}\cos\alpha}}_{T_1\ \text{factor}} \cdot \underbrace{e^{-T_E/T_2^*}}_{T_2^*\ \text{factor}} \tag{2.4.8}$$

and thus can be varied through the choice of the repetition time T_R, the echo time T_E, and the flip angle α of the excitation pulse.

- ***PD* dependence:** see Sect. 2.4.2.1
- ***T_1* dependence:** In contrast to the SE sequence, the T_1 contrast behavior of the FLASH sequence is not only influenced by the repetition time T_R, but also by the choice of the flip angle α. In order to illustrate this, the T_1 contrast between white and gray brain matter is plotted in Fig. 2.4.17 as a function of the repetition time T_R for different flip angles. As can be seen, the T_1 contrast at low flip angles is only different from 0 if very short repetition times are selected. If the flip angle is increased, then the T_1 contrast maximum is shifted toward larger T_R values and approximates the known T_1 contrast behavior of the SE sequence. For a given value of T_R/T_1, the T_1 factor of the signal Eq. 2.4.8 is maximized, when α is given by the so-called Ernst angle

  $$\alpha_E = \arccos(e^{-T_R/T_1}). \tag{2.4.9}$$

  However, this does not imply that for this angle the tissue contrast between two structures is at its maximum. In Fig. 2.4.18 the tissue contrast between white and gray brain matter is plotted for $T_E << T_2^*$, i.e., $\exp(-T_E/T_2) \approx 1$, as a function of the repetition time T_R and the flip angle α. For low flip angles, two contrast regions can be distinguished: for short T_R times, the T_1 contrast dominates (T_1-weighted images), for longer T_R times, the *PD* contrast (*PD*-weighted image).

Example: In order to illustrated the discussed contrast behavior, Fig. 2.4.19 shows a T_1-weighted ($T_R/T_E/\alpha$ = 150/6/60°) and a *PD*-weighted FLASH image (400/6/20°).

- ***T_2* dependence:** In order to acquire a T_2^*-weighted FLASH image, the influence of T_1 relaxation effects need to be minimized. For an SE sequence, this condition can only be fulfilled if a large repetition time T_R is chosen ($T_R >> T_1$). This is different in FLASH imaging. As Fig. 2.4.18 shows, the recovery due to T_1 relaxation can be neglected for much shorter T_R values if the flip angle is chosen rather small. The T_2^* contrast of a FLASH image can be varied through the choice of the echo time T_E. When doing this, however, one needs to remember that, due to the rapid T_2^* decay, T_2^* weighting happens already at markedly shorter T_E times than in SE imaging (see Sect. 2.4.3.4).

The influence of the acquisition parameters on the contrast of a FLASH image is summarized in Table 2.4.4.

2.4.3.3 Example trueFISP

In 1986, Oppelt et al. introduced a GRE sequence with the acronym FISP (fast imaging with steady precession), which considerably differs in its contrast from the FLASH sequence. This sequence was later renamed to trueFISP (see below). The pulse and gradient scheme of this sequence is shown in Fig. 2.4.20. Instead of the spoiler gra-

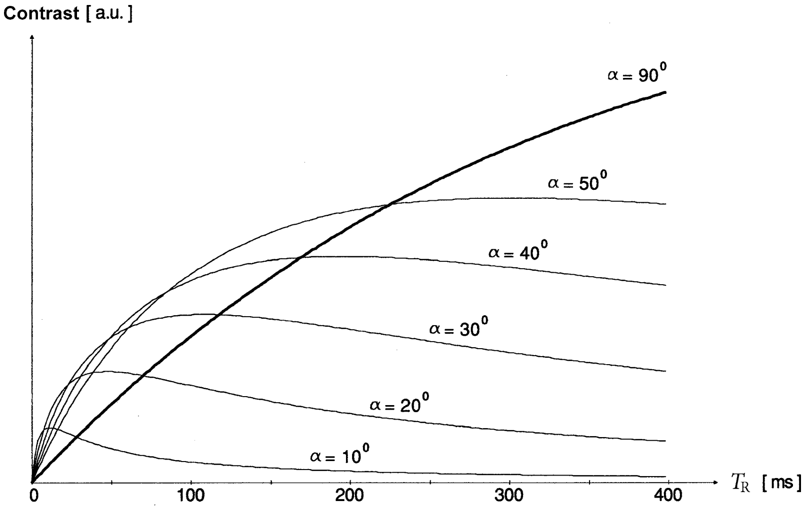

Fig. 2.4.17 Influence of the acquisition parameters T_R and α on the T_1 contrast of a FLASH image. For low excitation angles α, there will only be a considerable T_1 contrast (here between white and gray brain matter) when short repetition times are selected. If the flip angle is increased, the T_1 contrast maximum will shift to a higher T_R value

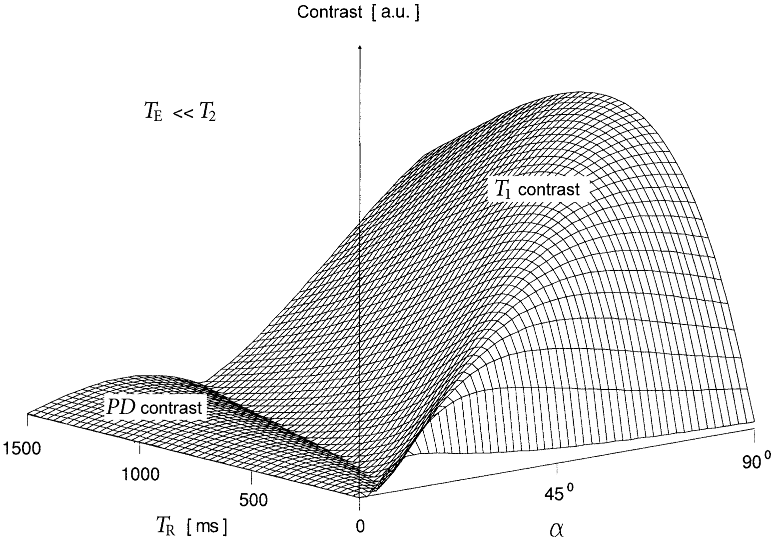

Fig. 2.4.18 Parameter weighting in FLASH imaging. Plotted is the contrast between white and gray brain matter as a function of the repetition time T_R and the flip angle α for $T_E << T_2^*$. Two different contrast regions can be distinguished for low flip angles: for short T_R times, the T_1 contrast dominates (T_1-weighted image), for longer T_R times, the *PD* contrast (*PD*-weighted image). If the flip angle is increased, then the T_1 contrast curve will gradually approach the known contrast behavior of the SE sequence ($\alpha = 90°$). Correspondingly, long repetition times need to be chosen in order to acquire *PD*-weighted or T_2-weighted images

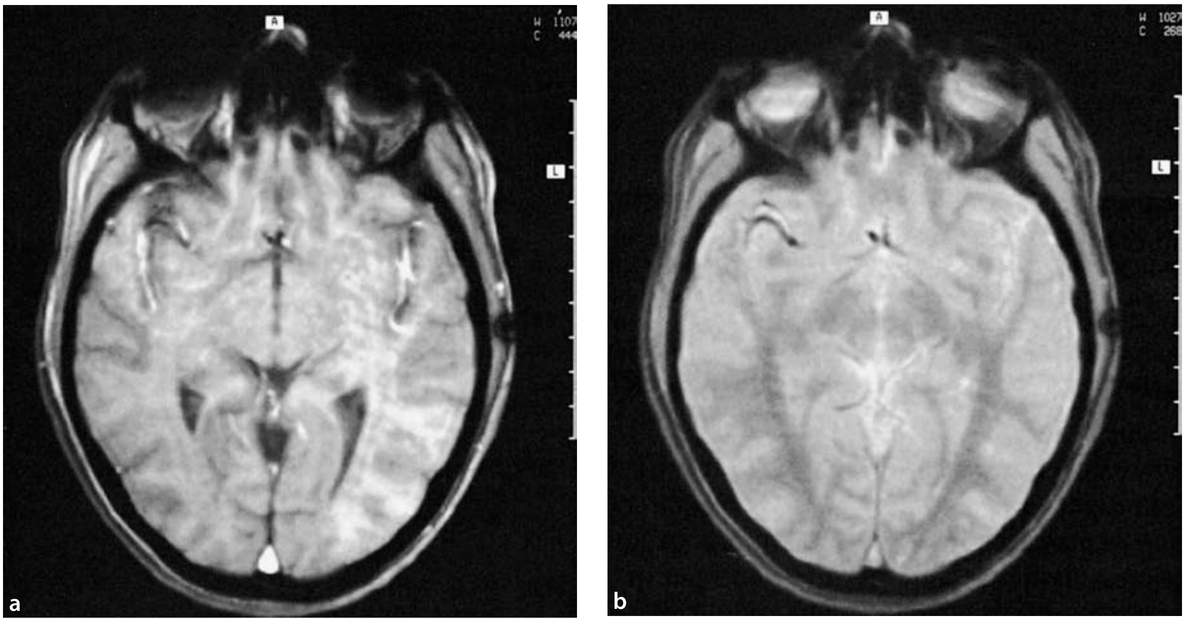

Fig. 2.4.19 FLASH images of a transversal head section with a thickness of 5 mm. **a** T_1-weighted image ($T_R/T_E/\alpha/N_{AQ} = 150/6/60°/4$) **b** *PD*-weighted image (400/6/20°/4)

dient of the FLASH sequence, refocusing gradient pulses are introduced in slice-selection direction as well as in the direction of frequency and phase encoding, through which the transverse magnetization is not destroyed after the data acquisition of the MR signal, but rather rephased or refocused (Fig. 2.4.21).

Remark: As practice has shown, the trueFISP sequence is very susceptible to inhomogeneities of the static magnetic field, which are rendered visible as disturbing image artifacts. A more favorable behavior is achieved by omitting the gradient pulses (which have been shaded darkly in Fig. 2.4.20). In this case, only the dephasing of the transverse magnetization caused by the slice selection and phase-encoding gradient is completely compensated. This realization is called FISP sequence.

In the trueFISP sequence, not only the longitudinal, but also the transversal magnetization reaches an equilibrium state after several sequence cycles. As both magnetization components are different from zero at the end

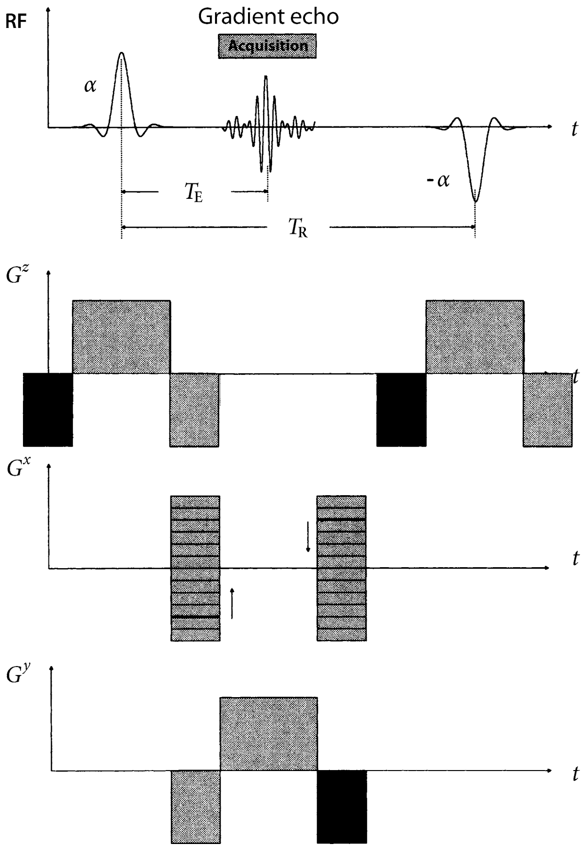

Fig. 2.4.20 Pulse and gradient scheme of the trueFISP sequence. α flip angle of the excitation pulse, G^z slice-selection gradient, G^x phase-encoding gradient, G^y readout gradient. Instead of the spoiler gradient used in the FLASH sequence, there are refocusing gradient pulses in all three gradient directions, so that the transversal magnetization after acquisition of the gradient-echo is not destroyed but reconstructed (see Fig. 2.4.21). In practice, the gradient pulses (marked *darkly*) here is frequently omitted in order to reduce the susceptibility of the sequence for artifacts leading to a FISP sequence

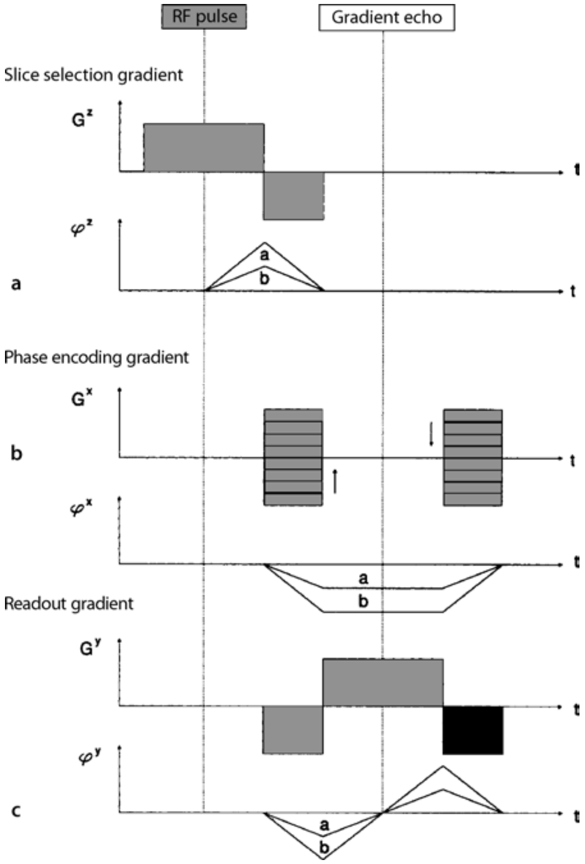

Fig. 2.4.21 Gradient refocusing of the FISP sequence. Due to the complex gradient switching, the dephasing of the transversal magnetization caused by the three gradients is completely compensated after acquisition of the gradient-echo, so the transversal magnetization is restored before irradiation of the subsequent excitation pulse. The figure shows the de- and rephasing process for two magnetization components (**a**,**b**), which are at different positions and therefore precess with different Larmor frequencies under the influence of the gradient fields. φ_x, φ_y, and φ_z are the corresponding phase angles. At the end of the sequence, both magnetization components are in phase again ($\varphi_x = \varphi_y = \varphi_z = 0$), independent of their spatial position

of a sequence cycle, they will be mixed by the following RF pulse, i.e., a part of the longitudinal magnetization is flipped into the x–*y*-plane and a part of the transverse magnetization into the *z*-direction. Consequently, both magnetization components dependent on T_1 and on T_2. The T_2 dependence increases proportional to the magnitude of the transverse magnetization remaining at the end of the sequence cycle (i.e., with decreasing T_R/T_2 ratio). Vice versa, this means that the FISP signal for high T_R values ($T_R >> T_2$) will approximate the FLASH signal.

Remark: The difference in the latter case merely consists in the fact, that in the FLASH sequence the transverse magnetization is rapidly destroyed by a spoiler gradient after the acquisition of the FID, whereas in the FISP sequence it decays with the time constant T_2. Therefore, the FLASH sequence is more useful for the acquisition of T_1-weighted and *PD*-weighted images than is the FISP sequence.

As the discussion has shown, the characteristic signal behavior of the FISP sequence manifests itself only for very short repetition times. For this special situation, the dependence of the signal intensity of the FISP sequence on the tissue parameters T_1, T_2, and *PD* can be described

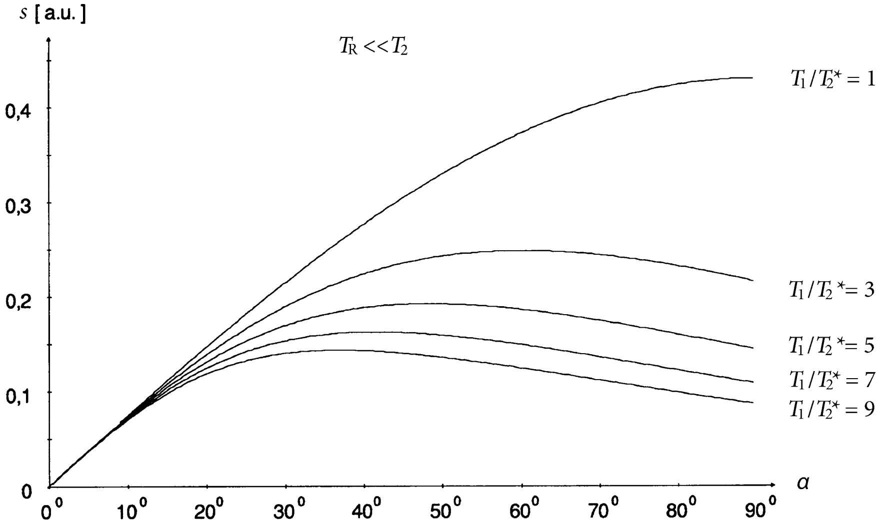

Fig. 2.4.22 T_1/T_2 dependence of the signal intensity of the trueFISP sequence. Plotted is the T_1/T_2 factor of the trueFISP signal equation as a function of the flip angle α for different T_1/T_2 ratios and very short repetition times ($T_R << T_2$). For a given flip angle α, the signal intensity will be the bigger, the smaller the ratio T_1/T_2 is

approximately by the expression

$$S_{\text{FISP}} = PD \cdot \underbrace{\frac{\sin\alpha}{1+T_1/T_2\ +(1-T_1/T_2)\cos\alpha}}_{T_1/T_2 \text{ factor}} \cdot \underbrace{e^{-T_E/T_2}}_{T_2 \text{ factor}}, \tag{2.4.10}$$

which is independent of the repetition time T_R. As this equation shows, the signal intensity of a FISP image for $T_R << T_2$ and $T_E << T_2$ depends only on the ratio of the tissue-specific relaxation times T_1/T_2, not on absolute values. The FISP sequence is therefore also denoted as T_1/T_2-weighted GRE sequence.

- ***PD dependence:*** see Sect. 2.4.2.1
- ***T_1/T_2 dependence:*** In Fig. 2.4.22, the T_1/T_2 factor of the FISP signal Eq. 2.4.10 is plotted as a function of the flip angle α for different T_1/T_2 ratios. As one can see, the signal intensity at a given flip angle is the bigger the more similar the relaxation times T_1 and T_2 are. The absolute maximum is obtained for α = 90° and $T_1 = T_2$. For a given value of T_1/T_2, the T_1/T_2 factor is maximized, when the flip angle is given by

$$\alpha_{\text{opt}} = \arccos\left(\frac{T_1/T_2\ -1}{T_1/T_2\ +1}\right). \tag{2.4.11}$$

Remark: The considerations are only valid for stationary spins. If the phase coherence and thus the steady-state magnetization are disturbed by flow, as is the case in blood vessels or in liquor spaces, then the signal maximum will be shifted toward lower excitation angles.

In practice, flip angles between 70° and 90° and repetition times between 35 and 50 ms are used for the acquisition of T_1/T_2-weighted trueFISP images. In these images, tissues with lower T_1/T_2 ratio (i.e., fatty tissue and liquor) are more signal intensive than are tissues with high T_1/T_2 ratio (e.g., white and gray brain matter). For the acquisition of T_1-weighted and *PD*-weighted images, the FLASH sequence is better suited than is the trueFISP sequence.

Example: Figure 2.4.23 shows a T_1/T_2-weighted trueFISP image ($T_R/T_E/\gamma$ = 35/7/80°). The comparison of this image with the T_1-weighted FLASH image shown in Fig. 2.4.19 reveals the complementary contrast behavior of the two GRE sequences.

2.4.3.4 Influence of Magnetic Field Inhomogeneities

Opposite to conventional imaging sequences (i.e., the SE and the IR sequence), the dephasing of spins due to static magnetic field inhomogeneities cannot be compensated in GRE sequences, due to the missing rephasing 180° RF pulse (see Sect. 2.4.3.1). Consequently, the transverse magnetization M_{xy} does not decay with the tissue-specific transverse relaxation time T_2, but with the time constant T_2^* (cf. Sect. 2.2.5.2 and Fig. 2.2.22). Compared with T_2, T_2^* shortens proportional to an increase in local magnetic field inhomogeneity. If the magnetic field inhomogeneity per voxel is denoted as ΔB, the relation between the three quantities can be expressed as

$$1/T_2^* = 1/T_2 + \gamma\Delta B/2. \tag{2.4.12}$$

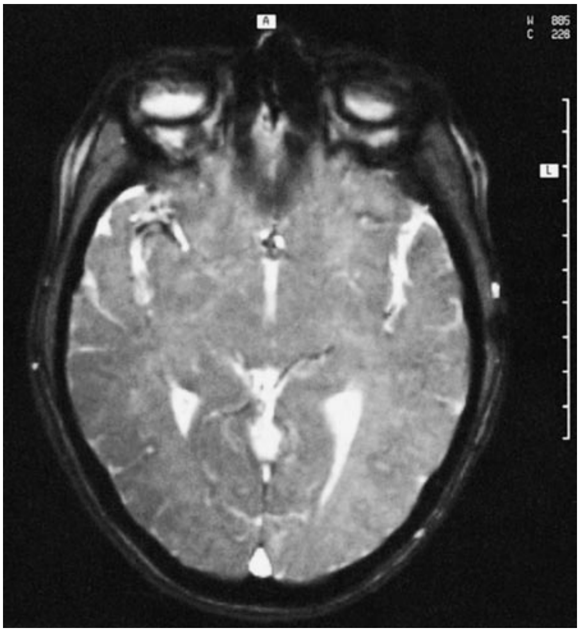

Fig. 2.4.23 T_1/T_2-weighted trueFISP image ($T_R/T_E/\alpha/N_{AQ}$ = 35/7/80°/4) of a transversal head section with a thickness of 5 mm. (Compare this image with the T_1-weighted FLASH image shown in Fig. 2.4.19a)

Numerical examples are given in Table 2.4.5.

In MR imaging, local field inhomogeneities have essentially three reasons:

- ***Technical imperfections of the main magnetic field.*** They increase with the distance from the center of the magnet and can cause severe signal losses in the outer zone. When using GRE sequences, one therefore has to remember that the body region to be analyzed should not be too far away from the center of the magnet.

Example: In modern MR tomographs, the magnetic field inhomogeneity over a sphere of 50 cm diameter is smaller than 5 ppm. Assuming that the magnetic field changes linearly with distance to the center of the magnet, a magnet field inhomogeneity of about 0.02 ppm per pixel is obtained for a matrix size of 256 × 256 and a field of view of 50 cm (Table 2.4.5).

- ***Para- or ferromagnetic implants.*** Such implants (e.g., prostheses or clips) cause strong magnetic field inhomogeneities in the surrounding tissues. As a consequence, T_2* times of these tissues are drastically reduced which results in signal losses in the vicinity of the implants. In these cases, conventional imaging techniques have to be used, which are less susceptible to field inhomogeneities.
- ***Susceptibility effects.*** As discussed in Sect. 2.2.8, the magnetic field distribution within the human body depends on the position, size, form, and magnetic susceptibility of the various tissues and organs in the body. Whereas the magnetic field is locally homogeneous in larger uniform organs or tissue regions, there are local field inhomogeneities at the interfaces of anatomical structures, which differ in their magnetic susceptibility. They can be strong enough to cause—via a reduction of the T_2* times—signal losses in the vicinity of the interface. One can observe this effect in GRE images mainly in the vicinity of air–tissue interfaces, such as in the lung or in paranasal tissues. Even though susceptibility artifacts are unavoidable in GRE imaging, they can be minimized by two techniques: by shortening the echo time T_E of the sequence and by reducing the voxel size, especially the slice thickness. By both means the average field inhomogeneity per voxel is reduced.

Table 2.4.5 Reduction of the transverse relaxation time T_2* due to inhomogeneities ΔB of the static magnetic field

ΔB/voxel (ppm)	$2/\gamma\Delta B$ (ms)	T_2 (ms)	T_2* (ms)
0.02	250	100	71
		1,000	200
0.2	25	100	20
		1,000	24

2.4.3.5 Influence of the Chemical Shift

As shown in Fig. 2.3.7, the ^{1}H spectrum of the human organism consists of two dominant peaks, whose resonance frequencies differ due to the chemical shift by about 3.5 ppm. The two resonance peaks are assigned to hydrogen nuclei in water molecules and those in methylene groups of fatty acids. If both components contribute to the MR signal of a tissue, for instance fatty tissue or bone marrow, then a modulation of the signal intensity of these tissues can be observed in GRE imaging in dependence on the echo time T_E.

This interesting phenomenon is due to the fact that the transverse magnetization of the water component precesses after RF excitation a little faster than the fat component, so both magnetization components are oriented parallel or antiparallel in regular intervals (Fig. 2.4.24). As the detected GRE signal is proportional to the vector sum of the two magnetization components, this periodic behavior manifests in a modulation of the signal intensity: the intensity is at its highest when the two components are oriented parallel; it is at its minimum

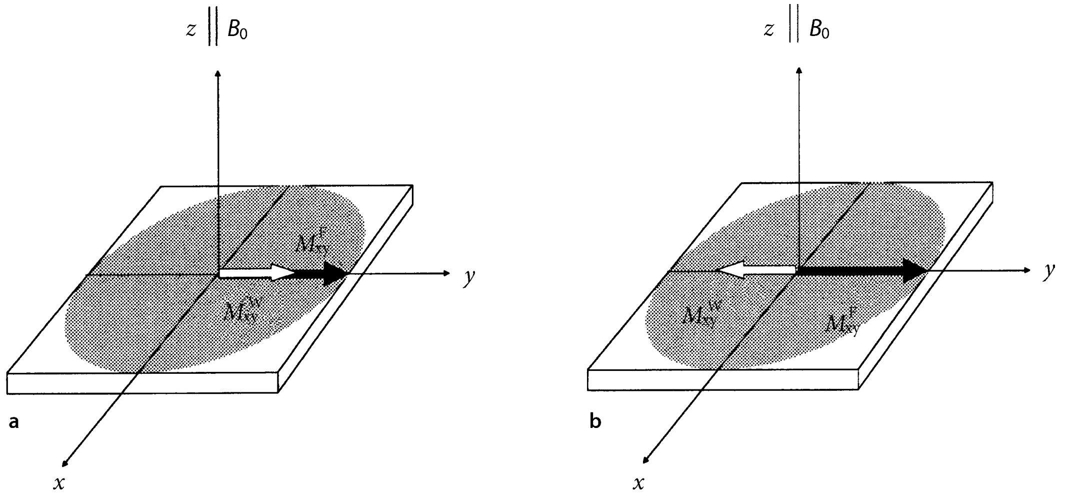

Fig. 2.4.24 Temporal evolution of the transversal magnetization in fatty tissue. In fat-containing tissues, two pools of hydrogen nuclei contribute to the MR signal, whose resonance frequencies differ by about 3.5 ppm. They are assigned to ^{1}H nuclei in water and in methylene groups of fatty acids. As the transversal magnetization of the water component (M_{xy}^w) after RF excitation precesses slightly faster than the methylene component (M_{xy}^F), the two magnetization vectors are oriented **a** parallel or **b** antiparallel in regular intervals. The figure shows this in a rotating frame, in which the transversal magnetization of the fat component does not rotate

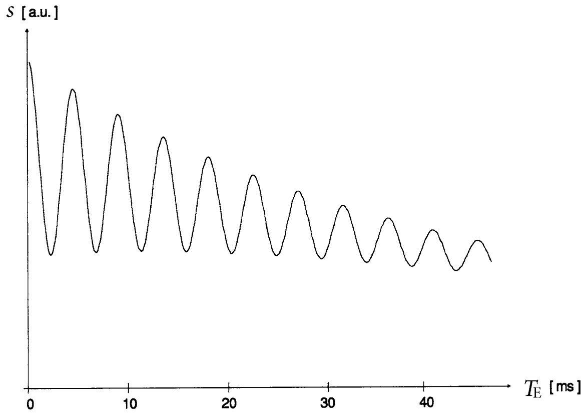

Fig. 2.4.25 Modulation of the GRE signal in fat-containing tissues. At a magnetic flux density of 1.5 T, the difference between the resonance frequencies of the water and methylene protons is about 220Hz, so that the transversal magnetization of the two proton components is oriented parallel or antiparallel every 2.3 ms (see Fig. 2.4.24). This periodic behavior results in a modulation of the measured GRE signal: the signal intensity is at its maximum if the two transversal magnetizations are parallel; it is at its minimum if they are antiparallel

when they are antiparallel. The amplitude of the signal modulation depends on the ratio of the two signal components.

Example: At a magnetic flux density of $B_0 = 1.5$ T, the frequency difference between the fat and the water component is about $\Delta\omega / 2\pi = 220$ Hz. This implies that the two magnetization components are oriented parallel or antiparallel after RF excitation in equidistant time intervals of $\Delta\tau = \pi / \Delta\omega = 2.3$ ms. Figure 2.4.25 illustrates the signal modulation at 1.5 T for a realistic example.

2.4.4 Modification of *k*-Space Sampling

2.4.4.1 Half-Fourier Technique

In 2D Fourier imaging, the MR image is reconstructed via a Fourier transformation from the acquired raw data set, the *k*-space matrix. Even though for the reconstruction of an MR image with $N \times N$ pixels a raw data matrix with $N \times N$ data points is required, it is sufficient to measure only the first $N/2$ rows of the raw matrix, when the symmetry of the *k*-space is taken into account (half-Fourier technique) (Feinberg et al. 1986).

To illustrate this aspect, Fig. 2.4.26 shows a raw matrix that has been acquired with the SE sequence shown in Fig. 2.4.1. The data points of the *k*-space matrix are positioned symmetrically to the center of the matrix. Due to this fact, it is sufficient to measure only the data points of the upper half of the *k*-space and to fill the lower half through (conjugate) point reflection of the measured data in the center of the matrix (Fig. 2.4.27).

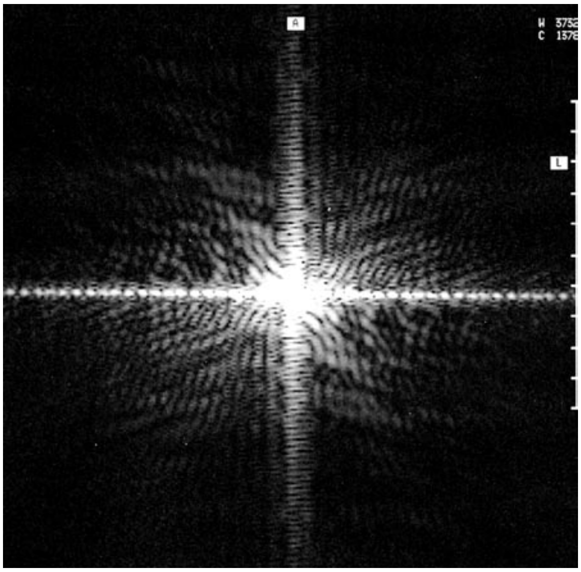

Fig. 2.4.26 *k*-Space matrix. The raw data matrix shown has been acquired with the SE sequence shown in Fig. 2.4.1. As can be seen, the data points are positioned symmetrical to the center of the matrix. This symmetric property of the *k*-space matrix is utilized in the half-Fourier technique (see Fig. 2.4.27)

Remark: In order to generate this raw data matrix row by row, the sequence has been repeated N times for different values of the phase-encoding gradient $G^x = n\Delta G^x$ $(-N/2 < n \leq N/2)$ with the SE signal being measured N times in the presence of the readout gradient in equidistant steps Δt symmetrically to the echo time T_E at each sequence cycle (see Fig. 2.4.28a).

With this technique, the number of sequence cycles N_{PH} required for phase encoding can be halved without reducing the spatial resolution, which—according to Eq. 2.4.5—also implies a 50% reduction of the acquisition time. The reduction of acquisition time, however, results in a reduction of the S/N ratio by the factor $\sqrt{2}$.

Remark: In practice, some more rows of the *k*-space matrix are acquired, which makes it possible to perform a phase correction. Due to this reason, the reduction of the acquisition time is slightly less than 50%.

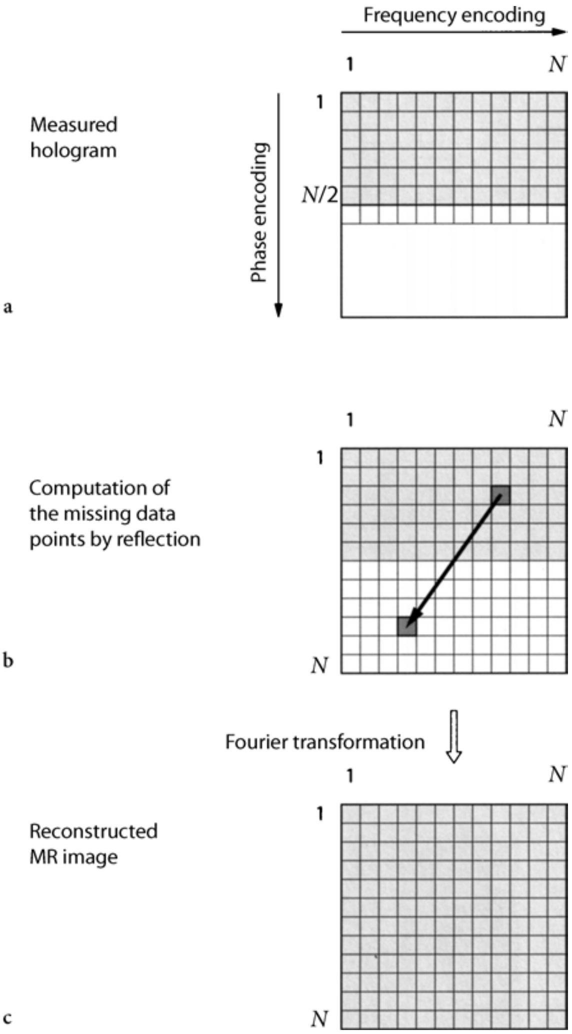

Fig. 2.4.27 Half-Fourier technique. **a** In this technique, only the data points of one half of the raw matrix are measured. **b** The missing points are generated through (conjugate) point reflection of the measured data in the center of the matrix (see Fig. 2.4.26). **c** After this preparatory step, the MR image can be reconstructed as usual by a 2D Fourier transformation of the *k*-space matrix

2.4.4.2 Fourier Interpolation

The measurement time can also be reduced by sampling only the central segment of the *k*-space matrix. However, Fourier transformation of such a sparsely sampled *k*-space matrix yields an image that is only coarsely sampled (i.e., has large voxel dimensions) in the phase-encoding direction(s). This may result in severe partial volume effects in case of small tissue structures, such as vessels in MR angiography. The nominal resolution of the reconstructed image can be improved when the “missing” lines of the *k*-space are “zero filled” before Fourier transformation. This approach, denoted as Fourier interpolation, increases the number of pixels in the reconstructed image and thus the image resolution, but does not, of course, improve the physical resolution of the imaging process. Nevertheless, this trick improves the appearance of the reconstructed images and reduces partial volume effects.

Fourier interpolation is routinely used in 2D imaging as, for example, to display a 512 × 512 image matrix reconstructed from a *k*-space matrix with only 256 × 256

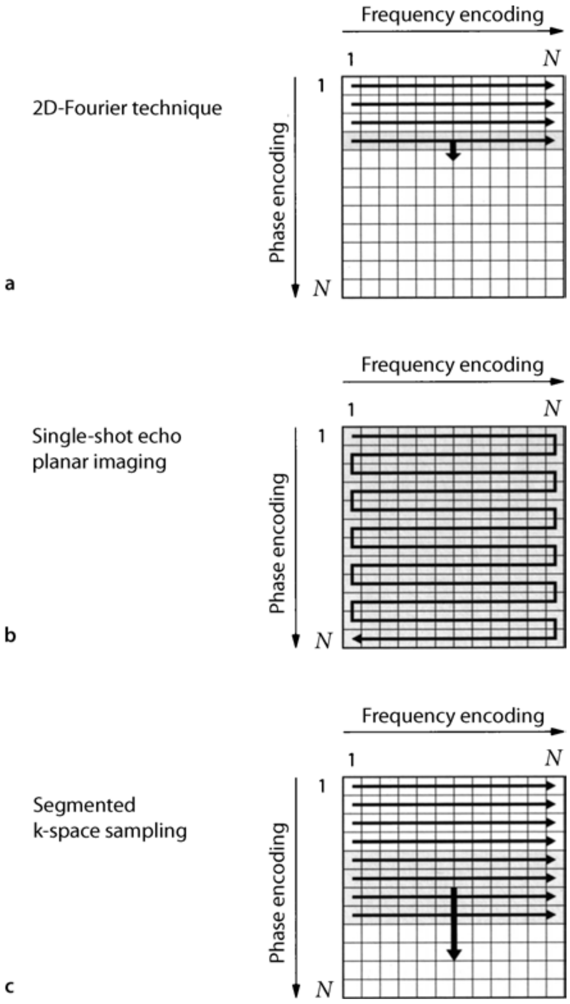

Fig. 2.4.28 Possible sampling schemes for the *k*-space matrix. **a** In the conventional 2D Fourier technique, only one row of the *k*-space matrix is acquired per sequence cycle so that *N* sequence cycles are required to completely construct the raw data matrix. **b** In the single-shot echo planar technique, all rows of the *k*-space matrix are detected in one single sequence cycle. The figure shows one possible sampling strategy. **c** In segmented *k*-space sampling, several rows of the *k*-space matrix are acquired per sequence cycle. The figure indicates the rows of the raw matrix that are acquired in one sequence cycle in *gray*

measurement points. The concept can be extended to 3D imaging, in particular to compensate for the sparse sampling of the *k*-space matrix in the direction of the second phase-encoding gradient (slab direction).

Remark: A special application is the VIBE (volume interpolated breath-hold examination) technique, which is being used to reconstruct images from a sparsely sampled *k*-space matrix acquired with a fast 3D imaging sequence within a single breath hold.

2.4.4.3 Parallel Imaging

What happens, when the number of phase-encoding steps N_{PH}—and thus the image acquisition time—is halved, while the sampling interval of the phase-encoding gradient, here ΔG^x, is doubled? According to the sampling theorem discussed in Sect. 2.3.3.1, the field of view FOV_x that can be imaged in x-direction without reconstruction errors is inversely proportional to ΔG^x. Therefore, the FOV_x is also halved by the modified sampling strategy. In contrast, the spatial resolution $\Delta x = X/N$ is not changed. The modification discussed has thus—apart from a reduction of the S/N ratio due to the reduced number of measurements—no effect on the reconstructed MR image, as long as the object size X in direction of the phase-encoding gradient is less than $FOV_x/2$. However, if the object size X is greater, then this will result in aliasing artifacts, i.e., the portions of the object outside of the reduced field of view get mapped to an incorrect location inside this field of view. The reason is that at these positions the phase angles ϕ induced by the phase-encoding gradient are greater than 2π or 360°) and thus cannot be distinguished from phase angles in the interval $0–2\pi$ (see Fig. 2.3.9) that encode positions inside the reduced field of view. The missing information, however, can be obtained by using two adjacent coil elements in an RF receive array with non-overlapping sensitivity profiles, each of which detects the MR signals from only one half of the full field of view. This strategy is called parallel imaging. Obviously, the number of phase-encoding steps N_{PH}—and thus the acquisition time—can be further decreased if receive arrays with more than two coil elements are used (see Sect. 2.5). Parallel imaging offers the major advantage that it can be combined with any existing imaging sequence (e.g., SE, GRE, and echo planar imaging sequences) and that the contrast behavior of the sequence used is not changed.

When implementing parallel imaging techniques, one has to deal with the problem that the sensitivity profiles of the coil elements are not rectangular but rather overlap. To avoid image artifacts arising from this fact, sophisticated image reconstruction techniques have been developed. They can be classified into two major groups, image-based reconstruction (e.g., SENSE, or sensitivity encoding) and *k*-space–based reconstruction techniques (e.g., GRAPPA, or generalized autocalibrating partially parallel acquisitions).

2.4.4.4 Segmented *k*-Space Sampling

The basic idea of the echo planar imaging (EPI) technique, described by P. Mansfield in 1976 (Mansfield et al. 1976), aims at generating a series of spin or gradient-echoes in a short period of time after excitation of the spin system by an RF pulse, which are differently phase encoded by an appropriate gradient-switching scheme. In this way, all rows of the *k*-space matrix can be acquired within one single sequence cycle. The various published versions of the EPI technique only differ in the way the phase-encoding gradients are switched, i.e., in what order the data points of the raw data matrix are sampled. One possible sampling scheme is shown in Fig. 2.4.28b. The limiting factor evidently is the speed with which the transverse magnetization decays after RF excitation. If the acquisition time is markedly longer than the decay constant (T_2 or T_2*, respectively), the different rows of the *k*-space matrix are differently T_2 or T_2* weighted, depending on the sampling scheme. This means that distinct spatial frequencies are over- and others are underweighted. In order to prevent this problem, the entire data set needs to be acquired within a time interval, which is comparable to the decay constant of the transverse magnetization. The EPI technique therefore challenges the gradient system.

The mentioned problems in EPI can be avoided by sampling only few rows of the *k*-space matrix during each sequence cycle. If N_E echoes are generated per excitation, then the number of sequence repetitions necessary to completely fill the raw data matrix and, in consequence, the acquisition time can be reduced by the factor $1/N_E$ as compared with the conventional 2D Fourier technique. In contrast to the EPI technique, the demands on the gradient system for this so-called segmented *k*-space sampling strategy are much lower.

2.4.5 Preparation Techniques

In MR imaging, there are two major pools of hydrogen nuclei that contribute to the image signal: the ^{1}H nuclei of freely moveable water molecules and those of the CH_2 groups of mobile fatty acids (see Fig. 2.3.7). In contrast, the MR signal from hydrogen nuclei which are bound in relatively immobile macro-molecular structures (such as proteins, cell membranes, etc.) cannot be detected due to their very short T_2 times (cf. Sect. 2.2.5.3). Nevertheless, they affect indirectly the magnetization of the "free" ^{1}H nuclei in water and thereby also modify the image signal. Based on these facts, different methods have been developed, which offer the possibility to modify the magnetization detectable in MR imaging by preparation pulses.

2.4.5.1 Fat Saturation

As already discussed in Sect. 2.3.3.1, the chemical shift of about 3.5 ppm between ^{1}H nuclei in water and fatty acids becomes evident in the fact that fat- and water-containing tissue structures of the body are slightly shifted against one another. This image artifact, which is especially pronounced in EPI, can be avoided by reducing the contribution of the fatty acids to the MR signal.

One possibility to reduce the signal from fatty acids has already been discussed in relation with the STIR sequence (see Sect. 2.4.2.2), in which the magnetization is prepared (here inverted) by an inversion pulse. If the inversion time is chosen so that the longitudinal magnetization of the fatty acids is almost zero at this point in time, only the water pool will contribute to the STIR image (see Fig. 2.4.10b). A drawback of this technique is, however, that the inversion time is determined by the T_1 time of the ^{1}H nuclei in fatty acids, and thus the T_1 contrast of the images cannot be chosen freely. This problem can be avoided by utilizing not the specific relaxation properties of fatty tissues (see Table 2.2.2) for fat suppression, but the chemical shift between ^{1}H nuclei in water and in fatty acids. The latter strategy offers the opportunity to selectively saturate the magnetization of the fatty acids by frequency-selective RF pulses, so-called CHESS (chemical shift selective) pulses, and to use the remaining magnetization of the water pool for image generation. In the simplest case, the CHESS pulse is a frequency-selective 90° pulse, which flips the longitudinal magnetization of the CH_2 groups into the *x*–*y*-plane, where it will be dephased by a spoiler gradient (Frahm et al. 1985; Haase et al. 1985). However, this places high demands on the homogeneity of the magnetic field within the patient; in order to separate the two resonance lines, the field homogeneity must be better than 3 ppm. In practice, this condition can only be rendered if the homogeneity of the magnetic field is adjusted by a special shim procedure before the examination of the patient. In order to avoid this procedure, optimized CHESS pulses for fat suppression have been developed (e.g., binominal pulses).

2.4.5.2 Magnetization Transfer

In biological tissues, there are two pools of hydrogen nuclei that differ markedly regarding their biophysical properties: ^{1}H nuclei in water molecules with high mobility (^1H_f, or free water protons), and ^{1}H nuclei in macromolecules with reduced mobility (^1H_r). Whereas the T_1 relaxation times of the two pools do not differ markedly ($T_1 > 100$ ms), the T_2 times differ strongly (see Fig. 2.2.16). The T_2 times of the ^1H_f nuclei are generally higher than 40 ms, whereas for ^1H_r nuclei they are less than 100 μs due to the strong dephasing effect of neighboring spins. The different T_2 times are mirrored in the ^{1}H spectrum (Fig. 2.4.29). As the width $\Delta\omega$ of a resonance line is inversely proportional to the T_2 time (see Sect. 2.2.6), the ^1H_f pool has a line width of a few Hertz, whereas the spectral width of the ^1H_r nuclei is more than 10 kHz. It is crucial that the two ^{1}H pools interact due to intermolecular processes (spin–spin interaction) and/or chemical exchange processes (Wolff and Balaban 1989). Due to this reason, any change in the magnetization in one pool results in an alteration of magnetization of the other pool. This effect is called magnetization transfer (MT).

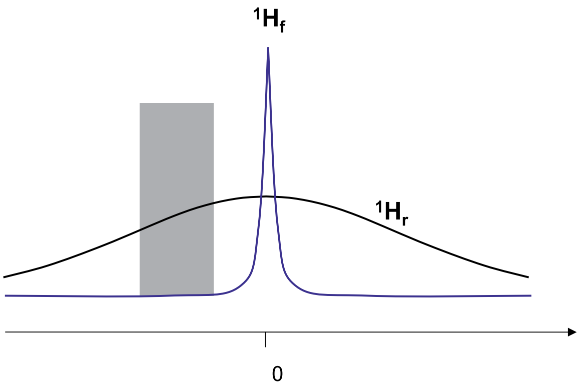

Fig. 2.4.29 Schematic depiction of a ^1H spectrum of biological tissues. Apart from the resonance line of ^1H nuclei in free water (^1H_f), with a low spectral line width (< 20 Hz), there is a broad underground due to ^1H nuclei in macromolecules with reduced mobility (^1H_r), the MR signal of which cannot be detected directly because of their short T_2 times. Note that the spectral widths are not depicted in true scale. The frequency spectrum of a MT preparation pulse is marked in *gray*

To utilize this effect for MR imaging, the magnetization of the ^1H_r pool is saturated by frequency-selective preparation pulses (saturation transfer). Due to the MT effect, this leads to a significant reduction of the MR signal of ^1H_f nuclei and thereby to a reduction of the image signal. In the simplest case, the frequency spectrum of the preparation pulse is defined by a rectangular function below and/or above the resonance frequency of the ^1H_f pool, as is shown in Fig. 2.4.29. When doing this, the offset frequency has to be chosen big enough, so that local variations of the resonance frequencies of the ^1H_f nuclei due to inhomogeneities of the static magnetic field and differences in tissue susceptibilities do not lead to a direct effect on the ^1H_f magnetization.

MT preparation pulses are often used in MR angiography to increase the blood-tissue contrast. This interesting application is based on the fact that the MT effect reduces the ^1H_f magnetization of stationary tissue, whereas the magnetization of the flowing blood is not affected.

2.4.6 Sequence Families

Imaging in magnetic resonance is based on spin warp imaging but is commonly referred to as Fourier imaging. The main underlying principle is the use of magnetic field gradients to prepare the slice-selective excitation and to phase and frequency encode the signal that is induced by the rotating transverse magnetization. The motivation of continued sequence development is fuelled by the aim to improve the tissue distinction and the shortening of measurement time. In recent years, a great number of sequences have been developed (see Table 2.4.6), each of which are utilized in routine clinical applications. The following paragraph provides a systematic overview of the sequence families.

Table 2.4.6 The most important MRI sequences

Acronym	Phrase	Explanation	Synonyms
CISS	Constructive interference in steady state	Data merging of two 3D trueFISP sequences with and without RF phase alternation to eliminate destructive interference pattern	PC-3D-FIESTA
DESS	Double-echo steady state	Image data merging of FISP and PSIF appearing in adjacent acquisition windows	
DRIVE		TSE with a –90° RF pulse at the end of an echo train in order to increase the signal for tissue with a long T_2 relaxation time	RESTORE, FRFSE
EPI	Echo planar imaging	Single-shot technique using only one excitation, followed by multiple phase-encoded gradient-echoes to fill the *k*-space	
FFE	Fast field echo	GRE with low–flip angle excitation and rephasing in the direction of phase encoding after data acquisition of a single Fourier line	FISP, GRASS
FIESTA	Fast imaging–employing steady-state acquisition	GRE with low–flip angle excitation and rephasing in all directions after data acquisition of a single Fourier line	trueFISP, bFFE

Table 2.4.6 *(continued)* The most important MRI sequences

Acronym	Phrase	Explanation	Synonyms
FISP	Fast imaging with steady-state precession	GRE with low–flip angle excitation and rephasing in the direction of phase encoding after data acquisition of a single Fourier line	FFE, GRASS
bFFE	Balanced FFE	GRE with low–flip angle excitation and rephasing in all directions after data acquisition of a single Fourier line	trueFISP, FIESTA
FLASH	Fast low-angle shot	GRE with low–flip angle excitation and “spoiling” after data acquisition of a single Fourier line	T_1-FFE, SPGR
FLAIR	Fluid-attenuated inversion recovery	Liquor suppressed imaging protocol using an IRM sequence (long inversion time)	–
FRFSE	Fast-recovery fast spin echo	FSE with a –90° RF pulse at the end of an echo train in order to increase the signal for tissue with a long T_2 relaxation time	DRIVE, RESTORE
FSE	Fast spin echo	SE using multiple phase–encoded echoes for faster filling of *k*-space	TSE, RARE
FSPGR	Fast spoiled GRASS	Spoiled GRASS with inversion or saturation pulse preceding the whole measurement in order to establish T_1 weighting or for the nulling of the signal of a specific tissue	TFL, TFE
GRASE	Gradient and spin echo	FSE with multiple phase–encoded gradient-echoes within a SE envelope	TGSE
GRASS	Gradient-recalled acquisition in the steady state	GRE with low–flip angle excitation and rephasing in the direction of phase encoding after data acquisition of a single Fourier line	FISP, FFE
HASTE	Half-Fourier single-shot turbo spin echo	TSE utilizing the half-Fourier technique	
IR	Inversion recovery	SE with preceding RF inversion pulse	
MP-RAGE	Magnetization prepared rapid gradient echo	3D TFL version	
T_1-FFE	T_1 fast field echo	GRE with low–flip angle excitation and “spoiling” after data acquisition of a single Fourier line	FLASH, SPGR
PSIF	Backward-running FISP	Acquiring an RF refocused signal using a time reversed FISP sequence	T_2-FFE, SSFP
RARE	Rapid acquisition with relaxation enhancement	SE using multiple phase–encoded echoes for faster filling of *k*-space	TSE, FSE
RESTORE	Fast-recovery fast spin echo	TSE with a –90° RF pulse at the end of an echo train in order to increase the signal for tissue with a long T_2 relaxation time	DRIVE, FRFSE
SE	Spin echo	90–180° sequence	
SPGR	Spoiled gradient-recalled acquisition in the steady state	GRE with low–flip angle excitation and “spoiling” after data acquisition of a single Fourier line	FLASH, T_1-FFE
STEAM	Stimulated echo acquisition mode	Sequence using three 90° RF pulses	

Table 2.4.6 *(continued)* The most important MRI sequences

Acronym	Phrase	Explanation	Synonyms
STIR	Short T_1 inversion recovery	TIRM sequence using a short inversion time suitable for suppressing the signal from fat	
TGSE	Turbo gradient spin-echo	TSE with multiple phase–encoded gradient-echoes within an SE envelope	GRASE
TIR	Turbo inversion recovery	TSE with preceding inversion pulse (phase sensitive)	IR-FSE
TIRM	Turbo inversion recovery magnitude	TSE with preceding inversion pulse and utilizing only the magnitude of the signal (phase insensitive)	
trueFISP	True fast imaging with steady-state precession	GRE with low–flip angle excitation and rephasing in all directions after data acquisition of a single Fourier line	FIESTA, bFFE
TSE	Turbo spin echo	SE using multiple phase–encoded echoes for faster filling of *k*-space	FSE, RARE
TFE	Turbo field echo	T_1-FFE with inversion or saturation pulse preceding the whole measurement in order to establish T_1 weighting or for the nulling of the signal of a specific tissue	TFL, FSPGR
TFL	Turbo fast low-angle shot	FLASH with inversion or saturation pulse preceding the whole measurement in order to establish T_1 weighting or for the nulling of the signal of a specific tissue	TFE, FSPGR
VIBE	Volume-interpolated breath-hold examination	3D GRE with low–flip angle excitation and “spoiling” after data acquisition of a single Fourier line and Fourier interpolation in the direction of partition encoding	

2.4.6.1 Sequence Classification

A first sequence classification can be performed in assigning the type of sequence in either a spin-echo or a gradient-echo group. The main difference between SE and GRE is the influence of susceptibility gradients on image contrast. In general, in GRE imaging susceptibility gradients lead to a faster decay of the signal, whereas in SE imaging dephasing mechanisms that are fixed in location and consistent over time are refocused by the 180° refocusing RF pulse. SE image contrast depends on the tissue specific transversal relaxation time T_2, whereas GRE image contrast is a function of the transversal relaxation time T_2*. Some GRE techniques utilize the excitation pulse also as a refocusing pulse, causing spin-echo components to contribute to the image contrast.

Within the SE and the GRE group, the contrast can be manipulated by preparing the longitudinal magnetization prior to starting the imaging sequence or prior to the measurement of a Fourier line.

In multi-echo imaging, the transverse magnetization is refocused and reutilized after the collection of a Fourier line, omitting the necessity of a further excitation for the collection of another Fourier line. This method is applicable within the SE group as well as the GRE group. Again, a preparation of the magnetization is generating another sequence family. Using only one excitation and multiple phase–encoded echoes to acquire all required *k*-space lines without a further excitation is called a single-shot technique. Figure 2.4.30 shows an overview scheme that provides one possible sequence-classification.

Within the SE sequences, there are:

- The conventional SE sequence (see Sect. 2.4.2.1)
- The IR sequences (see Sect. 2.4.2.1)
- The multi-echo sequences (e.g., TSE, FSE)
- The multi-echo sequences with preparation of the magnetization (e.g., TIR, TIRM, IR-FSE, RESTORE, DRIVE, FRFSE)
- The single-shot techniques (e.g., SS-FSE, or using a Half-Fourier technique [see Sect. 2.4.4.1] like in HASTE)
- The single-shot techniques with preparation of the magnetization (e.g., HASTIRM)

Multi-echo sequences use several phase–encoded echoes in order to fill the *k*-space (see Sect. 2.4.4.2). They are called fast spin-echoes (FSE), turbo spin-echoes (TSE), and RARE (rapid acquisition with relaxation enhancement). The combination of the basic TSE technique and an inversion pulse for the preparation of the longitudinal magnetization is called TRIM (turbo inversion recovery magnitude) or TIR (turbo inversion recovery). If one

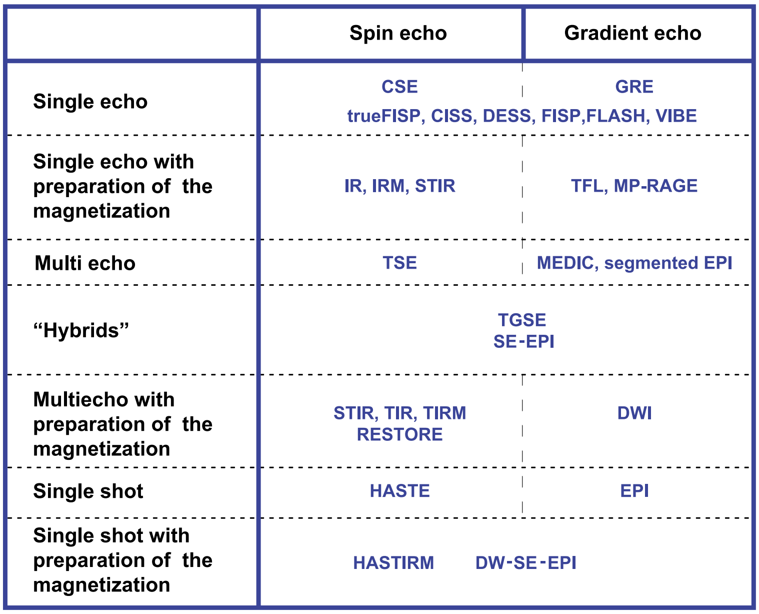

<table>
<tr><th></th><th>Spin echo</th><th>Gradient echo</th></tr>
<tr><td rowspan="2">Single echo</td><td>CSE</td><td>GRE</td></tr>
<tr><td colspan="2">trueFISP, CISS, DESS, FISP,FLASH, VIBE</td></tr>
<tr><td>Single echo with preparation of the magnetization</td><td>IR, IRM, STIR</td><td>TFL, MP-RAGE</td></tr>
<tr><td>Multi echo</td><td>TSE</td><td>MEDIC, segmented EPI</td></tr>
<tr><td>“Hybrids”</td><td colspan="2">TGSE
SE-EPI</td></tr>
<tr><td>Multiecho with preparation of the magnetization</td><td>STIR, TIR, TIRM
RESTORE</td><td>DWI</td></tr>
<tr><td>Single shot</td><td>HASTE</td><td>EPI</td></tr>
<tr><td>Single shot with preparation of the magnetization</td><td colspan="2">HASTIRM DW-SE-EPI</td></tr>
</table>

Fig. 2.4.30 The sequence family. The shown sequence table provides an overview of the sequence classification

combines the Half-Fourier method with a TSE sequence to a degree at which only a single excitation pulse suffices to fill the raw-data matrix with following spin-echoes, one applies the so-called HASTE technique (half-Fourier single-shot turbo spin-echo). The mix of spin-echoes with gradient-echoes or, more precisely the acquisition of gradient-echoes within an SE envelope leads to the TGSE (turbo gradient-echo sequence) sequence, also called GRASE (gradient and spin-echo). As expected, with the introduction of gradient-echoes within a multi-echo spin-echo sequence, the contrast behavior is also T_2* related. This sequence is also called a hybrid.

Similar to the SE sequences, the GRE sequences can be grouped into:

- Conventional GRE sequences (e.g., FLASH, FISP, trueFISP, DESS, CISS, PSIF)
- GRE sequences with preparation of the magnetization (e.g., turboFLASH, MP-RAGE)
- Multi-echo GRE sequences (e.g., MEDIC, segmented EPI)
- Multi-echo GRE sequences with preparation of the magnetization (e.g., segmented DW-SE-EPI)
- Single-shot GRE sequences (EPI)
- Single-shot GRE sequences with preparation of the magnetization (e.g., DW-SE-EPI)

As indicated above, conventional GRE sequences can be further divided into:

- SSI group (steady-state incoherent), which only aims at a steady state in the longitudinal magnetization (e.g., FLASH, SPGR, T_1-FFE)

and

- The SSC group (steady-state coherent), during which the steady state of the transversal magnetization equally contributes to the signal (e.g., FISP, trueFISP, GRASS, FIESTA, FFE, bFFE).

Acronyms of the SSI group are FLASH (fast low-angle shot), SPGR (spoiled gradient-recalled acquisition in the steady state), and T_1-FFE (T_1-fast field echo). In the SSC group there are trueFISP (fast imaging with steady precession), GRASS (gradient-recalled acquisition in the steady state), and FFE (fast field echo).

Within the SSC group, there is a slow transition toward spin-echoes, as excitation pulses do not only excite, but also refocus various echo paths of a remaining or refocused transverse magnetization. The extreme form is PSIF (a backward-running FISP), also named SSFP (General Electric) or T_2-FFE (Philips). In these techniques, the excitation pulse of the following measurement operates as a refocusing pulse for the transverse magnetization of the previous excitation. The contrast is T_2 weighted, as the effective echo time amounts to almost two repetition times. A combination of FISP echo and PSIF echo is called DESS (double-echo steady state), and having the FISP and PSIF echo coincide in time will result in a CISS (constructive interference steady state) or a trueFISP sequence.

The same preparation of the magnetization utilized for SE techniques can be applied to GRE techniques. With a very rapid GRE sequence (RAGE, or rapid acquired gradient-echoes), with the aim of measuring as fast as possible, the T_R is set to a minimum and consequently so is T_E, and the excitation angle is set to an optimum (Ernst angle) in order to generate as much signal as possible. To reestablish a T_1 weighting, a saturation or inversion pulse is applied, but not prior each Fourier line as in SE imaging, but at the beginning of the whole measurement. Those techniques are called turboFLASH, FSPGR (fast spoiled gradient-recalled acquisition in the steady state), TFE (turbo field echo) or, placing the inversion within the partition loop of a 3D sequence, MP-RAGE (magnetization prepared rapid acquired gradient-echoes).

As is the case in fast SE sequences, GRE sequences also can make use of multi-echo acquisitions. MEDIC (multi-echo data image combination) uses multiple echoes for averaging, thus improving SNR and T_2* contrast.

The classical form of a single-shot GRE technique, during which the raw data matrix is filled after a single excitation with several phase-encoded gradient-echoes, is called EPI (echo planar imaging). Simply collecting the free induction decay with multiple phase–encoded gradient-echoes is called FID-EPI. Placing the gradient-echoes beneath an SE envelope is called SE-EPI.

The most common magnetization prepared single shot gradient-echo technique is the diffusion–weighted spin-echo echo planar imaging sequence (DW-SE-EPI).

2.4.6.2 Fast Spin-Echo Techniques

The idea of using multiple phase-encoded spin-echoes to fill the *k*-space more rapidly as compared with conventional imaging has surfaced as early as 1986, with the acronym RARE—rapid acquisition with relaxation enhancement (Fig. 2.4.31). The number of applied echoes is directly proportional to the potential reduction in measurement time. The overall image contrast is dominated by the weighting of those Fourier lines acquired in the center of *k*-space (effective echo time). The qualities of the early images were not close to the quality of conventional T_2-weighted SE imaging. In the course of hard- and software developments, Mulkern and Melki "re-discovered" multi-echo SE imaging during a search for a fast T_2-localizer, creating the acronym FSE (fast spin-echo). Siemens and Philips use the acronym TSE for turbo spin-echo. Since the higher spatial frequencies, the "outer" *k*-space lines, are usually acquired using late echoes, early concern has been that small objects might be missed. Fortunately, the time saving achieved with the use of multiple echoes has been utilized to improve the contrast by selecting longer repetition times and to improve the spatial resolution by increasing the matrix size. Both measures have more than compensated the effect of an under-representation of high spatial frequencies within the *k*-space matrix. T_2-weighted TSE has replaced conventional spin-echo imaging in all clinical applications. The acquired phase-encoded echo train can also be used to create *PD*-weighted and T_2-weighted images similar to conventional dual-echo spin-echo imaging. The use of phase-encoded echoes for the *k*-space of the *PD*-weighted image as well as the *k*-space of the T_2-weighted image is customary and this procedure is called shared echo.

T_1-weighted TSE imaging is also an option for some applications, although additional echoes will increase (unwanted) T_2-weighting. T_1-weighted TSE imaging is rarely applied to the central nervous system as the use of additional echoes prolongs the time needed for a single slice and the number of necessary slices may not fit into the desired T_R. For the genitourinary system (uterus, cervix, bladder, etc.) about three echoes are used to improve SNR or to reduce measurement time. In areas where the amount of T_1-weighting is less of an issue, e.g. T_1-weighted imaging of the cervical and the lumbar spine for degenerative disease, TSE is usually used with an echo train length (ETL) of five echoes. The same protocol is applied for enhanced and unenhanced studies of suspected vertebral metastases. T_1-weighted TSE imaging for the abdomen is not an issue, since the restriction of the measurement time down to a breath hold period is suggesting T_1-weighted GRE imaging.

The remaining point of concern in comparing TSE imaging with conventional SE imaging is the reduced sensitivity to susceptibility artifacts. Hemorrhagic lesions appear less suspicious on TSE imaging as compared with conventional SE imaging. The Fourier transformation assumes a consistent signal contribution for all Fourier lines. Any violation of this assumption will lead to over- or under-representation of spatial frequencies, with a correlated image blurring. Although TSE violates this assumption in using multiple phase–encoded echoes to

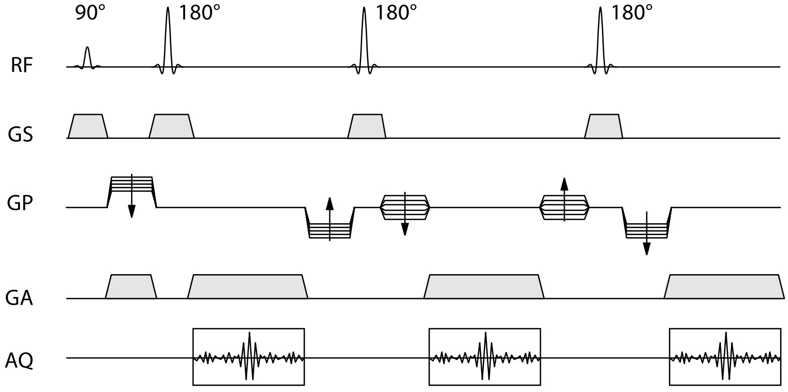

Fig. 2.4.31 Structure of the TSE sequence. Excitation, refocusing, frequency, and phase encoding are done as in the conventional SE sequence. The dephasing done for the purpose of spatial encoding is rephased prior to generating another spin-echo using a 180° RF pulse followed by another phase-encoding step

fill the k-space, where the signal amplitude of the echoes diminishes following T_2 decay, there are several parameter that can be utilized to minimize the artifacts related to the T_2 decay–related k-space asymmetry:

- First, especially for T_2-weighted imaging, the signal amplitudes for the late and closely spaced echoes can be approximated as being constant. TSE sequences are mainly used for the acquisition of T_2-weighted images. As lesions usually have a long T_2 relaxation time, the signal loss caused by the T_2 decay does not play a major role during data acquisition.
- Second, the matrix dimensions used in TSE imaging are usually higher as compared with conventional SE imaging. This will significantly minimize the risk of missing small objects.
- Third, in T_2-weighted TSE imaging, the repetition time is increased considerably, which leads to a remarkable improvement in contrast, again reducing the potential risk of missing small objects due to k-space asymmetry.

In a typical TSE protocol, 13–15 echoes per excitation are used for imaging, implying a theoretical shortening of measurement time of the factor 13–15. In practice, the shortening is about the factor 2–6. Longer repetition times are selected for improved *PD* and T_2 weighting, and larger image matrices are used for improved spatial resolution, diminishing the potential shortening of the measurement time when using multiple phase–encoded echoes. As the mentioned influence on the space encoding is only present in the direction of the phase encoding, the effect can be demonstrated by exchanging of the frequency-and phase-encoding gradients. Figure 2.4.32 shows this in the example of the cauda equine. Apart from use for high-resolution images, TSE sequences are also applied in cardiology, as shown in Fig. 2.4.33. With the help of TSE sequences, T_2-weighted images of the beating heart can be acquired based on the breath-hold method. Other acronyms for equal or similar techniques are FSE (fast spin-echo [Mulkern et al. 1990]) and RARE (rapid acquisition with relaxation enhancement [Henning et al. 1986]). The 3D encoding is another application of the TSE sequence that would lead to intolerable measurement times in conventional SE (see Fig. 2.4.36). Here, the slice-selection gradient is provided with a second phase-encoding gradient, as has been discussed in Sect. 2.3.4.3. Thus, thinner slices than in the 2D technique can be obtained. Furthermore, there are no slice gaps and the problem of "crosstalk," which is found in multiple-slice techniques can be avoided (see Sect. 2.3.5).

Fast spin-echo imaging demonstrates two essential differences in imaging appearance as compared with conventional spin-echo imaging: Fat appears bright, and there is a reduced sensitivity to hemorrhagic lesions. The bright appearance of fat is related to the J-coupling. The so-called J-coupling (see Sect. 2.2.9) of the carbon-bound protons provides a slow dephasing of transversal magnetization in conventional SE imaging, in spite of the refocusing pulse. If the refocusing pulses follow shortly after

Fig. 2.4.32 Image of the cauda equina, acquired with a TSE sequence with **a** the phase-encoding direction from left to right, and **b** the phase-encoding direction from head to foot. The longitudinal structures of the relatively thin nerves will be better visible, if the frequency-encoding direction is perpendicular to the nerve fiber. The resolution in frequency-encoding direction is not influenced as much by the T_2 decay as by the resolution in phase-encoding direction

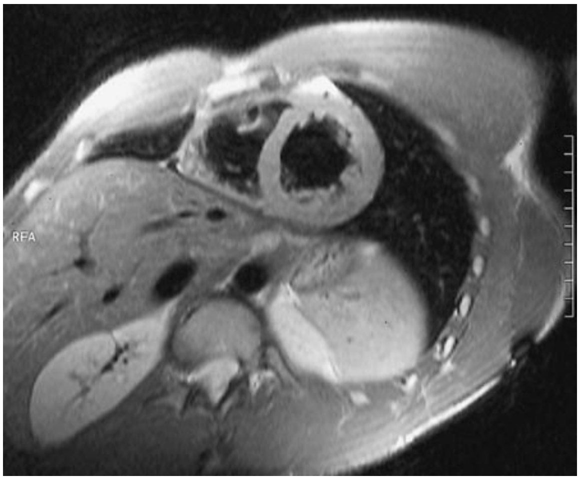

Fig. 2.4.33 T_2-weighted image of the heart in short-axis perspective. Duration of data acquisition 20 s (with ECG triggering at breath holding) (TSE 900/57, slice thickness = 8 mm)

one another, as is the case in TSE imaging, the J-coupling will be overcome; the dephasing will be suppressed. Consequently, fat tissue appears brighter in the TSE image than it does in a conventional image. If desired fat saturation or fat suppression (see Sect. 2.4.5.1) can be utilized to suppress this appearance. The susceptibility-related artifact of hemorrhagic lesions in spin-echo imaging is due to diffusion in between excitation, refocusing, and data acquisition. Reducing this diffusion time by rapidly succeeding refocusing pulses will also reduce the related artifacts, thus making TSE imaging less sensitive for hemorrhagic lesions.

2.4.6.2.1 Fast Spin-Echo Techniques with Inversion to Suppress the Signal from Fat

The TSE sequence, like the conventional SE technique, can be used with an inversion pulse for preparation of the longitudinal magnetization. Thus, it becomes possible to yield a suppression of the fat signal, based on the short relaxation time of fat (see Fig. 2.4.10b). Relaxation dependent fat suppression using an inversion pulse prior to the fast spin-echo train is routinely used to demonstrate bone infarctions and bone marrow abnormalities like bone marrow edema, e.g., in sickle cell anemia. This fat suppression scheme is also used in genitourinary applications, where the high signal intensity of fat may obscure contrast-enhanced tumor spread. Since only the fat suppression is desired, the used inversion recovery technique is not phase sensitive, only the magnitude of the longitudinal magnetization is used. The acronym used in this case is TIRM (turbo inversion recovery with magnitude consideration). The structure of a turbo inversion recovery (TIR) sequence is presented in Fig. 2.4.34.

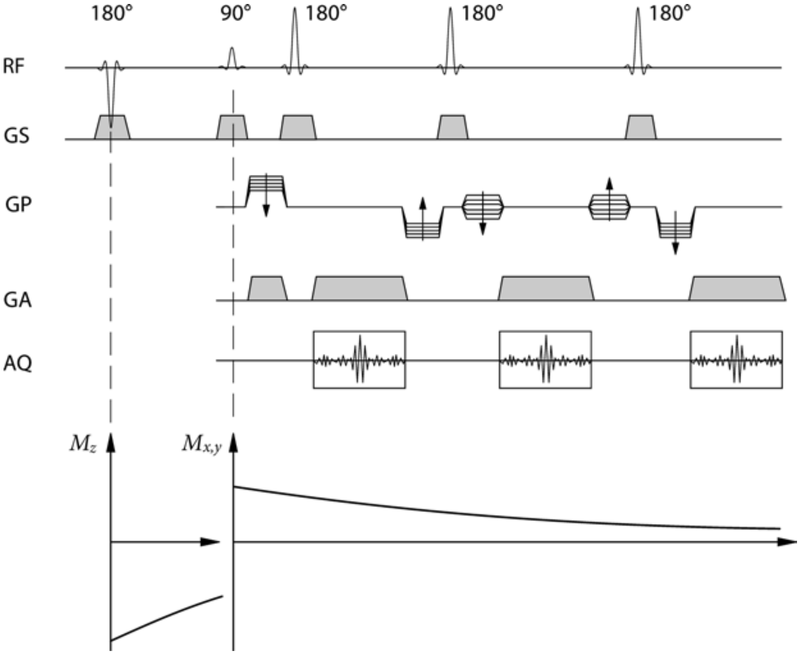

Fig. 2.4.34 Structure of the turbo inversion recovery (TIR) sequence

2.4.6.2.2 Fast Spin-Echo Techniques with Inversion to Suppress the Signal from Fluid

The reduction in measurement time due to the utilization of multiple phase-encoded spin-echoes permits the use of inversion times in the order of 2 s, keeping the measurement time acceptable. An inversion time of 1.9 s will provide a relaxation dependent suppression of the cerebral spinal fluid (CSF) signal (Fig. 2.4.35). The utilization of a long inversion time is called fluid-attenuated inversion recovery, or FLAIR. In combination with TSE imaging (the structure of a 3D TSE sequence is presented in Fig. 2.4.36), the technique is called turboFLAIR or simply TIRM. Since CSF has the longest T_1 relaxation time, the longitudinal magnetization within all other tissues will be aligned parallel to the main magnetic field, and it is not necessary to have a phase sensitive IR method for this application. The attenuated CSF signal allows a better differentiation of periventricular lesions and has demonstrated a superior sensitivity for focal white matter changes in the supratentorial brain, whereas posterior fossa located lesions can be missed. The turboFLAIR method apparently allows the identification of hyperacute subarachnoid hemorrhage with MR, precluding the need for an additional CT.

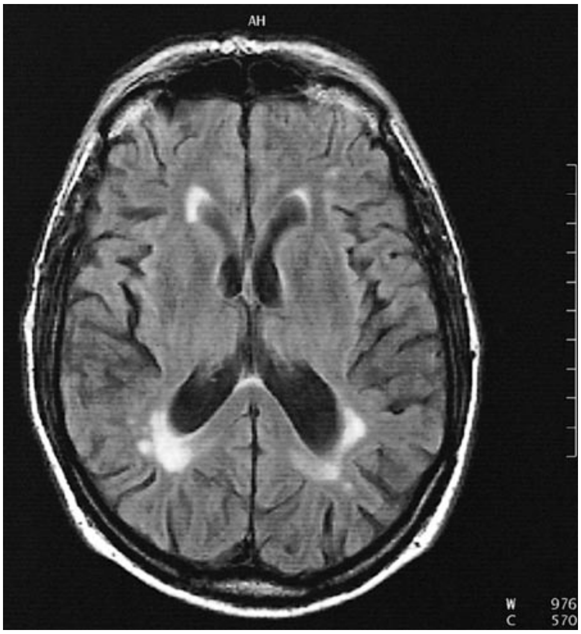

Fig. 2.4.35 Axial head image measured with a TIR sequence. The cerebrospinal fluid (CSF) does not contribute any signal, as the inversion time is selected for the CSF not to have a longitudinal component at the time of excitation (TIRM 8,000/2,200/105, slice thickness = 6 mm)

2.4.6.2.3 Fast Spin-Echo Techniques with Inversion to Improve T_1 Contrast

The time-consuming IR method has been used in the past for studying the development of white matter tracts in developmental pediatrics. This technique has been replaced using an inversion pulse prior to a spin-echo train of a TSE sequence. The selected inversion time (~350 ms) allows a better delineation of small differences in T_1 relaxation times, e.g., for the documentation of the development of the pediatric brain. The improved tissue characterization between gray matter and white matter tracts allows, e.g., the demonstration of mesial temporal sclerosis and visualizing hippocampal atrophy. For this application a so-called phase-sensitive inversion recovery is required to differentiate nuclear magnetization aligned parallel to the magnetic field as compared with antiparallel alignment at the time of excitation. The according acronym is TIR.

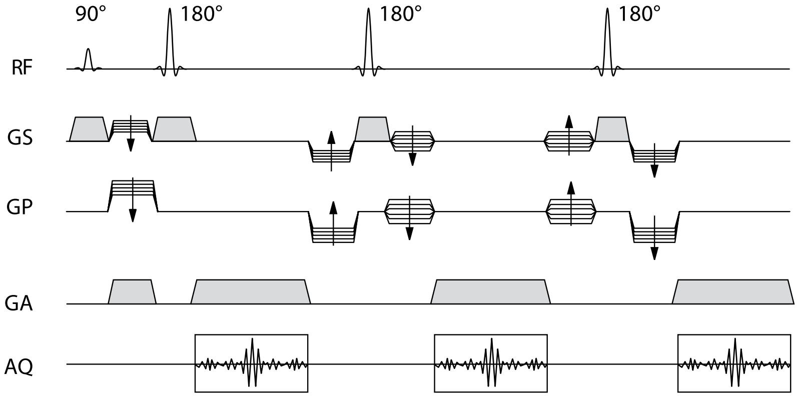

Fig. 2.4.36 Structure of the 3D TSE sequence (additional phase-encoding gradients in direction of slice selection)

2.4.6.2.4 Driven Equilibrium or Restore Techniques

The residual transverse magnetization after measuring a single Fourier line, or, in case of multi-echo imaging, after measuring the "package" of Fourier lines, is usually spoiled. A later-introduced concept refocuses the transverse magnetization at the end of the echo train and uses an RF pulse to "restore" the residual transverse magnetization back to the longitudinal direction. The method "improves" the recovery of the longitudinal magnetization for tissue with long relaxation times, allowing a further shortening of the repetition time without loss of contrast. The technique is called RESTORE (SIEMENS), fast recovery fast spin-echo FRFSE (GE) and DRIVE (Philips). It does not make a difference whether the magnetization is prepared after the measurement of a Fourier line or at the very beginning of a new excitation cycle. For this reason it is justified to list RESTORE as a turbo spin-echo scheme with preparation of the longitudinal magnetization.

2.4.6.2.5 Dark-Blood Preparation Scheme

Multi-echo spin-echo imaging has the potential to acquire T_1- and/or T_2-weighted spin-echo imaging of the beating heart within a breath hold. The only obstacle that needs to be addressed is the significant flow artifacts caused by the flowing blood. The introduction of dark-blood preparation scheme finally revolutionized cardiac MR imaging. With this preparation scheme, it is now possible to acquire T_1- and T_2-weighted images of the beating heart within a breath hold, without any flow artifacts.

The magnetization of the whole imaging volume is inverted nonselectively, followed by a selective reinversion of the slice. This is done at end diastole, with the detection of the QRS complex. During the waiting period to follow, most of the reinverted blood will be washed out of the slice, being replaced by the inverted blood—and the spin-echo train acquired again toward end diastole will show "black" blood. A double inversion pulse will even allow not only the black-blood preparation, but also the suppression of fat signal, which will be helpful in characterizing fatty infiltration of the myocardium in arrhythmogenic right ventricular dysplasia (ARD).

2.4.6.2.6 Single-Shot Spin-Echo Imaging

Single shot, per definition, refers to a single excitation pulse and the use of multiple phase–encoded echoes to fill the required Fourier lines. The original RARE has been published as a single-shot spin-echo technique. Other acronyms found in the literature are SS FSE for single-shot fast spin-echo (GE) or SS TSE of single-shot turbo spin-echo (Philips). The combination with a half-Fourier technique allows a further reduction in measurement time and has been named HASTE: half-Fourier acquired single-shot turbo spin-echo. As elaborated on earlier, the first and the last data point of a Fourier line are characterized by the transverse magnetization of adjacent voxel pointing into opposite direction. The same situation is found for the first and last Fourier line within *k*-space, considering the transverse magnetization within adjacent voxel aligned in the direction of phase encoding. *k*-Space is symmetrical. Although this hermitian symmetry is ideal and reality is slightly different, it has been claimed, that the deviation from the ideal situation are only of coarse nature and that a few (e.g., eight) Fourier lines measured beyond the center of *k*-space should be sufficient to correct for this insufficiency. As an example for a 128*256 matrix, a single-shot spin-echo technique using the half Fourier approach would use $128/2+8=72$ phase-encoded echoes to fill the *k*-space. The measurement time using this acquisition method is about a second per slice. The high numbers of echoes suggest that this technique is only useful for T_2-weighted imaging and the blurring effect due to signal variation in *k*-space as a result of T_2 decay will be prohibitive for high resolution studies. Nevertheless, it is an alternative, even in the brain, for a fast T_2-weighted study for patients who are not able or willing to cooperate. Since it is the perfect technique to visualize fluid-filled cavities, HASTE is used, e.g., for MRCP (magnetic resonance cholangiopancreatography). A typical result of this sequence is shown in Fig. 2.4.37.

Progress in hardware development and the correlated improvement in image quality, together with the pioneering research within this field have recently led to an impressive increase in HASTE utilization for obstetric imaging. Although sonography remains the imaging technique of choice for prenatal assessment, the complementary role of MR imaging is getting more and more important in the early evaluation of brain development of the unborn child or even in the early detection of complications within the fetal circulatory system.

2.4.6.3 Gradient-Echo Techniques

The search for shorter measurement times for faster imaging led to the group of gradient-echoes (GRE) in 1983. An MR signal can be detected immediately after the excitation pulse. That signal is the free induction decay (FID). In addition to the spin–spin interaction causing the T_2 relaxation, other dephasing mechanism will contribute to the image contrast, dephasing mechanisms that are based on differences in precessional frequencies due to magnetic field variations across a voxel. The main sources of local magnetic field variations are differences in tis-

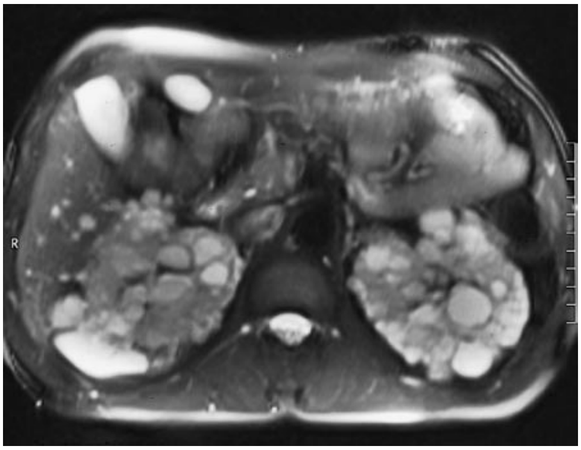

Fig. 2.4.37 Axial abdominal image acquired with HASTE. Every image is produced with a single excitation, followed by a train of phase-encoded spin echoes. The scan time of the image was 570 ms; the slice thickness is 8 mm

sue-specific susceptibility values. Since these dephasing mechanisms are fixed in location and are constant over time, they are refocused using a 180° RF refocusing pulse in SE imaging. Omitting this pulse will lead to a contribution of these dephasing mechanisms to the image contrast. The observed tissue specific relaxation parameter is then called T_2^* rather than T_2.

$$\frac{1}{T_2^*} = \frac{1}{T_2} + \frac{1}{T_2'},$$

with T_2' being both machine and sample dependent. Although the missing 180° RF refocusing pulse will cause a rapid dephasing of the transverse magnetization and with that a rapidly dephasing MR signal, the echo time can be reduced as well and so can the repetition time. The shorter echo time will allow, in most cases, a detection of a signal despite the rapid dephasing of the transverse magnetization. Since the echo is now formed by using a bipolar gradient pulse in the direction of frequency encoding, these techniques are called GRE. With shorter repetition times an extension of phase encoding for the direction of slice or slab selection can be considered, and 3D imaging becomes feasible.

The short excitation pulses used in common GRE imaging will result in a less perfect slice profile as compared with the slice profile achieved with a 90–180° combination of longer RF pulses as typically utilized in SE imaging. As a result, there will be significant contributions of the low angle–excited outer regions of a slice, explaining the basic difference in contrast between a GRE image as compared with an SE image, even if a 90° excitation angle is utilized.

2.4.6.3.1 Spoiled Techniques

Similar to the spin-echo sequence acquisition scheme, there is residual transverse magnetization left at the end of the acquisition of one Fourier line—and similar to the spoiling of the transverse magnetization at the end of the measurement in SE imaging, the same process can be applied to GRE imaging as well. Spoiling can be done with a gradient pulse, distributing the transverse magnetization evenly, so that the next excitation pulse will not generate a stimulated echo. Or the phases of the excitation pulses can be randomized in order to avoid the buildup of a steady state for the transverse magnetization (RF spoiling). Spoiled gradient-echo imaging has been introduced as fast low angle shot (FLASH), T_1-weighted fast field echo (T_1-FFE), or spoiled gradient recalled acquisition in the steady state (SPGR). FLASH imaging allows multislice imaging in measurement times short enough to allow breath hold acquisitions. Since the contrast mainly depends on the T_1 relaxation time, FLASH images are usually called T_1 weighted. In clinical routine, FLASH sequences have been introduced for diagnosing cartilage lesions (Fig. 2.4.38), for abdominal breath-hold T_1-weighted imaging (Fig. 2.4.39), and in dynamic contrast enhanced studies.

As has been discussed in Sect. 2.4.3.2, not only the amplitude of the signal can be controlled, but also the basic contrast behavior can be influenced. For instance, when using an extremely small excitation angle and moderate repetition times, one can minimize the influence of the T_1 relaxation time (see Fig. 2.4.17). Thus, one can obtain

Fig. 2.4.38 Sagittal 2D image of an ankle using a FLASH sequence (FLASH 770/11/60° SD = 3 mm, 512 × 512 matrix)

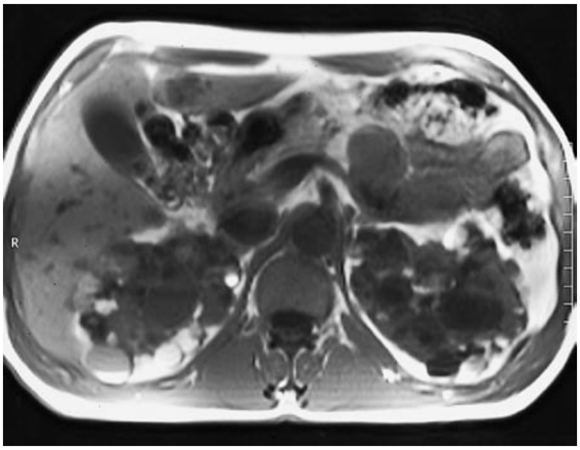

Fig. 2.4.39 Axial T_1-weighted image of the abdomen acquired with a FLASH sequence during a breath hold (2D FLASH 174/4/80°, 23 slices)

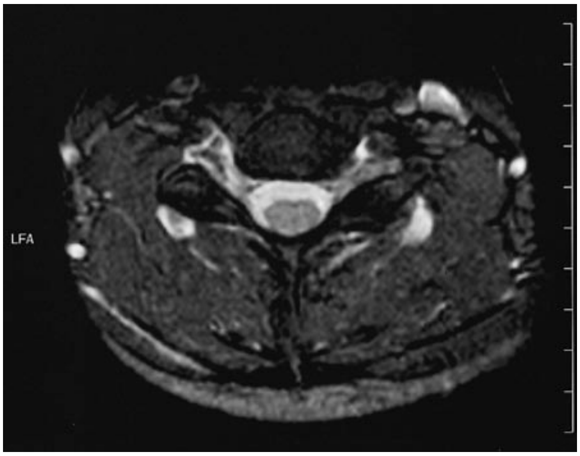

Fig. 2.4.40 Axial image of the cervical spine (MR myelography), acquired with a FLASH sequence with relatively small excitation angle at a magnetic field strength of 0.2 T (2D FLASH 1,200/50/40°, slice thickness = 4 mm)

PD-weighted or T_2-weighted images in spite of short repetition times. This effect is used in MR myelography (see Fig. 2.4.40).

2.4.6.3.2 Refocused Techniques

The alternative to spoiling the residual transverse magnetization after the end of the Fourier line acquisition is to rephase what has been dephased for spatial encoding. This was introduced as fast imaging with steady precession (FISP) (Oppelt et al. 1986), later to be called trueFISP. The original implementation and publication of FISP uses a gradient refocusing in phase encoding as well as in frequency-encoding direction and slice-select direction. As this sequence was susceptible to artifacts at the time, the implemented and released FISP sequence, still used today, is only refocused in the direction of phase encoding, and no refocusing in readout and slice-selection direction. Such a sequence has been called ROAST (resonant offset acquired steady state [Haacke et al. 1991]). For the FISP sequence, the phase encoding is reversed after the acquisition of the Fourier line, undoing the dephasing that was applied for spatial encoding. This approach will lead to a steady state not only for the longitudinal magnetization, but also for the transverse magnetization—for tissue with long T_2 relaxation times. Differences in FISP contrast as compared with FLASH applications will only be visible for short repetition times; large excitation angles and will only enhance signal within tissue with long T_2 relaxation times. General Electric introduced this technique as gradient-recalled acquisition in the steady state (GRASS). Philips is using the fast field echo (FFE).

2.4.6.3.3 Balanced Techniques

If one rephases at the end of the measurement of a Fourier line, all parts of the transverse magnetization that have been dephased for spatial encoding and if one compensates in advance for the dephasing to be expected while the slice selection gradient is switched on, one obtains the trueFISP sequence (Fig. 2.4.41). This technique combines the advantages of the FISP sequence and the PSIF sequence, with further echo paths contributing to the overall signal. A clinical application of this sequence is shown in Fig. 2.4.42. This original approach of refocusing all transverse magnetization at the end of the mea-

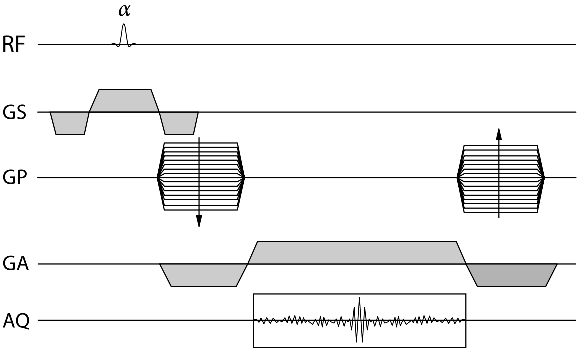

Fig. 2.4.41 Structure of the trueFISP sequence. The sequence seems to be "balanced" due to a symmetry in time. All components of the transverse magnetization are refocused at the end of the measurement, leading to a steady state

surement of one Fourier line will not only cause a steady state for the transverse magnetization, but also the next excitation pulse will also operate as a refocusing pulse. The excitation pulse will not only convert longitudinal magnetization to transverse magnetization, but will also generate a spin-echo. The sequence seems to be symmetric, balanced. The challenge is to get all the generated echoes to have one phase, otherwise the echoes will destructively interfere, causing band-like artifacts. The positions of these bands also depend on the starting phase of the RF pulse. Adding another acquisition with a phase shifted RF will lead to a technique called constructive interference steady state technique, (CISS), or phase-cycled fast imaging–employing steady-state acquisition (PC-FIESTA, the acronym used by GE). Since CISS contains spin-echo components, the technique is even useful in regions with significant susceptibility gradients, e.g., nerve imaging at the base of the skull. Since this technique is a fast technique with hyperintense appearance of fluid filled cavities, it is primarily applied to study abnormalities of the internal auditory canal. The originally published FISP is the trueFISP, where all the dephasing is reversed and even the slice selection gradient is preparing the dephasing to be expected during the first half of the next excitation pulse. The trueFISP technique is a fast gradient-echo sequence with spin-echo contributions leading to hyperintense appearance of all tissues with long T_2 relaxation times. The technique is primarily used

Fig. 2.4.42 Sagittal T_2-weighted image of the head, measured with a trueFISP sequence (7/3/80°, 512 × 512, 4 acquisitions, overall scan time = 13 s)

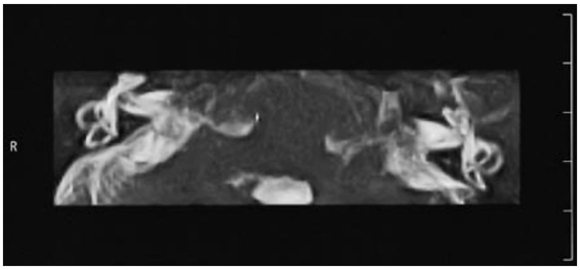

Fig. 2.4.44 Image of the cochlea using a maximum intensity projection (MIP) applied to an image stack, produced by a 3D PSIF sequence (3D PSIF 17/7/80°, slice thickness = 0.5 mm)

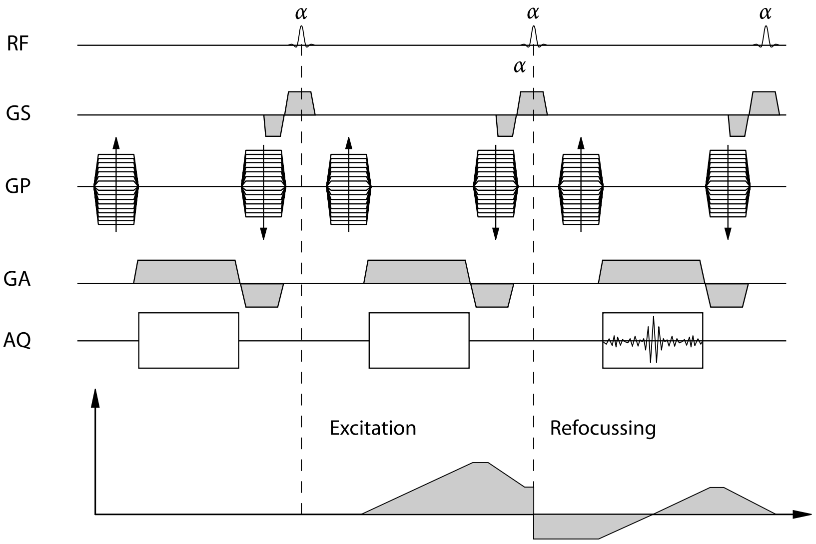

Fig. 2.4.43 Structure of the PSIF sequence

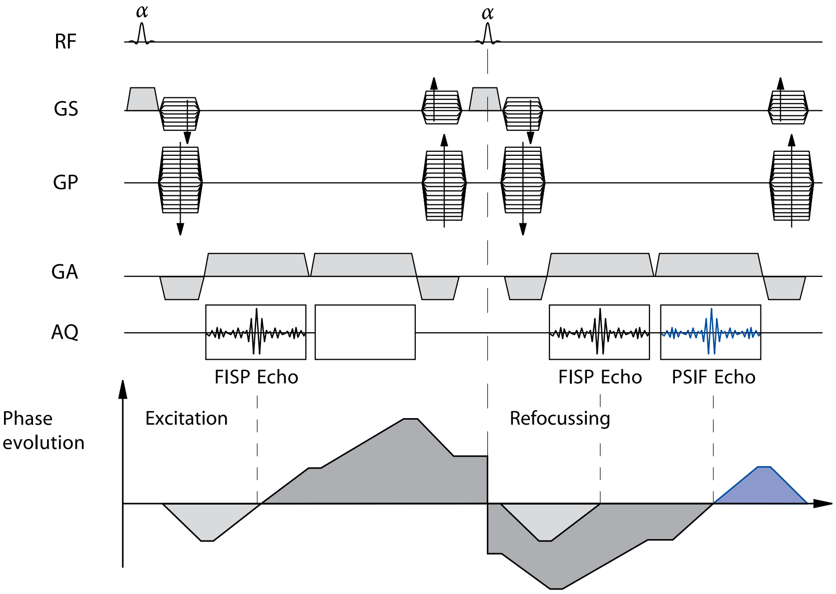

Fig. 2.4.45 Structure of the DESS sequence. FISP and PSIF signals are acquired in adjacent acquisition windows and later added prior to image reconstruction. DESS is used as a 3D technique

in fast cardiac imaging, for cine snapshots of the beating heart. General Electric is using the acronym FIESTA for the same technique. Philips is using bFFE (balanced fast field echo) as the acronym for his technique.

2.4.6.3.4 The Gradient Echo That is a Spin Echo

The previously mentioned spin-echo component of a balanced technique can be isolated and can be used to generate an image. The PSIF sequence shown in Fig. 2.4.43 appears to be violating the causality at first: a FISP sequence running backward. The signal inducing transverse magnetization is produced with the first excitation at the end of the first cycle, refocused with the second excitation at the end of the second cycle, and inducing a signal at the beginning of the third cycle. The effective echo time therefore amounts to almost two repetition times. The resulting images consequently show a remarkable T_2 weighting. (Note that in this case, it is a spin-echo and not a gradient-echo.) The PSIF sequence is insensitive to susceptibility gradients. In contrast to CISS, the PSIF is very sensitive to flow and motion, thus it is not applied for IAC imaging but rather used as an adjunct to demonstrate abnormal CSF flow pattern. General Electric is calling this technique simply steady state free precession (SFFP), while Philips is using the acronym T_2-FFE. Imaging of the cochlea (Fig. 2.4.44) is no longer performed with PSIF but rather with CISS, due to the intrinsic flow insensitivity of the latter. When combining a FISP image with a PSIF image, one obtains an image with a T_2* weighting via the GRE signal and a T_2 weighting via the SE signal. Such a sequence is called double echo steady state (DESS, Fig. 2.4.45). The DESS sequence is routinely used in orthopedic imaging (Fig. 2.4.46). It links the advantages of the FISP sequence with the additional signal enhancement of the PSIF sequence for tissues with long T_2 (e.g., edema and joint effusion).

Fig. 2.4.46 Sagittal image of a knee acquired with a DESS sequence using a special excitation pulse, which only excites the water protons (water excitation) (DESS 26/9 or 45/40°)

2.4.6.3.5 Gradient-echo Single-Echo Imaging with Preparation of the Magnetization

In theory, all the magnetization preparation schemes previously applied for the SE group can also be applied for the GRE sequences. However, it has to be kept in mind that GRE sequences are usually using shorter T_E and shorter T_R than SE imaging does, and therefore some preparation schemes should be slightly altered. As, for an example, the fat saturation scheme: The time necessary for a spectral saturation pulse followed by a gradient spoiler will add up to the slice-loop time for an otherwise short T_R GRE sequence. A feasible modification is to skip the fat saturation for a few slices—this is referred to as "quick fat sat." Although a slice-dependent recovery of the fat signal is observed, the compromise is in general acceptable, since the fat signal stays low and more slices can be measured per T_R.

Composite Spectral Saturation Pulses: to Suppress Signal from Adipose Tissue, or to Excite just Water

The quality of a spectral saturation pulse depends on the overall homogeneity within the imaging volume. In addition, the spectral fat saturating RF pulse is very close to the water resonance, causing a loss in overall SNR. For a nonselective excitation, it is theoretically possible to also simply excite either fat or water using the tissue specific Larmor frequency. In practice, such an approach is very prone to artifacts due to imperfect field homogeneity within the volume of interest. Better results in water excitation or fat excitation have been achieved with binomial pulses (1-1, 1-2-1, or 1-3-3-1). The mechanism of e.g., a 1-2-1 RF pulse is described as follows, leading finally to a 90° RF excitation pulse for just water. After an initial 22.5° RF pulse, there will be a waiting period, allowing the magnetization within fat to fall behind the magnetization of water. At the point of opposite position of the magnetizations, a 45° excitation angle will than move the magnetization within water to a 67.5° position with respect to the longitudinal direction, whereas the magnetization within fat will be flipped back to the 22.5° position. After the previously mentioned waiting period, another 22.5° excitation pulse will accomplish the 90° excitation for water, while the magnetization of fat will be restored to the longitudinal position, not contributing to the MR signal. Another advantage of these binomial pulses is that they can be either executed using nonselective RF pulses or selective RF pulses. In the latter case, they are called spatial spectral frequency or simply composite pulses.

Inversion Pulse prior to the Measurement to Improve T_1 Contrast

Short T_R, short T_E GRE imaging, utilizing the Ernst angle leads to *PD*-weighted images rather than T_1-weighted images. In SE imaging, the T_1 contrast is improved by placing an inversion pulse prior to the acquisition of the Fourier line. This approach is not feasible in GRE imaging, since the inversion time would be much larger than the commonly used repetition times. In fast GRE imaging, an inversion pulse is used prior to the whole imaging sequence (Fig. 2.4.47). That concept has been introduced as turboFLASH (snapshotFLASH (Haase et al. 1989), fast SPGR (FSPGR) or turbo Field Echo (TFE)). The minor drawback is that the longitudinal magnetization, and consequently the generated transverse magnetization, will change throughout the measurement. The resulting violation of *k*-space symmetry will cause an under- or over-representation of some spatial frequencies producing a slight image blurring, typical for turboFLASH imaging.

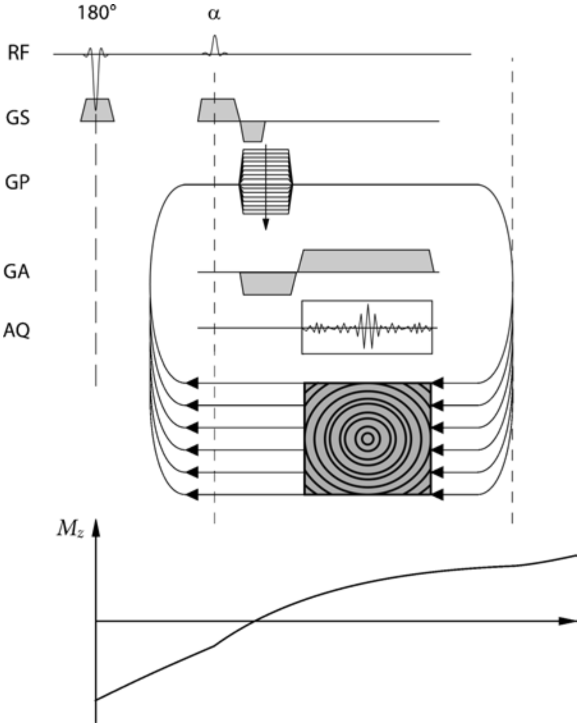

Fig. 2.4.47 Structure of the TFL sequence. After an inversion pulse and an inversion time, the small-angle excitation is repeated several times until the raw data matrix is filled

When using this method, one has to consider the following three facts:

1 The longitudinal component of the macroscopic magnetization will recover after the inversion pulse with the T_1 relaxation time. This relaxation process also takes place during data acquisition. The various measured Fourier lines will have different T_1 weightings. The image contrast is dominated by the T_1 weighting of the Fourier line measured at the center of *k*-space.

2 The recovery of the longitudinal magnetization is influenced by the excitation angles of the rapid GRE data

acquisition. In order to minimize this influence and to obtain a maximum effect of the preparation-pulse on the image contrast, the rapid GRE acquisition needs to be executed with small excitation angles.

3 Every Fourier line is measured with a different phase encoding gradient and contains the spatial information of the object in direction of phase encoding. The *k*-space symmetry is significantly violated due to the change in signal contribution for each spatial frequency measured as a consequence of T_1 relaxation during sampling. As a result, the images appear to be blurred, with imprecise edges and coarse signal oscillations parallel to the edges.

With the introduction of short T_R gradient-echo acquisition schemes, 3D imaging became feasible. The application of an inversion pulse prior to a 3D acquisition scheme is not very promising, since the preparation of the longitudinal magnetization would vastly diminish during the relatively long measurement time and the significant number of low angle excitation pulses. A feasible alternative is to repeat the preparation of the longitudinal magnetization in either the partition-encoding loop, or the phase-encoding loop. Although the timesavings would be larger for placing the inversion pulse prior to the longer phase encoding loop, fortunately at the time it was only possible to place the inversion pulse prior to the partition-encoding loop. Fortunately, because the previously described turboFLASH-artifact based on the over- and under-representation of *k*-space lines is now omitted. The phase-encoding gradient is prepared; the inversion pulse is set followed by a rapid execution of the partition-encoding loop, during which the amount of longitudinal magnetization will change according to the course of the T_1 relaxation (recovery influenced by the low-angle excitation pulses). After this, the next phase-encoding line is prepared, the inversion pulse set, and again the whole partition loop executed. The amount of signal within each partition is identical for all phase-encoding steps and the *k*-space is again symmetric, resulting in artifact-free images. This technique has been introduced as magnetization prepared rapid acquired gradient-echoes (MP-RAGE, Mulger and Brookeman 1990) (Fig. 2.4.48). Figure 2.4.49 shows as a typical application of the MP-RAGE sequence showing the medial–sagittal T_1-weighted slice out of 64 of an examination covering the entire skull in less than 5 min.

The sequence had some promise to replace the conventional T_1-weighted spin-echo imaging of the brain, since it allows the gapless coverage of the whole brain in less than 6 min. But, it is a gradient-echo sequence. Susceptibility gradients especially at the base of the skull will cause geometric distorted representation of the anatomy or even signal voids. Another disturbing effect is the appearance of contrast enhancement in active lesions. Due to the commonly "squishy" content of lesions, the appear-

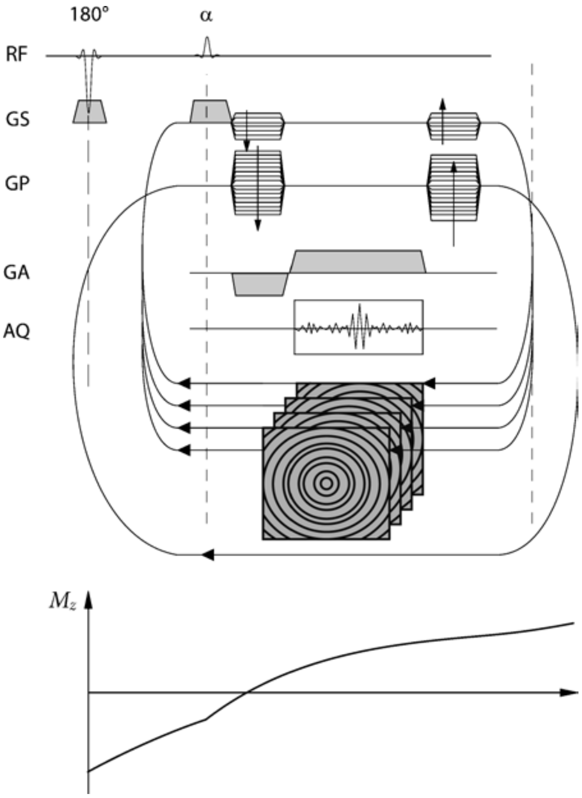

Fig. 2.4.48 Structure of the MP-RAGE sequence. Similar to the TFL sequence there is an inversion of the longitudinal magnetization prior to the partition-encoding loop

Fig. 2.4.49 Sagittal T_1-weighted-head study, acquired with a MP RAGE sequence (12/5/15°, 64 slices, partition thickness = 2 mm, no slice gaps, scan time = 5 min)

ance is usually iso- to hypointense in T_1-weighted imaging. MP-RAGE allows better control over T_1 weighting, potentially causing the lesion to be more hypointense as compared with SE imaging. In conjunction with contrast uptake, lesions will show up hyperintense on T_1-weighted SE imaging. They may or may not show up hyperintense on MP-RAGE imaging. The appearance has been reported to be inconsistent, likely to be due to the better T_1-weighting (a hypointense lesion may show up isointense after contrast uptake).

Inversion Pulse prior to the Measurement for Tissue-Selective Signal Suppression

The rapid acquisition of a gradient-echo or steady state sequence following an inversion is sometimes referred to as single-shot technique. This is not quite correct since as many low angle excitation pulses are applied as Fourier lines are needed to fill the *k*-space. But the single-shot nomenclature allows a differentiation compared to the segmented, or multi-phase, imaging of the beating heart. Similar to the STIR approach used in fat signal–suppressed imaging, the inversion pulse prior to a single-shot technique enables the nulling of signal for a specific tissue (depending on the T_1 relaxation time).

The turboFLASH technique is used to study the first-pass of a contrast bolus through the cardiac chamber, showing a delayed enhancement in perfusion restricted ischemic myocardium. The inversion time is adjusted, so that normal myocardium will give no signal. In the early phase normal myocardium will be perfused with the T_1-shortening contrast agent, whereas the perfusion restricted ischemic myocardium will remain hypointense.

The same method of tissue signal nulling can be applied to the trueFISP. This technique has been used to demonstrate the late enhancement of infarcted myocardium. An advantage for the trueFISP versus turboFLASH is that the additional signal contributions due to refocusing and balancing (spin-echo components), allowing a higher bandwidth acquisition correlated with a shorter T_E, a shorter T_R, and therefore a shorter measurement time (~450 ms). In addition, the trueFISP has a significant lower sensitivity to flow and motion artifacts as compared to the turboFLASH, leading to (almost) artifact-free images.

Both methods are currently evaluated regarding their value in characterizing myocardial viability.

2.4.6.4 Single-Shot Gradient-echo Imaging

The single-shot gradient-echo imaging is echo planar imaging (EPI). Similar to TSE imaging, EPI makes use of several phase-encoded echoes to fill the raw data matrix (Fig. 2.4.50). There are multiple ways to acquire the data. A single excitation can be utilized, followed by multiple phase–encoded gradient-echoes with a small, constant phase-encoding gradient activated during readout period. Such a technique would be called FID-EPI, since signal sampling is done during free induction decay. Another variant is placing the gradient-echoes under an SE envelope (Fig. 2.4.51). In this case the central *k*-space contains a T_2 contrast, in opposition to the T_2* contrast of the FID-EPI version. The SE-EPI sequence shows a lower sensitivity for susceptibility gradients. Fig. 2.4.51 shows a SE-EPI with an alternative approach to phase encoding. In this example, phase encoding is done using gradient "blips" during the ramping time of the frequency-encoding gradient. Such a technique is called blipped EPI. Figure 2.4.52 shows a blipped EPI T_2-weighted image of the head.

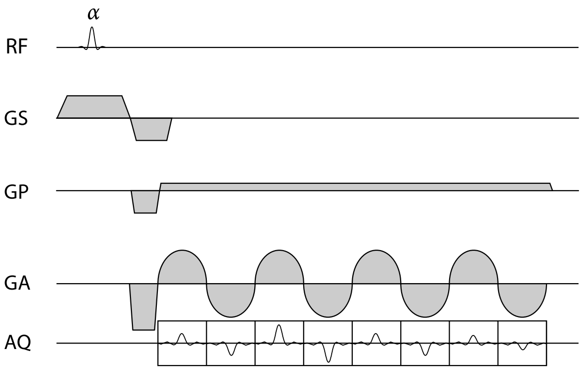

Fig. 2.4.50 Classical FID-EPI sequence. After an excitation pulse, multiple GREs are generated using an oscillating frequency–encoding gradient. In this example the phase encoding is achieved with a low-amplitude, constant phase-encoding gradient throughout the measurement

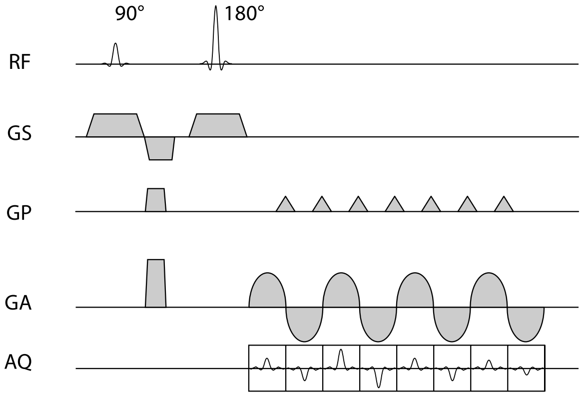

Fig. 2.4.51 SE-EPI sequence. After an excitation and refocusing-pulse, multiple GREs are generated using an oscillating frequency–encoding gradient. The phase encoding is achieved in this sequence using small gradient pulses (blips) during ramping of the frequency-encoding gradient

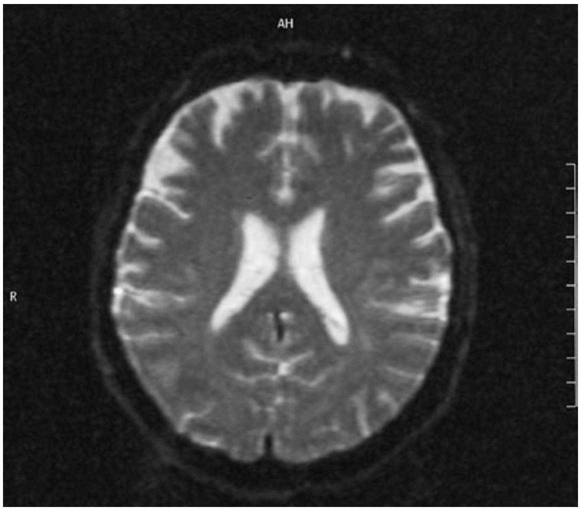

Fig. 2.4.52 Axial T_2-weighted-head-image, acquired with an SE-EPI sequence (TE 70, measurement time per slice = 180 ms, slice thickness = 3 mm). There is only one excitation per slice. No repeated excitations are necessary. All data are acquired using multiple phase–encoded gradient echoes

Addressing a different way of *k*-space sampling, both, the frequency-encoding" gradient and the "phase-encoding" gradient may oscillate, causing a spiral trajectory through *k*-space. Such a method is known as spiral EPI. The quotation marks are used to indicate that the magnetic field gradients do no longer have the apparent meaning of frequency and phase encoding. The high sensitivity of EPI to local field inhomogeneities is utilized in (brain) perfusion imaging and for monitoring the oxygen level to identify cortical activation in BOLD (blood oxygenation level–dependent) imaging.

In spite of many limitations, the EPI sequences have attained high clinical potential in functional imaging and in perfusion studies.

2.4.6.5 Single-Shot Gradient-echo Imaging with Preparation of Magnetization (Diffusion-Weighted Imaging)

The preparation of the longitudinal magnetization is not only possible with the previously described multi-shot techniques, but also with the single-shot version. Single shot, per definition, means one excitation pulse and multiple phase–encoded gradient-echoes for sampling of all Fourier lines. The primary preparation scheme for single-shot gradient-echo imaging is diffusion weighting. Any magnetic field gradient in the presence of a transverse magnetization will cause the Larmor frequency to be a function of location. Sometimes this effect is desired, as in any phase encoding, and sometimes it is a byproduct of another desired functionality, e.g. the frequency encoding. To rephase or refocus the dephased transverse magnetization, a magnetic field gradient of opposite polarity can be used prior to the frequency-encoding gradient. But, this will only work if the transverse magnetization does not change the position in the meantime, as is the case for diffusion. If the transverse magnetization changed positions, then the phase history will be different as compared with stationary tissue at that new location, and the rephasing will be insufficient. Insufficient rephasing will result in a reduced signal. The signal drop is characterized by

$$S \approx e^{-bD}, \qquad (2.4.13)$$

with b being a system or method specific parameter, and D being the diffusion coefficient for the tissue. The method specific parameter b

$$b = \gamma^2 \cdot G^2 \cdot \delta^2 \cdot (\Delta - \delta / 3) \qquad (2.4.14)$$

is a function of the gradient amplitude G used, the duration δ for each amplitude and the temporal distance Δ between the two gradient amplitudes. Δ is also called the diffusion time. A typical value for $b = 1{,}000\ \mathrm{s/mm^2}$. A sequence illustration is given in Fig. 2.4.53. The result of the application of such a technique to a patient with an acute infarction is shown in Fig. 2.4.54. Diffusion-weighted imaging allows an evaluation of the extent of cerebral ischemia in a period where possible interventions could limit or prevent further brain injury. The diffusion anisotropy potentially measured with this method allows the mapping of neuronal connectivity and offers an exciting perspective to brain research.

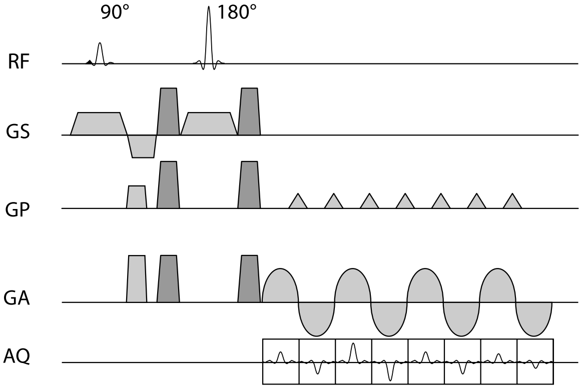

Fig. 2.4.53 Diffusion-weighted SE-EPI sequence. Diffusion weighting is provided using high gradient pulses placed symmetrically around the RF refocusing pulse. This method of diffusion weighting is called Stejskal-Tanner approach

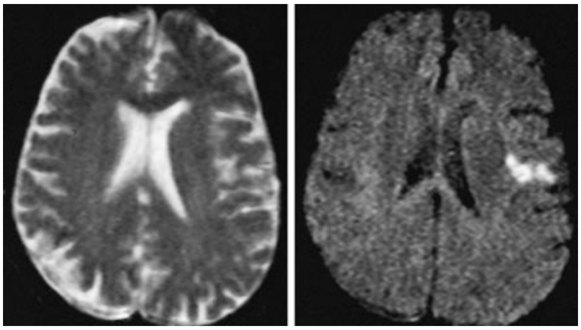

Fig. 2.4.54 The left image shows an axial head image acquired with an EPI sequence without diffusion weighting. The *right* image shows the result of the same technique with diffusion weighting. The infarcted region is only visible with diffusion weighting. (This example was provided by Dr. R. Edelmann, Beth Israel Hospital, Boston, Mass.)

2.4.6.6 Hybrid Techniques

The turbo gradient spin-echo sequence (TGSE), also called gradient and spin-echo (GRASE) is a combination of multiple gradient-echoes that are acquired within multiple SE envelopes of a TSE sequence, as shown in Fig. 2.4.55. This method holds several advantages in comparison to the "simple" TSE sequence: The use of several phase-encoded gradient-echoes has the potential of further shortening measurement time. Figure 2.4.56 shows a transversal T_2-weighted head image with a matrix size of 1,024, which has been measured with a TGSE sequence in 2.56 min. Another advantage is the fact that with the use of several gradient-echoes per spin-echo envelope, the gap between the refocusing pulses widens. Therefore, the J-coupling remains intact. Fat appears darker, and the contrast approaches the contrast of conventional SE sequences. Further, the enhanced sensitivity toward the susceptibility gradients that has been introduced with the gradient-echoes allows for a better depiction of blood-decay products, similar to conventional SE-imaging.

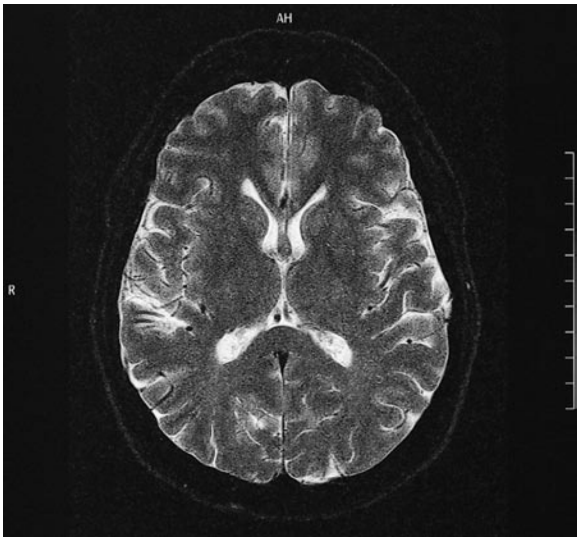

Fig. 2.4.56 Axial T_2-weighted head image acquired with a TGSE sequence (matrix 1024 × 1024, TGSE 7,000/115, slice thickness = 3 mm, measurement time = 2.56 min)

References

1. Bottomley PA, Hardy CJ, Argersinger RE et al (1987) A review of ^{1}H nuclear magnetic resonance relaxation in pathology: are $T1$ and $T2$ diagnostic? Med Phys 14:1–37
2. Brix G, Schad LR, Lorenz WJ (1990) Evaluation of proton density by magnetic resonance imaging: phantom experiments and analysis of multiple component proton transverse relaxation. Phys Med Biol 35:53–66
3. Feinberg DA, Hale JD, Watts JC et al (1986) Halving MR imaging time by conjugation: demonstration at 3.5 kG. Radiology 161:527–531
4. Frahm J, Haase A, Hänicke W, Matthaei D, Bomsdorf H, Helzel T (1985) chemical shift selective MR imaging using a whole-body magnet. Radiology 156:441–444
5. Haacke EM, Wielopolski PA, Tkach JA (1991) A comprehensive technical review of short TR, fast, magnetic resonance imaging. Rev Magn Res Med 3:53

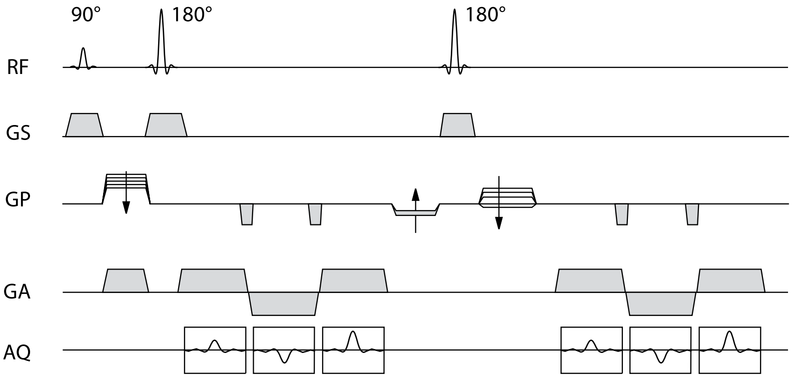

Fig. 2.4.55 Structure of the TGSE sequence. Several phase encoded GRE are produced within the spin-echo envelope. (In this example, three gradient-echoes are acquired within a spin-echo envelope)

6. Haase A (1990) Snapshot FLASH MRI. Application to T_1, T_2, and chemical-shift imaging. Magn Reson Med 13:77–89
7. Haase A, Frahm J, Hänicke W, Matthaei D (1985) ^{1}H-NMR chemical shift selective (CHESS) imaging. Phys Med Biol 30:341–344
8. Haase A, Frahm J, Matthaei D et al (1986) FLASH imaging: rapid NMR imaging using low flip angle pulses. J Magn Reson 67:258–266
9. Haase A, Matthaei W, Bartkowski R, Duhmke E, Leibfritz D (1989) Inversion recovery snapshot FLASH MR imaging. J Comput Assist Tomogr 13:1036
10. Henning J, Nauerth A, Friedburg H (1986) RARE-imaging: a fast imaging method for clinical MR. Magn Reson Med 3:823–833
11. Mansfield P, Mosley AA, Baines T (1976) Fast scan proton density imaging by NMR. J Phys 9:271–278
12. Mugler JP, Brookeman JR (1990) Three-dimensional magnetization-prepared rapid gradientecho imaging (3D MP RAGE). Magn Res Med 15:152
13. Mulkern RV, Wong STS, Winalski C, Jolesz FA (1990) Contrast manipulation and artifact assessment of 2D and 3D RARE sequences. Magn Reson Imag 8:557–566
14. Oppelt A, Graumann R, Barfuß H, Fischer H, Hartl W, Schajor W (1986) FISP: eine neue schnelle Pulssequenz für die Kernspintomographie. Electromedica 54:15–18
15. Pfannenstiel P, Just M, Higer HP et al (1987) Erste klinische Ergebnisse der Gewebecharakterisierung durch T1, T2 und Protonendichte bei der Kernspintomographie. RoFo 146:591–596
16. Wolff S, Balaban R (1989) Magnetization transfer via cross relaxation. Magn Reson Med 10:135–144

Suggested Reading

1. Bruder H, Fischer H, Graumann R, Deimling M (1988) A new steady-state sequence for simultaneous acquisition of two MR images with clearly different contrast. Magn Reson Med 7:35
2. Haacke EM, Brown RW, Thompson MR, Venkatesan R (1999) Magnetic resonance imaging: physical principles and sequence design. Wiley, New York
3. Heidemann RM, Özsarlak Ö, Parizel PM et al (2003) A brief review of parallel magnetic resonance imaging. Eur Radiology 13:2323–2337
4. Higer HP, Bielke G (1986) Gewebecharakterisierung mit T_1, T_2 und Protonendichte: Traum und Wirklichkeit. ROFO 144/5:597–605
5. Kiefer B, Grässner J, Hausmann R (1994) Image acquisition in a second with half-Fourier acquired single shot turbo spin echo. JMRI 4:86
6. Mansfield P, Pykett IL (1978) Biological and medical imaging by NMR. J Magn Reson 29:355–373 [see also German patent no. 2755956 C2 from 15 December 1977, Government Patent Office, Germany)
7. Margosian P, Schmitt F, Purdy D (1986) Faster MR imaging: imaging with half the data. Health Care Instrum 1:195
8. Oppelt A (ed) (2005) Imaging systems for medical diagnostics. Publicis MCD, Erlangen
9. Oshio K, Feinberg DA (1991) Magn Reson Med 20:344
10. Pfannenstiel P, Just M, Higer HP et al. (1987) Erste klinische Ergebnisse der Gewebecharakterisierung durch T_1, T_2 und Protonendichte bei der Kernspintomographie [in German]. RoFo 146/5:591–596
11. Vlaardingerbroek MT, den Boer JA (2004) Magnetic resonance imaging: theory and practice. Springer, Berlin Heidelberg New York

2.5 Technical Components

M. Bock

Clinical MR systems come in various types and shapes; however, the fundamental components of a clinical MR tomograph are essentially the same. These are:

- The **magnet**: The magnet creates a static and homogeneous magnetic field B_0, which is needed to establish a longitudinal magnetization.
- The **gradients**: The gradient coils generate additional linearly ascending magnetic fields that can be switched on and off. The gradient fields allow assigning a spatial location to the received MR signals (spatial encoding). For an image acquisition three independent gradient systems in x-, y-, and z-direction are required.
- The **radio frequency (RF) system**: To rotate the longitudinal magnetization from its equilibrium orientation along B_0 into the transverse plane, an oscillating magnetic field B_1 is required. This RF field is generated by a transmitter and coupled into the patient via an antenna, the RF coil. Radio frequency coils are also used to receive the weak induced MR signals from the patient, which are then amplified and digitized.
- The **computer system**: Measurement setup and image post-processing are performed by (distributed) computers that are controlled by a host computer. At this host computer, new measurements are planned and started and the reconstructed images are stored and analyzed.

A schematic of the components of a clinical MR system is shown in Fig. 2.5.1; more detailed descriptions can be found in the works of Oppelt (2005), Vlaardingerbroek et al. (2002), and Chen and Hoult (1989). In the upper part, a cross-section through a superconducting magnet can be seen, with field-generating magnet windings embedded in a cryostatic tank. Closer to the patient, the gradient coil and the whole-body RF coil are located outside the cryostat. The magnet is surrounded by an electrically conducting cabin (Faraday cage) which is needed to optimally detect the weak MR signals, without RF background from other RF sources (e.g., radio transmitters). In the lower part, the computing architecture and the hardware control cabinets are shown. A hardware computer controls the gradient amplifier, the RF transmitter, and the receiver. The received and digitized MR signals are passed on to an image-reconstruction computer, which finally transfers the reconstructed image data sets to the host computer for display and storage.

2.5.1 Magnet

To generate the main magnetic field three different types of magnets can be utilized: permanent magnets, resistive magnets, and superconducting magnets (Oppelt 2005; Vlaardingerbroek 2002; Chen 1989). The choice of an individual magnet type is determined by the requirements on the magnetic field. Important characteristics are the field strength B_0, spatial field homogeneity, temporal field stability, patient accessibility, as well as construction and servicing costs.

As outlined in Sect. 2.2 a high magnetic induction is desirable as the MR signal S is approximately proportional to B_0^2, and the signal-to-noise ratio (SNR) increases approximately linearly with B_0. It is thus expected that with increasing field strength the measurement time can be substantially decreased. The field strength is limited however for the following reasons:

- For tissues in typical magnetic fields of 0.5 T and higher, the longitudinal relaxation time T_1 increases with field strength. If the same pulse sequence with identical measurement parameters (T_R, T_E, etc.) would be used at low field and high field, the T_1 contrast would be less pronounced in the high-field image, since image contrast typically depends on the ratio of T_R over T_1. To achieve a similar T_1 contrast with a conventional SE or GRE pulse sequence, T_R (and thus the total measurement time) needs to be increased.
- The resonance frequency ω_0 increases linearly with field strength according to $\omega_0 = \gamma B_0$. At higher frequencies the wavelength of the RF waves are of the order of or even smaller than the dimensions of the objects to be imaged. Under these circumstances, standing waves can be created in the human body, which manifests in areas of higher RF fields (hot spots) and neighboring areas of reduced RF intensity. These unwanted RF inhomogeneities are difficult to control, as they are dependent on the geometry and the electric properties of the imaged object.
- The power that is deposited in the tissue during RF excitation rises quadratically with ω_0 (and thus with B_0). To ensure patient safety at all times during the imaging procedure the specific absorption rate (SAR), i.e., the amount of RF power deposited per kilogram of body weight, is monitored and limited by the MR system. With increasing field strength, the RF power generated by a pulse sequence increases, and thus the flip angle needs to be lowered to stay within the guidelines of SAR monitoring. Since most pulse sequences require certain flip angles (e.g., a 90–180° pulse pair for an SE), the RF pulses need to be lengthened at higher field strength to reduce the RF power per pulse. Additionally, the time-averaged power can be lowered by increasing the T_R.
- At field strengths above 1 T, only superconducting magnets are used for whole-body imaging systems. These magnets become very heavy and expensive. A typical 1.5-T MR magnet weighs about 6 t, whereas a 3-T magnet already has a weight of about 12 t. Shielding of the stray fields, which is, e.g., necessary to avoid

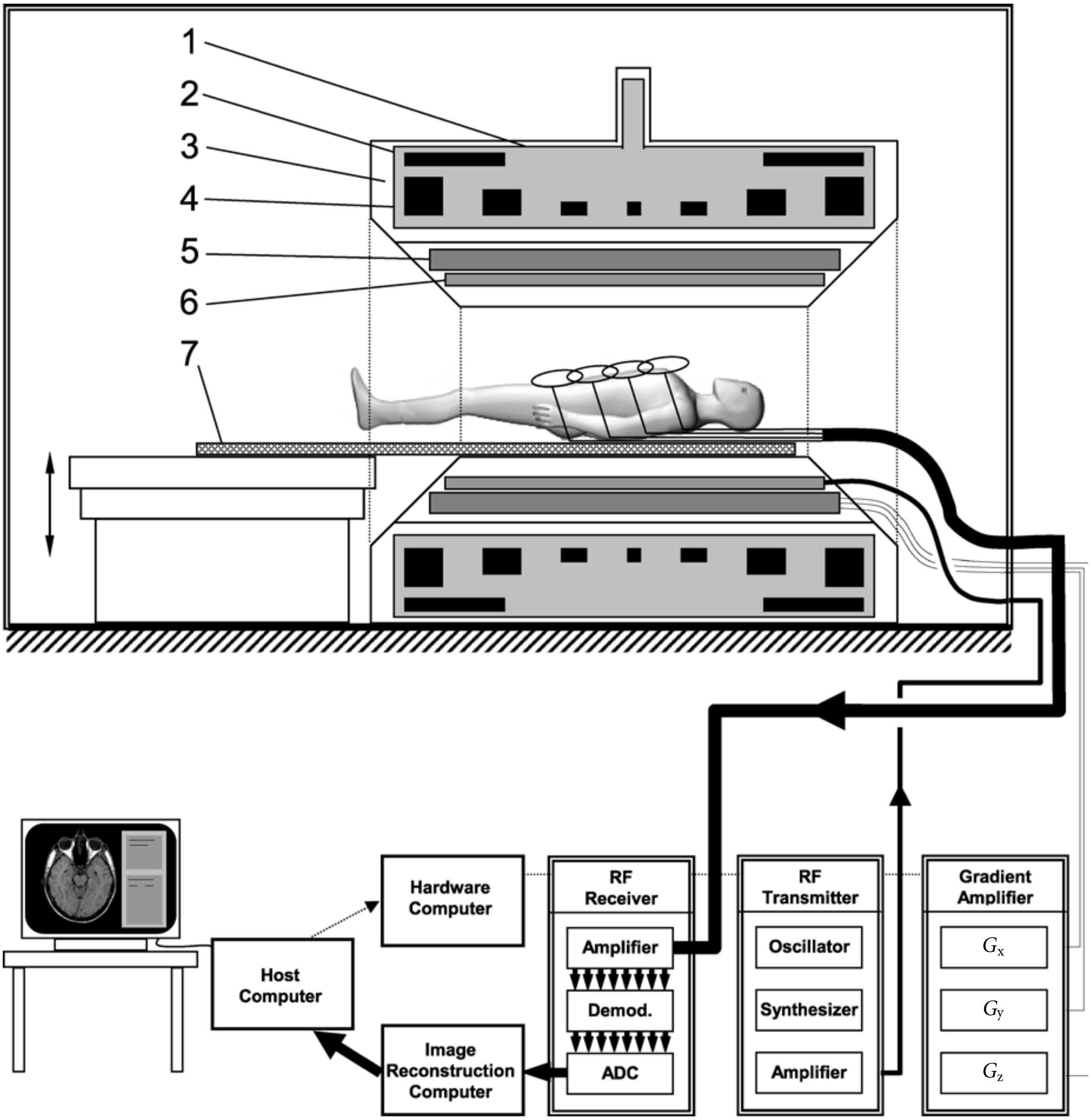

Fig. 2.5.1 Schematic of a clinical MR system. The main magnet is located in an RF cabin to suppress external RF signals. The superconducting, actively shielded solenoid magnet shown here consists of a cryotank (*1*) that is filled with liquid helium. The cryotank also houses the primary magnet coils (*4*) together with the shielding coils (*2*) that create the magnetic field. The cryotank is embedded in a vacuum tank (*3*). In a separate tubular structure in the magnet bore, the gradient coil (*5*) and the RF body coil (*6*) are mounted. An MR measurement is initiated by the user from the host computer. The timing of the sequence is monitored by the hardware computer, which controls (among others) the RF transmitter, RF receiver, and the gradient system. During the measurement, the RF pulses generated by the transmitter are applied (typically) via the integrated body coil, whereas signal reception is done with multiple receive coils. The digitized MR signals are reconstructed at the image-reconstruction computer, which finally sends the image data to the host for further post-processing and storage

interference with cardiac pacemakers, becomes increasingly difficult.

- The absolute differences in resonance frequency between chemical substances increase with field strength. This effect is beneficial for high-resolution spectroscopy, as high field strengths allow separating the individual resonance lines. During imaging, however, a substantially increased chemical shift artifact (i.e., a geometric shift of the fatty tissues versus the water-containing tissues) is seen, which can only be compensated using higher readout bandwidths.
- Differences in magnetic susceptibility between neighboring tissues create a static field gradient at the tissue boundaries. The strength of these unwanted intrinsic field gradients scales with B_0. Therefore, increasingly higher imaging gradients are required at higher field strength to encode the imaging signal without geometric distortion; however, gradient strengths are technically limited. On the other hand, in neurofunctional MRI (fMRI) the increased sensitivity at higher field strengths is utilized to visualize those brain areas where local susceptibility differences in the blood are modulated during task performance.

In the clinical environment, magnetic field strengths between 0.2 and 3 T are common. Low-field MR systems ($B_0 < 1$ T) are often used for orthopedic or interventional MRI, where the access to the patient during the imaging procedure is important. High field strengths between 1 T and 3 T are used for all other diagnostic imaging applications. Recently, whole body MR systems with field strengths up to 9.4 T have been realized (Robitaille et al. 1999). With these systems, in particular neurofunctional studies, high-resolution imaging and spectroscopy as well as non-proton imaging (e.g., for molecular imaging) are planned, since these applications are expected to profit most from the high static magnetic field.

In the following, the three different types of magnet are described that are used to create the static magnetic field.

2.5.1.1 Permanent Magnets

Permanent MRI magnets are typically constructed of the magnetic material NdBFe. Permanent magnet materials are characterized by the hysteresis curve, which describes the non-linear response of the material to an external magnetic field. If an external field is slowly increased, the magnetization of the material will also increase until all magnetic domains in the material are aligned—at this point the magnet is saturated, and no further amplification of the external field is possible. If the external field is then switched off a constant, non-vanishing magnetic field remains in the material because some of the domains remain aligned. Permanent magnets offer very high remanence field strength.

Fig. 2.5.2 C-arc–type permanent magnet 0.35-T MR system (Magnetom C!, Siemens) with a weight of 16 t. The vertical magnetic field is created by two pole shoes that have a free opening of 38.5 cm for imaging

Permanent magnets require nearly no maintenance because they provide the magnetic field directly without any electrical components. Permanent magnets often use a design with two poles, which are either above or below (Fig. 2.5.2) or at the sides of the imaging volume. Within this volume the magnetic field lines should be as parallel as possible (high field homogeneity), which is achieved by shaping of the pole shoes. Due to their construction, the magnetic field is typically orthogonal to the patient axis, whereas high-field superconductors use solenoid magnets with a parallel field orientation. Magnetic field lines are always closed; therefore, an iron yoke is used in permanent magnets to guide the magnetic flux between the pole shoes.

With increasing field strength permanent magnets become very heavy (10 t and more), and the high price of the material NdBFe becomes a limiting factor. Additionally, to achieve high temporal field stability the material requires a constant room temperature, which should not vary by more than 1 K. For these reasons, permanent magnets are typically used only for field strengths below 0.3 T.

2.5.1.2 Resistive Magnets

If an electrical current is flowing through a conductor, a magnetic field is created perpendicular to the flow direction that is proportional to the current amplitude. Unfortunately, in conventional conductors (e.g., copper wire) the electric resistance converts most of the electric energy into unwanted thermal energy and not into a magnetic field. Therefore, a permanent current supply is required to maintain the magnetic field and to compensate for the Ohmic losses in the wire. Additionally, to dissipate the thermal energy resistive magnets need permanent water cooling as their power consumption reaches several 100 kW.

Resistive magnets use iron yokes to amplify and guide the magnetic field created by the electric currents. The iron yoke is surrounded by the current-bearing wires so that the field lines stay within the iron. In the simplest form, the closed iron yoke has a gap at the imaging location and the magnet takes the form of a C-arc, which can also be rotated by 90° to provide a good access for the patient (Fig. 2.5.3). Other magnet designs use two or four iron posts that connect the pole shoes.

The magnetic field of a resistive magnet is typically not as homogeneous as that of a superconducting magnet of the same size. To achieve high field homogeneity within the imaging field-of-view, the diameter of the pole shoes should not be less than 2.5 times the desired diameter of the imaging volume (D_{FOV}), and the pole separation should be more than 1.5 D_{FOV}. At a typical pole separation of 45 cm, the imaging volume would thus have a diameter of 30 cm, and the pole shoe diameter amounts to 75 cm.

Resistive magnets are susceptible to field variations caused by instabilities of the electric power supply. To minimize this effect the magnetic field of the magnet can be stabilized using an independent method to measure the field strength (e.g., electron spin resonance). The difference between actual and desired field strength is then used to regulate the current in the magnet in a closed feedback loop.

2.5.1.3 Superconducting Magnets

To create magnetic fields of more than 0.3 T with a bore size of 60 cm or more, today, typically superconducting magnets are utilized (Fig. 2.5.4). In principle, these magnets operate in a similar fashion as resistive magnets without iron yoke—superconducting magnets also generate their magnetic field by wire loops that carry a current. Instead of copper wire, superconductors use special metallic alloys such as niobium–titanium (NbTi). The alloys completely lose their electric resistance below a certain transition temperature that is characteristic for the material; this effect is called superconductivity. The transition temperature itself is a function of the magnetic field, so that lower temperatures are required when a current is flowing through the wire. Unfortunately, an upper limit for the current density in the wire exists, which is also a function of the temperature and the magnetic field. To maintain the required low temperatures cooling with liquid helium is typically necessary ($T < -270$°C).

Fig. 2.5.3 Iron-frame electromagnet 0.6-T MR system (Upright$^{\mathrm{TM}}$ MRI, FONAR) with a horizontal magnetic field. This special construction of the MR systems allows for imaging in both upright and lying positions. This flexibility is especially advantageous for MR imaging of the musculoskeletal system

The imaging volume of the MR system is typically kept at room temperature ($T = 20$°C), whereas the surrounding superconducting wires require temperatures near the absolute zero (−273.15°C). To maintain this enormous temperature gradient, the field-generating superconducting coils are encased in an isolating tank, the cryostat. The cryostat is a non-magnetic steel structure that contains radiation shields to prevent heat diffusion, heat conduction, and heat transport. If this isolation is not working properly and the wire is locally warming up over the transition temperature, then this section of the wire will become normally conducting, and the energy stored in the current will be dissipated as heat. The heat will then be transported to adjacent sections of the wire, which will also lose their superconductivity. This very rapid process is called a *quench*. When the magnet wire is heating up the liquid helium will evaporate, and the cryo-

Fig. 2.5.4 Conventional 1.5-T superconducting MR magnet (Magnetom Symphony, Siemens) with a magnet length of 160 cm and a free open–inner bore diameter of 60 cm. The system is equipped with an in-room monitor (*left*), which allows controlling the MR system from within the RF cabin

stat is exposed to an enormous pressure. To prevent the cryostat from exploding, a so-called quench tube is connected to superconducting magnets with helium cooling, which safely guides the cold helium vapor out of the magnet room.

Recently also ceramic superconducting materials on the basis of niobium–tin (Nb_3Sn) alloys have been used to make superconducting wires. The brittle Nb_3Sn alloys show a higher transition temperature (–263°C) and thus do not necessarily require liquid helium cooling. If the cryostat is equipped with a good thermal vacuum isolation, a conventional cooling system (e.g., Gifford-McMahon cooler) can be used to maintain the temperature. This technology has been realized both in a dual-magnet system (General Electric SP, B_0 = 0.5 T) and a low-field open MR system (Toshiba OPART, B_0 = 0.35 T). Because a helium-filled cryostat requires more space than does a system without helium, these magnets can be installed in smaller areas than can comparable magnets with helium.

In the recent years, several MR magnets have been equipped with helium liquefiers to regain the evaporated helium gas in the magnet. Once filled with helium these so-called zero boil-off magnets can operate in principle without any additional helium filling. Magnets without helium liquefiers require replenishment of the helium at intervals between several months and 1–2 years, depending on the quality of the cryostat and the usage of the MR system.

The most widespread form of a superconducting magnet is the solenoid, where the windings of the superconducting wire form loops around the horizontal bore of the cylindrical magnet. At a typical inner bore diameter of 60 cm for clinical MRI systems, solenoid magnets can create very homogeneous magnetic fields with variations of only a few parts per million (ppm). Because the relatively bulky magnet structure limits access to the patient, shorter magnets of 1.5 m length with wider diameters of 70 cm have been designed (Siemens Magnetom Espree, B_0 = 1.5 T) (Fig. 2.5.5). In these magnets, obese patients can be imaged more conveniently, claustrophobic patients feel more at ease and some MR-guided percutaneous interventions might become feasible. Another variant of the solenoid is a dual magnet MR system consisting of two collinear short solenoid magnets (General Electric SP, B_0 = 0.5 T) — here the imaging area is located in between the two magnets and even intra-operative MR imaging is possible. Recently, also two-pole systems with a magnet design similar to low-field resistive magnets have become, which offer a good patient access in combination with higher field strengths (Fig. 2.5.6).

Outside a superconducting magnet, the field strength his falling off with the inverse third power of the distance ($1/r^3$) so that the stray fields can extend far outside the MR room. Magnetic fields in commonly accessible areas must not exceed 0.5 mT, because higher fields can affect pace makers and other active electric devices (Fig. 2.5.7). For this reason, two shielding technologies have been utilized to reduce the magnetic fringe fields. With *passive shielding* ferromagnetic materials such as steel are mounted near the magnet. This shielding technique confines the field lines to the interior of the shielding material, and the stray fields are reduced. Unfortunately, the amount of shielding material rapidly increases with increasing magnetic field, and between 400 t and 600 t of steel are required to shield a 7-T magnet (Schmitt et al. 1998).

With *active shielding* a second set of wire loops is integrated in the cryostat of the magnet. The shielding

Fig. 2.5.5 Clinical 1.5-T superconducting MR system (Magnetom Espree, Siemens) with a very short magnet (125-cm length) and an open-bore diameter of 70 cm. The additional 10 cm in bore diameter over conventional MR system with solenoid magnets and the shorter magnet length offer a better access to the patient, so that, e.g., percutaneous interventions can be performed in this magnet structure

Fig. 2.5.6 Superconducting 1-T MR system (Panorama 1 T, Philips) with a two-pole open configuration and a vertical magnetic field

coils create a magnetic field in the opposite direction of the imaging field so that the stray field falls off more rapidly. The shielding coils have a larger diameter than do the field-generating primary coils. Thus, the desired magnetic field within the magnet can be maintained by increasing the current in both coil systems. Additionally, the shielding coils and the primary coils repel each other (Lorentz forces), which requires a magnet design with more stable coil formers. The attractive forces acting on paramagnetic or ferromagnetic objects near such an actively shielded magnet are significantly higher than near an unshielded magnet; device compatibility and safety should thus always be specified with regard to the investigated magnet type.

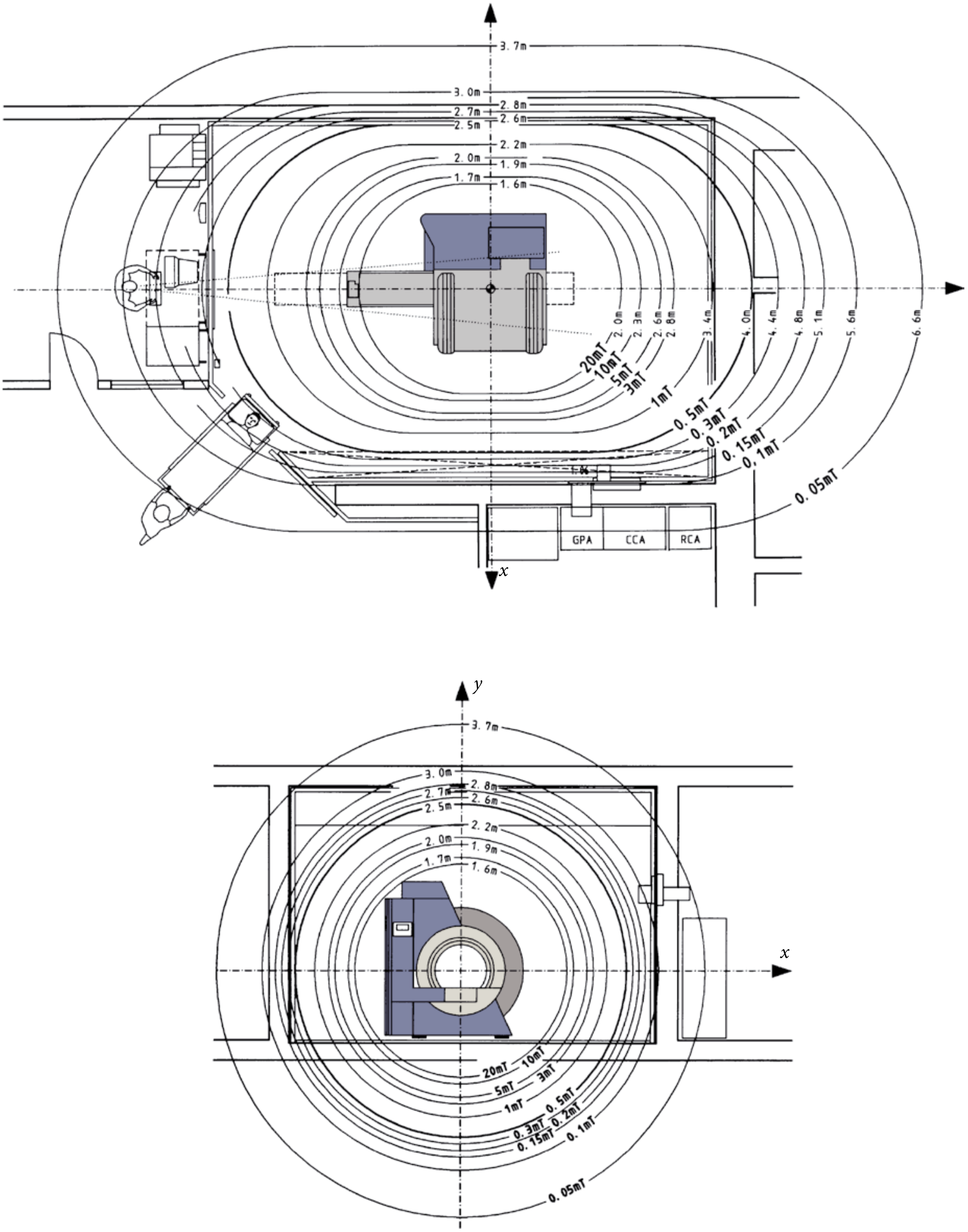

Fig. 2.5.7 Magnetic field line plots for an actively shielded 1.5-T magnet (Magnetom Symphony, Siemens). In the horizontal plane (*top*) the 0.5-mT (5 Gs) line stays within the RF cabin or the adjacent walls, so that access needs to be restricted to the RF cabin (controlled area) only. In vertical direction (*bottom*) the 0.5-mT line extends partly into the lower floor (here: the basement), and warning signs need to be mounted to avoid involuntary exposure to the static magnetic field

2.5.2 Gradients

To localize the MR signals emitted by the imaging object, a linearly increasing magnetic field, the gradient G, is superimposed on the static magnetic field B_0. The gradient fields are created by gradient coils that are located between the magnet and the imaging volume (Schmitt et al. 1998). For each spatial direction (x, y, and z) a separate gradient coil is required, and angulated gradient fields are realized by linear superposition of the physical gradient fields. In a cylindrical bore superconducting magnet, the gradient coils are mounted on a cylindrical structure, which is often made of epoxy resin. This gradient tube reduces the available space in the cryostat from typically 90 cm, without gradient coils, to 60 cm, with gradient coils.

The functional principle of a gradient system is best illustrated by a setup of two coaxial wire loops with a radius a that are separated by a distance d (Fig. 2.5.8). If the two coils both carry the same current, however, in counterpropagating directions, their respective magnetic fields cancel at the iso-center of the setup. At distances not too far from iso-center the magnetic field will increase linearly, which is exactly the desired behavior of a gradient field. To achieve this linear gradient field the condition $d = \sqrt{3}a$ must be met (Maxwell coil pair) (Jin 1999). In commercially available gradient system, much more complicated wiring paths are utilized, which are optimized using the so-called target field approach (Turner 1993). This often results in wire patterns that, when plotted on a sheet of paper, resemble fingerprints (fingerprint design). Nevertheless, a common feature of all gradient systems is the absence of current at the central plane, which allows separating the gradient coils, e.g., for C-arc–type magnets.

The quality of the gradient system is characterized by several parameters: the maximum gradient strength $G_{\max}$, the slew rate $s_{\max}$, the homogeneity, the duty cycle, the type of shielding, and gradient pulse stability and precision. Today, clinical MR systems have maximum gradient strengths of up to $G_{\max} = 40$ mT/m at bore diameters of 60 cm. Even higher gradient strengths of 80 mT/m and more can be realized when so-called gradient inserts with smaller diameters are used (e.g., for head imaging). The maximum gradient strength is limited by the capabilities of the power supply of the gradient system—modern gradient systems use power supplies that can deliver voltages up to 2,000 V and currents up to 500 A. Another limiting factor for $G_{\max}$ is gradient heating: With increasing current through the gradient coil, the windings heat up to levels at which the gradient could be destroyed. Therefore, to remove the heat from the gradient tube, pipes are integrated in the gradient coils for water-cooling.

The maximum slew rate $s_{\max}$ is the ratio of $G_{\max}$ over the shortest time required to switch on the gradient (rise time). When the current in the gradient coil is increased during gradient switching, according to Lenz's law the coil will produce a current, which opposes the change. Thus, it counteracts the switching process, and the rise time cannot be made infinitely short. During MR imaging, however, it is desirable to have very short rise times (i.e., high slew rates), as these times only prolong the imaging process. Clinical MRI systems have slew rates between 10 mT/m/ms and 200 mT/m/ms. If the gradient coil is connected to a capacitance via a fast switch,

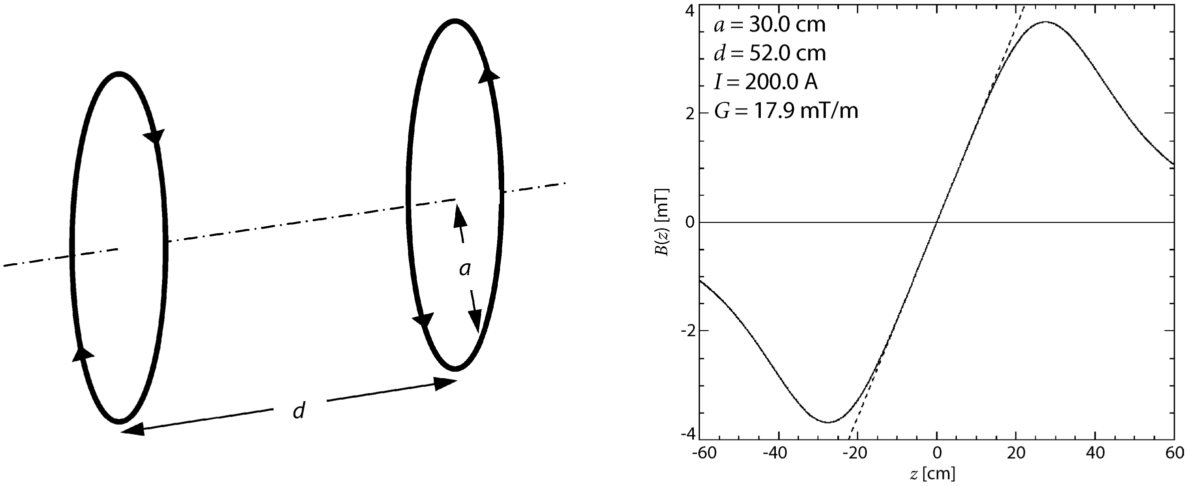

Fig. 2.5.8 Magnetic field of two wire loops (radius a, distance d) that are carrying a current I with opposite polarity. Over a certain range between the loops, the magnetic field increases linearly with the position z (*dashed line*). With realistic values of $a = 30$ cm, $d = 52$ cm, and $I = 200$ A, a gradient amplitude of 18 mT/m is achieved

very short rise times can be achieved, as the inductance of the gradient coil and the capacitance form a resonance circuit. Such a resonant gradient system has the disadvantage that the characteristic frequency of the resonance circuit determines the possible rise times. Additionally, gradients can only be switched on after the capacitances have been charged. Resonant gradient systems have nevertheless been successfully applied to EPI studies, in which the sinusoidal gradient waveforms are beneficial, and multistage resonant systems have been utilized to approximate the trapezoidal gradient waveforms (Harvey 1994).

When the gradient is switched on, the maximal rate of field change is observed at the ends of the gradient coil (i.e., $\mathrm{FOV}_{\max}/2$): $\mathrm{d}B/\mathrm{d}t = s_{\max}\ \mathrm{FOV}_{\max}/2$. A changing magnetic field induces currents in electrically conducting structures in its vicinity—outside the gradient coil this structure is given by the cryostat, and on the inside the patient can act as a conductor. To avoid these parasitic currents (eddy currents) in the cryostat, which in turn create magnetic fields counteracting the gradients, often a second outer gradient structure is integrated in the gradient tube. The inner and outer gradient coils are designed so that their combined gradient field vanishes everywhere outside the gradient coil, whereas the desired gradient amplitudes are realized on the inside. This technique is called *active shielding*, and is conceptionally similar to the active shielding of superconducting magnets (Mansfield and Chapman 1986; Harvey 1994).

Gradient-induced currents in the human body pose a more severe problem, as these currents can potentially lead to painful peripheral nerve stimulation or, at higher amplitudes, to cardiac stimulation (Mansfield and Harvey 1994; Schaefer 1998; Liu et al. 2003). These physiologic effects are not only dependent on the amplitude, but also on the frequency of field change. For clinical MR systems, different theoretical models have been established to determine the threshold for peripheral nerve stimulation. To make the best use of the available gradient system some fast pulse sequences (e.g., for contrast-enhanced MRA or EPI) operate very close to these threshold values. As individuals are more or less susceptible to peripheral nerve stimulation, for some patients the individual threshold might be exceeded, and they experience a tickling sensation during fast MR imaging. This physiologic effect currently prohibits the use of stronger gradient systems.

Since the field change is lower at shorter distances from iso-center, peripheral nerve stimulation can be avoided if shorter gradient systems are used. Unfortunately, a shorter gradient system only covers a limited FOV, and the anatomical coverage is compromised. To overcome this limitation a combined gradient system with a shorter, more powerful inner coil and a longer, less intense outer coil has been proposed (twin gradients) (Harvey 1999). Such a system can be used, e.g., to rapidly image the beating heart with the small coil, or to acquire image data from the surrounding anatomy at lower frame rates.

When the gradient system is mounted in the MR magnet, strong mechanical forces act on the gradient tube, which are proportional to the gradient current. These forces are generated by the interaction of the gradient field with the static magnetic field and thus increase with B_0. The permanent gradient switching creates time-varying forces that lead to acoustic noise. Several techniques have been proposed to reduce noise generation, which in some cases can exceed dangerous sound pressure levels of 110 dB. The wire paths in the coil can be designed in such a way that the forces are locally balanced, the gradient tube can be mechanically stabilized, the gradients can be integrated in a vacuum chamber to prevent sound propagation in air, or the gradient system can be mounted externally to reduce acoustic coupling to the cryostat (Pianissimo gradient, Toshiba). Another possibility to reduce acoustic noise is to limit the slew rates in the pulse sequences to lower values than technically possible; in some pulse sequences (e.g., spin-echo sequences), this does not significantly affect the pulse sequence performance, but severely increase patient comfort.

2.5.3 Shim

Shimming is a procedure to make the static magnetic field in the MR system as homogeneous as possible. Inhomogeneities of the magnetic field that are caused during the manufacturing of the magnet structure can be compensated with small magnetic plates (passive shim). After a localized measurement of the initial magnetic field, the position of the plates is calculated, and the plates are placed in the magnet. This procedure is repeated until the desired homogeneity of the field is achieved (e.g., 0.5 ppm in a sphere of radius 15 cm).

During MR imaging, objects are present in the static magnetic field that distort the homogeneous static field. Field distortion is caused by susceptibility differences at the tissue interfaces and is thus specific for each patient. To at least locally compensate these field distortions, adjustable magnetic fields are required (active shim). If the field distortion is linear in space, then the gradient coils can be used for compensation. For higher-order field variations, additional shim coils are required. Typically, shim coils up to fifth order are present in an MR system.

Higher-order shimming is particularly important for MR spectroscopy, where the field homogeneity directly affects the spectral line width. To optimize the shim currents, an interactive measurement process (the shim) is started after the patient is positioned in the magnet. During active shimming the field homogeneity is measured (e.g., using localized MR spectroscopy or a field mapping technique), and the currents are then adjusted to improve the field homogeneity (Webb and Macovski 1991).

2.5.4 Radiofrequency System

The radiofrequency (RF) system of an MR scanner is used to both create the transverse magnetization via resonant excitation and to acquire the MR signals (Oppelt 2005; Vlaardingerbroek et al. 2002; Chen and Hoult 1989). The RF system consists of a transmit chain and a receive chain. In the following, the details of the RF system are described.

2.5.4.1 RF Cabin

The MR signals, which are acquired by the RF coils of the MR system, are typically very low. To optimally detect these low signals, any other electromagnetic signals (e.g., radio waves) must be suppressed. Therefore, the MR system is placed in a radiofrequency cabin (also called a Faraday cage), which dampens RF signals at the resonance frequency by typically 100 dB and more.

In low-field MR tomographs, the RF screening is sometimes realized as a wire mesh that is integrated in the MR system. This has the advantage that RF-emitting equipment such as television screens can be placed very close to the MR unit. At larger magnet dimensions, these local screens are often not suitable. Here, the whole MR room is designed as an RF cabin, and the screening material is integrated into the walls, doors, and windows. For screening often copper sheets are used, which are glued to the wall panels, or the cabin consists completely of steel plates.

To be able to transmit signals to and receive signals from the RF cabin, openings are integrated in the cabin. In general, one distinguishes between so-called *filter plates*, which contain electronic filters and open *waveguides*. Waveguides are realized as open tubes with a certain length-to-diameter ratio, which is dependent on the wavelength of the RF frequency. Waveguides are used to deliver anesthesia gases to the RF cabin and to guide the quench tube out of the shielded room.

2.5.4.2 Transmitter

At the beginning of the transmit chain the RF transmitter is found, which consists of a synthesizer with high-frequency stability and an RF power amplifier. The low-power synthesizer oscillates at the Larmor frequency. Its output signal is modulated by a digitally controlled pulse shaper to form the RF pulse, which is then amplified by the power amplifier. For typical clinical MR systems, the transmitter needs to provide peak power output at the Larmor frequency of 10 kW and more. Besides high peak power, the RF transmitter should also allow for a high time-averaged power output, as several pulse sequences such as fast spin-echo sequences require RF pulses at short repetition times. The RF power is then transferred into the RF cabin via a shielded cable, and is delivered to the transmit RF coil.

To guarantee a safe operation of the transmitter and to limit the RF power to values below the regulatory constraints for the specific absorption rates (SAR), directional couplers are integrated in the transmission line. These couplers measure the RF power sent to the RF coil as well as the reflected power. High power reflection is an indicator of a malfunctioning of the connected coil, which could endanger the patient. If the reflected power exceeds a given threshold (e.g., 20% of the forward power), then the RF amplifier could be damaged by the reflected RF power and the transmitter is switched off.

2.5.4.3 RF Coils

To couple the RF power of the RF transmitter to the human body an RF antenna is required, the so-called RF coil. Before MR imaging starts, the coil is tuned to the resonance frequency of the MR system (RF tuning). Simultaneously, the properties of the connecting circuitry are dynamically changed to match the resistance of the coil with the imaging object (loaded coil) to the resistance of the transmit cable (RF matching).

Once the coil is tuned and matched, the transmitter is adjusted. During this procedure, the MR system determines the transmitter voltage required to create a certain flip angle. For a given reference RF pulse shape $S_{\mathrm{ref}}(t)$, the transmitter voltage U_{ref} is varied until the desired flip angle α_{ref} (e.g., 90°) is realized. During the subsequent imaging experiments, use is made of the fact that the flip angle is linearly proportional to the (known) integral over the RF pulse shape, so that the required voltages can be computed from the reference values by linear scaling.

Radiofrequency coils are categorized into *transmit* (Tx) coils, *receive* (Rx) coils, and *transmit/receive* (TxRx) coils. Tx coils are only used to expose the imaging object to an RF B_1 field during RF excitation, whereas Rx coils detect the weak echo signal emitted from the human body—only if a coil performs both tasks, is it called a TxRx coil. A typical example of a TxRx coil is the body coil integrated into most superconducting MR systems; however, in some modern MR systems, it is used as a Tx coil only due to its suboptimal receive characteristics. Rx-only RF coils are the typical local coils found in MR systems that possess a (global) body coil, and local TxRx coils are used in all other MR systems without a body coil (ultra-high field, dedicated interventional systems, open-configuration low field).

During signal reception, the oscillating magnetization in the human body induces a voltage in the RF coil. For an optimal detection of this weak signal, the RF coil should be placed as close to the imaging volume as possible. For this reason, optimized imaging coils exist for nearly any part of the human body. The largest coil of an MR system is typically the body coil (if present), which is often integrated in the magnet cover. To image the head or the knee, smaller volume resonators are used, where the imaging volume is in the interior of the RF coil (Fig. 2.5.9). Flexible coils exist, that can be wrapped around the imaging volume (e.g., the shoulder). Small circular surface coils are used to image structures close to the body surface (e.g., eyes). Unfortunately, the sensitivity of these coils is rapidly decreasing with distance from the coil center, so that they are not suitable for imaging experiments, where a larger volume needs to be covered.

During RF transmission, Rx coils need to be deactivated, because a tuned and matched Rx coil would ideally absorb the transmitted RF power, and a significant amount of the RF energy would be deposited in the coil. To avoid any electronic damages, the coil is actively detuned during RF transmission; this is often accomplished by fast electronic switches (e.g., PIN diodes), which connect a dedicated detuning circuitry.

Fig. 2.5.9 Various receive coils on the patient table of a clinical 1.5-T MR system (Magnetom Avanto, Siemens) with 32 receive channels and the possibility to connect a total of 76 coil elements. The head coil with 12 coil elements is combined with a neck coil (4 elements), and the remaining parts of the anatomy are imaged with multiple flexible anterior phased-array coils (2 × 3 elements) and the corresponding posterior coils, which are integrated in the patient table. For smaller imaging volumes dedicated surface coils (flexible coil, open loop coil, small loop coil) can be used, which share a common amplifier interface

To combine the high sensitivity of small surface coils with the volume coverage of a large volume resonator, the concept of the so-called phased-array coils has been introduced (Roemer et al. 1990). A phased-array coil consists of several small coil elements, which are directly connected to individual receiver channels of the MR system. The separate reconstruction of the coil elements is technically demanding, because a full set of receiver electronics (amplifiers, analog-to-digital converters) as well as an individual image reconstruction are required for each coil element. The signals of the individual coil elements are finally combined using a sum-of-squares algorithm, which yields a noise–optimal signal combination. Under certain conditions when SNR can be sacrificed, also a suboptimal image reconstruction can be achieved by a direct combination of the coil element signals, which reduces the number of receive channels and shortens the image reconstruction time. To be able to manually adjust SNR versus reconstruction overhead, special electronic mixing circuits have been introduced which allow combining, e.g., three coil elements into a primary, a secondary, and a tertiary signal (Total Imaging Matrix Tim, Siemens).

In a phased-array coil, the coil elements are positioned in such a way that an induced voltage in one element does not couple to the adjacent element—this can be achieved by an overlapping arrangement of the coil elements (geometric decoupling). Phased-array coils with up to 128 elements have been realized; however, typically the number of elements ranges between 4 and 32. Today, MRI systems with 32 independent receiver channels are available, at which up to 76 coil elements can be positioned simultaneously. The individual coil elements can be selected manually or automatically to achieve the highest possible SNR for a given imaging location.

Phased-array coils are not only required to achieve a high SNR. The individual coil elements can also be used to partially encode the spatial location in the image; this procedure is called *parallel imaging*. The simplest version of parallel imaging uses two adjacent coil elements with non-overlapping sensitivities. If one wants to image the full FOV covered by both coils only FOV/2 needs to be encoded, since each coil element is sensitive over this distance only. If the phase-encoding direction is chosen in this direction, the phase FOV can be reduced by a factor of 2, which in turn halves the total acquisition time. In practice, the sensitivity profiles of the coil elements overlap and more sophisticated techniques such as SMASH Sodickson and Manning 1997) or SENSE (Dumooulin et al. 1993) are required to reconstruct the image. Nevertheless, in parallel imaging the intrinsic spatial encoding present in the different locations of the imaging coils is exploited to reduce the number of phase encoding steps.

Because the phase encoding direction is different for different slice orientations, the optimal phased-array coil for parallel imaging offers coil elements with separated sensitivity profiles in all directions.

For MR spectroscopy and non-proton imaging, RF coils with resonance frequencies for the respective nuclei are required. These non-proton coils can also incorporate a coil at the proton resonance frequency to acquire proton images without the need for patient repositioning. Double-resonant coils are also important in situations when both frequencies are used at the same time as, e.g., in decoupling experiments.

For interventional MRI, dedicated tracking coils have been developed that are attached to the interventional devices (e.g., catheters or needles). The signal from these coils can be used for high-resolution imaging (e.g., of the vessel wall), but it is often only utilized to determine the position of the device (Doumoulin et al. 1993). In these tracking experiments, the signal of the coil is encoded in a single direction using a non-selective RF excitation, and the position of the coil in this direction is extracted after a one-dimensional Fourier transform.

2.5.4.4 Receiver

The MR signal received by the imaging coil is a weak, analog, high-frequency electric signal. To perform an image reconstruction or a spectral analysis, this signal must be amplified, digitized, and demodulated. The signal amplification is typically performed very close to the imaging coil to avoid signal interference from other signal sources. If the RF coil is a TxRx coil, then the signal passes a transmit–receive switch that separates the transmit from the receive path.

The amplified analog signal still contains the high-frequency component of the Larmor frequency. To remove this unwanted frequency component, the signal is sent to a demodulator, which receives the information about the current Larmor frequency from the synthesizer of the transmitter. After demodulation, the MR signal contains only the low-frequency information imposed by the gradients. Finally, the analog voltage is converted into a digital signal using an analog-to-digital converter (ADC). Over the recent years the conversion into a digital signal has increasingly been performed at an earlier stage in the receiver chain (e.g., before demodulation), and all subsequent steps were carried out in the digital domain. At the end of the receiver chain, the digital signal is then handed over to the image reconstruction computer.

2.5.5 Computer System

The computing system of an MR tomograph is typically realized by a system of distributed computers that are connected by a local high-speed network. The requirements for the computing system are manifold: For the user of the system it should provide an intuitive interface for measurement control, image processing, archiving, and printing. During sequence execution, the computers should control the hardware (i.e., gradients, RF, ADCs, patient monitoring, etc.) in real time. Additionally, the computing system must reconstruct and visualize the incoming MR data.

Since a single computer cannot perform all of these tasks at the same time, typically three computers are used in an MR system: the host computer for interaction with the user, the hardware control computer for real-time sequence control, and the image reconstruction computer for high-speed data reconstruction.

2.5.5.1 Host Computer

The host computer provides the interface between the user and the MR system. Through the MR user interface, the whole MR system can be controlled, MR measurements can be started, and the patient monitoring is visualized. At the host computer, the incoming images are sorted into an internal database for viewing, post-processing, and archiving.

The internal database stores and sorts the images by patients, studies, and series. The database is often connected to the picture archiving and communication system (PACS) of the hospital, from where it retrieves the patient information to maintain a unique patient registry. A 256 × 256 MR image typically requires about 130 KB of storage space, and for each patient investigation between 100 and 1,000 images are acquired. On an average working day between 10 and 30 patients can be examined. The data of all of these patients need to be stored in the database so that a storage volume of about 4 GB per day should be provided. With increasing matrix sizes and image acquisition rates, these numbers can easily be multiplied by factors of 10 and more.

The host computer is also used to transfer the acquired data to archiving media such as magneto-optical disks (MOD), tapes, compact disks (CD), digital versatile disks (DVD), or external computer archives (typically, the PACS). Data transfer is increasingly accomplished using the image standard DICOM (digital imaging and communications in medicine), which regulates not only the image data format, but also the transfer protocols. It is due to this imaging standard that images can be exchanged between systems from different vendors and can be shared between different modalities.

For post-processing, typically different software packages are integrated. In MR spectroscopy, software packages for spectral post-processing are available to calculate, e.g., peak integrals automatically. For MR diffusion measurements, the apparent diffusion coefficient can be mapped. With flow-evaluation software, the flow velocities and flow volumes can be assessed. To visualize three-dimensional data sets often multi-planar reformatting tools or projection techniques such as the maximum intensity projection (MIP) are used. All of these software packages retrieve the image data from the integrated image database, into which the calculated images are finally stored.

Dedicated computer monitors are connected to the host computer for image visualization, which fulfill the special requirements for diagnostic imaging equipment. In addition, these screens must not be susceptible to distortions due to the magnetic field; for this reason liquid crystal monitors based on the thin-film transistor (TFT) technology are increasingly used. For interventional MR, shielded monitors for in-room image display have been designed, where the monitor is shielded against electromagnetic interference. These monitors can be used within the Faraday cage of the MR system without interfering with the image acquisition.

2.5.5.2 Hardware-Control Computer

The control of the imaging hardware (i.e., the gradients in x, y, and z, the RF sub-system, the receiver, and the patient-monitoring system) requires a computer with a real-time operating system. Compared with conventional operating systems where the instructions are processed in an order and at a time that are influenced by many factors, a real-time operating system ensures that operations are executed on an exactly defined time scale. This real-time execution is necessary to maintain, e.g., the phase coherence during spin-echo MRI or to ensure that a given steady state is established during balanced SSFP imaging.

During sequence execution, the different instructions for the hardware are typically sent by the control program to digital signal processors (DSP) that control the individual units. Thus, new instructions can be prepared by the control program, whereas the actual execution is controlled close to the individual hardware. To ensure that enough hardware instructions are available, many time steps are computed in advance during sequence execution.

For real-time pulse sequences, this advance calculation needs to be minimized to be able to interactively change sequence parameters such as the slice position (controlled by the RF frequency) or orientation (controlled by the gradient rotation matrix). In real-time sequences, the information about the current imaging parameters is thus retrieved not only once at the beginning of the scan, but continuously during the whole imaging experiment.

2.5.5.3 Image-Reconstruction Computer

The reconstruction of the data arriving at the ADCs is performed by the image-reconstruction computer. To estimate the amount of data this computer needs to process the following estimate can be used: During high-speed data acquisition about 256 raw data points (i.e., 256 × 16 bytes) arrive per imaging coil at time intervals of $T_R = 2$ ms, so that with 10 Rx coils a data rate of 20 MB/s results. These incoming data need to be rearranged, corrected, Fourier transformed, combined, and geometrically distorted before the final image is sent to the host computer. To perform this task today multiprocessor CPUs are used to perform some of these tasks in parallel. In particular, the image reconstruction for multiple coils lends itself naturally to parallelization, since each of the coils is independent of the other.

Additionally, some manufacturers are including simple post-processing steps into the standard image reconstruction. Since the reconstruction computer does not provide a direct user interface, these reconstruction steps need to be designed in such a way that no user interaction is necessary. This is the case for the calculation of activation maps in fMRI, for MIP calculations under standard views in MR angiography, or for the calculation of the arrival time of a contrast agent bolus in perfusion studies. At the end of the image reconstruction, the image data are transferred to the host computer via the internal computer network.

2.5.6 Patient Monitoring

Special MR imaging techniques require additional MR components that are not necessarily available at any MR scanner. These components often monitor certain physiologic signals such as the electrical activity of the heart (electrocardiogram, ECG) or breathing motion (Fig. 2.5.10). Typically, the measured physiologic signals are not used to assess the health status of the patient but to synchronise the image acquisition with the organ motion, since heart and breathing motion can cause significant artifacts during abdominal imaging.

Synchronization of the image acquisition is performed either with *prospective* or *retrospective* gating. With prospective gating (or triggering), the imaging is started with the arrival of a certain physiologic signal (e.g., the R wave in the ECG). Therefore, the physiologic signal is post-processed (e.g., thresholding and low-pass filtering) to create a trigger signal when the physiologic condition is present. With retrospective gating, the measurement is not interrupted, but data are acquired continuously, and for each measured data set, the physiologic state is stored with the data (e.g., the time duration after the last R wave). During image reconstruction, the measured data

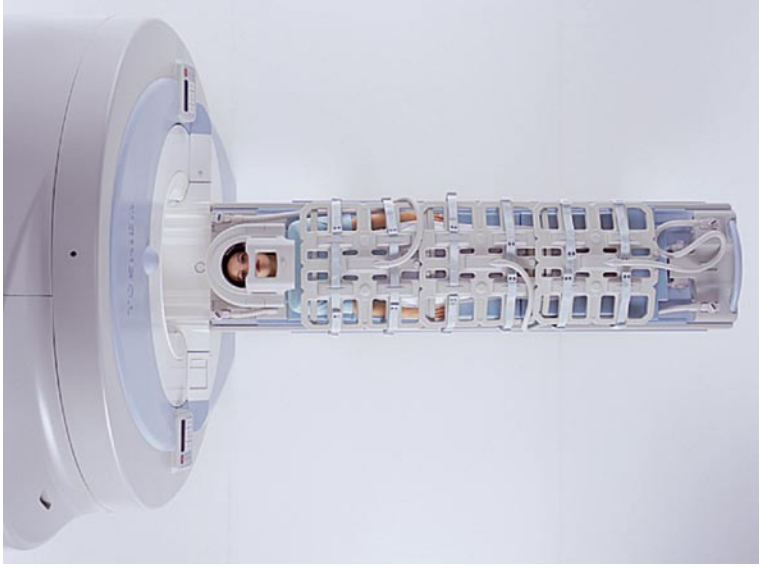

Fig. 2.5.10 Whole-body imaging with array coils covering the patient from head to toe (Exelart Vantage™, Toshiba). Since not all coils are in the imaging volume of the MR system at the same time, a lower number of receiver channels (here: 32) are sufficient for signal reception

are sorted in such a way that images are formed from data with similar physiologic signals (e.g., diastolic measurements).

The advantage of the retrospective over the prospective data acquisition is the continuous measurement without gaps that could lead to artifacts in steady state pulse sequences. The post-processing effort of retrospectively acquired data is higher because data need to be analyzed and sorted before image reconstruction. Additionally, on average more data need to be acquired as compared to prospective triggering to ensure that for each physiologic condition at least one data set is present (over-sampling).

2.5.6.1 Electrocardiogram

To measure the ECG in the MR system MR-compatible electrodes made of silver–silver chloride (Ag/AgCl) are used. The measurement of the ECG in an MR system is difficult, because the switching of the gradients can induce voltages in the ECG cables that completely mask the ECG signal. This effect can be minimized, if short and loopless ECG cables are utilized. Short ECG cables are additionally advantageous since long cables with a loose contact to the skin can be the cause for patient burns that are induced by the interaction with the RF field during RF excitation (Kugel et al. 2003).

To reduce this potential danger to a minimum, ECG systems have been developed that amplify the ECG signal close to the electrodes, and which transmit the ECG signal to the MR system either via optical cables (Felblinger et al. 1994) or as an RF signal at a frequency different from the Larmor frequency. With this technology, ECG signals can be acquired even during echo planar imaging when gradients are permanently switched on and off (Ives et al. 1993).

It should be noted that the ECG signal in the MR system significantly differs from the signal outside the magnet.

The electrically conducting blood is flowing at different velocities in the cardiac cycle. Within the magnetic field the blood flow induces velocity-dependent electric fields (Hall effect) across the blood vessels, which in turn change the electric potentials measured at the ECG electrodes. Typically, the T wave of the ECG is augmented, an effect that is more pronounced at higher field strengths (Kangarlu and Robitaille 2000). For this reason, the ECG acquired in the MR system should not be regarded as of diagnostic quality.

2.5.6.2 Pulse Oximetry

Pulse oximeters measure the absorption of a red and an infrared light beam that is sent through perfused tissue (e.g., a finger). The absorption is proportional to the oxygen content, so that devices can determine the partial oxygen pressure (pO_2). Additionally, the pulsation of the blood leads to a pulse-related variation of the transmitted light signal, which is used in the MR systems to derive a pulse-related trigger signal (Shellock et al. 1992). Since the pulse wave arrives at the periphery with a significant delay after the onset of systole, it is difficult to use the pO_2 signal for triggering in systolic MR imaging. Pulse oximeters consist solely of non-magnetic and non-conduction optical elements, so that they are not susceptible to any interference with the gradient or RF activity.

2.5.6.3 Breathing Synchronization

To detect breathing motion, several mechanical devices such as breathing belts or cushions have been introduced. Essentially, all these systems are air filled and change their internal pressure as a function of the breathing cycle when they are attached to the thorax of the patient. The pressure is continuously monitored and is used as an indicator for breathing status. As with the pulse oximeters, these systems are also free of any electrically conducting elements, so that no RF heating is expected. However, in clinical practice breathing triggering can pose a problem in long-lasting acquisitions since patients start to relax over time, and the initial breathing pattern is not reproduced.

An alternative approach to the measurement of the breathing cycle is offered by the MR itself: If a single image line is excited in head–foot direction through the thorax (using, e.g., a 90° and 180° slice that intersect along the desired line), then the signal of this line has high contrast at the liver–lung interface. This diaphragm position can be detected automatically and can be used to extract the relative position in the breathing cycle. This technique is called a navigator echo (Ehman and Felmlee 1989), since an additional echo for navigation needs to be inserted into the pulse sequence. Similar approaches using low-resolution two- or three-dimensional imaging can be used to correct for patient motion in long-lasting image acquisitions such as fMRI (Welch et al. 2002). Here, the change in position is determined and used to realign the imaging slices (prospective motion correction).

2.5.6.4 Electroencephalogram

For neurofunctional studies, electroencephalogram (EEG) systems have been developed that can be operated in the MR tomography (Muri et al. 1998). Compared with the ECG, the voltages induced during brain activity are about 100 times smaller in EEG recording, which poses a significant detection problem (Goldman et al. 2000; Sijbersa et al. 2000). Blood pulsation, patient motion, as well as induced voltages during gradient and RF activity can cause spurious signals in the EEG leads, which obscure the true EEG signal. To remove the imaging-related artifacts, dynamic filtering can be used, which removes all signal contributions associated with the basic frequencies of the MR system.

2.5.7 Summary

A large variety of MR systems with different magnet types, coil configurations, and gradient sets is currently available for diagnostic and interventional MR imaging. To choose from these systems, the desired imaging applications as well as economic factors need to be considered: A small hospital might with few MR patients might want to use a low-field permanent magnet system with low maintenance cost, whereas a university hospital with a diverse patient clientele and high patient throughput should better offer a high-field MR system with state-of-the-art gradient systems.

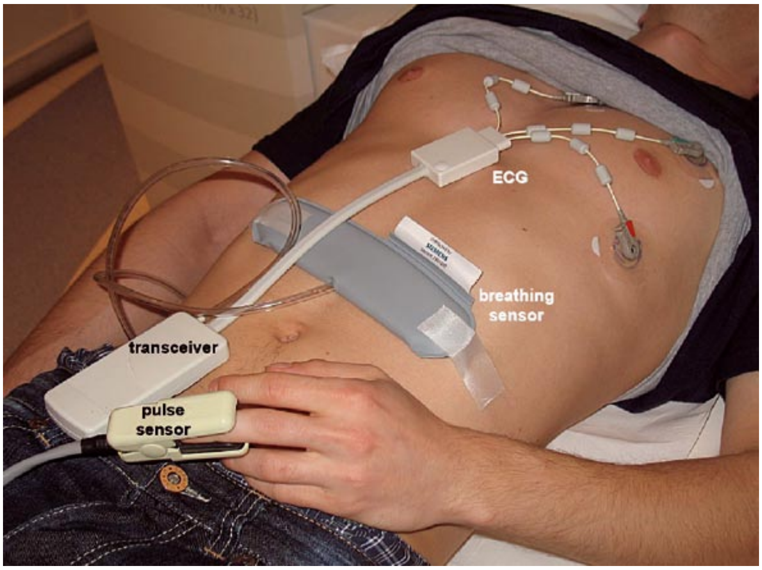

Fig. 2.5.11 Physiologic monitoring and triggering units. The three electrodes of the ECG system as well as the tube of the breathing sensor are connected with a transceiver that transmits both signals to the patient monitoring unit of the MR system. The optical pulse sensor is attached to the finger, and the signals are guided via optical fibers to the detection unit. For increased patient safety the ECG system must be used together with a holder system (not shown here), which provides additional distance between the ECG leads and the patient body

References

1. Chen CN, Hoult DI (1989) Biomedical magnetic resonance technology. Adam Hilger, Bristol
2. Dumoulin CL, Souza SP, Darrow RD (1993) Real-time position monitoring of invasive devices using magnetic resonance. Magn Reson Med 29:411–415
3. Ehman RL, Felmlee JP (1989) Adaptive technique for high-definition MR imaging of moving structures. Radiology 173:255–263
4. Felblinger J, Lehmann C, Boesch C (1994) Electrocardiogram acquisition during MR examinations for patient monitoring and sequence triggering. Magn Reson Med 32:523–529
5. Goldman RI, Stern JM, Engel J Jr, Cohen MS (2000) Acquiring simultaneous EEG and functional MRI. Clin Neurophysiol 111:1974–1980
6. Harvey PR (1999) The modular (twin) gradient coil—high resolution, high contrast, diffusion weighted EPI at 1.0 Tesla. MAGMA 8:43–47
7. Harvey PR, Mansfield P (1994) Resonant trapezoidal gradient generation for use in echo planar imaging. Magn Reson Imaging 12:93–100
8. Ives JR, Warach S, Schmitt F, Edelman RR, Schomer DL (1993) Monitoring the patient's EEG during echo planar MRI. Electroencephalogr Clin Neurophysiol 87:417–420
9. Jin J (1999) Electromagnetic analysis and design in magnetic resonance imaging. CRC Press, Boca Raton
10. Kangarlu A, Robitaille PML (2000) Biological effects and health implications in magnetic resonance imaging. Concepts Magn Reson 12:321–359
11. Kugel H, Bremer C, Puschel M, Fischbach R, Lenzen H, Tombach B, Van Aken H, Heindel W (2003) Hazardous situation in the MR bore: induction in ECG leads causes fire. Eur Radiol 13:690–694
12. Liu F, Zhao H, Crozier S (2003) On the induced electric field gradients in the human body for magnetic stimulation by gradient coils in MRI. IEEE Trans Biomed Eng 50:804–15
13. Mansfield P, Chapman B (1986) Active magnetic screening of coils for static and time-dependent magnetic field generated in NMR imaging. J Phys E: Sci Instrum 19:540–545
14. Mansfield P, Harvey PR (1993) Limits to neural stimulation in echo planar imaging. Magn Reson Med 29:746–758
15. Mispelter J, Lupu M, Briguet A (2006) NMR probeheads for biophysical and biomedical experiments: theoretical principles and practical guidelines. World Scientific, London
16. Muri RM, Felblinger J, Rosler KM, Jung B, Hess CW, Boesch C (1998) Recording of electrical brain activity in a magnetic resonance environment: distorting effects of the static magnetic field. Magn Reson Med 39:18–22
17. Oppelt A (ed) (2005) Imaging systems for medical diagnostics: fundamentals, technical solutions and applications for systems applying ionizing radiation, nuclear magnetic resonance and ultrasound, 2nd edn. Publicis, New York
18. Pruessmann KP, Weiger M, Scheidegger MB, Boesiger P (1999) SENSE: sensitivity encoding for fast MRI. Magn Reson Med 42:952–962
19. Robitaille PM, Warner R, Jagadeesh J, Abduljalil AM, Kangarlu A, Burgess RE, Yu Y, Yang L, Zhu H, Jiang Z, Bailey RE, Chung W, Somawiharja Y, Feynan P, Rayner DL (1999) Design and assembly of an 8 Tesla whole-body MR scanner. J Comput Assist Tomogr 23:808–820
20. Roemer PB, Edelstein WA, Hayes CE, Souza SP, Mueller OM (1990) The NMR phased array. Magn Reson Med 16:192–225
21. Schaefer DJ (1998) Safety aspects of switched gradient fields. Magn Reson Imaging Clin N Am 6:731–748
22. Schmitt F, Stehling MK, Turner R (1998) Echo planar imaging: theory, technique and application. Springer, Berlin Heidelberg New York
23. Shellock FG, Myers SM, Kimble KJ (1992) Monitoring heart rate and oxygen saturation with a fiber-optic pulse oximeter during MR imaging. AJR Am J Roentgenol 158:663–664
24. Sijbersa J, Van Audekerke J, Verhoye M, Van der Linden A, Van Dyck D (2000) Reduction of ECG and gradient related artefacts in simultaneously recorded human EEG/MRI data. Magn Reson Imaging 18:881–886
25. Sodickson DK, Manning WJ (1997) Simultaneous acquisition of spatial harmonics (SMASH): Fast imaging with radiofrequency coil arrays. Magn Reson Med 38:591–603
26. Turner R (1993) Gradient coil design: a review of methods. Magn Reson Imaging 11:903–920
27. Vlaardingerbroek MT, den Boer JA, Luiten A (2002) Magnetic resonance imaging: theory and practice, 2nd rev. edn. Springer, Berlin Heidelberg New York
28. Webb P, Macovski A (1991) Rapid, fully automatic, arbitrary-volume in vivo shimming. Magn Reson Med 20:113–122
29. Welch EB, Manduca A, Grimm RC, Ward HA, Jack CR Jr (2002) Spherical navigator echoes for full 3D rigid body motion measurement in MRI. Magn Reson Med 47:32–41

2.6 Contrast Agents

A. Huppertz and C.J. Zech

During the pioneer period of MR imaging, expectations were that the high inherent contrast in MR imaging makes the use of contrast agents superfluous. However, increasing use of the modality in the clinical setting has revealed that a number of diagnostic questions require the application of a contrast agent. Similar to other imaging modalities, the use of contrast agents in MR imaging aims at increasing sensitivity and specificity and, thereby, the diagnostic accuracy.

2.6.1 Physicochemical Properties of MR Contrast Agents

The main contrast parameters in MR imaging are proton density, relaxation times, and magnetic susceptibility (ability of a material or substance to become magnetized by an external magnetic field). MR imaging contrast agents focus upon relaxation time and susceptibility changes. Most of them are either para- or superparamagnetic. The most efficient elements for use as MR imaging contrast agents are gadolinium (Gd), manganese (Mn), dysprosium (Dy), and iron (Fe).

The magnetic field produced by an electron is much stronger than that produced by a proton. However, in most substances the electrons are paired, resulting in a weak net magnetic field. Gd with its seven unpaired electrons possesses the highest ability to alter the relaxation time of adjacent protons (relaxivity).

For MR contrast agents, differentiation between *positive* and *negative* agents has to be made. Paramagnetic contrast agents Gd and Mn have a similar effect on T_1 and T_2 and are classified as positive agents. Since the T_1 of tissues is much higher than the T_2, the predominant effect of these contrast agents at low concentrations is that of T_1 shortening. Thus, tissues that take up Gd- or Mn-based agents become bright in T_1-weighted sequences.

On the other hand, negative-contrast agents influence signal intensity by shortening T_2 and T_2*. Superparamagnetic agents belong to this group and produce local magnetic field inhomogeneities of the local magnetic field. T_2 is reduced due to the diffusion of water through these field gradients. Magnetite, Fe_3O_4, is such a paramagnetic particle. Coated with inert material (e.g., dextranes, starch), it can be used for oral or intravenous applications.

In addition to the classification in positive or negative agents, MR contrast agents can be differentiated according to their target tissue. The targeting of an agent is determined by the pharmaceutical profile of the substance. In the clinical environment, we differentiate currently three classes of agents:

- Unspecific extracellular fluid space agents
- Blood-pool and intravascular agents
- Targeted and organ-specific agents

Unspecific extracellular fluid space agents. Low-molecular-weight paramagnetic contrast agents distribute into the intravascular and extracellular fluid space (ECF) of the body. Their contrast effect is caused by the central metal ion. All approved ECF agents contain a Gd ion, which contains seven unpaired electrons. Because Gd itself is toxic, the ion is bound in highly stable complexes. The different complexes and the physicochemical properties of all clinically used agents are listed in Table 2.6.1. The agents are not metabolized and are excreted in unchanged form via the kidneys. Bound, they form low-molecular-weight, water-soluble contrast agents. Gadopentetate dimeglumine (Magnevist, Bayer Schering Pharma, Berlin, Germany) and gadoterate meglumine (Dotarem, Laboratoires Guerbet, Aulnay-Sous-Bois, France) are ionic high-osmolality agents, whereas gadodiamide (Omniscan, GE Healthcare, Buckinghamshire, UK) and gadoteriol (ProHance, Bracco Imaging, Milan, Italy) are non-ionic low-osmolality agents. Due to the low total amount of contrast agent usually applied in MR imaging, no difference in tolerance between both classes could be demonstrated (Oudkerk et al. 1995; Shellock 1999). An estimated 50% of ECF agents (as for example in gadopentetate dimeglumine, size 590 Da) is cleared from the vascular space into the extravascular compartment on the initial passage through the capillaries.

Two agents in the group of ECF agents have to be mentioned separately. Gadopentate dimeglumine (MultiHance, Bracco Imaging) is an agent with a weak protein binding (about 10%) in human plasma. The bound fraction of the agent has a higher relaxivity than does the unbound fraction. In sum, the relaxivity of gadopentate dimeglumine is 50% higher as compared with gadopentetate dimeglumine at 1.5 T/37°C in plasma. The effect of higher relaxivity is highest at low field strengths (Table 2.6.1). The concentration of the contrast agent is 0.5 mol/l. Gadopentate dimeglumine was primarily developed as a liver-specific MR imaging agent, and is currently approved both in the indication detection of focal liver lesions and in MR angiography. Most of the injected dose of gadopentate is excreted unchanged in urine within 24 h, although a fraction corresponding to 0.6–4.0% of the injected dose is eliminated through the bile and recovered in the feces (Spinazzi et al. 1999). The second particular ECF agent, gadobutrol (Gadovist, Bayer Schering Pharma) is approved in a higher concentration (1 M) than all other available MR imaging contrast agents. In addition, gadobutrol has a higher relaxivity than most extracellular 0.5 M contrast agents on the market (Table 2.6.1). The higher concentration has revealed to be particularly useful for MR perfusion studies and MR angiography (Tombach et al. 2003).

Table 2.6.1 Physicochemical properties of Gd-based MR ECF contrast media

INN code	Gadopentetate dimeglumine	Gadodiamide	Gadoterate meglumine	Gadoteriol	Gadobutrol	Gadopentate dimeglumine
Tradename	Magnevist®	Omniscan™	Dotarem	Prohance™	Gadovist®	Multihance™
Manufacturer	Bayer Schering Pharma AG, Germany	GE Bioscience Healthcare, UK	Laboratoires Guerbet, France	Bracco Imaging, Milan, Italy	Bayer Schering Pharma AG, Germany	Bracco, Italy
Concentration (mol/l)	0.5	0.5	0.5	0.5	1	0.5
Osmolality (mOsmol/kg H_2O at 37°C)	1,960	780	1,350	630	1,603	1,970
Viscosity (mPA s at 37°C)	2.9	1.9	2.0	1.3	4.96	5.30
Relaxivity r_1 in plasma 40°C (l/mmol^{-1}s^{-1} at 0.47 T)	3.8 ± 0.2	4.4 ± 0.3	4.3 ± 0.2	4.8 ± 0.3	6.1 ± 0.4	9.2 ± 0.6
Relaxivity r_1 in plasma at 37°C (l/mmol^{-1}s^{-1} at 1.5 T)	4.1 ± 0.3	4.3 ± 0.3	3.6 ± 0.2	4.1 ± 0.3	5.2 ± 0.3	6.3 ± 0.4
Relaxivity r_1 in plasma at 37°C (l/mmol^{-1}s^{-1} at 3 T)	3.7 ± 0.2	4.0 ± 0.2	3.5 ± 0.2	3.7 ± 0.2	5.0 ± 0.3	5.5 ± 0.3

Blood-pool and intravascular agents. Blood-pool agents stay within the intravascular space with no or only slow physiologic extravasation. The agents can be used for first-pass imaging and delayed blood-pool phase imaging. The prolonged imaging window allows more favorable image resolution and signal-to-noise ratio. The absence of early extravasation also improves the contrast-to-noise ratio. The pharmacokinetic properties of blood-pool agents are expected to be well suited to MR angiography and coronary angiography, perfusion imaging, and permeability imaging (detection of ischemia and tumor grading).

Currently, three types of blood-pool agents are being developed:

1 Gd compounds with a strong but reversible affinity to human proteins such as albumin
2 Macromolecular-bound Gd complexes
3 Ultra small or very small super-paramagnetic particles of iron oxide (USPIO and VSOP)

There are important differences between the three groups regarding pharmacokinetics in the body, i.e., distribution and elimination.

Gd compounds with a strong but reversible affinity to human proteins such as albumin exhibit prolonged plasma elimination half-life and increased relaxivity. The elimination is done by glomerular filtration of its unbound fraction. Given that there is equilibrium between the bound and unbound fraction in the presence of albumin, the excreted molecules are immediately substituted due to dissociation of agent from the agent–albumin complex. Two agents with affinities to albumin were developed and tested in clinical trials: gadofosveset (Vasovist®, Bayer Schering Pharma) 80–96% bound in human plasma (Lauffer et al. 1998) and gadocoletic acid (B22956/1, Bracco Imaging), with a protein binding of approximately 95% in humans (Cavagna et al. 2002; La Noce et al. 2002).

Currently, gadofosveset is the only blood-pool agent approved (for MRA in Europe). All other contrast agents with blood-pool characteristics are in clinical or in earlier phase development. Gadofosveset is a stable Gd diethylenetriaminepentaacetic acid (Gd-DTPA) chelate substituted with a diphenylcyclohexylphosphate group. The mean plasma concentration at 1, 4 and 24 h after the bolus injection of 0.03 mmol/kg body weight dose were 56%, respectively 41% and 14% of the concentration reached 3 min after injection.

The mean half-life of the distribution phase ($t_{1/2\alpha}$) was 0.48 ± 0.11 h. Relative to the reported clearance values of the non–protein-bound MRI contrast agents, the clearance values of gadofosveset are markedly slower. Gadofosveset is provided in a concentration of 0.25 mol/l and a dose of 0.03 mmol/kg body weight is recommended for MRA (Perrault et al. 2003). As a further benefit, Gd compounds with a strong, but reversible affinity to human proteins provide a long-lasting blood-pool effect even when small amounts of the substance leak out of the vasculature. The blood-pool effect persists because albumin remains highly concentrated in plasma while it shows a two- to three-times lower concentration in the extravascular space. Thus, even when Vasovist® leaks from the vasculature, the receptor-induced magnetization enhancement (RIME) effect within the vascular spaces ensures that the signal enhancement in the blood dominates the MRI contrast. In rabbits, enhancement with gadofosveset persisted at relatively constant levels from two minutes to up to 1 h, whereas the enhancement of ECF had virtually disappeared within 60 min (Lauffer et al. 1998).

The second blood-pool agent with binding to human serum albumin, gadocoletic acid has been tested in coronary MRA (Paetsch et al. 2006). Compared with gadofosveset, the slightly higher percentage of bounded agent may result in a lower percentage of extravasation and a further decreased elimination period.

Macromolecular Gd-based blood-pool agents are large molecules with sizes between 30 and 90 kDa. They are eliminated rapidly by glomerular filtration. Due to their large size, they do not extravasate into the interstitial space. The two agents used in clinical trials were Gadomer (Schering) and P 792 (Laboratoires Guerbet, Aulnay-Sous-Bois). Gadomer contains multiple Gd molecules (24 Gd atoms, M_r 35,000). P792 is a monodisperse monogadolinated macromolecular compound with M_r 6.47 kDa, based on a gadoterate meglumine core (Port et al. 2001). Four hydrophilic arms account for its intravascular properties. In a preclinical study, P792 allowed acquisition of high-quality MR angiograms. Image quality was rated as superior for P792 in the post-bolus phase images compared with ECF agents. The intravascular properties lead to an excellent signal in the vasculature with limited background enhancement (Ruehm et al. 2002).

The first clinical use of USPIO was done in specific parenchymal organ imaging due to the incorporation of USPIO/SPIO into cells of the reticuloendothelial system of the liver, bone marrow, spleen, or lymphatic tissue. These particles produce a strong augmentation of the local magnetic field. Predominant shortening of T_2 and T_2* produces a loss of signal intensity on MR images. The agents that have been developed as blood-pool agents provide different characteristics with a predominating T_1 effect and a prolonged intravascular residence time due to the small size of the particles. NC 100150 (Clariscan, GE Healthcare) was the first USPIO tested for MRA (Taylor et al. 1999: Weishaupt et al. 2000). It is a strictly intravascular agent with an oxidized starch coating and has an approximate diameter of 20 nm. The half-life is 45–100 min, and it has shown to reduce blood T_1 to below 100 ms (Wagenseil 1999).

Another iron oxide particle MR contrast agent in the phase of clinical development is VSOP-C184 (Ferupharm, Teltow, Germany). It is classified as a VSOP with a core diameter of 4 nm and a total diameter of 8.6 nm. VSOP-C 184 is coated with citrate. The relaxivities in water at 0.94 T are (T_1) 20.1 and (T_2) 37.1 l/[mmol*s]. The plasma elimination half-life at 0.045 mmol Fe/kg was 21.3 ± 5.5 minutes in rats and 36.1 ± 4.2 minutes in pigs, resulting in a T_1 relaxation time of plasma of <100 ms for 30 min in pigs (Wagner et al. 2002).

Qualitative evaluation of image quality, contrast, and delineation of vessels showed that the results obtained with VSOP-C184 at doses of 0.025 and 0.035 mmol Fe/kg was similar to those of gadopentetate dimeglumine at 0.1 and 0.2 mmol Gd/kg. VSOP-C184 is suitable for first-pass MRA and thus, in addition to its blood-pool characteristics, allows for selective visualization of the arteries without interfering venous signal (Schorr et al. 2004).

Another USPIO is SH U 555 C (Supravist, Bayer Schering Pharma), an optimized formulation of carboxydextran-coated ferucarbotran (Resovist; Bayer Schering Pharma), which was formerly identified as SH U 555 A, with respect to T_1-weighted MR imaging. SH U 555 C has a mean core particle size of about 3–5 nm and a mean hydrodynamic diameter of about 20 nm in an aqueous environment. Relaxivity measurements yielded an r_1 of 22 s^{-1} $(mmol/l)^{-1}$ and an r_2 of 45 s^{-1} $(mmol/l)^{-1}$ at 40°C and 20 MHz in water (Reimer et al. 2004).

2.6.2 Dependency of Contrast Agents from the Magnetic Field Strength

The efficacy of MRI contrast agents is not just determined by their pharmacokinetic properties (distribution and time dependence of their concentration in the area of interest), but also by their magnetic properties, described by their T_1 and T_2 relaxivities. For all commercially available MRI contrast agents, relaxivities are published and listed in the respective package inserts. However, the most commonly used field strength for relaxation measurements (0.47 T) is different from the currently most frequently used field strength of clinical MRI instruments (1–3 T). Rohrer et al. evaluated in a well-conducted and standardized phantom measurement study the T_1 and T_2 relaxivities of all currently commercially available MR contrast agents in water and in blood plasma at 0.47, 1.5, 3, and 4.7 T, as well as in whole blood at 1.5 T (Rohrer et al. 2005). They quantified significant dependencies of relaxivities on the field strength and solvents (Table 2.6.2). Protein binding leads to both increased field strength and solvent dependencies and hence to significantly altered T_1 relaxivity values at higher magnetic field strengths.

2.6.3 Safety of MR Contrast Agents

MR contrast agents are in clinical use since 1988, and a wide experience is reported. Severe or acute reactions after single intravenous injection of Gd-based ECF agents are rare. In two large multiple-year surveys including, respectively, 21,000 and more than 9,000 examinations, an incidence of acute adverse reactions between 0.17 and 0.48% were reported (Li et al. 2006: Murphy et al. 1996). The severity of these adverse reactions was classified as mild (75–96%), moderate (2–20%), and severe (2–5%).

Typical nonallergic adverse reactions include nausea, headache, taste perversion, or vomiting, and typical reactions resembling allergy include hives, diffuse erythema, skin irritation, or respiratory symptoms. The incidence of severe anaphylactoid reaction is very low and was reported to be between 0.0003 and 0.01% in the literature (De Ridder et al. 2001; Li et al. 2006: Murphy et al. 1996). The reported life-threatening reactions resembling allergy were severe chest tightness, respiratory distress, and periorbital edema.

Known risk factors for the development of adverse reactions are prior adverse reactions to iodinated contrast media, prior reactions to a Gd-based contrast agent, asthma, and history of drug/food allergy.

Concerning liver-specific contrast media, a higher percentage of associated adverse reactions were reported for mangafodipir trisodium (7–17%) and ferumoxides (15%) (Runge 2000). The recently approved bolus-injectable agent ferucarbotran (Resovist, Bayer Schering Pharma) has proven a better tolerance profile during the clinical development compared to ferumoxides. Even bolus injections caused no cardiovascular side effects, lumbar back pain, or clinically relevant laboratory changes (Reimer and Balzer 2003). For the two approved Gd-based agents gadopentate dimeglumine and gadoxetic acid, far fewer patients have been examined to date. According to the results of the clinical trials conducted for the approval of both agents, they are comparable to Gd-based ECF agents in terms of safety (Bluemke et al. 2005; Halavaara et al. 2006; Huppertz et al. 2004). Post-marketing surveillance of gadopentate dimeglumine reporting approximately 100,000 doses revealed an overall adverse event incidence of <0.03%, with serious adverse eventss reported for <0.005% of patients (Kirchin et al. 2001).

In the class of blood-pool agents, only gadofosveset (Bayer Schering Pharma) has been approved recently in some European countries. The tolerance of the agent must be estimated based on the clinical trials. Based on these data, gadofosveset is well tolerated, and the incidence and profile of undesired side effects is very similar to ECF agents (Goyen et al. 2005; Petersein et al. 2000; Rapp et al. 2005).

Magnetic resonance contrast agents, particularly the Gd-based agents, are extremely safe (Niendorf et al. 1994) and lack in the usually applied diagnostic dosage the nephrotoxicity associated with iodinated contrast media. Nevertheless, health care personnel should be aware of the (extremely uncommon) potential for severe anaphylactoid reactions in association with the use of MR contrast media and be prepared should complications arise.

Nephrogenic systemic fibrosis (NSF) is a rare disease occurring in renal insufficiency that only has been described since 1997. In 2006, a first report about a potential relationship with intravenous administration of Gd-based MR contrast medium gadodiamide was published (US Food and Drug Administration 2007). NSF appears to occur in patients with kidney failure, along with high levels of acid in body fluids (a condition known as metabolic acidosis) that is common in patients with kidney failure. The disease is characterized by skin changes that mimic progressive systemic sclerosis with a predilection for peripheral extremity involvement that can extend to the torso. However, unlike scleroderma, NSF spares the face and lacks the serologic markers of scleroderma. NSF may also result in fibrosis, or scarring, of body organs. Diagnosis of NSF is done by looking at a sample of skin under a microscope.

The risk of NSF in patients with advanced renal insufficiency does not suggest being the same for all Gd-based contrast agents, because distinct physicochemical properties affect their stabilities and thus the release of free Gd ions (Bundesinstitut für Arzneimittel und Medizinprodukte [Federal Institute for Drugs and Medical Devices] 2007). Some Gd-based contrast media are more likely than are others to release free Gd^{3+} through a process called transmetallation, with endogenous ions from the body (Thomsen et al. 2006). These agents have the largest amount of excess chelate. Gadodiamide and gadoversetamide differ from other Gd-based contrast media because of an excess of chelate and is more likely to release free Gd^{3+} as compared with other agents. Cyclic molecules offer better protection and binding to Gd^{3+}, compared with linear molecules (Thomsen et al. 2006). The non-linear, non-ionic chelates gadodiamide and gadoversetamide seem to be associated with the highest risk of NSF (Broome et al. 2007; Sadowski et al. 2007).

The recommendations to prevent development of NSF are nonspecific (US Food and Drug Administration 2007):

- Gd-containing contrast agents, especially at high doses, should be used only if clearly necessary in patients with advanced kidney failure (those currently

Table 2.6.2 r_1 and r_2 relaxivities of MR contrast media in water and plasma at 37°C at 1.5 and 3 T

INN code	Trade name	Class	Water				Plasma			
			1.5 T		3 T		1.5 T		3 T	
			r_1	r_2	r_1	r_2	r_1	r_2	r_1	r_2
Gadopentetate dimeglumine	Magnevist	0.5 M ECF	3.3 ± 0.2	3.9 ± 1.1	3.1 ± 0.3	3.7 ± 0.3	4.1 ± 0.2	4.6 ± 0.8	3.7 ± 0.2	5.2 ± 0.9
Gadoteridol	Prohance		2.9 ± 0.2	3.2 ± 0.7	2.8 ± 0.2	3.4 ± 0.3	4.1 ± 0.4	5.0 ± 0.8	3.7 ± 0.2	5.7 ± 0.9
Gadoterate meglumine	Dotarem		2.9 ± 0.2	3.2 ± 0.7	2.8 ± 0.2	3.3 ± 0.3	3.6 ± 0.2	4.3 ± 0.9	3.5 ± 0.2	4.9 ± 0.9
Gadodiamide	Omniscan		3.3 ± 0.2	3.6 ± 0.6	3.2 ± 0.3	3.8 ± 0.3	4.3 ± 0.3	5.2 ± 1	4 ± 0.2	5.6 ± 0.9
Gadoversetamide	Optimark		3.8 ± 0.2	4.2 ± 0.7	3.6 ± 0.3	4.5 ± 0.3	4.7 ± 0.3	5.2 ± 0.9	4.5 ± 0.3	5.9 ± 0.9
Gadobutrol	Gadovist	1 M ECF	3.3 ± 0.2	3.9 ± 0.8	3.2 ± 0.3	3.9 ± 0.3	5.2 ± 0.3	6.1 ± 0.9	5 ± 0.3	7.1 ± 0.9
Gadopentate dimeglumine	Multihance	0.5 M, low protein binding	4.0 ± 0.2	4.3 ± 0.5	4.0 ± 0.3	4.7 ± 0.3	6.3 ± 0.3	8.7 ± 0.9	5.5 ± 0.3	11 ± 1
Gadoxetic acid	Primovist®		4.7 ± 0.2	5.1 ± 0.6	4.3 ± 0.3	5.5 ± 0.3	6.9 ± 0.4	8.7 ± 0.9	6.2 ± 0.3	11 ± 1
Gadofosveset	Vasovist	0.25 M, large-protein binding	5.2 ± 0.3	5.9 ± 0.6	5.3 ± 0.3	6.1 ± 0.4	19 ± 1	34 ± 2	9.9 ± 0.5	60 ± 4
Gadomer	NA	Macromolecular Gd	17.3 ± 0.9	22 ± 1	13 ± 0.7	23 ± 1	16 ± 1	19 ± 1	13 ± 1	25 ± 2
Ferumoxide	Endorem®	SPIO	4.7 ± 0.3	41 ± 2	4.1 ± 0.3	93 ± 6	4.5 ± 0.3	33 ± 2	2.7 ± 0.2	45 ± 3
Ferucarbotran	Supravist	USPIO	13.2 ± 0.7	44 ± 3	7.3 ± 0.4	57 ± 3	10.7 ± 0.6	38 ± 2	5.6 ± 0.3	95 ± 9

NA not applicable

requiring dialysis or with a glomerular filtration rate (GFR) = 15 ml/min or less).

- It may be prudent to institute prompt dialysis in patients with advanced kidney dysfunction who receive a Gd contrast MRA. Although there are no data to determine the utility of dialysis to prevent or treat NSF in patients with decreased kidney function.

2.6.4 Value of Contrast Agents in Clinical Practice

2.6.4.1 Contrast Agents in Neuroimaging

The use of contrast agents in neuroimaging is an accepted standard for the assessment of pathological processes, which utilizes the extravasation of contrast agents through a compromised blood–brain or blood–spinal cord barrier. Compared with contrast-enhanced CT, MR imaging with Gd-based contrast agents is far more sensitive and depicts even subtle disruptions of the blood–brain barrier that are caused by a variety of noxious agents as, for example neoplastic or inflammatory processes and ischemic stress. Moreover, MR contrast agents are increasingly used to evaluate brain perfusion in clinical practice for a variety of applications, including tumor characterization, stroke, and dementia. The contrast-enhanced brain perfusion MR examination is based on a magnetic susceptibility contrast phenomenon that occurs owing to the T_2 and T_2* relaxation effects of rapidly intravenous bolus–injected contrast agents.

The contrast agents in current use are the standard ECF Gd chelates (Table 2.6.1). These extracellular agents show no appreciable differences in their enhancement properties and biologic behavior (Akeson et al. 1995; Brugieres et al. 1994; Grossman et al. 2000; Oudkerk et al. 1995; Valk et al. 1993; Yuh et al. 1991). They equilibrate rapidly between the intra- and extracellular spaces of soft tissues and enter central nervous system lesions only at sites of damaged blood–brain barrier. The standard dose for MR imaging of the central nervous system is 0.1 mmol/kg body weight; however, it has been shown that a higher dose of Gd chelate–based contrast agents may help reveal more subtle disease states of the blood–brain barrier regardless whether caused by tumors or by inflammatory lesions (Bastianello et al. 1998; Haustein et al. 2003; Yuh et al. 1994). This raises the question, in how far Gd contrast agents with a higher concentration as for example gadobutrol or agents with a higher relaxivity as for example gadopentate dimeglumine help to increase the sensitivity and accuracy to detect lesions as compared to standard Gd chelates.

For gadobutrol, no comparative studies to standard Gd chelates exist up to now; however, based on smaller cohorts it can be assumed that the higher amount of Gd, which can be achieved by the higher Gd concentration, is of value for lesion detection and characterization (Vogl et al. 1995). Moreover, based on animal experiments the amount of Gd in gliomas was higher after injection of gadobutrol in comparison to gadopentetate dimeglumine although identical doses of Gd per kilogram body weight were injected for both contrast agents (Le Duc et al. 2004).

Gadopentate dimeglumine proved significantly superior tumor enhancement of intraaxial enhancing primary and secondary brain tumors at a dosage of 0.1 mmol/kg body weight as compared with the same dosage of gadopentetate dimeglumine (Knopp et al. 2004). Similar results were also obtained in comparison of gadopentate dimeglumine with other contrast agents as well as in special populations as for example in pediatric patients (Colismo et al. 2001, 2004, 2005). The increased contrast enhancement resulted also in an increased number of detected brain metastases.

Dynamic susceptibility-weighted (DSC) contrast agent-enhanced MR imaging is increasingly used for the assessment of cerebral perfusion in many different clinical settings, such as ischemic stroke (Parsons et al. 2001), neurovascular diseases (Doerfler et al. 2001), brain tumors (Essig et al. 2004), and neurodegenerative disorders (Bozzao et al. 2001). Unlike MR angiography, which depicts the blood flow within larger vessels, perfusion-weighted MR techniques are sensitive to perfusion on the level of the capillaries. The technique is based on the intravenous injection of a T_2*-relaxing contrast agent and subsequent bolus tracking using a fast susceptibility-weighted imaging sequence. After converting voxel signal into concentration values, parametric maps of regional cerebral blood volume (rCBV) and blood flow (rCBF) can be calculated by unfolding tissue concentration curves and the concentration curve of the feeding artery. The contrast agents used for dynamic susceptibility-weighted MR perfusion are usually standard Gd chelates; however, the dosages of Gd per kilogram of body weight as well as the value of higher concentrated agents have been widely discussed. During the first pass of the Gd chelate, the high intravascular concentration of Gd causes the T_2* effects, which can be measured by rapid imaging techniques. The length and the peak concentration of the bolus seem to have influence on the resulting measured signal with a highly concentrated small bolus of contrast agent being advantageous for MR brain perfusion imaging (Essig et al. 2002; Heiland et al. 2001). In between the standard Gd chelates, no notably different behavior of the available agents has been published up to now. The recommended dose for DSC perfusion MRI is in the range of 0.15–0.30 mmol/kg body weight, with most authors preferring a value of 0.2, because the volume of the bolus gets too high when higher dosages are applied (Bruening et al. 2000). Therefore, the use of higher concentrated contrast agents or agents with higher relaxivity are also interesting for cerebral perfusion MRI. Again, studies were able to demonstrate the value of the 1 M gabobutrol and gadopentate dimeglumine. Tombach et al. (2003) showed that 1 M gadobutrol resulted in a significantly improved quality of the perfusion examination in comparison to 0.5 M gadobutrol at the same dosage of 0.3 mmol/kg body weight. The results were explained by the sharper, more concentrated bolus, which could be achieved due to the smaller injection volume. Essig et al. directly compared 1 M gadobutrol and 0.5 M gadopentate dimeglumine at 1.5 T with a similar dosage of 0.1 mmol/kg body weight and found no significant differences between the two agents (Essig 2006). The benefit of a double dose of 0.2 mmol was observed only as a trend; however, it was not considered to be of clinical relevance. Similar results in a comparison between the two agents were recently obtained also on a 3-T system (Thilmann et al. 2005). For both agents sufficient high-quality perfusion examinations can be achieved with an acceptable injection volume, which is helpful for their clinical application in daily practice and can be considered superior to standard Gd chelates (Essig et al. 2004; Thiman et al. 2005; Tombach et al. 2003).

In a limited number of proof-of-concept studies, USPIO were also used in neuroimaging (Corot et al. 2004; Manniger et al. 2005). The long blood-circulating time and the progressive macrophage uptake in inflammatory tissues of USPIOs are two properties of major importance for pathologic tissue characterization.

In the human carotid artery USPIO, accumulation in activated macrophages induced a focal drop in signal intensity compared with unenhanced MRI. The USPIO signal alterations observed in ischemic areas of stroke patients is probably related to the visualization of inflammatory macrophage recruitment into human brain infarction, since animal experiments in such models demonstrated the internalization of USPIO into the macrophages localized in these areas. In brain tumors, USPIO particles that do not pass the ruptured blood–brain barrier at early times post injection can be used to assess tumoral microvascular heterogeneity. Twenty-four hours after injection, when the cellular phase of USPIO takes place, the USPIO tumoral contrast enhancement was higher in high-grade than in low-grade tumors. Several experimental studies and a pilot multiple sclerosis clinical trial in 10 patients have shown that USPIO contrast agents can reveal the presence of inflammatory lesions related to multiple sclerosis. The enhancement with USPIO does not completely overlap with the Gd-chelate enhancement.

2.6.4.2 Contrast Agents in MR Angiography

During the last few years magnetic resonance angiography (MRA) has been established as a non-invasive alternative to conventional X-ray angiography in the diagnosis of arteriosclerotic and other vascular diseases (Meany et al. 1997; Meany 1999). With the exception of imaging intracerebral vessels (Gibbs et al. 2005; Ozsarlak et al. 2004), contrast-enhanced techniques have revealed superiority over non–contrast-enhanced techniques as the time-of-flight (TOF-MRA) or phase-contrast (PC MRA) technique (Sharafuddin et al. 2002). The main advantages over unenhanced techniques are the possibilities to acquire larger volumes, allowing, e.g., demonstration of the carotid artery from its origin to the intracranial portion, shorter acquisition times, and reduced sensibility to flow artifacts.

Contrast-enhanced MR angiography can be performed during the first-pass of a contrast agent, preferably in breath-hold technique, after rapid bolus injection or during steady-state conditions after injection of vascular specific blood-pool agents.

Most experiences were reported for first-pass MRA after injection of ECF contrast agents. The demands on the agent are a high influence on the signal intensity on blood after injection and the possibility of fast and compact bolus injection. The most commonly applied group of contrast agents are 0.5 molar ECF.

In the last years, two novel ECF agents with innovative properties were used for MRA. The first one, the 0.5 M contrast agent gadopentate dimeglumine offers a higher T_1 relaxivity. In studies in which gadopentate dimeglumine is compared at equal dose with other Gd-based MR contrast agents without relevant protein binding in plasma, gadopentate dimeglumine has consistently shown significantly better quantitative and qualitative performance (Goyen and Debatin 2003). Even at lower doses compared with gadopentetate dimeglumine injected at a dose of 0.2 mmol/kg body weight, the greater relaxivity of gadopentate dimeglumine provides higher intravascular signal and signal-to-noise ratio (Pediconi et al. 2003). Thus, gadopentate dimeglumine can be considered to have a very favorable risk–benefit ratio for MRA.

The second one, gadobutrol is available in 1 M concentration. In combination with a higher relaxivity compared to other ECF agents, the agent has revealed in quantitative evaluations a significant increase in signal-to-noise and contrast-to-noise ratios in comparison to gadopentetate dimeglumine in pelvic MRA and in whole body MRA (Goyen et al. 2001, 2003). Better delineation of arterial morphology was reported especially for small vessels, but no statistically significant difference in image quality could be seen. Two different options for injection have been described: reduction of the injection rate by 50% compared to injection protocols using 0.5 M ECF (equimolar dosing) or reduction of the injection time by 50%. The equimolar dosing mainly exploits the higher relaxivity potential of gadobutrol. In this case, the injection duration is identical to a corresponding protocol using a 0.5M contrast agent a similar bolus geometry, and contrast delivery in the ROI is obtained (e.g., in a 70-kg-weighing patient 7 ml of gadobutrol are injected at 1 ml/s compared with 14 ml of gadopentetate dimeglumine injected at 2 ml/s). Hence, well-known protocols can be adopted with good results. The second option keeps the injection speed unchanged in comparison to the 0.5 M agent protocol, resulting in shortening of the initial bolus duration by a factor of two (Fink et al. 2004). The philosophy is to use a very compact, high-relaxivity bolus and to fully exploit the potential of 1 M gadobutrol. This approach is particularly recommended in conjunction with very fast acquisition techniques, e.g., time-resolved (often referred to as 4D) MRA. Although the effective bolus geometry in the respective ROI is broadened, dependent on individual physiology and mainly influenced by the lung passage, this approach requires higher demands on precise bolus timing and is recommended to users with advanced MRA experience and ultrafast imaging equipment.

In addition, a further approach was reported by reducing the amount of contrast agent by a factor of two in abdominal MRA (Vosshenrich et al. 2003). The injection speed was kept constant in comparison to a 0.5 M agent protocol, resulting in very short total bolus duration. Vosshenrich et al. used an amount of 0.1 mmol/kg body weight. They compared the examinations qualitatively and quantitatively to exams acquired after injection of gadopentetate dimeglumine (0.2 mmol/kg), and concluded that for MRA of the hepatic arteries and the portal veins, gadobutrol can be used at half the dosage as recommended for a standard 0.5 M contrast agent.

The concept of contrast-enhanced MRA based on ECF agents has some limitations. The primary problem is the rapid extravasation of the contrast agents limiting acquisition time and therefore spatial resolution as well as contrast-to-noise-ratio. To improve spatial resolution it is necessary to prolong imaging time. Intravascular contrast agents are able to overcome the restrictions of spatial resolution. The longer acquisition period can be used to decrease voxel size, to repeat measurements, or to trigger acquisitions by ECG and/or respiratory gating. The second limitation of currently used MRA is the quantification of artery stenoses, which still seems to be inferior to invasive catheter angiography. The cause is the inferior spatial resolution in MRA using ECF agents, with which the increase of spatial resolution is limited by the acquisition time during first-pass (arterial phase). With intravascular contrast agents, a longer data acquisition during the distribution phase is possible. The spatial resolution can be increased on a similar level compared with catheter angiography and, therefore, the accuracy of stenosis quantification is significantly increased.

Optimally, a blood-pool agent permits a long acquisition window including first-pass MRA as well as the possibility of separate imaging of arteries and veins by timing the injection and data acquisition. Gadofosveset, the first MR blood-pool agent approved for clinical use, permits both a high-resolution approach with a long acquisition windows and first-pass contrast-enhanced MRA (Fig. 2.6.1). The approval was based on the data of clinical trials in all different types of arterial vessels including high-flow vessels with large diameter (e.g., the pelvic arteries), low-flow vessels (e.g., foot arteries), and high-flow vessels with a small diameter (e.g., the renal arteries).

2.6.4.3 Contrast Agents for Soft-Tissue Lesions

ECF contrast agents are widely used in MR imaging of soft-tissue lesions. The enhancement in either inflammatory or neoplastic lesions makes their use inevitable for the detection and characterization of soft tissue lesions.

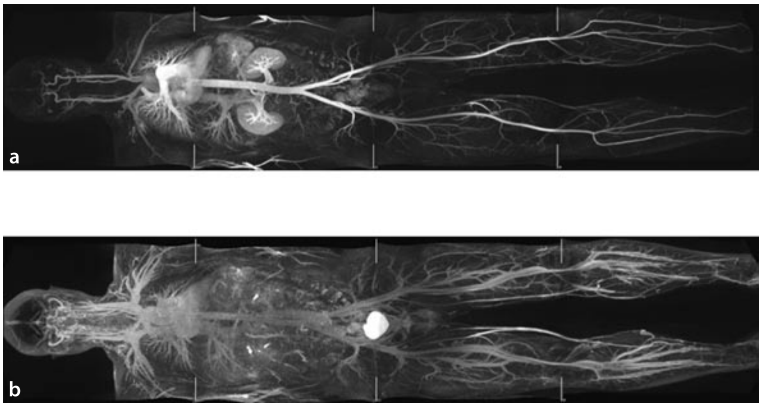

Fig. 2.6.1 Whole-body MRA of a healthy volunteer after bolus injection of gadofosveset (0.025 mmol/kg body weight). First-pass and steady-state acquisition acquired immediately (**a**) and 10 min (**b**) after injection of the contrast agent. T_1-weighted 3D gradient recalled echo sequence ($T_R/T_E/\alpha$ 3.1/1.1/25, spatial resolution 1.6 × 1 × 1.5 mm). First-pass imaging depicts exclusively the arteries. Steady-state imaging shows an enhancement of both arteries and veins. Due to the higher concentration of the contrast agent during first-pass imaging the absolute level of enhancement is higher (**a**)

Relevant anatomical sites that in the daily clinical practice are subject to MR imaging are the female breast and the soft tissue related to the musculoskeletal system.

For the female breast, MR imaging with extracellular contrast agents (MR mammography) is nowadays widely used for the detection and for the characterization of unclear breast tumors Morris et al. 2002). The histopathological basis of the different enhancement patterns in breast masses is not yet fully understood; however, it is well known that angiogenesis with the formation of new vessels, is an important aspect (Knopp et al. 1999). The amount of angiogenesis and contrast agent extravasation is considered different for several benign and malignant lesions; however, the visible phenomenon of different enhancement is usually too small to be analyzed only visually. The discrete changes of contrast-agent enhancement are usually evaluated by using a semiquantitative evaluation with region-of-interest measurements at different time-points (Kuhl et al. 2005). The thereby achieved enhancement kinetics, as represented by the time–signal intensity curves, differ significantly for benign and malignant enhancing lesions, and are used as an aid in differential diagnosis. Usually four to six measurements with an interval of 1–2 min are applied in the daily clinical practice (Kuhl et al. 1999; Pediconi et al. 2005). A recently published study showed that the temporal resolution for the assessment of time–signal intensity curves is not as critical as the spatial resolution; therefore, the recommendations for the dynamic postcontrast MR imaging tend toward a 2-min interval with a high spatial resolution (e.g., full 512 imaging matrix) (Kuhl et al. 2005). A more detailed evaluation of perfusion parameters needs, however, a very high temporal resolution in a range of 3–5 s. First results for the differentiation of unclear breast tumors in an investigational setting are very promising; however, due to the high temporal resolution only single slices can be measured, which is not feasible for daily practice (Brix et al. 2004). Usually standard Gd chelates at a dose of 0.1 mmol/ kg body weight are used for contrast-enhanced MR mammography. First results indicate that the use of the high-relaxivity MR contrast agent gadopentate dimeglumine in the same dosage can achieve a superior detection and identification of malignant breast lesions at MR imaging as compared with gadopentetate dimeglumine. However, up to now gadopentate dimeglumine is not officially approved for this indication.

There are also first approaches to perform MR mammography with blood-pool contrast agents. A major limitation of ECF is that they extravasate nonselectively from the vasculature into the interstitium of both normal and pathological tissues in the breast. It is hypothesized that the degree of microvascular endothelial disruption inherent to cancer vessels with the resulting extravasation of macromolecular contrast agents may predict tumor aggressiveness and tumor grade more accurately that with standard Gd chelates (Daldrup-Link and Brasch 2003; Daldrup-Link et al. 2003). First results with USPIO have shown an improved characterization of unclear breast tumors at the expense of tumor enhancement, which is important for tumor detection. An interesting approach is also the use of small molecular Gd chelates, which bind reversibly to plasma proteins as for example gadofosveset. This might allow for a sensitivity and specificity due to the presence of small and large molecules (Daldrup-Link et al. 2003). The assessment of microvascular changes in experimental breast tumors seem not to be reliably depicted with theses agents in contrast to the macromolecular albumin-Gd-(DTPA)30 (Daldrup-Link et al. 2003; Turetscheck et al. 2001). However, clinical experience on breast tumors does not exist now. Although potential diagnostic applications have been investigated with various sized albumin-Gd-DTPA, this contrast agent is considered a poor candidate for development as a clinical drug due to slow and incomplete elimination and a potentially immunologic toxicity (Daldrup-Link and Brasch 2003).

For soft-tissue or bone lesions in the musculoskeletal system, the application of extracellular Gd-contrast agents has become a clinical standard for characterization, staging of the local extent, biopsy planning, and the therapy monitoring (Verstraete and Lang 2000). The basic principle of contrast-enhanced imaging is as described above the distribution of the Gd chelates in the intravascular space, showing enhancement in tumors with dense vascularity and neoangiogenesis as well as distribution into the extracellular space. For these clinical standard applications, there seem to be no relevant differences in the diagnostic performance between the different extracellular Gd chelates, similar to neuroimaging.

The role of Gd-enhanced MRI for exact tissue characterization is still very limited. A differential diagnosis in between different sarcomas, nerve sheath tumors, or other mesenchymal tumors is not possible based on the contrast agent behavior up to know. The differentiation between benign and malignant tumors is also often very limited, even with tools like dynamic time-resolved contrast-enhanced MRI (Verstraete and Lange 2000). Nevertheless, surrogate parameters for angiogenesis like histological tumor-vessel density can be correlated with this method (van Dijke et al. 1996). One major limitation is the extravasation of standard Gd chelates through the intact endothelium so that pathological extravasation in tumor vessels disrupted endothelium cannot be separated from the physiological distribution. Therefore, the experimental studies mainly focus on contrast agents which show no or only minor physiological extravasation. Different studies—mainly in the animal-experimental stage—were able to show that characterization in benign and malignant tumors, evaluation of angiogenesis, and even tumor grading is feasible with blood-pool contrast agents (Daldrup et al. 1998; Kobayashi et al. 2001; Preda et al. 2004a, b). There have been promising results with albumin-Gd-(DTPA); however, as mentioned above this agent is unlikely to be available for diagnostic use in humans (Daldrup et al. 1998; Daldrup-Link and Brasch 2003). Similar to breast tumors, USPIO have also been utilized for the evaluation of perfusion and for the characterization of soft-tissue tumors in the past (Bentzen et al. 2005).

2.6.4.4 Hepatobiliary Imaging

The basic group of contrast agents for hepatobiliary imaging is the group of ECF Gd-based contrast agents. However, there are also tissue-specific contrast agents available, which allow for an increased detection and characterization of focal and diffuse liver disease.

Liver-specific contrast agents can be divided into two groups: On the one hand, there are iron-oxide particles (SPIO, or superparamagnetic particles of iron oxide), which are targeted to the reticuloendothelial system (RES) to the so-called Kupffer cells. These agents cause a signal decrease in T_2/T_2*-weighted sequences by inducing local inhomogeneities of the magnetic field. On the other hand, there is the group of hepatobiliary contrast agents, which are targeted directly to the hepatocyte and are excreted via the bile. These agents cause signal increase in T_1-weigthed sequences by shortening of the T_1 relaxation time. In Europe there are five different liver specific contrast agents available on the market (Table 2.6.3).

The basic principle behind SPIO is the fact, that there are usually no Kupffer cells in malignant liver tumors, in contrast to the normal liver parenchyma and to solid benign liver lesions. Therefore, in the liver specific phase, which starts for ferucarbotran after about ten min and for ferumoxide after about 30 min, high contrast is produced in between malignant liver lesions and normal liver parenchyma. Due to the signal loss in normal liver parenchyma the malignant lesions are contrasted as hyperintense lesions in T_2*-weighted and T_2-weighted sequences against the dark liver parenchyma. The first SPIO on the market in Europe has been ferumoxide (Endorem®, Guerbet, Aulnay Sous Bois, France). Since 2001 in most European countries and in Asia the bolus-injectable ferucarbotran (Resovist®, Bayer Schering Pharma AG, Berlin, Germany) is available. With regard to the basic principle of imaging there is no difference between the two agents; however, direct comparative studies have not been performed so far. The most striking advantage of ferucarbotran is the better workflow due to the possibility to inject ferucarbotran as a bolus. Bolus-applicability is possible for ferucarbotran due to the different particle sizes and the coating of the particles; this is also responsible for the fewer rate of side effects (especially fewer events of severe back pain), which are encountered with ferucarbotran.

In earlier clinical trials the effects of SPIO particles were evaluated almost exclusively on T_2-weighted FSE and T_2^*-weighted GRE sequences, whereas usually not much attention was paid to the T_1-effects. However, the effect of SPIO particles on proton relaxation is not confined to T_2 and T_2^*. They also influence T_1 relaxivity with increased signal intensity on T_1-weighted GRE sequences at low concentrations (Chambon et al. 1993). This gave raise to the hope, that with the bolus-injectable ferucarbotran vascularity of focal liver lesions could be depicted; however, investigations have been shown, that the ferucarbotran-enhanced early dynamic examination with T_1-weighted sequences does not permit to evaluate lesion vascularity, since (with exception of the cotton-wool paddling of hemangioma) the expected enhancement pattern cannot be seen with reliability (Zech et al. 2005).

With regard to the T_2/T_2* effects there might be differences between both agents, which could be related to the different average particle size of both agents (approximately 150 nm for ferumoxide and 60 nm for ferucarbotran).

With help of SPIO-enhanced MR an accurate liver lesion detection can be achieved. There have been several studies comparing SPIO to CT during arterial portography (CTAP), which has been considered as best practice and reference standard. These studies showed detection rates of more than 90% (Ba-Ssalamah et al. 2000; Vogl et al. 2003). In comparison to CTAP this detection rate

Table 2.6.3 Liver-specific MR imaging contrast agents

Product name	Generic Name	Group	Manufacturer
Endorem® Ferridex™	Ferumoxide	SPIO/RES specific	Guerbet, Aulnay Sous Bois, France Berlex Laboratories, NY
Resovist®	Ferucarbotran	SPIO/RES specific	Bayer Schering Pharma AG, Berlin, Germany
Teslascan®	Mangafodipir trisodium	Hepatobiliary	GE Healthcare Biosciences, Buckinghamshire, UK
MultiHance®	Gadopentate dimeglumine	Hepatobiliary	Bracco Imaging, Milano, Italy
Primovist®	Gadoxetic acid	Hepatobiliary	Bayer Schering Pharma AG, Berlin, Germany

was comparable; moreover, SPIO-enhanced MR is more specific than CTAP, in which false positive lesions are encountered frequently. The above cited references investigated SPIO-enhance MR in a mixed collective of patients; publications focusing on the cirrhotic liver showed, that in these patients the combination of SPIO and extracellular Gd-contrast agents have to be considered as the gold-standard for lesion detection (Ward et al. 2000). With regard to lesion characterization SPIO particles can be of help for the differential diagnosis of focal liver lesions based on the cellular composition and function of the different lesions (or rather based on different Kuppfer cell density and function). When the same MR sequence is acquired pre-contrast and after a definite time interval, then the signal loss in normal liver parenchyma and in different focal liver lesions can be quantitatively evaluated. This is helpful for the differentiation of benign and malignant lesions; when a threshold of 25% signal loss is chosen, than lesions with less signal loss are of a malignant nature with over 90% sensitivity and specificity (Namkung and Zech et al. 2007). However, the sequence must have the same parameters (including the same acceleration in case parallel imaging is used), since application of parallel imaging makes systematic changes in the spread of image-noise (Zech et al. 2004).

The second important group is the group of hepatobiliary contrast agents. The basic principle behind this group of contrast agents is the specific uptake directly into the hepatocyte. Since the agents all shorten the T_1 relaxation times, they cause a signal increase in normal liver parenchyma and in solid benign lesions, whereas in malignant lesions like metastases no specific uptake can be seen. These lesions contrast as hypointense lesions against the bright liver parenchyma. Approved agents in Europe are the manganese-based agent mangafodipir trisodium (Teslascan®, GE Healthcare), and the Gd-based agents gadopentate dimeglumine and gadoxetic acid (Primovist®, Bayer Schering Pharma).

Mangafodipir has the drawback that it must not be administered as a bolus, but only as a short infusion; therefore, dynamic studies are not possible with mangafodipir. However, the liver specificity is high and the high uptake in normal liver parenchyma enables imaging of, e.g., metastases with high contrast to the surrounding liver parenchyma. Gadopentate dimeglumine and gadoxetic acid are injectable as boluses. With both contrast agents, a valid early dynamic examination is feasible, allowing differentiation of lesions with regard to their hyper- or hypovascularity (Huppertz et al. 2005; Petersein et al. 2000b). Due to the lower liver specificity of gadopentate dimeglumine, the imaging time-point of the liver-specific phase starts about 40 min after injection; whereas gadoxetic acid allows for imaging at 20 min after injection. This can be of value with regard to the workflow in the MR department. Similar to the situation at SPIO agents, direct comparative studies between the agents have not been published yet; therefore, the following remarks again hold true for all hepatobiliary contrast agents. However, with regard to lesion characterization, only gadoxetic acid has the official approval to be used for this indication.

All three hepatobiliary agents are approved for lesion detection. In comparison to SPIO agents, the potential advantage of hepatobilary agents is the fact that T_1-weighted sequences usually can be performed with less acquisition time, less artifacts, and substantial higher spatial resolution. This holds true especially for T_1-weighted 3D-GRE sequences derived from MR angiography sequences as, for example, VIBE, or volumetric interpolated breathhold examination (Siemens Medical Solutions, Erlangen, Germany), or LAVA, for liver acquisition with volume acceleration (GE Healthcare). In how far these high-resolution sequences with a slice thickness of usually below 3 mm allow further increasing the detection of small (<1 cm) malignant lesions has to be investigated in the future. The present date for the hepatobiliary agents was acquired mostly with conventional 2D-GRE sequences and a slice thickness between 6 and 8 mm; however even in this setting the detection of lesions <1 cm was improved in comparison to baseline MRI and spiral CT (Bartolozzi et al. 2004; Gehl et al. 2001; Huppertz et al. 2004; Peterseing et al. 2000b). An earlier trial showed slight superiority of SPIO-enhanced MRI versus hepatobiliary MRI in detection of liver metastases; however, the potential advantaged of modern T_1-weighted 3D GRE sequences were not available for this evaluation (Del Frate et al. 2002). A recent evaluation showed comparable detection rates between these two contrast agent groups (Kim et al. 2005).

For the diagnosis of solid benign liver lesions (as focal nodular hyperplasia [FNH] and hepatocellular adenoma), the basis is still the extracellular contrast agent behavior with flush-like, mostly homogenous arterial hypervascularization and fast, but only faint washout, being in portovenous and equilibrium phase mostly slightly hyperintense (and not hypointense in contrast to the strong washout in malignant lesions). Contrast agents used for patients with suspected solid benign lesions must enable that this information can be acquired. Therefore, SPIO agents or mangafodipir alone are not sufficient for this indication; however, especially SPIO can contribute to the diagnosis of these lesions in combination with extracellular contrast agents, which have to show the abovementioned enhancement pattern. With SPIO agents solid benign lesions typically show liver-specific uptake of the substance in the range of normal liver parenchyma, thereby allowing the differentiation from malignant lesions as for example hepatocellular carcinoma (HCC). With regard to the differential diagnosis between FNH and adenoma, results in a limited number of patients indicated that the quantification of iron uptake can be helpful for this issue, because in our cohort, adenoma showed stronger iron uptake in comparison to FNH, with only minimal overlap of the percentage signal intensity loss (PSIL) measured in a T_2-weighted FSE sequence with fat-sat (Namkung and Zech et al. 2007). With the hepatobiliary contrast agents gadopentate dimeglumine and gadoxetic acid, diagnosis of FNH and adenoma is also possible on the one hand based on the extracellular contrast phenomena, on the other based on the liver specific uptake of the agents into these lesions (Grazioli et al. 2001, 2005; Huppertz et al. 2005). There is also valid data indicating that the differentiation between FNH and adenoma is feasible with hepatobiliary contrast agents. Therefore, with the bolus-injectable agents of this class a time- and presumably cost-effective diagnosis can be achieved (Fig. 2.6.2).

In patients with extrahepatic malignoma, confirmation or ruling out of liver metastasis is often crucial for the therapeutic management. Moreover, the exact staging of metastatic disease of the liver is getting more and more important, since sophisticated, stage-adapted therapeutic regimens with different options from atypical liver resection over local ablative minimally invasive treatment (e.g., radiofrequency ablation) up to extended liver resection exist. Therefore, contrast agents used for this indication have to provide an excellent detection rate for focal liver lesions; however, the characterization of these lesions is also important, especially the differential diagnosis of small cystic metastases and small benign cysts or atypical hemangioma. After injection of extracellular contrast agents, the vascularity can be differentiated in hypo- und hypervascular metastases. Hypovascular metastases appear as hypointense lesions in the portovenous phase, whereas hypervascular metastases appear as hyperintense lesions in the arterial-dominant phase. In contrast to the enhancement pattern of benign lesions, the nodular "cotton-wool"-like paddling in hemangioma or the homogeneous enhancement of FNH or adenoma metastases typically show a heterogeneous, ring-like enhancement with strong washout in the portovenous and equilibrium phase, resulting in first hyper-, and then hypointense lesions. However, in very small lesions the morphology of vascularization between the different en-

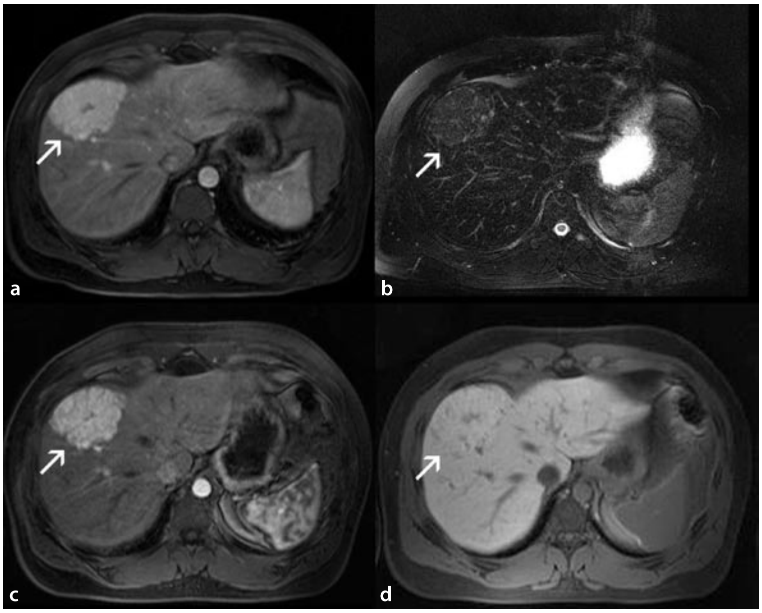

Fig. 2.6.2 MR images of a 27-year-old male patient with a formerly unclear liver lesion. The primary MR examination (*upper row*) with gadopentetate dimeglumine and ferucarbotran shows a lesion (*arrow*) with strong arterial enhancement in the Gd-enhanced T_1-weighted 3D-GRE sequence (**a**) (T_R, 5.02 ms; T_E, 1.77 ms; flip angle 15°) and ongoing washout in portovenous and equilibrium phase (not shown). The T_2-weighted FSE sequence with fat-saturation 10 min after application of ferucarbotran (**b**) depicts the lesion as nearly liver isointense. The calculated percentage iron uptake compared to the pre-contrast T_2-weighted sequence was about 40%, showing the benignity of the lesion. Based on these imaging features and the lobulated margins as well as the central scar, the diagnosis of a FNH was made. The follow-up study (*lower row*) was performed with gadoxetic acid after a single bolus injection. In the T_1-weighted 3D-GRE sequence (same parameters as above) in the arterial phase (**c**), the same enhancement characteristics as the in prior study can be delineated. In the delayed T_1-weighted 2D-GRE sequence (**d**), the presence of hepatocytes is proven due to the liver-specific enhancement. Note the excellent delineation of the central scar in the delayed images. In contrast to the *upper row*, the follow-up study gave information about vascularity and tissue composition, with a single contrast agent injection only

tities is getting more and more similar, so that the present or missing liver-specific uptake is an additional criterion for differentiation. Several publications have shown that detection of metastasis is feasible with the highest accuracy with help of liver-specific contrast agents, regardless if SPIO or hepatobiliary. According to the literature for detection of liver metastases, all liver-specific agents can be used with a very high diagnostic reliability and superiority to merely extracellular MRI or spiral CT (Bartolozzi et al. 2004; Ba-Ssalamah et al. 2000; Del Frate et al. 2002; Gehl et al. 2001; Huppertz et al. 2004; Kim et al. 2005; Petersein et al. 2000b; Vogl et al. 2003).

A difficult situation is liver imaging in cirrhotic liver. It is known that extracellular agents are helpful for detection and characterization of HCC nodules, the sensitivity is with T_1-weighted 3D-GRE sequences 76 and 75% specificity (Burrel et al. 2003). Moreover, for diagnosis a HCC according to the accepted guidelines, hypervascularity has to be demonstrated. Therefore, a valid early dynamic phase is a mandatory part for imaging in the cirrhotic liver. Because regenerative nodules, which can be found frequently in the cirrhotic liver, also can show hypervascularity differentiation between these nodules and HCC nodules, it is a crucial issue for the management of patients suffering from liver cirrhosis. This is the reason that liver-specific contrast agents play an important role for imaging of the cirrhotic liver.

It has been demonstrated that HCC shows no relevant uptake of SPIO particles in contrast to benign regenerative nodules (Bhartia et al. 2003; Imai et al. 2000; Ward et al. 2000; Namkung and Zech et al. 2007). Since in the cirrhotic liver fibrotic areas are present frequently, SPIO alone are not sufficient to evaluate the cirrhotic liver. A reasonable approach for the diagnosis of HCC based on imaging alone is the correlation of hypervascularity and missing or at least decreased iron uptake (Bhartia et al. 2003; Ward et al. 2000). However, there is also an indefinite area of overlapping phenomena between dysplastic nodules and well-differentiated HCC, which is the reason for false negative findings—meaning well-differentiated HCC with substantial iron uptake (Imai et al. 2000). With regard to lesion detection, the availability of high-resolution MR sequences gives advantages for Gd-enhanced arterial-phase imaging alone (Kwak et al. 2004) or in combination with SPIO as double contrast (Ward et al. 2000).

Imaging with hepatobiliary contrast agents is considered as inferior in comparison to SPIO agents in the cirrhotic liver, mainly due to substantial overlapping in the liver-specific uptake between well-differentiated HCC and regenerative nodules.

2.6.4.5 Lymph Node Imaging

The assessment of lymph node affections by extranodal tissue, i.e., lymph node metastasis, is currently based on morphologic parameters including, lymph node size, shape, irregular border, and signal intensity inhomogeneities (Brown et al. 2003; Zerhouni et al. 1996). For all parameters, no clear cut-off values or cut-off characteristics can be defined. The definition of a cut-off value in individual studies is the result of finding a compromise between sensitivity and specificity (e.g., larger values around 10 mm give a high specificity but low sensitivity, whereas the reverse of low specificity and high sensitivity is observed when smaller diameter <10 mm are defined). The use of unspecific Gd-based extracellular contrast agents has not revealed to overcome this limitation.

Lymphotropic MR contrast agents were, therefore, developed to increase the diagnostic accuracy of positive lymph node involvement. Currently, none of these agents is approved for clinical use, and the experience with different formulations is limited to clinical studies. The most frequently used agents are USPIOs. They are administered intravenously and, as a result of their small diameter and their electrical neutrality, pass the first lymphatic barriers, i.e., the liver and the spleen. In the lymphatic nodes, they are phagocytosed by local macrophages. In healthy lymphatic tissue, the local concentration of iron oxides is resulting in a significant decrease of T_2 and T_2* relaxation, resulting in a marked decrease of signal in T_2- and T_2*-weighted sequences. In contrast, metastatic tissue replacing the lymphatic tissue shows no relevant uptake of USPIO, and no relevant change in signal intensity can be observed. Gradient-recalled echo T_2-weighted sequences are considered the most accurate to detect the signal loss in nonmetastatic nodes. The application of USPIOs offers not only the possibility to differentiate between tumor-free, reactive (Koh et al. 2004) and tumor-positive lymph nodes, but enables to depict micrometastasis in case sequences when high spatial resolutions are used (Harisinghani et al. 2003).

One representative of the group of lymph node–specific USPIO, ferumoxtran-10 (Sinerem® Guerbet, Paris, France) is infused after dilution. The recommended dose is 2.6 mg Fe/kg body weight. The optimal time-point for postcontrast imaging is 24–36 h after application. During their clinical development, USPIOs have shown to be effective in staging lymph nodes of patients with various primary malignancies (Deserno et al. 2004; Jager et al. 1996; Michel et al. 2002; Nguyen et al. 1999). The usual way for diagnosis is to perform an initial precontrast scan and to compare the images with postcontrast images acquired 24–36 h after infusion of USPIOs for signal changes between both time-points. The type, onset, and intensity of adverse events after application of ferumoxtran-10 was evaluated in phase III studies and seems to be similar to those related to infusion of ferumoxides (Anzai et al. 2003).

In patients with esophageal or gastric cancer, USPIOs revealed a sensitivity of 100% and specificity between 92.6 and 95.4% (diagnostic accuracy between 94.8 and

96.2%) for diagnosis of metastatic nodes (Nishimura et al. 2006; Tatsumi et al. 2006). In patients with carcinomas of the upper aerodigestive tract, application of ferumoxtran-10 has shown to increase the sensitivity from 64 to 94% while maintaining a specificity of 78.9%, compared with precontrast imaging (Curvo-Semedo et al. 2006). In patients with rectum cancer, USPIOs have shown well-predictable signal characteristics in normal and reactive lymph nodes, and were able to differentiate the latter from malignant lymph nodes (Koh et al. 2004).

Dissimilarly, Keller et al. studied females with uterine carcinoma and were able to show high specificity, but a low sensitivity for metastatic lymph nodes; mainly micro-metastases around 5 mm diameter were missed. A possible way to further improve the diagnostic accuracy for detection of small positive lymph nodes could be the use of 3-T high magnetic field strength scanner resulting in a lower spatial resolution (Heesakkers et al. 2006).

Different results were published concerning the necessity of both pre- and postcontrast images. Whereas the majority of clinical publications using USPIO for lymph node imaging used both pre-and postcontrast images and Stets et al. (2002) were able to statistically prove the advantage of pre- and postcontrast studies, Harisinghani et al. (2003) were showed that on ferumoxtran-10–enhanced MR lymphangiography, contrast-enhanced images alone may be sufficient for lymph node characterization. However, a certain level of interpretation experience seems to be required before contrast-enhanced images can be used alone.

Both USPIOs (Rogers et al. 1998) and SPIOs (Maza et al. 2006) can alternatively be administered with subcutaneous or submucosal injection. This application route is able to identify sentinel lymph nodes and lymphatic drainage patterns (Fig. 2.6.3).

Additionally, high diagnostic accuracy of interstitial MR lymphography using blood-pool Gd-based agents has been described (Herborn et al. 2002, 2003).Using different macromolecular agents or Gd-based agents with high protein binding in animal models, Herborn et al. were able to show that the differentiation of tumor-bearing lymph nodes from reactive inflammatory and normal nodes based on a contrast uptake pattern assessed qualitatively as well as quantitatively is possible. In difference to the intravenous administration, subcutaneous injection gives the possibility to acquire the MR images as early as some min after application.

The use of Gd-based non-lymphotropic blood-pool agents induced a relatively short and inhomogeneous lymph node enhancement (Misselwitz et al. 2004). With the aim to become more specific, a new generation of lymphotropic T_1 contrast agents was developed and tested in animal models after subcutaneous injection. These perfluorinated Gd chelates were able to visualize fine lymphatic vasculature, even the thoracic duct in animal models (Staatz et al. 2001).

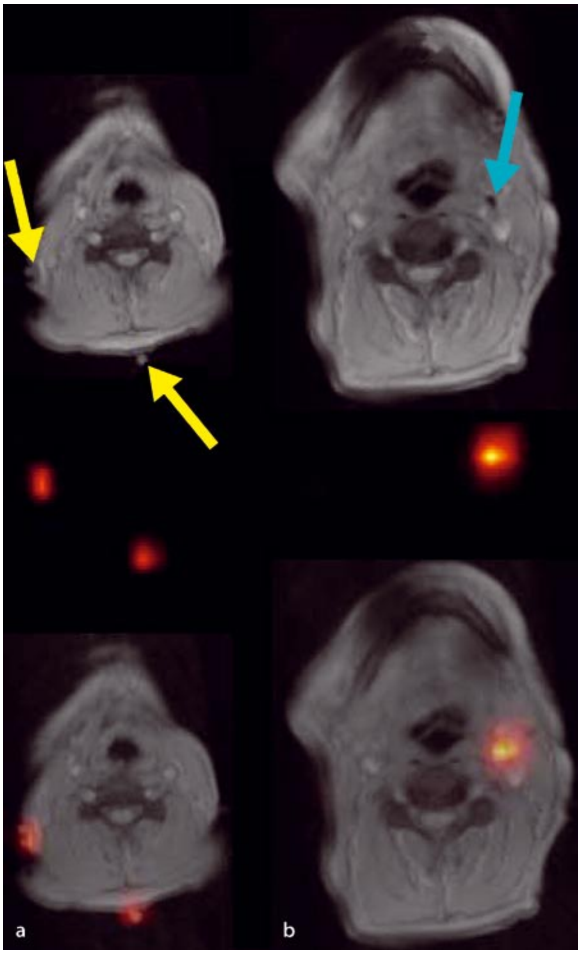

Fig. 2.6.3 Lymphatic drainage of a mucosal melanoma in the left nasal cavity to a lymph node located in the left submandibular region. MR images (*upper row*) and SPECT images (*lower row*). **a** Concordant alignment of hot spots caused by the skin markers on the SPECT images with the vitamin E caps on the MR images (*yellow arrows*). **b** Accurate sentinel lymph node localization (*blue arrow*) after subcutaneous injection of ferucarbotran (mg Fe/kg body weight). T_2*-weighted 2D gradient–recalled echo sequence $T_R/T_E/a$ 997/15/90. Homogeneous signal intensity decrease in the depicted lymph node (*arrow*) indicates normal lymphatic tissue and, thereby, metastatic involvement can be ruled out (Maza et al. 2006)

2.6.4.6 Gastrointestinal Imaging

Bowel MR contrast agents are generally classified as either positive (bright lumen) or negative (dark lumen) agents. In addition to enteral contrast agents especially approved for MR imaging, several existing pharmaceutical agents, such as methyl cellulose, mannitol, and polyethylene glycol preparations, licensed for other enteric application than MRI, have also been exploited.

The specific demands for enteral contrast media include:

- Opacification of intraluminal space for better delineation of bowel structures and clear differentiation to extraintestinal structures
- Suppression of bowel signal in non-enteral indications (MRCP and MR urography)
- No interaction with enteral mucosa for clear delineation of bowel wall
- Distension of bowel for visualization of the entire wall and lumen
- High contrast between bowel lumen and bowel mucosa
- Excellent safety profile and no contrast absorption trough the enteral mucosa

For enteral and rectal application a special formulation of gadopentetate dimeglumine was developed (Magnevist enteral, Schering). The agent contains a total of 15 g mannitol/l to prevent the absorption of the fluid simultaneously introduced in the GI tract, thus allowing homogeneous filling, distension, and constant Gd concentration during the entire examination period. In the early development, an increase in diagnostic accuracy in examinations of the pancreas in the diagnostics of abdominal lymphoma and in pelvic MR imaging was shown (Claussen et al. 1988).

Negative agents provide desirable contrast to those pathologic processes that are signal intense. They have been shown to improve the quality of images obtained by techniques such as MR cholangiopancreaticography (MRCP) and MR urography by eliminating unwanted signal from fluid-containing adjacent bowel loops, thus allowing better visualization of the pancreatic/biliary ducts and the urinary tract. An alternative to oral SPIOs was described by using ordinary pineapple juice. It was demonstrated that pineapple juice decreased T_2 signal intensity on a standard MRCP sequence to a similar degree than a commercially available negative contrast agent (ferumoxsil) (Riordan et al. 2004).

Oral SPIO preparations usually contain larger particles than injectable agents do. In Europe, two SPIO preparations with the INN code ferumoxsil are approved for oral use: Lumirem (Laboratoires Guerbet, France) with a particle size of 300 nm, and (oral magnetic particles) Abdoscan (GE Healthcare) with a particle size of 350 nm. They are coated with a non-biodegradable and insoluble matrix (siloxane for Lumirem and polystyrene for Abdoscan), and suspended in viscosity-increasing agents (usually based on ordinary food additives, such as starch and cellulose). These preparations can prevent the ingested iron from being absorbed, particles from aggregating, and improve homogeneous contrast distribution throughout the bowel. If SPIO particle aggregating occurs, magnetic susceptibility artifact may result, especially when high magnetic field strength and gradient-echo pulse sequence are used (Wang et al. 2001).

Lumirem is composed of crystals of approximately 10 nm; the hydrodynamic diameter is approximately 300 nm (Debatin and Patak 1999). The recommended concentration is 1.5–3.9 mmol Fe/l.

Oral SPIO are administered over 30–60 min, with a volume of 900 ml for contrast enhancement of the whole abdomen, and 400 ml for imaging of the upper abdomen. Oral SPIO suspensions are well tolerated by the patients (Haldemann et al. 1995); the iron is not absorbed and the intestinal mucosal membrane is not irritated.

Combination of Gd-enhanced T_1-weighted sequences and T_2-weighted sequences after oral contrast with SPIO has revealed highest accuracy in the evaluation of Crohn's disease (Maccioni et al. 2006). Furthermore, it has been shown that MRI with negative superparamagnetic oral contrast is comparable to endoscopy in the assessment of ulcerative colitis. In difference to patients with Crohn's disease, the double-contrast imaging does not provide more information than single oral contrast (De Ridder et al. 2001). In MRCP, negative oral contrast agents can be given before the examination to provide non-superimposed visualization of the bile and pancreatic ducts. There is no negative influence of the oral contrast agents on the diameter of the ducts (Petersein et al. 2000a).

2.6.4.7 Cardiac Imaging

In cardiac MRI, contrast agents are obligatory for the assessment of myocardial perfusion, for the evaluation of enhancement of cardiac masses, and for the evaluation of myocardial viability. In addition, contrast agents are frequently used when MR angiography of the coronary arteries is performed.

2.6.4.7.1 Myocardial Perfusion

Myocardial perfusion imaging is a promising and rapidly increasing field in cardiac MR imaging. In comparison to radionuclide techniques, MR imaging has several advantages, including higher spatial resolution, no radiation exposure, and no attenuation problem related to anatomical limitations. The examination is performed after rapid intravenous administration (e.g., 3–5 ml/sec) of a contrast agent and evaluation of the first-pass transit of the agent through the myocardium. With the use of fast scan techniques, perfusion imaging can be performed as a multislice technique, with imaging of three to five slice levels per heartbeat, possibly allowing coverage of the entire ventricle. From a series of images, signal intensity–time curves are derived from regions of interest in the myocardial tissue for generation of parametric images. The majority of data are published using ECF agents. In clinical practice, most investigators are using fast T_1-weighted imaging and bolus injection of doses of 0.025 up to 0.05 mmol/kg body weight (Edelman 2004).

For the evaluation, both quantitative and qualitative approaches can be used. In case of ECF agents, generally semiquantitative assessments are applied. To quantify myocardial perfusion a calculation was published by Wilke et al. on the basis of first-pass data acquired after fast bolus injection of 0.025 mmol/kg body weight of ECF agents (Wilke et al. 1997). In practice, Gd concentrations between 0.2 and 1.2 mmol/l result in a linear progression of the MR signal compared with the concentration of the agent itself. Above this dose, the maximal relative increase in signal intensity begins to saturate (Schwitter et al. 1997). When the evaluation is performed by visual evaluation, a higher dose of 0.1–0.2 mmol/kg should be preferred to reach better myocardial enhancement and image quality. Good correlation between the perfusion reserve with MR imaging and the coronary flow reserve with Doppler ultrasonography could be proven.

Blood-pool agents have the potential to be applied for quantitative measurements also because their volume of distribution is limited to the intravascular space. A requirement for quantitative perfusion measurements is that the relation between the measured signal intensity on the MR images and the contrast agent concentration in the blood is known (Brasch 1991). There are two major differences between first-pass curves obtained from blood-pool agents and extracellular contrast agents. First, blood-pool contrast agents reach a lower tissue signal because their volume of distribution is limited to the intravascular space (Wendland et al. 1997; Wilke et al. 1995). Second, there is a better return to baseline for blood-pool contrast agents. The wash-in kinetics and the signal intensity in the myocardial tissue depend on the concentration of the contrast agent, the coronary flow rate, diffusion of the contrast agent into the interstitium, relative tissue volume fractions, bolus duration, and recirculation effects (Burstein et al. 1991). Absolute quantification of myocardial perfusion has been performed in animal models using NC100150. A high absolute quantification correlation was found between MRI and contrast-enhanced ultrasound (Johansson et al. 2002).

2.6.4.7.2 Myocardial Viability

Delayed enhancement allows direct visualization of necrotic or scarred tissue and is an easy and robust method to assess myocardial viability. By measuring the transmural extent of late enhancement, a prognosis toward the degree of functional recovery of cardiac tissue may be possible. Although several studies have been aimed at describing the mechanisms of late enhancement, these could not be fully explained up to now. The extent of late enhancement possibly depends on the time-point after injection as well as the time-point after myocardial infarction. Relevant publications about delayed enhancement are reporting data after the administration of 0.5 M ECF agents in a dose range of 0.1–0.2 mmol/kg.

ECF agents are probably more efficient in assessing the cellular integrity when they are distributed homogenously through damaged myocardium (Wendland et al. 1997), but homogenous distribution is not always the case, as in microvascular obstruction (Kroft and de Roos 1995). Differences exist between the distribution patterns of extracellular and blood-pool agents, and hypo-enhanced cores may be observed earlier using blood-pool agents (Schwitter et al. 1997).

The sensitivity of blood-pool agents for myocardial infarction and, therefore, their potential value for the evaluation of myocardial viability, is unknown.

A different strategy to determine myocardial viability is the use of necrosis-specific MR contrast agents. Gadophrin-2 and -3 (Schering) have shown to possess a marked and specific affinity for necrotic tissue components and showed persistent enhancement in necrotic tissue (40 min to 12 h in myocardial infarction). In preclinical studies, the agent has not proven superiority in estimation of infarcts compared with ECF agents, and the further development of the agent was, therefore, not continued (Barkhausen et al. 2002).

2.6.4.7.3 Coronary MRA

To depict coronary arteries in MRI, both unenhanced and contrast-enhanced techniques are used. A frequently performed contrast-enhanced examination strategy with acquisition of multiple 3D slaps in breath-hold depicting each coronary artery separately was primarily described by Wielopolski et al. (1998). For 3D coronary MR angiography, however, the contrast between blood and myocardium in relation to the inflow of unsaturated protons is reduced. Thus, the use of an intravascular contrast agent may be particularly convenient due to the T_1 relaxation time reduction in blood. The application of ECF agents has proven to be most effective for breath-hold acquisitions. However, the concentration of ECF agents declines rapidly as they extravasate into the interstitial space, thereby reducing the contrast between blood and myocardium. Newly developed strategies use high-resolution free-breathing MR sequences for coronary MRA. In this situation, ECF agents are less beneficial due to the relatively long acquisition time of these free breathing 3D sequences. This problem can be solved by the use of intravascular contrast agents. An additional benefit from application of a blood-pool agent is a longer acquisition window, which may be used to further increase both the signal-to-noise ratio and/or image resolution (Nassenstein et al. 2006). In an animal model use of the macromolecular Gd-based agent P792 with a free-breathing technique allowed more distal visualization of the coronary arteries than did an ECF agent or non-enhanced MR images (Dirksen et al. 2003).

References

1. Akeson P, Jonsson E, Haugen I, Holtas S (1995) Contrast-enhanced MRI of the central nervous system: comparison between gadodiamide injection and Gd-DTPA. Neuroradiology 37:229–233
2. Anzai Y, Piccoli CW, Outwater EK, Stanford W, Bluemke DA, Nurenberg P, Saini S, Maravilla KR, Feldman DE, Schmiedl UP, Brunberg JA, Francis IR, Harms SE, Som PM, Tempany CM (2003) Evaluation of neck and body metastases to nodes with ferumoxtran 10-enhanced MR imaging: phase III safety and efficacy study. Radiology 228:777–788
3. Barkhausen J, Ebert W, Debatin JF, Weinmann HJ (2002) Imaging of myocardial infarction: comparison of magnevist and gadophrin-3 in rabbits. J Am Coll Cardiol 39:1392–1398
4. Bartolozzi C, Donati F, Cioni D et al (2004) Detection of colorectal liver metastases: a prospective multicenter trial comparing unenhanced MRI, MnDPDP-enhanced MRI, and spiral CT. Eur Radiol 14:14–20
5. Ba-Ssalamah A, Heinz-Peer G, Schima W et al (2000) Detection of focal hepatic lesions: comparison of unenhanced and SHU 555 A-enhanced MR imaging versus biphasic helical CTAP. J Magn Reson Imaging 11:665–672
6. Bastianello S, Gasperini C, Paolillo A et al (1998) Sensitivity of enhanced MR in multiple sclerosis: effects of contrast dose and magnetization transfer contrast. AJNR 19:1863–1867
7. Bellin MF, Lebleu L, Meric JB (2003) Evaluation of retroperitoneal and pelvic lymph node metastases with MRI and MR lymphangiography. Abdom Imaging 28:155–163
8. Bentzen L, Vestergaard-Poulsen P, Nielsen T et al (2005) Intravascular contrast agent-enhanced MRI measuring contrast clearance and tumor blood volume and the effects of vascular modifiers in an experimental tumor. Int J Radiat Oncol Biol Phys 61:1208–1215
9. Bhartia B, Ward J, Guthrie JA, Robinson PJ (2003) Hepatocellular carcinoma in cirrhotic livers: double-contrast thin-section MR imaging with pathologic correlation of explanted tissue. AJR Am J Roentgenol 180:577–584
10. Bluemke DA, Sahani D, Amendola M, Balzer T, Breuer J et al (2005) Efficacy and safety of MR imaging with liver-specific contrast agent: US multicenter phase III study. Radiology 237:89–98
11. Bozzao A, Floris R, Baviera ME, Apruzzese A, Simonetti G (2001) Diffusion and perfusion MR imaging in cases of Alzheimer's disease: correlations with cortical atrophy and lesion load. AJNR Am J Neuroradiol 22:1030–1036
12. Brasch RC (1991) Rationale and applications for macromolecular Gd-based contrast agents. Magn Reson Med 22:282–287
13. Brix G, Kiessling F, Lucht R et al (2004) Microcirculation and microvasculature in breast tumors: pharmacokinetic analysis of dynamic MR image series. Magn Reson Med 52:420–429
14. Broome DR, Girguis MS, Baron PW, Cottrell AC, Kjellin I, Kirk GA (2007) Gadodiamide-associated nephrogenic systemic fibrosis: why radiologists should be concerned. AJR Am J Roentgenol 188:586–592
15. Brown G, Richards CJ, Bourne MW, Newcombe RG, Radcliffe AG, Dallimore NS, Williams GT (2003) Morphologic predictors of lymph node status in rectal cancer with use of high-spatial-resolution MR imaging with histopathologic comparison. Radiology 227:371–377
16. Bruening R, Berchtenbreiter C, Holzknecht N, Essig M et al (2000) Effects of three different doses of a bolus injection of gadodiamide: assessment of regional cerebral blood volume maps in a blinded reader study. AJNR Am J Neuroradiol 21:1603–1610
17. Brugieres P, Gaston A, Degryse HR et al (1994) Randomized double blind trial of the safety and efficacy of two Gd complexes (Gd-DTPA and Gd-DOTA). Neuroradiology 36:27–30
18. Bundesinstitut für Arzneimittel und Medizinprodukte (Federal Institute for Drugs and Medical Devices) (2007) Public assessment reports increased risk of nephrogenic fibrosing dermopathy/nephrogenic systemic fibrosis and Gd-containing MRI contrast agents. http://www.bfarm.de. Cited 21 March 2007
19. Burrel M, Llovet JM, Ayuso C et al (2003) MRI angiography is superior to helical CT for detection of HCC prior to liver transplantation: an explant correlation. Hepatology 38:1034–1042
20. Burstein D, Taratuta E, Manning WJ (1991) Factors in myocardial "perfusion" imaging with ultrafast MRI and Gd-DTPA administration. Magn Reson Med 20:299–305
21. Cavagna FM, Lorusso V, Anelli PL, Maggioni F, de Haen C (2002) Preclinical profile and clinical potential of gadocoletic acid trisodium salt (B22956/1), a new intravascular contrast medium for MRI. Acad Radiol 9(Suppl 2): S491–S494
22. Chambon C, Clement O, Blanche RL et al (1993) Superparamagnetic iron oxides as positive MR contrast agents: in vitro and in vivo evidence. Magn Reson Imaging 11:509–519
23. Claussen C, Kornmesser W, Laniado M, Kaminsky S, Hamm B, Felix R (1988) Oral contrast media for magnetic resonance tomography of the abdomen. III. Initial patient research with Gd-DTPA. RoFo 148:663–689
24. Colosimo C, Ruscalleda J, Korves M et al (2001) Detection of intracranial metastases: a multicenter, intrapatient comparison of gadopentate dimeglumine-enhanced MRI with routinely used contrast agents at equal dosage. Invest Radiol 36:72–81
25. Colosimo C, Knopp MV, Barreau X et al (2004) A comparison of Gd-BOPTA and Gd-DOTA for contrast-enhanced MRI of intracranial tumors. Neuroradiology 46:655–665

26. Colosimo C, Demaerel P, Tortori-Donati P et al (2005) Comparison of gadopentate dimeglumine (Gd-BOPTA) with gadopentetate dimeglumine (Gd-DTPA) for enhanced MR imaging of brain and spine tumors in children. Pediatr Radiol 35:501–510
27. Corot C, Petry KG, Trivedi R, Saleh A, Jonkmanns C, Le Bas JF, Blezer E, Rausch M, Brochet B, Foster-Gareau P, Baleriaux D, Gaillard S, Dousset V (2004) Macrophage imaging in central nervous system and in carotid atherosclerotic plaque using ultrasmall superparamagnetic iron oxide in magnetic resonance imaging. Invest Radiol 39:619–625
28. Curvo-Semedo L, Diniz M, Migueis J, Juliao MJ, Martins P, Pinto A, Caseiro-Alves F (2006) USPIO-enhanced magnetic resonance imaging for nodal staging in patients with head and neck cancer. J Magn Reson Imaging 24:128–131
29. Daldrup-Link HE, Brasch RC (2003) Macromolecular contrast agents for MR mammography: current status. Eur Radiol 13:354–365
30. Daldrup H, Shames DM, Wendland M et al (1998) Correlation of dynamic contrast-enhanced magnetic resonance imaging with histologic tumor grade: comparison of macromolecular and small-molecular contrast media. Pediatr Radiol 28:67–78
31. Daldrup-Link HE, Rydland J, Helbich TH et al (2003) Quantification of breast tumor microvascular permeability with feruglose-enhanced MR imaging: initial phase II multicenter trial. Radiology 229:885–892
32. D'Arienzo A, Scaglione G, Vicinanza G, Manguso F, Bennato R, Belfiore G, Imbriaco M, Mazzacca G (2000) Magnetic resonance imaging with ferumoxil, a negative superparamagnetic oral contrast agent, in the evaluation of ulcerative colitis. Am J Gastroenterol 95:720–724
33. De Ridder F, De Maeseneer M, Stadnik T, Luypaert R, Osteaux M (2001) Severe adverse reactions with contrast agents for magnetic resonance: clinical experience in 30,000 MR examinations. JBR-BTR 84:150–152
34. Debatin JF, Patak MA (1999) MRI of the small and large bowel. Eur Radiol 9:1523–1534
35. Del Frate C, Bazzocchi M, Mortele KJ et al (2002) Detection of liver metastases: comparison of gadopentate dimeglumine-enhanced and ferumoxides-enhanced MR imaging examinations. Radiology 225:766–772
36. Deserno WM, Harisinghani MG, Taupitz M et al (2004) Urinary bladder cancer: preoperative nodal staging with ferumoxtran-10-enhanced MR imaging. Radiology 233:449–456
37. Dijke C van, Brasch R, Roberts T et al (1996) Mammary carcinoma model: correlation of macromolecular contrast-enhanced MR imaging characterization of tumor microvasculature and histologic capillary density. Radiology 198:813–818
38. Dirksen MS, Lamb HJ, Kunz P, Robert P, Corot C, de Roos A (2003) Improved MR coronary angiography with use of a new rapid clearance blood pool contrast agent in pigs. Radiology 227:802–808
39. Doerfler A, Eckstein HH, Eichbaum M et al (2001) Perfusion-weighted magnetic resonance imaging in patients with carotid artery disease before and after carotid endarterectomy. J Vasc Surg 34:587–593
40. Edelman RR (2004) Contrast-enhanced MR imaging of the heart: overview of the literature. Radiology 232:653–668
41. Essig M, Wenz F, Scholdei R et al (2002) Effect of contrast media dosage and contrast media extravasation on dynamic susceptibility-contrast enhanced dynamic echo planar imaging of cerebral gliomas. Acta Radiol 43:354–359
42. Essig M, Waschkies M, Wenz F, Debus J, Hentrich HR, Knopp MV (2003) Assessment of brain metastases by means of dynamic susceptibility contrast enhanced MRI – initial results. Radiology 228:193–199
43. Essig M, Giesel F, Le-Huu M, Stieltjes B, von Tengg H, Weber MA (2004) Perfusion MRI in CNS disease: current concepts. Neuroradiology 46(Suppl 2):S201–S207
44. Essig M, Lodemann KP, Le-Huu M, Bruning R, Kirchin M, Reith W (2006) Intraindividual comparison of gadopentate dimeglumine and gadobutrol for cerebral magnetic resonance perfusion imaging at 1.5 T. Invest Radiol 41:256–263
45. Fink C, Bock M, Kiessling F, Lichy MP, Krissak R, Zuna I, Schmahl A, Delorme S, Kauczor HU (2004) Time-resolved contrast-enhanced three-dimensional pulmonary MR-angiography: 1 M gadobutrol vs. 0.5 M gadopentetate dimeglumine. J Magn Reson Imaging 19:202–208
46. Gehl HB, Bourne M, Grazioli L, Moller A, Lodemann KP (2001) Off-site evaluation of liver lesion detection by Gd-BOPTA-enhanced MR imaging. Eur Radiol 11:187–192
47. Gibbs GF, Huston J 3rd, Bernstein MA, Riederer SJ, Brown RD Jr (2005) 3.0-Tesla MR angiography of intracranial aneurysms: comparison of time-of-flight and contrast-enhanced techniques. J Magn Reson Imaging 21:97–102
48. Goyen M, Debatin JF (2003) Gadopentate dimeglumine (MultiHance) for magnetic resonance angiography: review of the literature. Eur Radiol 13(Suppl 3):N19–N27
49. Goyen M, Lauenstein TC, Herborn CU, Debatin JF, Bosk S, Ruehm SG (2001) 0.5 M Gd chelate (Magnevist) versus 1.0 M Gd chelate (Gadovist): dose-independent effect on image quality of pelvic three-dimensional MR-angiography. J Magn Reson Imaging 14:602–607
50. Goyen M, Herborn CU, Vogt FM, Kroger K, Verhagen R, Yang F, Bosk S, Debatin JF, Ruehm SG (2003) Using a 1 M Gd-chelate (gadobutrol) for total-body three-dimensional MR angiography: Preliminary experience. J Magn Reson Imaging 17:565-571
51. Goyen M, Edelman M, Perreault P, O'Riordan E, Bertoni H, Taylor J, Siragusa D, Sharafuddin M, Mohler ER 3rd, Breger R, Yucel EK, Shamsi K, Weisskoff RM (2005) MR angiography of aortoiliac occlusive disease: a phase III study of the safety and effectiveness of the blood-pool contrast agent MS-325. Radiology 236:825–833
52. Grazioli L, Morana G, Federle MP et al (2001) Focal nodular hyperplasia: morphologic and functional information from MR imaging with gadopentate dimeglumine. Radiology 221:731–739

53. Grazioli L, Morana G, Kirchin MA, Schneider G (2005) Accurate differentiation of focal nodular hyperplasia from hepatic adenoma at gadopentate dimeglumine-enhanced MR imaging: prospective study. Radiology 236:166–177
54. Grossman RI, Rubin DI, Hunter G et al (2000) Magnetic resonance imaging in patients with central nervous system pathology: a comparison of OptiMARK (Gd-DTPABMEA)and Magnevist (Gd-DTPA). Invest Radiol 35:412–419
55. Haen C, Anelli PL, Lorusso V, Morisetti A, Maggioni F, Zheng J, Uggeri F, Cavagna FM (2006) Gadocoletic acid trisodium salt (b22956/1): a new blood pool magnetic resonance contrast agent with application in coronary angiography. Invest Radiol 41:279–291
56. Halavaara J, Breuer J, Ayuso C, Balzer T, Bellin MF et al (2006) Liver tumor characterization: comparison between liver-specific gadoxetic acid disodium-enhanced MRI and biphasic CT—a multicenter trial. J Comput Assist Tomogr 30:345–354
57. Haldemann Heusler RC, Wight E, Marincek B (1995) Oral superparamagnetic contrast agent (ferumoxsil): tolerance and efficacy in MR imaging of gynecologic diseases. J Magn Reson Imaging 5:385–391
58. Harisinghani MG, Barentsz J, Hahn PF et al (2003) Noninvasive detection of clinically occult lymph-node metastases in prostate cancer. N Engl J Med 348:2491–2499
59. Haustein J, Laniado M, Niendorf HP et al (1993) Triple-dose versus standard-dose gadopentetate dimeglumine: a randomized study in 199 patients. Radiology 186:855–860
60. Heesakkers RA, Futterer JJ, Hovels AM, van den Bosch HC, Scheenen TW, Hoogeveen YL, Barentsz JO (2006) Prostate cancer evaluated with ferumoxtran-10-enhanced T_2*-weighted MR Imaging at 1.5 and 3.0 T: early experience. Radiology 239:481–487
61. Heiland S, Reith W, Forsting M, Sartor K (2001) How do concentration and dosage of the contrast agent affect the signal change in perfusion-weighted magnetic resonance imaging? A computer simulation. Magn Reson Imaging 19:813–820
62. Herborn CU, Lauenstein TC, Vogt FM, Lauffer RB, Debatin JF, Ruehm SG (2002) Interstitial MR lymphography with MS-325: characterization of normal and tumor-invaded lymph nodes in a rabbit model. AJR Am J Roentgenol 179:1567–1572
63. Herborn CU, Vogt FM, Lauenstein TC, Goyen M, Dirsch O, Corot C, Debatin JF, Ruehm SG (2003) Assessment of normal, inflammatory, and tumor-bearing lymph nodes with contrast-enhanced interstitial magnetic resonance lymphography: preliminary results in rabbits. J Magn Reson Imaging 18:328–335
64. Huppertz A, Balzer T, Blakeborough A et al (2004) Improved detection of focal liver lesions at MR imaging: multicenter comparison of gadoxetic acid-enhanced MR images with intraoperative findings. Radiology 230:266–275
65. Huppertz A, Haraida S, Kraus A, Zech CJ et al (2005) Enhancement of focal liver lesions at gadoxetic acid-enhanced MR imaging: correlation with histopathologic findings and spiral CT—initial observations. Radiology 234:468–478
66. Imai Y, Murakami T, Yoshida S et al (2000) Superparamagnetic iron oxide-enhanced magnetic resonance images of hepatocellular carcinoma: correlation with histological grading. Hepatology 32:205–212
67. Jager GJ, Barentsz JO, Oosterhof GO, Witjes JA, Ruijs SJ (1996) Pelvic adenopathy in prostatic and urinary bladder carcinoma: MR imaging with a three-dimensional TI-weighted magnetization-prepared-rapid gradient-echo sequence. AJR Am J Roentgenol 167:1503–1507
68. Johansson LO, Bjerner T, Bjornerud A, Ahlstrom H, Tarlo KS, Lorenz CH (2002) Utility of NC100150 injection in cardiac MRI. Acad Radiol 9(Suppl 1):S79-S81
69. Kim YK, Lee JM, Kim CS, Chung GH, Kim CY, Kim IH (2005) Detection of liver metastases: gadopentate dimeglumine-enhanced three-dimensional dynamic phases and one-h delayed phase MR imaging versus superparamagnetic iron oxide-enhanced MR imaging. Eur Radiol 15:220–228
70. Kirchin MA, Pirovano G, Venetianer C, Spinazzi A (2001) Safety assessment of gadopentate dimeglumine (MultiHance): extended clinical experience from phase I studies to post-marketing surveillance. J Magn Reson Imaging 14:281–294
71. Knopp MV, Weiss E, Sinn HP et al (1999) Pathophysiologic basis of contrast enhancement in breast tumors. J Magn Reson Imag 10:260–266
72. Knopp MV, Runge VM, Essig M et al (2004) Primary and secondary brain tumors at MR imaging: bicentric intraindividual crossover comparison of gadopentate dimeglumine and gadopentetate dimeglumine. Radiology 230:55–64
73. Kobayashi H, Sato N, Kawamoto S et al (2001) 3D MR angiography of intratumoral vasculature using a novel macromolecular MR contrast agent. Magn Reson Med 46:579–585
74. Koh DM, Brown G, Temple L et al (2004) Rectal cancer: mesorectal lymph nodes at MR imaging with USPIO versus histopathologic findings – initial observations. Radiology 231:91–99
75. Kroft LJ, de Roos A (1995) Blood pool contrast agents for cardiovascular MR Imaging. J Magn Reson Imaging 10:395–403
76. Kuhl CK, Mielcareck P, Klaschik S et al (1999) Dynamic breast MR imaging: are signal intensity time course data useful for differential diagnosis of enhancing lesions? Radiology 211:101–110
77. Kuhl CK, Schild HH, Morakkabati N (2005) Dynamic bilateral contrast-enhanced MR imaging of the breast: trade-off between spatial and temporal resolution. Radiology 236:789–800

78. Kwak HS, Lee JM, Kim CS (2004) Preoperative detection of hepatocellular carcinoma: comparison of combined contrast-enhanced MR imaging and combined CT during arterial portography and CT hepatic arteriography. Eur Radiol 14:447–457
79. La Noce A, Stoelben S, Scheffler K, Hennig J, Lenz HM, La Ferla R, Lorusso V, Maggioni F, Cavagna F (2002) B22956/1, a new intravascular contrast agent for MRI: first administration to humans—preliminary results. Acad Radiol 9(Suppl 2):S404–S406
80. Lauffer RB, Parmelee DJ, Dunham SU, Ouellet HS, Dolan RP, Witte S, McMurry TJ, Walovitch RC (1998) MS-325: albumin-targeted contrast agent for MR angiography. Radiology 207:529–538
81. Le Duc G, Corde S, Charvet AM et al (2004) In vivo measurement of Gd concentration in a rat glioma model by monochromatic quantitative computed tomography: comparison between gadopentetate dimeglumine and gadobutrol. Invest Radiol 39:385–393
82. Li A, Wong CS, Wong MK, Lee CM, Au Yeung MC (2006) Acute adverse reactions to magnetic resonance contrast media—Gd chelates. Br J Radiol 79:368–371
83. Maccioni F, Bruni A, Viscido A, Colaiacomo MC, Cocco A, Montesani C, Caprilli R, Marini M (2006) MR imaging in patients with Crohn disease: value of T_2- versus T_1-weighted Gd-enhanced MR sequences with use of an oral superparamagnetic contrast agent. Radiology 238:517–530
84. Manninger SP, Muldoon LL, Nesbit G, Murillo T, Jacobs PM, Neuwelt EA (2005) An exploratory study of ferumoxtran-10 nanoparticles as a blood–brain barrier imaging agent targeting phagocytic cells in CNS inflammatory lesions. AJNR Am J Neuroradiol 26:2290–2300
85. Maza S, Taupitz M, Taymorian K, Winzer KJ, Rückert J, Paschen C, Räber G, Schneider S, Trefzer U, Munz DL (2006) Multimodal fusion imaging ensemble for targeted sentinel lymph node management: initial results of an innovative promising approach for anatomically difficult lymphatic drainage in different tumor entities. Eur J Nucl Med Mol Imaging 34:378–383
86. Meaney JF (1999) Non-invasive evaluation of the visceral arteries with magnetic resonance angiography. Eur Radiol 9:1267–1276
87. Meaney JF, Weg JG, Chenevert TL, Stafford-Johnson D, Hamilton BH, Prince MR (1997) Diagnosis of pulmonary embolism with magnetic resonance angiography. N Engl J Med 336:1422–1427
88. Michel SC, Keller TM, Frohlich JM, Fink D, Caduff R, Seifert B, Marincek B, Kubik-Huch RA (2002) Preoperative breast cancer staging: MR imaging of the axilla with ultrasmall superparamagnetic iron oxide enhancement. Radiology 225:527–536
89. Misselwitz B, Platzek J, Weinmann HJ (2004) Early MR lymphography with gadofluorine M in rabbits. Radiology 231:682–688
90. Morris EA. Breast cancer imaging with MRI (2002) Radiol Clin North Am 40:443–466
91. Murphy KJ, Brunberg JA, Cohan RH (1996) Adverse reactions to Gd contrast media: a review of 36 cases. AJR Am J Roentgenol 167:847–849
92. Namkung S, Zech CJ, Helmberger T, Reiser MF, Schönberg SO (2007) Superparamagnetic iron oxide (SPIO)-enhanced liver MR Imaging with ferucarbotran: efficacy for characterization of focal liver lesions. J Magn Reson Imaging 25:755–765
93. Nassenstein K, Waltering KU, Eggebrecht H, Schlosser T, Hunold P, Barkhausen J (2006) [MR coronary angiography with MS-325, a blood pool contrast agent: comparison of an inversion recovery steady-state free precession with an inversion recovery fast low angle shot sequence in volunteers]. RoFo 178:508–514
94. Nguyen BC, Stanford W, Thompson BH, Rossi NP, Kernstine KH, Kern JA, Robinson RA, Amorosa JK, Mammone JF, Outwater EK (1999) Multicenter clinical trial of ultrasmall superparamagnetic iron oxide in the evaluation of mediastinal lymph nodes in patients with primary lung carcinoma. J Magn Reson Imaging 10:468–473
95. Niendorf HP, Alhassan A, Geens VR, Clauss W (1994) Safety review of gadopentetate dimeglumine. Extended clinical experience after more than five million applications. Invest Radiol 29(Suppl 2):S179–S182
96. Nishimura H, Tanigawa N, Hiramatsu M, Tatsumi Y, Matsuki M, Narabayashi I (2006) Preoperative esophageal cancer staging: magnetic resonance imaging of lymph node with ferumoxtran-10, an ultrasmall superparamagnetic iron oxide. J Am Coll Surg 202:604–611
97. Oudkerk M, Sijens PE, van Beek EJ, Kuijpers TJ (1995) Safety and efficacy of Dotarem (Gd-DOTA) versus Magnevist (Gd-DTPA) in magnetic resonance imaging of the central nervous system. Invest Radiol 30:75–78
98. Ozsarlak O, Van Goethem JW, Maes M, Parizel PM (2004) MR angiography of the intracranial vessels: technical aspects and clinical applications. Neuroradiology 46:955–972
99. Paetsch I, Jahnke C, Barkhausen J, Spuentrup E, Cavagna F, Schnackenburg B, Huber M, Stuber M, Fleck E, Nagel E (2006) Detection of coronary stenoses with contrast enhanced, three-dimensional free breathing coronary MR angiography using the Gd-based intravascular contrast agent gadocoletic acid (B-22956). J Cardiovasc Magn Reson 8:509–516
100. Parsons MW, Yang Q, Barber PA et al (2001) Perfusion magnetic resonance imaging maps in hyperacute stroke: relative cerebral blood flow most accurately identifies tissue destined to infarct. Stroke 32:1581–1587
101. Pediconi F, Fraioli F, Catalano C, Napoli A, Danti M, Francone M, Venditti F, Nardis P, Passariello R (2003) Gadopentate dimeglumine (Gd-DTPA) vs. gadopentetate dimeglumine (Gd-BOPTA) for contrast-enhanced magnetic resonance angiography (MRA): improvement in intravascular signal intensity and contrast to noise ratio. Radiol Med (Torino) 106:87–93

102. Pediconi F, Catalano C, Occhiato R et al (2005) Breast lesion detection and characterization at contrast-enhanced MR mammography: gadopentate dimeglumine versus gadopentetate dimeglumine. Radiology 237:45–56
103. Perreault P, Edelman MA, Baum RA, Yucel EK, Weisskoff RM, Shamsi K, Mohler ER III (2003) MR angiography with gadofosveset trisodium for peripheral vascular disease: phase II trial. Radiology 229:811–820
104. Petersein J, Reisinger W, Mutze S, Hamm B (2000a) Value of negative oral contrast media in MR cholangiopancreatography (MRCP). RoFo 172:55–60
105. Petersein J, Spinazzi A, Giovagnoni A et al (2000b) Focal liver lesions: evaluation of the efficacy of gadopentate dimeglumine in MR imaging—a multicenter phase III clinical study. Radiology 215:727–736
106. Port M, Corot C, Rousseaux O, Raynal I, Devoldere L, Idee JM, Dencausse A, Le Greneur S, Simonot C, Meyer D (2001) P792: a rapid clearance blood pool agent for magnetic resonance imaging: preliminary results. MAGMA 12:121–127
107. Preda A, Novikov V, Moglich M et al (2004a) MRI monitoring of Avastin antiangiogenesis therapy using B22956/1, a new blood pool contrast agent, in an experimental model of human cancer. J Magn Reson Imaging 20:865–873
108. Preda A, Wielopolski PA, Ten Hagen TL et al (2004b) Dynamic contrast-enhanced MRI using macromolecular contrast media for monitoring the response to isolated limb perfusion in experimental soft-tissue sarcomas. MAGMA 17:296–302
109. Prince MR, Narasimham DL, Stanley JC et al (1995) Breath-hold Gd-enhanced MR angiography of the abdominal aorta and its major branches. Radiology 197:785–792
110. Rapp JH, Wolff SD, Quinn SF, Soto JA, Meranze SG, Muluk S, Blebea J, Johnson SP, Rofsky NM, Duerinckx A, Foster GS, Kent KC, Moneta G, Middlebrook MR, Narra VR, Toombs BD, Pollak J, Yucel EK, Shamsi K, Weisskoff RM (2005) Aortoiliac occlusive disease in patients with known or suspected peripheral vascular disease: safety and efficacy of gadofosveset-enhanced MR angiography—multicenter comparative phase III study. Radiology 236:71–78
111. Reimer P, Balzer T (2003) Ferucarbotran (Resovist): a new clinically approved RES-specific contrast agent for contrast-enhanced MRI of the liver: properties, clinical development, and applications. Eur Radiol 13:1266–1276
112. Reimer P, Bremer C, Allkemper T, Engelhardt M, Mahler M, Ebert W, Tombach B (2004) Myocardial perfusion and MR angiography of chest with SH U 555 C: results of placebo-controlled clinical phase I study. Radiology 231:474–481
113. Riordan RD, Khonsari M, Jeffries J, Maskell GF, Cook PG (2004) Pineapple juice as a negative oral contrast agent in magnetic resonance cholangiopancreatography: a preliminary evaluation. Br J Radiol 77:991–999
114. Rogers JM, Jung CW, Lewis J, Groman EV /91998) Use of USPIO-induced magnetic susceptibility artifacts to identify sentinel lymph nodes and lymphatic drainage patterns. I. Dependence of artifact size with subcutaneous Combidex dose in rats. Magn Reson Imaging 16:917–23
115. Rohrer M, Bauer H, Mintorovitch J, Requardt M, Weinmann HJ (2005) Comparison of magnetic properties of MRI contrast media solutions at different magnetic field strengths. Invest Radiol 40:715–724
116. Ruehm SG, Christina H, Violas X, Corot C, Debatin JF (2002) MR angiography with a new rapid-clearance blood pool agent: Initial experience in rabbits. Magn Reson Med 48:844–851
117. Runge VM (2000) Safety of approved MR contrast media for intravenous injection. J Magn Reson Imaging 12:205–213
118. Sadowski EA, Bennett LK, Chan MR, Wentland AL, Garrett AL, Garrett RW, Djamali A (2007) Nephrogenic systemic fibrosis: risk factors and incidence estimation. Radiology 243:148–157
119. Schnorr J, Wagner S, Abramjuk C, Wojner I, Schink T, Kroencke TJ, Schellenberger E, Hamm B, Pilgrimm H, Taupitz M (2004) Comparison of the iron oxide-based blood-pool contrast medium VSOP-C184 with gadopentetate dimeglumine for first-pass magnetic resonance angiography of the aorta and renal arteries in pigs. Invest Radiol 39:546–553
120. Schwitter J, Saeed M, Wendland MF et al (1997) Influence of severity of myocardial injury on distribution of macromolecules: extravascular versus intravascular Gd-based magnetic resonance contrast agents. J Am Coll Cardiol 30:1086–1094
121. Sharafuddin MJ, Stolpen AH, Sun S, Leusner CR, Safvi AA, Hoballah JJ, Sharp WJ, Corson JD (2002) High-resolution multiphase contrast-enhanced three-dimensional MR angiography compared with two-dimensional time-of-flight MR angiography for the identification of pedal vessels. J Vasc Interv Radiol 13:695–702
122. Shellock FG (1999) Safety of MRI contrast agents. JMRI 10:477–484
123. Spinazzi A, Lorusso V, Pirovano G, Kirchin M (1999) Safety, tolerance, biodistribution, and MR imaging enhancement of the liver with gadopentate dimeglumine: results of clinical pharmacologic and pilot imaging studies in nonpatient and patient volunteers. Acad Radiol 6:282–291
124. Staatz G, Nolte-Ernsting CC, Adam GB, Grosskortenhaus S, Misselwitz B, Bucker A, Gunther RW (2001) Interstitial T1-weighted MR lymphography: lipophilic perfluorinated Gd chelates in pigs. Radiology 220:129–134
125. Stets C, Brandt S, Wallis F, Buchmann J, Gilbert FJ, Heywang-Kobrunner SH (2002) Axillary lymph node metastases: a statistical analysis of various parameters in MRI with USPIO. J Magn Reson Imaging 16:60–68

126. Tatsumi Y, Tanigawa N, Nishimura H, Nomura E, Mabuchi H, Matsuki M, Narabayashi I (2006) Preoperative diagnosis of lymph node metastases in gastric cancer by magnetic resonance imaging with ferumoxtran-10. Gastric Cancer 9:120–128
127. Taylor AM, Panting JR, Keegan J, Gatehouse PD, Amin D, Jhooti P, Yang GZ, McGill S, Burman ED, Francis JM, Firmin DN, Pennell DJ (1999) Safety and preliminary findings with the intravascular contrast agent NC100150 injection for MR coronary angiography. J Magn Reson Imaging 9:220–227
128. Thilmann O, Larsson EM, Bjorkman-Burtscher IM, Stahlberg F, Wirestam R (2005) Comparison of contrast agents with high molarity and with weak protein binding in cerebral perfusion imaging at 3 T. J Magn Reson Imaging 22:597–604
129. Thomsen HS, Morcos SK, Dawson P (2006) Is there a causal relation between the administration of Gd based contrast media and the development of nephrogenic systemic fibrosis (NSF)? Clin Radiol 61:905–906
130. Tombach B, Benner T, Reimer P et al (2003) Do highly concentrated Gd chelates improve MR brain perfusion imaging? Intraindividually controlled randomized crossover concentration comparison study of 0.5 versus 1.0 mol/l gadobutrol. Radiology 226:880–888
131. Turetschek K, Floyd E, Helbich T et al (2001) MRI assessment of microvascular characteristics in experimental breast tumors using a new blood pool contrast agent (MS-325) with correlations to histopathology. J Magn Reson Imaging 14:237–242
132. US Food and Drug Administration (2006) Public health advisory: Gd-containing contrast agents for magnetic resonance imaging (MRI): Omniscan, OptiMARK, Magnevist, ProHance, and MultiHance. http://www.fda.gov/cder/drug/advisory/Gd_agents.htm. Cited 21 March 2007
133. Valk J, Algra PR, Hazenberg CJ, Slooff WB, Slavand MG (1993) A double-blind, comparative study of gadodiamide injection and gadopentetate dimeglumine in MRI of the central nervous system. Neuroradiology 35:173–177
134. Verstraete KL, Lang P (2000) Bone and soft tissue tumors: the role of contrast agents for MR imaging. Eur J Radiol 34:229–246
135. Vogl TJ, Friebe CE, Balzer T et al (1995) Diagnosis of cerebral metastasis with standard dose gadobutrol vs. a high dose protocol. Intraindividual evaluation of a phase II high dose study. Radiologe 35:508–516
136. Vogl TJ, Schwarz W, Blume S et al (2003) Preoperative evaluation of malignant liver tumors: comparison of unenhanced and SPIO (Resovist)-enhanced MR imaging with biphasic CTAP and intraoperative US. Eur Radiol 13:262–272
137. Vosshenrich R, Engeroff B, Obenauer S, Grabbe E (2003) Kontrastmittel-gestützte 3D-Angiographie des arteriellen und portalvenösen Gefäßsystems der Leber mit unterschiedlicher KM-Konzentration. RoFo 175:1239–1243
138. Wagenseil JE, Johansson LO, Lorenz CH (1999) Characterization of t1 relaxation and blood-myocardial contrast enhancement of NC100150 injection in cardiac MRI. J Magn Reson Imaging 10:784–789
139. Wagner S, Schnorr J, Pilgrimm H, Hamm B, Taupitz M (2002) Monomer-coated very small superparamagnetic iron oxide particles as contrast medium for magnetic resonance imaging: preclinical in vivo characterization. Invest Radiol 37:167–177
140. Wang YX, Hussain SM, Krestin GP (2001) Superparamagnetic iron oxide contrast agents: physicochemical characteristics and applications in MR imaging. Eur Radiol 11:2319–31
141. Ward J, Guthrie JA, Scott DJ et al (2000) Hepatocellular carcinoma in the cirrhotic liver: double-contrast MR imaging for diagnosis. Radiology 216:154–162
142. Weishaupt D, Ruhm SG, Binkert CA, Schmidt M, Patak MA, Steybe F, McGill S, Debatin JF (2000) Equilibrium-phase MR angiography of the aortoiliac and renal arteries using a blood pool contrast agent. AJR Am J Roentgenol 175:189–195
143. Wendland MF, Saeed M, Lauerman K et al (1999) Alterations in T1 of normal and reperfused infarcted myocardium after Gd-BOPTA versus Gd-DTPA on inversion recovery EPI. Magn Reson Med 37:448–456
144. Wielopolski PA, van Geuns RJ, de Feyter PJ, Oudkerk M (1998) Breath-hold coronary MR angiography with volume-targeted imaging. Radiology 209:209–219
145. Wilke N, Kroll K, Merkle H et al (1995) Regional myocardial blood volume and flow: first-pass MR imaging with polylysine-Gd-DTPA. J Magn Reson Imaging 5:227–237
146. Wilke N, Jerosch-Herold M, Wang Y et al (1997) Myocardial perfusion reserve: assessment with multisection, quantitative, first-pass MR imaging. Radiology 204:373–384
147. Yuh WT, Fisher DJ, Engelken JD et al (1991) MR evaluation of CNS tumors: dose comparison study with gadopentetate dimeglumine and gadoteridol. Radiology 180:485–491
148. Yuh WT, Nguyen HD, Tali ET et al (1994) Delineation of gliomas with various doses of MR contrast material. AJNR Am J Neuroradiol 15:983–989
149. Zech CJ, Herrmann KA, Huber A et al (2004) High-resolution MR-imaging of the liver with T2-weighted sequences using integrated parallel imaging: comparison of prospective motion correction and respiratory triggering. J Magn Reson Imaging 20:443–450
150. Zech CJ, Namkung S, Helmberger T, Reiser MF, Schönberg SO (2005) Efficacy of ferucarbotran-enhanced early dynamic MR Imaging with T1-weighted sequences for characterization of focal liver lesions. Eur Radiol 15(Suppl 3):37
151. Zerhouni EA, Rutter C, Hamilton SR et al (1996) CT and MR imaging in the staging of colorectal carcinoma: report of the Radiology Diagnostic Oncology Group II. Radiology 200:443–451

2.7 Flow Phenomena and MR Angiographic Techniques

M. Bock

2.7.1 Introduction

> "Blut ist ein ganz besonderer Saft."
> [Blood is a very special juice.]
>
> *J. W. Goethe (1749–1832), Faust*

One of the strengths of MRI is the ability to visualize soft tissues with different image contrasts. Additionally, various two and three-dimensional MR imaging techniques for morphologic and functional examinations exist. Among the functional techniques the visualization and measurement of blood flow is of particular interest, since nearly all physiologic processes rely on an adequate blood supply.

As with many other MR imaging techniques, the sensitivity of MRI to blood flow was first observed in artifacts visible near larger blood vessels. To suppress these artifacts new imaging methods have been investigated. In a further refinement of these techniques the artifact (here: the blood flow) has been made the primary source of the imaging technique; thus, in search for new methods of flow artifact suppression the blood flow itself became the contrast-generating element.

The delineation of the vascular tree with MRI, MR angiography (MRA), is such a development: in T_1-weighted 3D gradient-echo data, it was observed that the blood vessel signal of the margin partitions was significantly higher than at the center of the image stack. Furthermore, signal voids were seen in regions of turbulent flow, and in blood vessels with pulsating flow, ghost images of the vessel were visible in phase encoding direction. In the following, the underlying physical phenomena of these artifacts will be discussed, as they form the basis for time-of-flight MRA, phase-contrast MRA, and MR flow measurements.

Since the pioneering work of Prince (1994), many MR angiographies are acquired using contrast-enhanced acquisition techniques. In contrast-enhanced MRA, the signal difference between the bright blood vessel and the dark surrounding tissue is induced by a reduction of the blood's T_1 relaxation time. Again, this technique has evolved from an unwanted vascular signal artifact in spin-echo images acquired after contrast agent injection into a major MR application. With the development of new contrast agents with a longer half-life in the vascular system, the so-called intravascular contrast agents, contrast-enhanced MRA has been developed even further. In this section, techniques for MRA with either intravascular or extracellular contrast agents will be presented.

2.7.2 MR Properties of Blood

The visualization of the blood vessels with MRI relies particularly on the specific properties of blood. Blood consists nearly entirely of liquids, so that blood has a very high spin density and thus yields a strong MR signal. The T_1 time of blood is long compared to that of other tissues (e.g., 1 200 ms at 1.5 T) (Gomori et al. 1987), and it depends on its oxygenation state. Long T_1 values are a disadvantage in T_1-weighted acquisition strategies as the signal decreases with increasing T_1. This disadvantage can be converted into an advantage if the blood signal needs to be suppressed (black-blood angiography) for visualization of the vessel walls. Furthermore, using an inversion (or saturation) recovery technique, the prepared magnetization can be tracked for a longer time, as the preparation persists much longer than in other tissues; this is the basis of arterial spin labeling techniques.

Typical T_2 values are of the order of 150–200 ms (at 1.5 T). This T_2 value is long enough to provide a high signal in the blood vessels using dedicated T_2-weighted image acquisition strategies. With conventional T_2-weighted spin-echo techniques, MR angiographies are difficult to acquire since the motion of the blood needs to be compensated; nevertheless, T_2-weighted MRA pulse sequences for imaging of the peripheral vasculature have been reported (Miyazaki et al. 2000). Another approach is the use of balanced SSFP pulse sequences, where the contrast is dependent on the ratio of T_1/T_2—these fast pulse sequences have found a widespread use in the visualization of the cardiac system.

In addition to the relaxation times, blood velocity is an important parameter. In healthy arterial vessels velocity values between 100 cm/s (e.g., in the aortic arch) and 30 cm/s (e.g., in the intracranial vessels) are common, whereas much lower values are found in the venous vasculature. High blood flow velocities lead to a pronounced inflow of fresh, unsaturated magnetization into an imaging slice, which increases the signal in the blood vessels—this is the well-known time-of-flight contrast. Furthermore, the velocity in the arterial system is not constant but changes as a function of time in the cardiac cycle. This pulsatility can be exploited to separate arterial from venous vessels, if image data are acquired with cardiac synchronization. All of the presented MRA techniques rely on these properties of the blood; some exploit only one of them, whereas others use a combination of them to increase the vascular contrast even further.

2.7.3 Time-of-Flight MRA

In any MR pulse sequence, the magnetization in a measurement slice is exposed to a series of radio frequency (RF) pulses. If the magnetization does not move out of

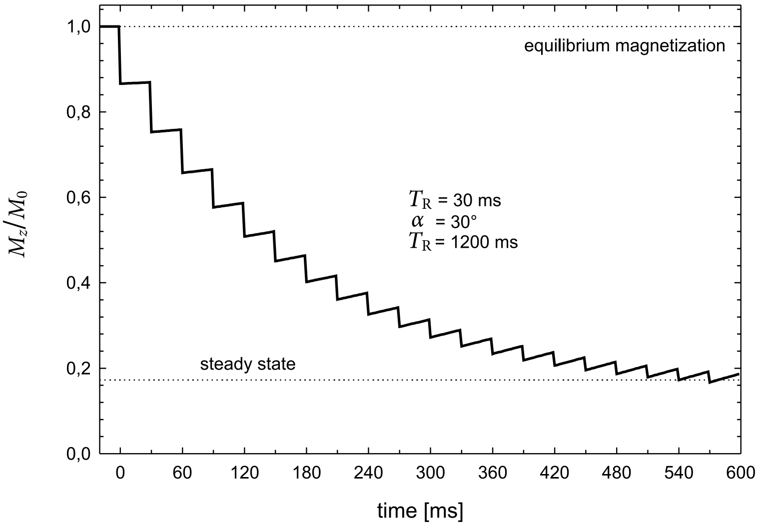

Fig. 2.7.1 Transient longitudinal magnetization, which is subjected to a series of excitation pulses (30°) at a repetition time of 30 ms after entering the readout slice at $t = 0$ during TOF MRA. The longer the blood spins remain in the slice the more they are saturated, and a differentiation between blood and surrounding tissue becomes difficult

the measurement slice (e.g., in static tissue) it approaches a so-called steady state which, for a spoiled gradient-echo pulse sequence, depends on the flip angle, the repetition time T_R, and the relaxation times T_1 and T_2. The steady state magnetization is smaller than the magnetization at the beginning of the experiment—it is partially saturated. Fresh, unsaturated blood flowing into the imaging slice is carrying the full magnetization and thus generates a significantly higher MR signal (Fig. 2.7.1); this is known as time-of-flight (TOF) contrast (Anderson and Lee 1993; Potchen et al. 1993).

A major disadvantage of TOF MRA is the sensitivity to blood signal saturation: the longer the inflowing blood remains in the measurement slice, the more its signal is saturated. In situations where the blood vessel is oriented over a long distance parallel to the imaging slice (or 3D slab), the inflowing magnetization is progressively saturated. Thus, blood appears bright near the entry site but is seen less intense with increasing distance from this position. To maintain the TOF contrast over the whole imaging volume TOF MRA should therefore be performed as a 2D acquisition with thin slices or, if a 3D acquisition technique is preferred, in the arterial vasculature where high-flow velocities result in fewer saturation pulses for the arterial blood.

The inflow effect can be maximized if the measurement slice is oriented perpendicular to the blood vessel. This is often possible for the straight arterial vessels (e.g., the carotids in the head), but can be difficult for extended vascular territories with tortuous vessels. In 3D acquisitions of larger vessel structures, the saturation effect can be partially compensated, if the flip angle is increased from the entry side of the slab to the exit side (Fig. 2.7.2). Thus, the saturation effect is less pronounced during entry, and the magnetization is still visible when it enters smaller vessels that are far away from the entry side. Often, an RF pulse with a linearly increasing flip angle is utilized (tilted optimized non-saturating excitation, or TONE [Nagele et al. 1995]). For an optimal vessel contrast the blood flow velocity, the repetition time, the mean flip angle, and the slope of the RF pulse profile are important parameters.

In 2D TOF MRA, a very strong TOF contrast can be achieved, if the slice thickness D is chosen such that the magnetization flowing with a velocity v is completely replaced during one T_R interval, i.e. $D \leq T_R \cdot v$. At a typi-

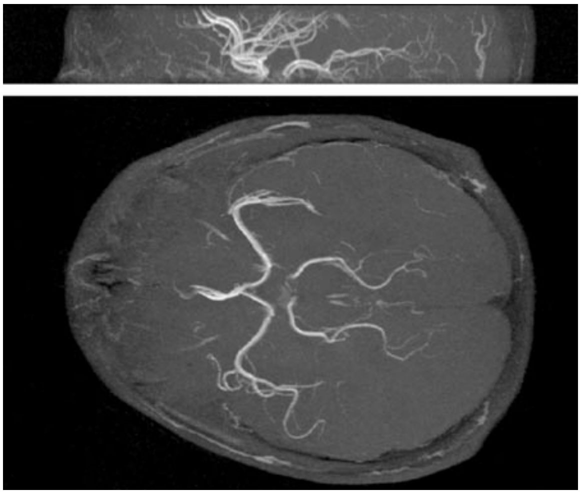

Fig. 2.7.2 3D TOF MRA data set of the intracranial vasculature in lateral (*top*) and axial (*bottom*) maximum intensity projection. To minimize saturation, a TONE RF pulse was used for excitation, and the signal from static brain tissue was additionally suppressed using magnetization transfer pulses

Fig. 2.7.3 Motion artifacts in lateral views of multi-slice 2D TOF MRA data sets of the arterial vasculature in the neck. Due to swallowing, the blood vessel can move from one acquisition to the next, and the edges appear with discontinuities in the lateral views of the maximum intensity projection

cal T_R of 10 ms and a blood flow velocity of 40 cm/s, the slice thickness should thus not be larger than 4 mm. With these small slice thicknesses, the data acquisition in larger vascular territories such as the legs is very time-consuming, and patient movements cannot be excluded during the several minutes of scan time. Patient movements lead to artificial vessels shifts between the imaging slices, which are particularly observed in orthogonal data reformats—these artifacts can mimic pathologies such as stenoses and thus significantly reduce the diagnostic quality of the data sets (Fig. 2.7.3).

3D TOF MRA is advantageous over sequential 2D TOF MRA because an isotropic spatial resolution in all directions can be achieved. To reduce the saturation effects in 3D TOF MRA not only one thick, but also several thinner 3D slabs are acquired consecutively. Thus, the saturation effects are smaller for the individual slabs and a stronger TOF contrast is seen. Unfortunately, the flip angle in fast 3D acquisitions is not constant over the slab, but is declining towards its margins. This inhomogeneous excitation results in a higher signal for the stationary tissue at the slab margin, providing an inhomogeneous signal background in lateral views of the data. Combined with a higher TOF contrast at the entry side compared with the exit side, spatially varying signal intensity is seen in lateral views of the whole data set (venetian blind artifact). To reduce this artifact, overlapping 3D slabs are acquired (multiple overlapping thin slab acquisition, or MOTSA [Parker et al. 1991]), and the marginal slices of each slab are removed; however, this results in an increased total scan time.

To increase the contrast between the blood vessels and the surrounding tissue in TOF MRA, often magnetization transfer pulses are included in the pulse sequences (Edelman et al. 1992). Using off-resonant RF pulses, the magnetization transfer contrast (MTC) selectively saturates those tissues where macromolecules are present. For brain tissue, these additional RF pulses can reduce the signal from background tissue by 40% and more, which increases the conspicuity especially of the smaller blood vessels. The use of magnetization transfer pulses however increases the minimally achievable T_R and, thus, the total acquisition time. Additionally, through the integration of the MTC pulses more RF power is applied to the patient, so that the regulatory power limits for the specific absorption rate (SAR) might be exceeded, an effect that is more pronounced at higher field strengths. Nevertheless, MTC is often included in intracranial TOF MRA protocols where longer T_Rs can be an advantage, as long T_Rs additionally reduce the saturation effect.

The flow velocity in arteries is typically not constant but varies over the cardiac cycle. Thus, the TOF contrast is a function of time, so that for image acquisition times that are longer than one cardiac cycle, a signal variation during *k*-space sampling is present. This periodic signal variation results in phantom images of the blood vessels in phase encoding direction after image reconstruction: the so-called pulsation artifacts or ghost images (Haacke and Patrick 1986; Wood and Henkelman 1985). To avoid pulsation artifacts, the image acquisition can be synchronized with the cardiac cycle using ECG triggering, which typically prolongs the total acquisition time, as only part of the measurement time is used for data acquisition. Another option to reduce pulsation artifacts is to saturate the inflowing blood in a slice upstream of the imaging slice. Therefore, a slice-selective RF excitation is applied in a (typically parallel) saturation slice, so that the magnetization of the inflowing blood is significantly reduced. Spatial presaturation avoids pulsation artifacts; however, the interior of the blood vessel now has a negative contrast, and the positive TOF contrast is gone.

Another important ingredient of a TOF MRA pulse sequence is flow compensation (cf. paragraphs on flow measurements, below): The movement of the spins causes an additional velocity-dependent phase shift that is seen in TOF MRA data sets without flow compensation as a displacement. If multiple velocities are present as in turbulent flow, the different phases can cause signal cancellation (intra-voxel dephasing) that manifests, e.g., as a signal void behind a stenosis (Saloner et al. 1996). With special compensation gradients the velocity-dependent phase shifts can be reduced; however, this typically prolongs the echo time T_E.

TOF MRA is susceptible to several artifacts and is strongly dependent on a sufficient inflow velocity of unsaturated blood. Therefore, 3D TOF MRA techniques are typically only used in the head, where the arterial flow velocities are high and enough time is available for imaging. For abdominal studies, TOF techniques are of minor interest, because long measurement times are not possible due to respiratory motion.

2.7.4 Arterial Spin Labeling

In conventional TOF MRA, the difference in longitudinal magnetization between the saturated stationary tissue and the unsaturated inflowing blood is exploited to create a positive contrast between blood and tissue. With arterial spin-labeling techniques, a similar approach is taken to the visualization of the inflowing blood; however, here only a certain fraction of the inflowing blood is tagged (or labeled) and subsequently visualized, whereas in TOF MRA all inflowing material is detected (Detre et al. 1994).

Spin-labeling pulse sequences consist typically of a labeling section, during which an RF pulse is applied to the spins upstream of the imaging slice (Fig. 2.7.4). For labeling often adiabatic inversion pulses are used, which are less susceptible to motion during the inversion and that allow inverting the magnetization even in RF coils with a limited transmit homogeneity (e.g., a transmit/receive head coil).

After an (often variable) inflow delay time T_I, during which the labeled blood is flowing into the vascular target structure, the signal in the imaging slice is acquired. For signal reception different image-acquisition strategies can be employed such as segmented spoiled gradient-echo (FLASH), fast spin-echo (RARE, HASTE), or even echo planar imaging (EPI). Note: This image data set contains both the signal from the labeled blood and the static background tissue.

In a second acquisition, the entire pulse sequence is repeated without labeling of the blood, and a second image data set is acquired. To selectively visualize only the labeled blood the two data sets are subtracted; since the signal intensity of the blood differs in both acquisitions, a non-vanishing blood signal is seen, whereas the signal contribution from static tissue cancels. If the phase of the second image data set is shifted by 180° compared to the first, labeled data set, the images can be added (the minus sign is provided by the phase), and the technique is called signal targeting with alternating radiofrequencies (STAR) (Edelman et al. 1994).

In clinical MRI systems, arterial spin labeling (ASL) is typically implemented with the described labeling pulses, which are applied only once per data readout; this approach is also termed pulsed arterial spin labeling (PASL). Another method for ASL uses a small transmit coil for the labeling pulse, which continuously applies an RF pulse to the arterial vessel, and thus achieves a much higher degree of inversion. Unfortunately, these continuous ASL techniques often cannot be used in a clinical MR system due to the regulatory constraints for the maximum RF power applied to the patient (SAR limits).

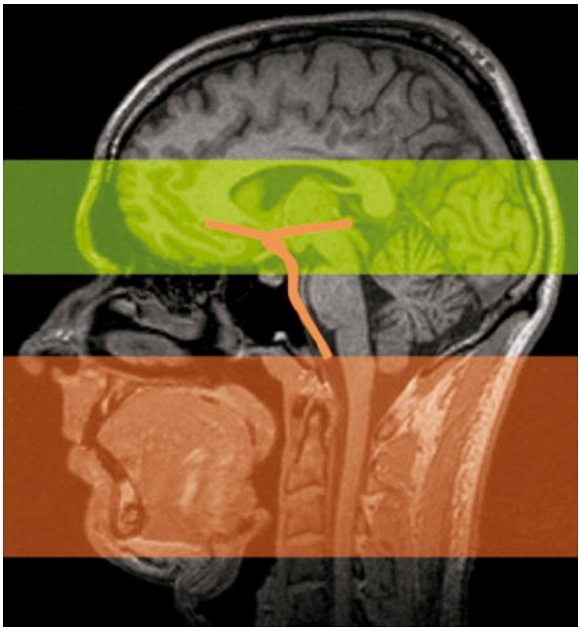

Fig. 2.7.4 Concept of arterial spin labeling: magnetization is prepared (e.g., using a slice-selective inversion pulse) in a section of the artery (*red*). After an inflow delay of several hundred milliseconds, the magnetization has reached the imaging slice (*green*), and an image is acquired. The procedure is repeated without preparation, and the two data sets are subtracted to remove the signal background from static tissue

ASL techniques are typically applied to study perfusion in the brain and other organs, where the inflow delay is chosen long enough for the labeled blood to have reached the capillary bed (Golay et al. 2004). Unfortunately, the labeling in the blood does not persist for much longer than one T_1 time (i.e., 1–2 s at 1.5 T), and the signal differences are generally very small (2–5% of the total signal), which makes perfusion measurement ASL a time-consuming procedure.

Another application to ASL is the time-resolved visualization of blood flow, e.g., in intracranial malformations (Essig et al. 1996), where saturation effects limit the diagnostic quality of conventional 3D TOF MRAs. Here, dynamic ASL data sets are acquired at a series of inflow delays to visualize the transit of the labeled bolus through the nidus of the malformation, and, more importantly, the arrival of the blood in the draining venous vessels,

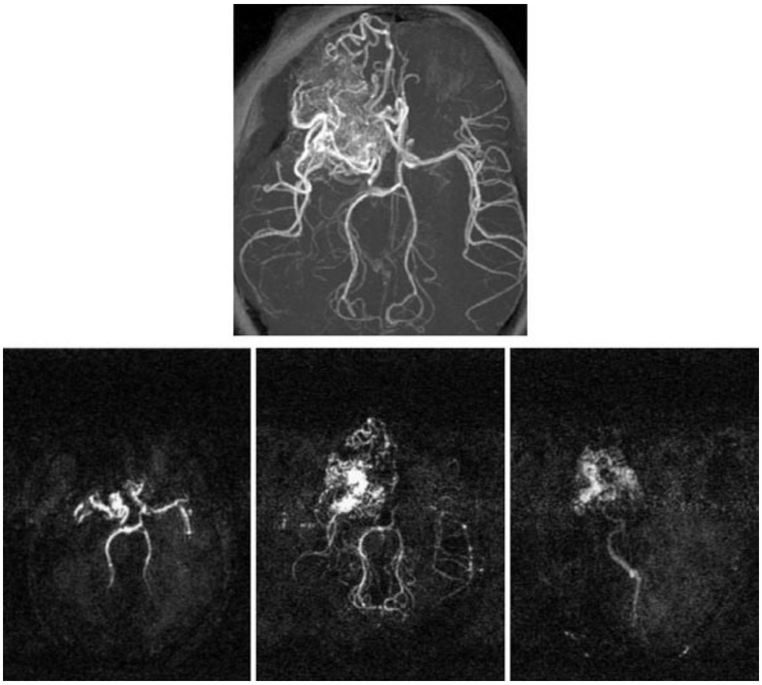

Fig. 2.7.5 TOF MRA (*top*) and time-resolved dynamic MRA with arterial spin labeling (*bottom*) of an intracranial arteriovenous malformation. In the TOF MRA, the nidus of the malformation is clearly seen, but the draining vein can hardly be identified because the inflowing blood is already completely saturated when it arrives in this part of the AVM. In the three ASL images acquired 100, 600, and 1 200 ms after signal preparation, the filling of the nidus and the drainage through the vein is clearly visible

that cannot be seen on the TOF data sets (Fig. 2.7.5). In addition to a morphologic representation of these blood vessels, transit-time measurement of the blood becomes feasible, which could be used as an indicator, e.g., for an increase in vascular resistance after a radiation therapy.

2.7.5 Native-Blood Contrast

MR angiographies can also be acquired using the special contrast properties of blood. In balanced steady state free precession pulse sequences (bSSFP, trueFISP, FIESTA), an image contrast is created that depends on the ratio of the relaxation times T_1 and T_2 (Oppelt et al. 1986). For blood, this ratio is high, and thus the interior of the blood vessels are shown with higher signal intensity than the surrounding tissue. Unfortunately, other liquid-filled spaces such as the ventricles also appear with a bright signal, so that conventional MRA post-processing strategies such as the maximum intensity projection cannot be used to visualize the vascular tree (Fig. 2.7.6).

Despite their short repetition times and balanced gradient schemes, these pulse sequences are susceptible to flow artifacts caused by intra-voxel dephasing, which can be compensated using flow-compensation gradients (Storey et al. 2004; Bieri and Scheffler 2005). Another problem with balanced steady state pulse sequences is the susceptibility to off-resonance artifacts: Since both transverse and longitudinal magnetizations contribute to the MR signal, perfect phase coherence must be maintained within one T_R to establish the desired contrast. In off-resonant regions, this phase coherence is perturbed, and a contrast variation is seen in the form of dark bands. The banding artifacts can be reduced using a repetition time that is shorter than the inverse of the off-resonance frequency, i.e., for a 200-Hz off-resonance, the T_R should be shorter than 5 ms. Off-resonance frequencies scale with field strength, so that banding artifacts become an increasing problem at higher field strengths. Nevertheless, fast balanced SSFP pulse sequences are increasingly used in MRA studies of the heart and the neighboring vessels in combination with ECG triggering to visualize the vascular anatomy and to assess.

2.7.6 Black-Blood MRA

In conventional spin-echo images, one often observes that the interior of the blood vessels is darker than the surrounding tissue. This so-called black-blood contrast is caused by an incomplete signal refocusing of the 180° pulse. Compared with TOF MRA with gradient-echo sequences, where the inflow of blood causes signal amplification, spin-echo sequences attenuate the signal from flowing blood because spins leave the imaging slice between the 90° excitation pulse and the 180° refocusing pulse, and thus do not contribute to the MR signal. Therefore, blood signal attenuation can be increased with a longer spacing between the two RF pulses, i.e., with longer echo times T_E. To further suppress signals from slowly flowing blood near the vessel walls, often addi-

Fig. 2.7.6 Balanced SSFP image (*left*) and contrast-enhanced MRA (*right*) of the heart and the abdominal aorta of a patient. In this image blood is seen with high signal intensity; however, the surrounding tissue also appears with a strong MR signal. In the ascending aorta, signal voids are seen which are caused by turbulent flow, and banding artifacts are visible in the subcutaneous fat. Nevertheless, balanced SSFP sequences provide good angiographic overview images in very short acquisition times, without the need for contrast agent injection. In the contrast-enhanced data acquisition, a better background suppression is possible, and the projection image of the 3D data set clearly delineates the aorta and the adjacent vessels

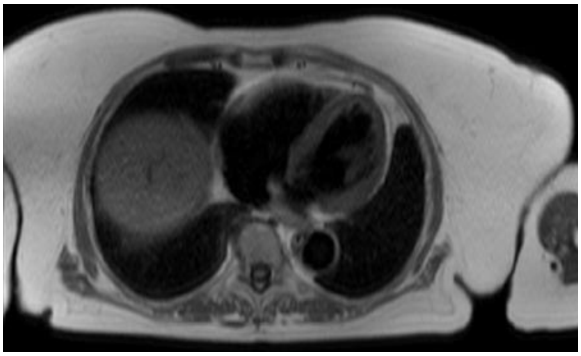

Fig. 2.7.7 ECG-triggered dark blood image of the heart acquired with a single-shot fast spin-echo technique (HASTE). The blood signal both in the heart and in the cross-section of the descending aorta is completely suppressed

tional strong gradients are introduced in the black-blood pulse sequences, which cause an increased intra-voxel dephasing and thus suppress the signal (Lin et al. 1993).

A different technique for blood signal suppression makes use of an inversion recovery blood signal preparation (Edelman et al. 1991): Similar to arterial spin labeling a non-selective 180° inversion pulse is applied; however, the signal in the imaging slice is reinverted by a subsequent slice-selective inversion pulse. With this preparation ‚the magnetization of the blood (and of all other tissues) outside the imaging slice is selectively inverted. After a delay-time that is chosen to achieve a zero crossing of the longitudinal magnetization of the inverted blood, an image is acquired. If the blood has been completely exchanged during the delay, then the signal of the labeled blood is nulled and only the static tissue is visible. This technique is often used in combination with cardiac triggering to visualize, e.g., the myocardium (Fig. 2.7.7). In cardiac black-blood applications, both techniques are combined, which is possible, because data are acquired during diastole when the heart is nearly at rest, whereas the signal preparation is applied during systole.

2.7.7 Velocity-Dependent Phase

The TOF contrast relies on the increase in signal amplitude due to the inflow of unsaturated magnetization. In addition to elevated signal amplitude, the spin movement can also create a change in the phase of the MR signal. If a gradient is turned on and blood moves along the gradient direction (here: the *x*-direction), the phase $\phi(\mathrm{t})$ of the MR signal is given by:

$$\begin{aligned} \varphi(t) &= \gamma \int_0^t G(t')x(t')\mathrm{d}t' \qquad (2.7.1) \\ &= x_0 \cdot \gamma \int_0^t G(t')\mathrm{d}t' + v_0 \cdot \gamma \int_0^t G(t')t'\,\mathrm{d}t' + \dots \\ &\approx \gamma(x_0 \cdot M_0 + v_0 \cdot M_1)\ . \end{aligned}$$

Here, the motion $x(t)$ of the magnetization is expressed as a Taylor series, and only the constant term (i.e., the initial position x_0) and the linear term (i.e., the velocity v_0) are considered. The two integrals M_0 and M_1 solely depend on the gradient timing and are called the zeroth and first moment of $G(t)$. The next higher order term is proportional to the acceleration of the spins; however, the proportionality constant M_2 only becomes large if long time scales are considered; thus, the estimation of the spin phase from the zeroth and first moments is justified for gradient-echo sequences with short echo times.

If the gradient timing is modified such that the first moment is zero, the gradients are called flow compensated. Flow compensation is important ingredient in many MR pulse sequences: If a range of velocities is present in a single voxel, then the MR signal amplitude is attenuated due to the incoherent addition of the signals. With flow compensation, the individual signals all have the same phase, and the signals of the different velocities add up coherently. Flow compensation is especially important in regions of high velocity gradients as, e.g., turbulent jets or in highly angulated vessels.

In general, both M_0 and M_1 will be non-vanishing, and the phase of the signal will become proportional to the local spin velocity. Unfortunately, many other factors such as off-resonance, field inhomogeneity, or chemical shift also affect the spin phase, so that a direct velocity measurement is not possible with a single MR experiment alone. To create an MR image that is dependent on the local velocity, a minimum of two image acquisitions are required. In the first, velocity-sensitized acquisition a gradient timing is used with a carefully selected, non-vanishing first gradient moment (the zeroth moment is defining the spatial encoding, i.e., the *k*-space trajectory). In a second, flow-compensated acquisition, a gradient timing is chosen that cancels M_1.

2.7.7.1 Flow Measurements

If the two phase images are directly subtracted, the result is a phase difference image that is linearly dependent on the spin velocity: this is the basis of an MR flow measurement (Bryant et al. 1984). Since phase data are only unambiguous in the angular range of ±180°, so is the velocity information in an MR flow measurement. To avoid artifacts due to multiple rotations of the spin phase (so-called wrap around artifacts), the first moment needs to be chosen such that the maximum velocity in the image creates a phase shift of 180°. In general, this velocity is set via the so-called velocity encoding, or VENC, parameter in the pulse sequence. Higher VENC values require weaker encoding gradients, which can be realized in shorter echo times. Despite an inadequate choice of the VENC value, MR flow measurements are susceptible to phase noise, which is present in regions of low signal amplitude. If the SNR is 1 or less, the phase in the image is nearly uniformly distributed between −180° and +180°; under these conditions a meaningful flow measurement is not possible. Unfortunately, phase noise is also often present near blood vessels (e.g., in the air-filled spaces of the lung, close to the pulmonary vessels). Here, the measurement of velocity values requires a very careful placement of the regions of interest (ROIs) to avoid systematic errors from included noise pixels.

In a conventional flow measurement, velocity encoding is typically performed in slice-selection direction only, because the orthogonal placement of the flow measurement slice induces a high TOF signal in the cross-section of the vessel lumen. Additionally, a parallel orientation of the velocity encoding direction with the image plane makes the image acquisition susceptible to systematic errors due to displacement, as, e.g., the readout gradient are used for both spatial encoding and velocity measurement simultaneously.

Flow measurements in arterial vessels are often performed with cardiac synchronization to account for the pulsatility of the blood flow. Cardiac synchronization can be performed by prospective ECG triggering or retrospective ECG gating. With prospective triggering, data acquisition is started by a trigger signal, which is generated by the ECG electronics during the QRS complex of the ECG (Fig. 2.7.8). After data have been acquired for a certain number of cardiac phases, the measurement sequence is stopped until a new cardiac trigger signal is detected. In retrospective gating, image data are continuously acquired, and the time between the last trigger and the current data set is stored. Later, data are resorted into predefined time intervals (bins) in the cardiac cycle, and the images are reconstructed. Prospective triggering is less time-consuming during image reconstruction and is very precise in the delineation of the cardiac activity; however, a temporal gap at the end of the cardiac cycle is required and thus flow measurements at late diastole are difficult.

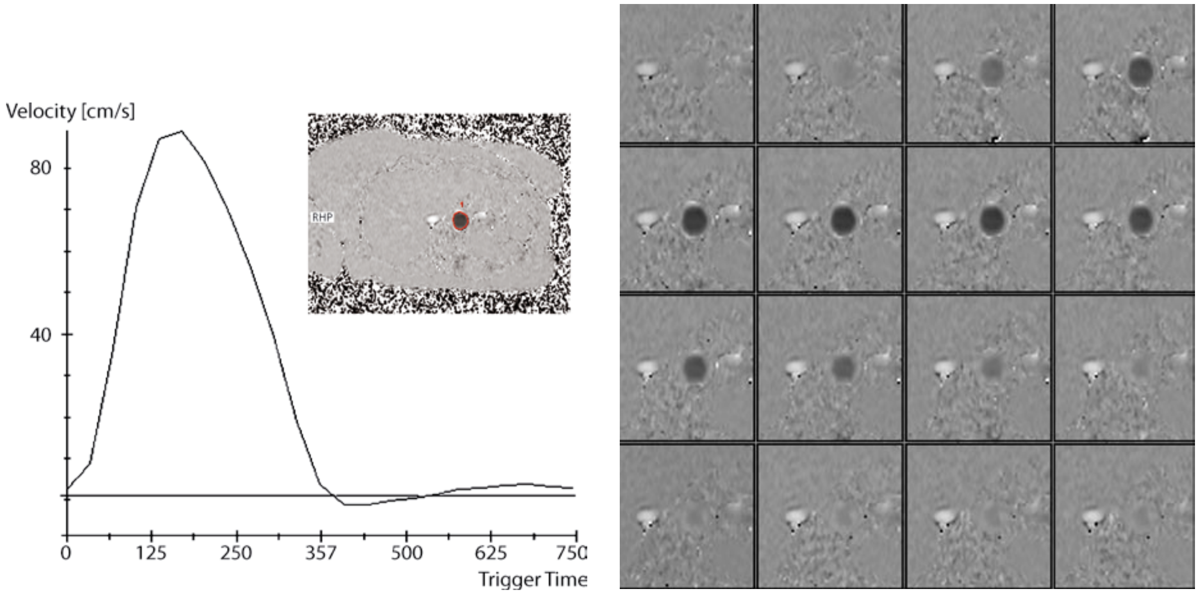

Fig. 2.7.8 ECG-triggered MR velocity measurement showing a typical velocity time curve in the aorta (*left*). From the phase-difference images, the mean velocity in the aorta are calculated after a region of interest is defined around the cross section of the blood vessel. (*right*) The enlarged region around the aorta and the vena cava shows the aortic pulsating flow (*dark, round region*) and the nearly constant flow (*bright region*) in the opposite direction

Prospective gating uses continuous image acquisition, and the magnetization steady state is always maintained. Unfortunately, more data need to be acquired than with prospective triggering to ensure a sufficient coverage of the cardiac cycle, and a temporal blurring due to the interpolation is seen in the velocity data.

2.7.7.2 Phase-Contrast MRA

When the complex image data of the two acquisitions are subtracted instead of the phases, and the magnitude of the difference is displayed, a so-called phase-contrast MRA image is created (Dumoulin 1995). This PC MRA image is not only dependent on the velocity of the spins, but also on the signal amplitude in both acquisitions; thus, every PC MRA data set always has an overlaid TOF contrast (Fig. 2.7.9). An advantage of PC MRA is the fact that signal background of the surrounding stationary tissue is almost completely suppressed, and vessels can be traced further into the vascular periphery than with TOF MRA, with comparable measurement parameters. In PC MRA, often not only the velocity in one spatial direction is encoded, but in all three directions. Since separate velocity-encoded acquisitions have to be performed for each direction, the measurement time of a PC MRA is two- to fourfold longer than that of a TOF MRA.

A careful selection of the VENC value is especially important in PC MRA. If, e.g., the maximum velocity in the imaging slice is twice the VENC value, a phase shift of 360° (or 0°, which cannot be distinguished) is created. Under these conditions, the velocity-encoded and the velocity-compensated acquisition have the same phase, and no PC MRA signal would be observable. As blood does not flow with a constant velocity and velocity values can be reduced by pathologies (aneurysms) or increased (stenoses), the optimum choice of VENC value is often difficult. Because PC MRA is more time-consuming, is susceptible to artifacts, and suffers from the same signal saturation as TOF MRA, it is rarely used in clinical routine.

2.7.8 Contrast-Enhanced MRA

With TOF and PC MRA techniques, the blood motion is used to create a signal difference between the vessel lumen and the surrounding tissue, whereas contrast-enhanced MRA utilizes the reduction of the longitudinal relaxation time T_1 after administration of a contrast agent. When a contrast agent is injected, the T_1 of blood is shortened from $T_{1\text{blood}}$ = 1.2 s (for B_0 = 1.5 T) to less than 100 ms during the first bolus passage (first pass). The relaxation rate R_1 (i.e., $1/T_1$) is a function of the local contrast agent concentration:

$$R_1(C) = \frac{1}{T_1} = \frac{1}{T_{1\,\text{blood}}} + r_1 \cdot C. \qquad (2.7.2)$$

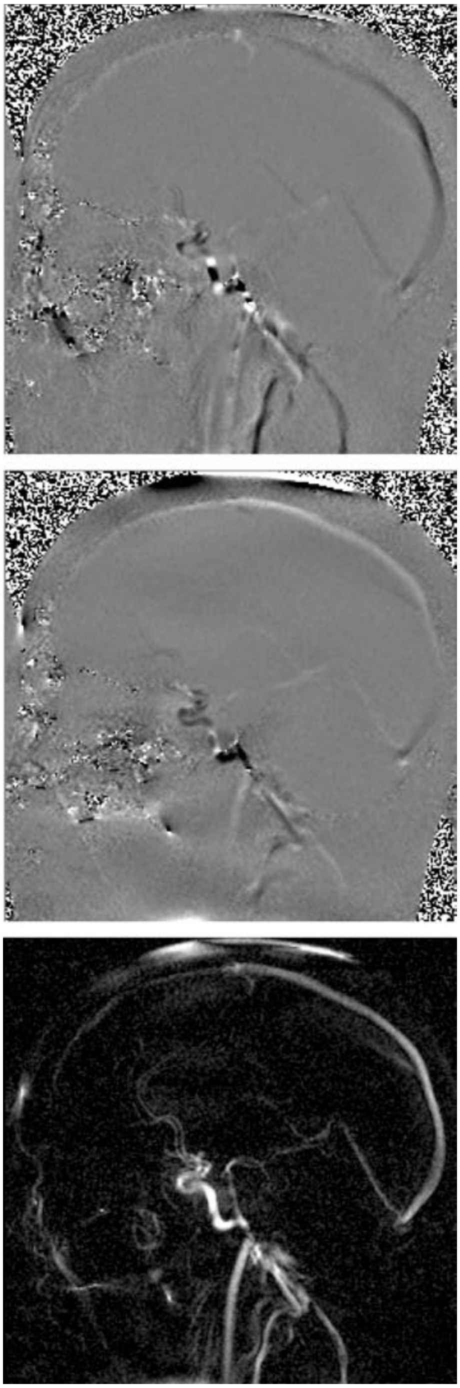

Fig. 2.7.9 Phase-contrast images encoding flow in head–foot (*top*) and left–right (*center*) direction, and phase contrast MRA image (*bottom*). In the flow images, a velocity-sensitive and a velocity-compensated data set are subtracted, whereas the PC MRA image is generated by complex subtraction of the respective signal amplitudes. Note, that the PC MRA image has nearly no background signal from static tissue

The proportionality constant between contrast agent concentration C and the change in relaxation rate is called the relaxivity r_1. The relaxivity is different for each contrast agent – typical values range from 4 to 10 $\text{mmol}^{-1}\text{s}^{-1}$. In general, high relaxivities are desirable because lower contrast-agent concentrations are needed to achieve the same change in image contrast.

To enhance the signal in the contrast agent bolus and to suppress the signal background from static tissue, heavily T_1-weighted spoiled gradient-echo sequences (FLASH) with very short repetition times ($T_R < 5$ ms) and high flip angles ($\alpha = 20^\circ$–50°) are used (Fig. 2.7.10). The use of short T_Rs is advantageous because very short acquisition times of only a few seconds can be achieved even for the acquisition of a complete 3D data set. These short acquisition times are needed, because the contrast agent is progressively diluted during the passage, which reduces the vessel-to-background contrast. Short acquisition times are also favorable because MRA data sets can thus be acquired in a single breath hold; for this reason, contrast-enhanced MRA techniques are especially suited for abdominal applications (Prince 1996; Sodickson and Manning 1997).

To ensure isotropic visualization of the vascular territories, typically 3D techniques are used for data acquisition. Conventional 3D techniques have measurement times of several minutes, so that even with short repetition times larger parts of the k-space data are acquired after the contrast agent concentration has fallen to levels where only a weak signal enhancement is observable. For this reason, the measurement times are reduced using partial k-space sampling, parallel imaging, and view sharing between subsequent 3D data sets (Sodickson and Manning 1997; Wilson et al. 2004; Goyen 2006).

In general, contrast agents can be categorized into extracellular agents that can leave the blood stream and intravascular agents that are specifically designed to remain in the vascular system. Historically, the first approved MR contrast agent was Gd-DTPA (gadopentate dimeglumine, Magnevist, Schering, Germany), an extracellular agent, which has the paramagnetic Gd^{3+} ion as the central atom in an open-chain ionic complex (chelate). Over the years, several similar extracellular agents such as Gd-BT-DO3A (Gadovist, Schering), Gd-DOTA (Dotarem, Guerbet, France), Gd-BMA (Omniscan, GE Healthcare), Gd-HP-DO3A (ProHance, Bracco Imaging, Italy), and Gd-BOPTA (MultiHance, Bracco, Italy) have been approved for clinical use, which only slightly differ in the stability of the Gd chelates, pharmacokinetic properties, and safety profiles. In general, the most recently approved contrast agents have higher relaxivities and thus allow acquiring MRA data sets with higher contrast at the same dose or with similar contrast at lower dose.

Only recently, the first intravascular contrast agent gadofosveset trisodium (Vasovist, Schering) has been approved for clinical use in Europe (Goyen 2006). This

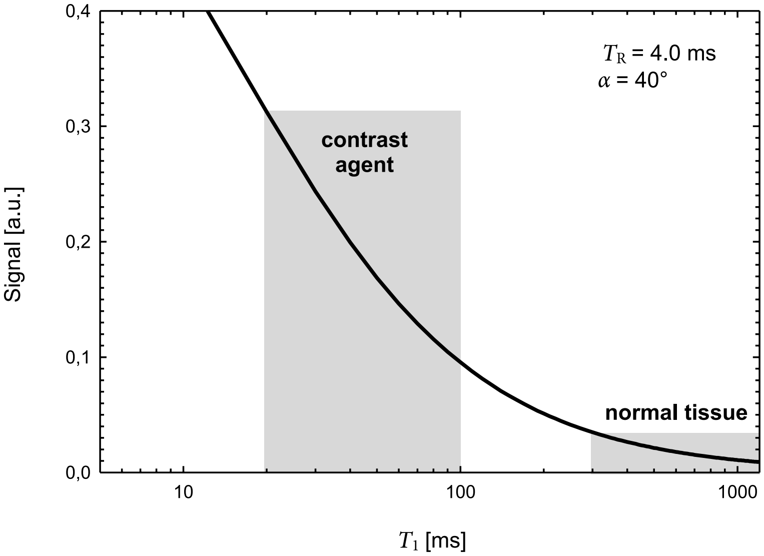

Fig. 2.7.10 Signal intensity as a function of T_1-contrast in a spoiled gradient-echo pulse sequence (FLASH). At high flip angles and short repetition times the signal from tissue (T_1 > 300 ms at 1.5 T) is nearly completely saturated, whereas a high intraluminal signal is seen due to the high concentrations of the contrast agent

molecule has a diphenylcyclohexyl group, which is covalently bound to a Gd complex, which creates a reversible, non-covalent binding of the molecule to serum albumin that significantly prolongs the half-life of the agent in blood to about 16 h. After injection of the agent, at first a more rapid decline of concentration is observed, because the fraction of the contrast agent bound to albumin is dependent on the contrast agent concentration; thus, a steady-state concentration is established after the unbound fraction is renally excreted.

Both extracellular and intravascular agents can be imaged during the first pass of the contrast agent, when a high vessel-to-background contrast is present, whereas intravascular contrast agents additionally allow angiographic imaging during the subsequent steady state.

2.7.8.1 First-Pass Studies

The T_1 shortening is dependent on the contrast agent concentration, which is getting smaller already a few seconds after infusion of the contrast agent, as the contrast agent bolus in the blood is increasingly diluted and, for the extracellular agents, the contrast agent is extravasculized. Therefore, contrast-enhanced MRA techniques usually use pulse sequences with very short acquisition times (T_A < 30 s).

The short passage time of the contrast agent bolus of a few seconds requires that imaging be precisely synchronized with the contrast agent infusion. The transit time of the bolus from the point of injection (usually a vein in the arm) through to the vascular target structure (e.g., the renal arteries) varies significantly with the heart rate and cardiac output and can be difficult to predict. Therefore, various synchronization and acquisition techniques have been proposed for a reliable MRA data acquisition:

- **Automatic Start**
  An automatic technique to start the 3D MRA data acquisition (SmartPrep™, General Electric) uses a fast pulse sequence before the 3D MRA, which continuously acquires the signal in the vascular target region (Prince et al. 1997). After administration of the contrast agent, this signal exceeds a certain signal threshold, and the 3D MRA acquisition is automatically started. If the signal threshold is selected too low, image noise can mimic a bolus arrival and the measurement is triggered too early, whereas a too high value of the threshold can lead to an omission of the data acquisition.
- **Test Bolus**
  With the test bolus technique, a small bolus of a few milliliters of the contrast agent is infused, and the passage of the bolus is imaged near the target vessel with a fast time-resolved 2D MR measurement (Earls et al. 1997). The trigger delay T_D for the subsequent 3D measurement is then calculated from the transit time of the bolus T_T and the acquisition time of the 3D MRA T_A as: $T_D = T_T - n_{echo} \times T_A$. Here, n_{echo} denotes the fraction of T_A before the center of k-space is acquired (Fig. 2.7.11).
- **MR Fluoroscopy**
  As in the automatic start of the sequence, fluoroscopic previews (CareBolus™, Siemens Medical Solutions) image the contrast bolus during its passage; however, here fast 2D sequences are used with real-time image reconstruction and display Riederer et al. 1988; Wilman et al. 1997). Once the bolus has reached the target region, the operator of the MR scanner manually switches to the predefined 3D MRA pulse sequence, which is then executed with minimal time delay.

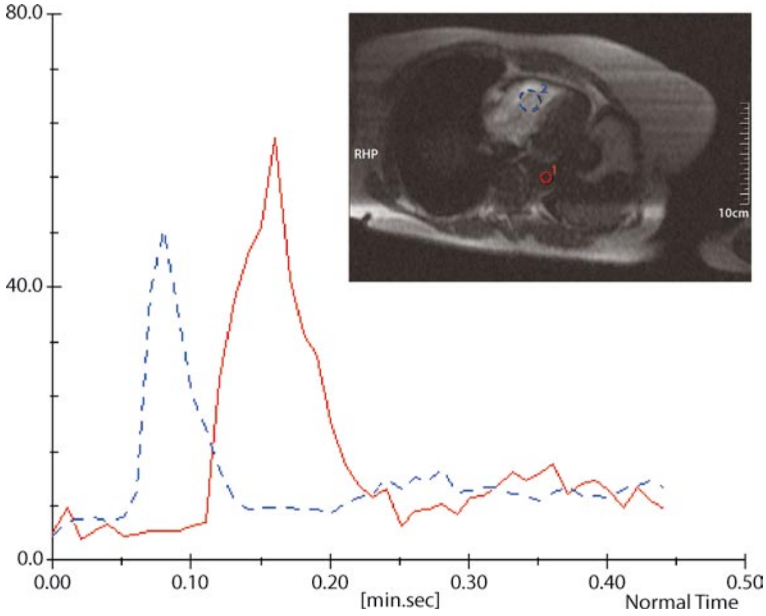

Fig. 2.7.11 Test bolus measurement in the heart (*blue*) and the aorta (*red*) of a patient. For an optimal visualization of the aortic arch, a time delay of 16 s is required between contrast agent injection and the acquisition of the central *k*-space lines

- **Multiphase MRA**
  Time-resolved MRA has been increasingly used to completely avoid manual or automated synchronization. Multiphasic acquisitions consecutively acquire 3D MRA data sets during the bolus passage so that the optimal vessel contrast is obtained in at least one of the data sets. Various methods of measurement acceleration are combined to ensure adequate temporal resolution; these include parallel imaging, asymmetric *k*-space readout, and temporal data interpolation (Korosec et al. 1996; Fink et al. 2005). Nevertheless, time-resolved MRA data sets are usually of a lower spatial resolution than are optimally acquired MRA data with bolus synchronization (Fig. 2.7.12).

Artifacts arise, if the 3D MRA data acquisition is not perfectly synchronized with the bolus passage. The appearance of these artifacts depends on the relative timing of the *k*-space acquisition and the concentration-time curve of the contrast agent. If the bolus arrives too late in the target vessel, then the center of the *k*-space has already been sampled and large structures, such as the interior of the blood vessel, appear dark, whereas fine structures, such as vessel margins, have a high signal if the bolus arrives during sampling of the *k*-space periphery. If the data acquisition is started too late, then the bolus has already reached the target vessel and the contrast has partly disappeared – thus, the signal is significantly reduced compared with an optimally synchronized data acquisition (Maki et al. 1996; Wilman et al. 2001; Svensson et al. 1999).

Another disadvantage of suboptimal bolus timing is the fact that the bolus may have passed from the arterial to the venous system in some vascular regions (e.g., the extremities) so that both veins and arteries are seen in the images. This venous contamination makes the interpretation of the image data difficult in cases where arterial and venous vessels are parallel to each other.

The variation in contrast agent concentration over time also results in a reduction in the achievable image resolution (Fain et al. 1999). The spatial resolution of an MR image sampled with Cartesian data acquisition is always uniquely defined by the measured number of *k*-space lines. With increasing number of *k*-space lines (i.e., larger *k*-space coverage), finer image details are encoded in the image. This so-called Nyquist scanning theorem only applies if the signal intensity is constant during data acquisition. Even with perfect synchronization with the contrast agent bolus, the contrast agent concentration is only optimal during acquisition of the central *k*-space lines. Later on, the concentration is reduced and the peripheral *k*-space regions are acquired with significantly reduced signal intensity (Fig. 2.7.13). This different weighting of the *k*-space regions results in a reduction in spatial resolution (blurring), which is mathematically described by the point-spread function, PSF. The PSF is the image of a point object – for linear imaging systems, it is used to describe the imperfections of the image acquisition system. The PSF depends on the acquisition time, the contrast agent dynamics, and the measurement parameters of the pulse sequence.

The deviation from an ideal PSF is particularly visible in those spatial directions that are acquired with the lowest sampling velocity. In conventional 3D acquisition, this is either the phase encoding direction or the partition encoding direction. To eliminate this asymmetry and to

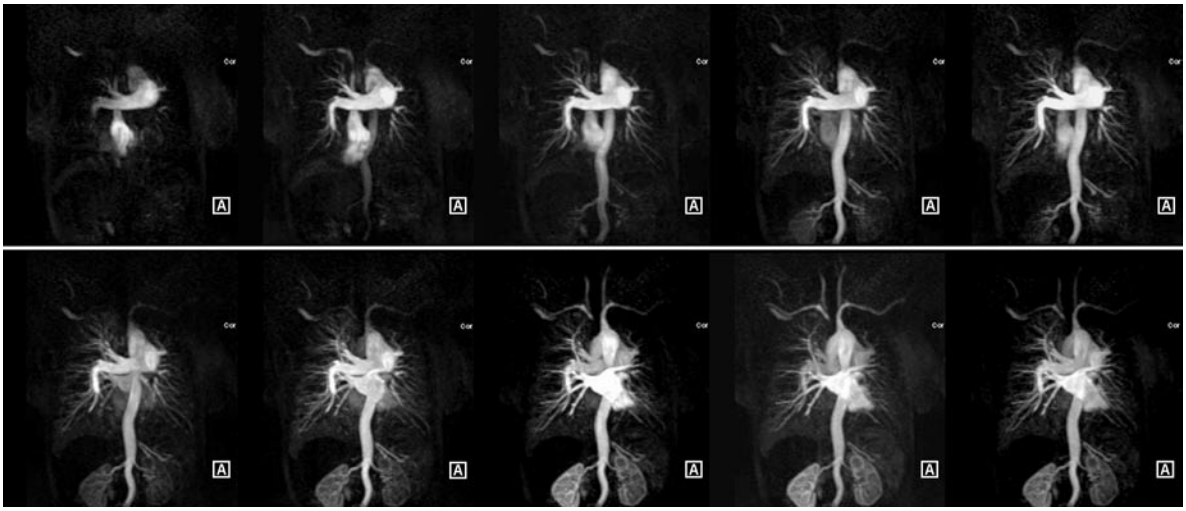

Fig. 2.7.12 Multiphase MRA of the lung vasculature in a patient with a patent ductus arteriosus. The irregular flow pattern of the early enhancing descending aorta is clearly identified in the time series of 3D MRA data sets. To achieve a high temporal resolution of 2.3 s, temporal interpolation techniques (TRICKS) were applied. In the later phases, additionally, a qualitative assessment of lung perfusion is possible

evenly distribute the blurring in both spatial directions, elliptical scanning of the phase and partition encoding steps has been proposed (Bampton et al. 1992; Wilman and Riederer 1996; Wilman et al. 1996), where the encoding steps are acquired along an elliptical path, starting from the center of the *k*-space.

Using the signal–time curve of a test bolus, the signal variation during data acquisition can be avoided. Therefore, an injection scheme is calculated for the signal–time curve using linear system theory, where the injection rate is modulated such that there is a constant contrast agent concentration (i.e., an ideal PSF) in the target region throughout the data acquisition. This technique requires a programmable contrast-agent injector and additional computations, and the constant concentration can only be achieved in a limited target volume. Another option for reducing the intensity changes is to induce a blood flow stasis for a brief period after contrast agent inflow. This can be achieved in the peripheral blood vessels, without endangering the patient using an inflatable cuff, which temporarily blocks the blood flow during data acquisition; this technique has been used successfully applied to contrast-enhanced MRA studies of the hand (Zhang et al. 2004) and the legs (Zhang et al. 2004; Vogt et al. 2004).

In addition to reducing T_1, an MR contrast agent always also reduces T_2 (and T_2*). The reduction in T_2* can lead to a significant signal reduction in the MRA image at high contrast agent concentrations; often the venous vessel through which the bolus is infused are seen dark in the MRA data sets (Albert et al. 1993). To avoid these artifacts, the contrast agent concentration or the echo time TE can be reduced. Besides reducing T_2*, the contrast agent also causes a concentration-dependent resonance frequency shift. Radial or spiral *k*-space data acquisitions especially susceptible to these frequency shifts that cause blurring artifacts, which can be compensated using dedicated off-resonance correction algorithms.

Contrast-enhanced MRA studies are also susceptible to artifacts known from TOF MRA. In particular, pulsation artifacts are visible in contrast-enhanced measurements (Al-Kwifi et al. 2004). Intra-voxel dephasing is observed, although the effect is much lower due to the shorter T_Es used here. To keep the acquisition time short, generally flow compensation is not integrated into contrast-enhanced MRA pulse sequences, because the additional gradients significantly prolong the measurement time.

Contrast-enhanced MRA offers substantial advantages over TOF or PC MRA, because the saturation effects seen in TOF MRA are almost completely avoided. Thus, extended vascular structures for example in the abdomen or the extremities can be visualized with a few slices oriented parallel to the vessel. The short acquisition times of contrast-enhanced MRA allow breath-held acquisitions ($T_A < 30$ s), which significantly reduces motion artifacts (Maki et al. 1997). The dynamic information of multiphase 3D MRA contains information about vascular anatomy, flow direction (e.g., in aortal aneurysms), tissue perfusion (e.g., in the kidney), and vascular anomalies, which might not be visible on a single MRA data set.

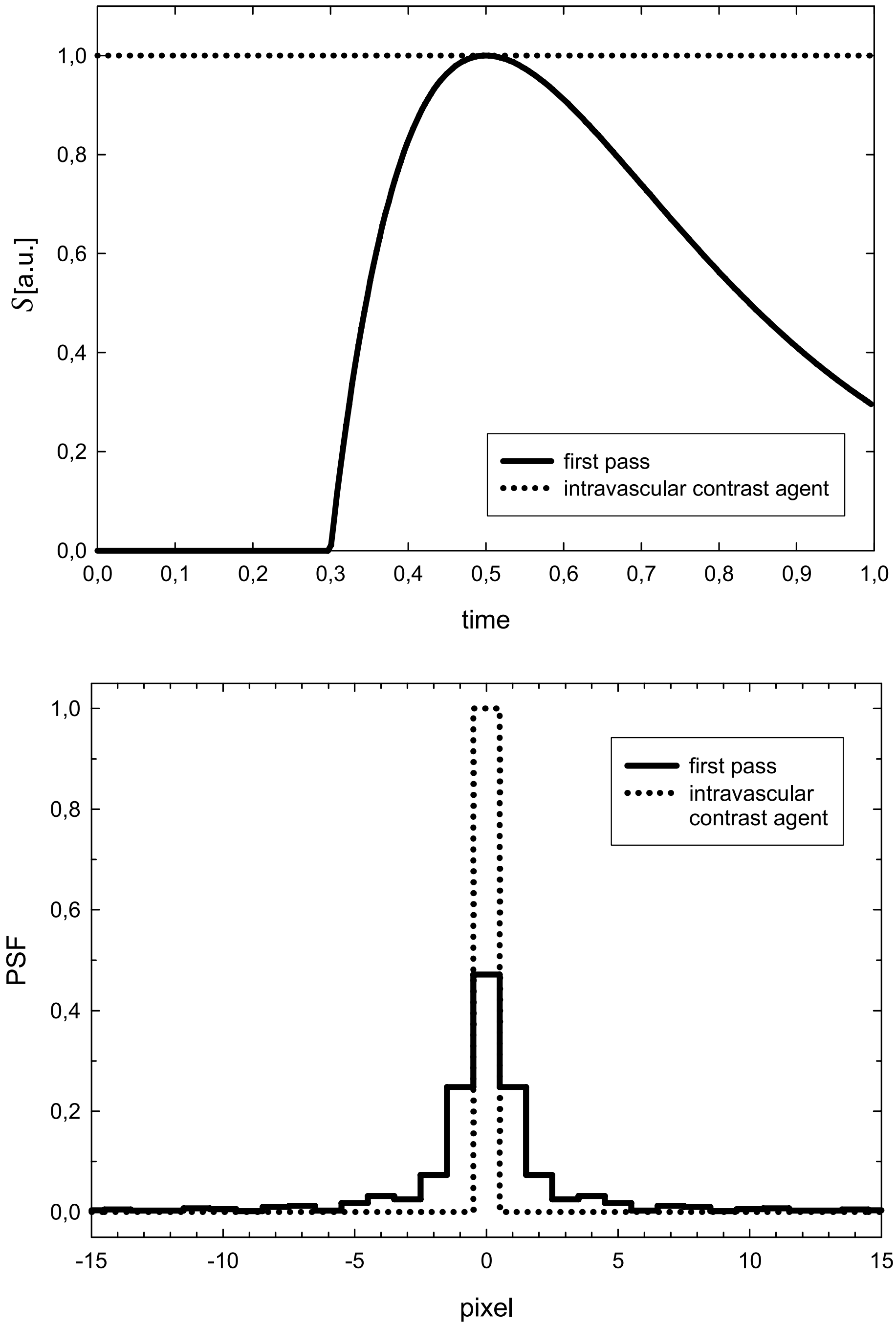

Fig. 2.7.13 (*Top*) Simulated signal–time curve during a first-pass MRA (*solid line*) and a study with an intravascular contrast agent (*dotted line*). At the center of the acquisition window, when the central k-space lines are acquired, a maximal signal is seen in the first-pass study, whereas a constant signal is present in with the intravascular contrast agent. (*Bottom*) The correspond point spread functions show that during a first-pass study objects appear blurred in phase-encoding direction, whereas the theoretical resolution of the data acquisition can be achieved when the concentration is constant

Fig. 2.7.14 Surface rendering (*left*) and MIP (*right*) visualization of an abdominal MRA with an intravascular contrast agent. The three-dimensional character of the data set is better captured with the surface display, whereas the finer details are better visualized on the MIP. The presence of venous signal is making the interpretation of the data more difficult; however, a significantly higher spatial resolution can be achieved with intravascular contrast agents

2.7.8.2 Intravascular Contrast Agents

Using intravascular agents, the contrast agent concentration in the blood is maintained over time spans of minutes to hours. In general, the same pulse sequences can be applied for MRA with intravascular contrast agents as with the extracellular contrast agents, as they share the same contrast mechanism; however, as the concentration of intravascular contrast agent in blood attains an equilibrium state after a few re-circulations (typically 20–40 s), MRA data sets can also be acquired over longer acquisition times. This prolonged acquisition window can be used to increase the image resolution, because an ideal PSF can be achieved and, thus, no blurring should be present (van Bemmel et al. 2003a; Grist et al. 1998).

Because data acquisition does not have to be synchronized with the contrast agent bolus, data acquisition can be started once the contrast agent concentration has reached equilibrium. The contrast agent injection does not need to be performed with a contrast agent pump, but can be infused manually via a venous access port even prior to the MR examination. With intravascular contrast agents, the acquisition time T_A is not limited by the transit time of the bolus, and data sets can be acquired over much longer acquisition periods. With longer acquisition times, special trigger and gating techniques (ECG triggering, respiratory gating, navigator echoes [Ahlstrom et al. 1999]) to suppress motion artifacts are required.

If image data are acquired in the equilibrium phase, venous overlay is a fundamental problem in MRA with intravascular contrast agents (Fig. 2.7.14). Venous contamination particularly makes those images hard to interpret that are calculated through a projection technique such as the maximum intensity projection (MIP), because here, the depth information is lost. A separation of arterial and venous vessels is possible with the help of dedicated post-processing software. Therefore, a region in an arterial vessel is identified and a region-growing algorithm is used to find all connected regions. Unfortunately, when arteries and veins are in close proximity the algorithm may artifactually connect arterial to venous vessels. With equilibrium-phase MRA, data sets of intravascular contrast agents, these artifacts are easier to avoid than in first-pass studies because of the higher spatial resolution. Nevertheless, for direct arteriovenous connections or shunts, a manual correction of the segmentation is always required (van Bemmel et al. 2003b; Svensson et al. 2002).

The use of intravascular contrast agent is not limited to the equilibrium phase, but can be combined with a first-pass study during the initial contrast agent injection to obtain both the dynamics of the contrast agent passage as well as the vascular morphology (Grist et al. 1998). Additionally, the dynamic information can be utilized to separate arteries from veins in the high-resolution equilibrium-phase 3D MRA data sets (Bock et al. 2000).

Although the long half-life of the intravascular contrast agent is advantageous for intraluminal studies, it can become a problem if a dynamic study has to be repeated. With extracellular contrast agents, this is possible within a few minutes, whereas up to several hours have to be waited after a study with an intravascular contrast agent. In practice, intravascular contrast agents are still advantageous for MRA, as they allow combining high spatial resolution in the equilibrium phase with dynamic information during first passage. Additionally, these contrast agents can be used to quantify perfusion (Prasad et al. 1999) or to delineate vessels during MR-guided intravascular procedures (Wacker et al. 2002; Martin et al. 2003).

2.7.9 Summary

Various techniques for MR angiography and MR flow measurements exist that make use of the different physical properties of blood: flow, pulsation, or signal variation following administration of contrast agent. TOF MRA is often used in anatomical regions where a high inflow is present, and long measurement times can be tolerated. Phase-contrast flow measurements provide a quantitative assessment of blood flow when combined with cardiac triggering. Contrast-enhanced studies are favorable in abdominal regions and the periphery, where saturation effects are a limiting factor for TOF MRA. Intravascular contrast agents further extend the capabilities of contrast-enhanced MRA because high-resolution data sets can be acquired over an extended time.

References

1. Ahlstrom KH, Johansson LO, Rodenburg JB, Ragnarsson AS, Akeson P, Borseth A (1999) Pulmonary MR angiography with ultrasmall superparamagnetic iron oxide particles as a blood pool agent and a navigator echo for respiratory gating: pilot study. Radiology 211:865–869
2. Albert MS, Huang W, Lee JH, Patlak CS, Springer CS Jr (1993) Susceptibility changes following bolus injections. Magn Reson Med 29:700–708
3. Al-Kwifi O, Kim JK, Stainsby J, Huang Y, Sussman MS, Farb RI, Wright GA (2004) Pulsatile motion effects on 3D magnetic resonance angiography: implications for evaluating carotid artery stenoses. Magn Reson Med 52:605–611
4. Anderson CM, Lee RE (1993) Time-of-flight techniques. Pulse sequences and clinical protocols. Magn Reson Imaging Clin N Am 1:217–227
5. Bampton AEH, Riederer SJ, Korin HW (1992) Centric phase-encoding order in three-dimensional MP-RAGE sequences: application to abdominal imaging. J Magn Reson Imaging 2:327–334
6. Bemmel CM van, Spreeuwers LJ, Viergever MA, Niessen WJ (2003a) Level-set-based artery-vein separation in blood pool agent CE-MR angiograms. IEEE Trans Med Imaging 22:1224–1234
7. Bemmel CM van, Wink O, Verdonck B, Viergever MA, Niessen WJ (2003b) Blood pool contrast-enhanced MRA: improved arterial visualization in the steady state. IEEE Trans Med Imaging 22:645–652
8. Bieri O, Scheffler K (2005) Flow compensation in balanced SSFP sequences. Magn Reson Med 54:901–907
9. Bock M, Schönberg SO, Flomer F, Schad LR (2000) Separation of arteries and veins in 3D MR angiography using correlation analysis. Magn Reson Med 43:481–487
10. Bryant DJ, Payne JA, Firmin DN, Longmore DB (1984) Measurement of flow with NMR imaging using a gradient pulse and phase difference technique. J Comput Assist Tomogr 8:588–593
11. Detre JA, Zhang W, Roberts DA, Silva AC, Williams DS, Grandis DJ, Koretsky AP, Leigh JS (1994) Tissue specific perfusion imaging using arterial spin labeling. NMR Biomed 7:75–82
12. Dumoulin CL (1995) Phase contrast MR angiography techniques. Magn Reson Imaging Clin N Am 3:399–411
13. Earls JP, Rofsky NM, DeCorato DR, Krinsky GA, Weinreb JC (1997) Hepatic arterial-phase dynamic gadolinium-enhanced MR imaging: optimization with a test examination and a power injector. Radiology 202:268–273
14. Edelman RR, Chien D, Kim D (1991) Fast selective black blood MR imaging. Radiology 181:655–660
15. Edelman RR, Ahn SS, Chien D, Li W, Goldmann A, Mantello M, Kramer J, Kleefield J (1992) Improved time-of-flight MR angiography of the brain with magnetization transfer contrast. Radiology 184:395–399
16. Edelman RR, Siewert B, Adamis M, Gaa J, Laub G, Wielopolski P (1994) Signal targeting with alternating radiofrequency (STAR) sequences: application to MR angiography. Magn Reson Med 31:233–238
17. Essig M, Engenhart R, Knopp MV, Bock M, Scharf J, Debus J, Wenz F, Hawighorst H, Schad LR, van Kaick G (1996) Cerebral arteriovenous malformations: improved nidus demarcation by means of dynamic tagging MR-angiography. Magn Reson Imaging 14:227–233
18. Fain SB, Riederer SJ, Bernstein MA, Huston J III (1999) Theoretical limits of spatial resolution in elliptical-centric contrast-enhanced 3D-MRA. Magn Reson Med 42:1106–1116
19. Fink C, Ley S, Kroeker R, Requardt M, Kauczor HU, Bock M (2005) Time-resolved contrast-enhanced three-dimensional magnetic resonance angiography of the chest: combination of parallel imaging with view sharing (TREAT). Invest Radiol 40:40–48
20. Golay X, Hendrikse J, Lim TC (2004) Perfusion imaging using arterial spin labeling. Top Magn Reson Imaging 15:10–27
21. Gomori JM, Grossman RI, Yu-Ip C, Asakura T (1987) NMR relaxation times of blood: dependence on field strength, oxidation state, and cell integrity. J Comput Assist Tomogr 11:684–690
22. Goyen M (2006) (ed) MR angiography with Vasovist®. ABW Wissenschaftsverlag, Berlin
23. Grist TM, Korosec FR, Peters DC, Witte S, Walovitch RC, Dolan RP, Bridson WE, Yucel EK, Mistretta CA (1998) Steady-state and dynamic MR angiography with MS-325: initial experience in humans. Radiology 207:539–544
24. Haacke EM, Patrick JL (1986) Reducing motion artifacts in two-dimensional fourier transform imaging. Magn Reson Imaging 4:359–376
25. Korosec FR, Frayne R, Grist TM, Mistretta CA (1996) Time-resolved contrast-enhanced 3D MR angiography. Magn Reson Med 36:345–351
26. Lin W, Haacke EM, Edelman RR (1993) Black blood angiography. In: Potchen EJ, Haacke EM, Siebert JE, Gottschalk A (eds) Magnetic resonance angiography, concepts and applications. Mosby, St. Louis pp 160–172
27. Maki JH, Prince MR, Londy FJ, Chenevert TL (1996) The effects of time varying intravascular signal intensity and *k*-space acquisition order on three-dimensional MR angiography image quality. J Magn Reson Imaging 6:642–651

28. Maki JH, Prince MR, Chenevert TL (1997) The effects of incomplete breath-holding on 3D MR image quality. J Magn Reson Imaging 7:1132–1139
29. Martin AJ, Weber OM, Saeed M, Roberts TP (2003) Steady-state imaging for visualization of endovascular interventions. Magn Reson Med 50:434–438
30. Miyazaki M, Sugiura S, Tateishi F, Wada H, Kassai Y, Abe H (2000) Non-contrast-enhanced MR angiography using 3D ECG-synchronized half-Fourier fast spin-echo. J Magn Reson Imaging 12:776–783
31. Nagele T, Klose U, Grodd W, Nusslin F, Voigt K (1995) Nonlinear excitation profiles for three-dimensional inflow MR angiography. J Magn Reson Imaging 5:416–420
32. Oppelt A, Grauman R, Barfuss H, Fischer H, Hartl W, Schajor W (1986) FISP—a new fast MRI sequence. Electromedica 54:15–19
33. Parker DL, Yuan C, Blatter DD (1991) MR angiography by multiple thin slab 3D acquisition. Magn Reson Med 17:434–451
34. Potchen EJ, Haacke EM, Siebert JE (1993) Magnetic resonance angiography. Mosby, St. Louis
35. Prasad PV, Cannillo J, Chavez DR, Pinchasin ES, Dolan RP, Walovitch R, Edelman RR (1999) First-pass renal perfusion imaging using MS-325, an albumin-targeted MRI contrast agent. Invest Radiol 34:566–571
36. Prince MR (1994) Gadolinium-enhanced MR aortography. Radiology 191:155–164
37. Prince MR (1996) Body MR angiography with gadolinium contrast agents. Magn Reson Imaging Clin N Am 4:11–24
38. Prince MR, Chenevert TL, Foo TK, Londy FJ, Ward JS, Maki JH (1997) Contrast-enhanced abdominal MR angiography: optimization of imaging delay time by automating the detection of contrast material arrival in the aorta. Radiology 203:109–114
39. Prince MR, Grist TM, Debatin JF (2003) 3D contrast MR angiography. Springer, Berlin Heidelberg New York
40. Pruessmann KP, Weiger M, Scheidegger MB, Boesiger P (1999) SENSE: sensitivity encoding for fast MRI. Magn Reson Med 42:952–962
41. Riederer SJ, Tasciyan T, Farzaneh F (1988) MR flouroscopy: technical feasibility. Magn Reson Med 8:1–15
42. Saloner D, van Tyen R, Dillon WP, Jou LD, Berger SA (1996) Central intraluminal saturation stripe on MR angiograms of curved vessels: simulation, phantom, and clinical analysis. Radiology 198:733–739
43. Sodickson DK, Manning W (1997) Simultaneous acquisition of spatial harmonics (SMASH): fast imaging with radiofrequency coil arrays. Magn Reson Med 38:591–603
44. Storey P, Li W, Chen Q, Edelman RR (2004) Flow artifacts in steady-state free precession cine imaging. Magn Reson Med 51:115–122
45. Svensson J, Petersson JS, Stahlberg F, Larsson EM, Leander P, Olsson LE (1999) Image artifacts due to a time-varying contrast medium concentration in 3D contrast-enhanced MRA. J Magn Reson Imaging 10:919–928
46. Svensson J, Leander P, Maki JH, Stahlberg F, Olsson LE (2002) Separation of arteries and veins using flow-induced phase effects in contrast-enhanced MRA of the lower extremities. Magn Reson Imaging 20:49–57
47. Vogt FM, Ajaj W, Hunold P, Herborn CU, Quick HH, Debatin JF, Ruehm SG (2004) Venous compression at high-spatial-resolution three-dimensional MR angiography of peripheral arteries. Radiology 233:913–920
48. Wacker FK, Wendt M, Ebert W, Hillenbrandt C, Wolf KJ, Lewin JS (2002) Use of a blood-pool contrast agent for MR-guided vascular procedures: feasibility of ultrasmall superparamagnetic iron oxide particles. Acad Radiol 9:1251–1254
49. Wentz K, Fröhlich J, von Weymarn C, Patak M, Jenelten R, Zollikofer C (2003) High-resolution magnetic resonance angiography of hands with timed arterial compression (tac-MRA). Lancet 361:49–50
50. Wilman AH, Riederer SJ (1996) Improved centric phase encoding orders for three-dimensional magnetization-prepared MR angiography. Magn Reson Med 36:384–392
51. Wilman AH, Riederer SJ, Breen JF et al (1996) Elliptical spiral phase encoding order: an optimal, field-of-view-dependent ordering scheme for breath-hold contrast-enhanced 3D MR angiography. Radiology 201:328–329
52. Wilman AH, Riederer SJ, King BF, Debbins JP, Rossman PJ, Ehman RL (1997) Fluoroscopically triggered contrast-enhanced three-dimensional MR angiography with elliptical centric view order: application to the renal arteries. Radiology 205:137–146
53. Wilman AH, Yep TC, Al-Kwifi O (2001) Quantitative evaluation of nonrepetitive phase-encoding orders for first-pass, 3D contrast-enhanced MR angiography. Magn Reson Med 46:541–547
54. Wilson GJ, Hoogeveen RM, Willinek WA, Muthupillai R, Maki JH (2004) Parallel imaging in MR angiography. Top Magn Reson Imaging 15:169–185
55. Wood ML, Henkelman RM (1985) MR image artifacts from periodic motion. Med Phys 12:143–151
56. Zhang HL, Ho BY, Chao M, Kent KC, Bush HL, Faries PL, Benvenisty AI, Prince MR (2004) Decreased venous contamination on 3D gadolinium-enhanced bolus chase peripheral MR angiography using thigh compression. Am J Roentgenol 183:1041–1047

2.8 Diffusion-Weighted Imaging and Diffusion Tensor Imaging

O. Dietrich

2.8.1 Introduction

Diffusion in the context of diffusion-weighted MRI or diffusion tensor imaging (DTI) refers to the stochastic thermal motion of molecules or atoms in fluids and gases, a phenomenon also known as Brownian motion. This motion depends on the size, the temperature, and in particular on the microscopic environment of the examined molecules. Diffusion measurements can therefore be used to derive information about the microstructure of tissue. In MRI, stochastic molecular motion can be observed as signal attenuation. This was first recognized in the NMR spin-echo experiment by E.L. Hahn in 1950 (Hahn 1950), long before the invention of actual magnetic resonance *imaging*. A number of more sophisticated experiments were described in following years that allowed the quantitative measurement of the diffusion coefficient (Carr and Purcell 1954; Torrey 1956; Woessner 1961). Of particular importance is the pulsed-gradient spin-echo (PGSE) technique proposed by Stejskal and Tanner in 1965 (Stejskal and Tanner 1965) that is described in detail in Sect. 2.8.3.1.

Diffusion as an imaging-contrast mechanism was first incorporated in MRI pulse sequences in 1985 (Taylor and Bushell 1985; Merboldt et al. 1985) and applied in vivo in 1986 (LeBihan et al. 1986). Its great potential for clinical MRI became evident in around 1990, when diffusion-weighted images were recognized to be extremely valuable for the early detection of stroke (Moseley et al. 1990a,b; Chien et al. 1990, 1992). Areas of focal cerebral ischemia appear hyperintense in diffusion-weighted images only minutes after the onset of symptoms (see also Chap. 3, Sect. 3.4). Having thus been pushed into publicity, diffusion-weighted imaging was evaluated in many other applications such as the characterization of brain tumors (Tien et al. 1994; Sugahara et al. 1999; Okamoto et al. 2000) and of multiple sclerosis lesions (Cercignani et al. 2000; Filippi and Inglese 2001), but none of these reached the clinical significance of stroke diagnosis. Mainly due to limitations of image quality, there are considerably fewer publications about diffusion-weighted imaging outside the central nervous system. Examples of these are studies with the purpose of differentiating osteoporotic and malignant vertebral compression fractures (Baur et al. 1998, 2003; Herneth et al. 2002) or benign and malignant lesions of the liver (Moteki et al. 2002; Taouli et al. 2003) and the kidneys (Cova et al. 2004).

Molecular diffusion is a three-dimensional process and is—depending on the tissue microstructure—in general anisotropic, i.e., the extent of molecular motion depends on spatial orientation. A physical quantity called the diffusion tensor is required to fully describe anisotropic diffusion. MRI techniques to measure the diffusion tensor have been introduced in the 1990s (Basser et al. 1994; Pierpaoli et al. 1996) and gained considerably more popularity when tracking algorithms were proposed for three-dimensional reconstruction of white matter fiber tracts (Mori et al. 1999; Conturo et al. 1999). Today, diffusion tensor imaging is a valuable research tool with applications, e.g., in neurodevelopment (Neil 2002; Snook et al. 2005), neuropsychiatry (Taber et al. 2002, Moseley et al. 2002, Sullivan and Pfefferbaum 2003), or aging (Moseley 2002, Sullivan and Pfefferbaum 2003, Sullivan et al. 2006).

2.8.2 Physics of Diffusion

2.8.2.1 Brownian Molecular Motion

All molecules in fluids or gases perform microscopic random motions. This motion is called molecular diffusion or Brownian motion after Robert Brown (1773–1858), who observed a minute motion of plant pollens floating in water in 1827 (Brown 1866). These pollens were constantly hit by fast-moving water molecules, resulting in a visible irregular motion of the much larger particles. Due to Brownian motion, a tracer such as a droplet of ink given into water will diffuse into its surroundings, resulting in spatially and temporally varying tracer concentrations, until the ink is diluted homogeneously in the water. However, Brownian molecular motion does not require concentration gradients, but occurs also in fluids consisting of only a single kind of molecule. The molecules of any arbitrary droplet of water within a larger water reservoir will stochastically disperse into their surroundings; this process is called diffusion or, to emphasize that the observed molecules do not diffuse into an external medium, self-diffusion. It should be noted that diffusion always refers to a stochastic and not directed motion and is strictly to be distinguished from any kind of directional flow of a liquid.

The molecules in fluids or gases perform random motions due to their thermal kinetic energy, E_{kin}, which is proportional to the temperature, T: $E_{\mathrm{kin}} = \frac{3}{2}kT$ ($k = 1.38 \times 10^{-23}$ J/K is the Boltzmann constant). This energy corresponds to a mean velocity[1] $v = \sqrt{2E_{\mathrm{kin}}/m}$ for a molecule of mass m; in the case of water at room temperature ($T = 300$ K), the mean velocity is about 650 m/s. Due to frequent collisions with other particles, however, mol-

---

[1] Strictly speaking, we calculate the square root of the mean value of squared velocity, i.e., $\sqrt{\mathrm{mean}\ (v^2)}$, which is slightly different (by a factor of $\sqrt{3\pi/8} \approx 1.085$, i.e., by 8.5%) from the actual mean value of the velocity due to the asymmetry of the Maxwell distribution.

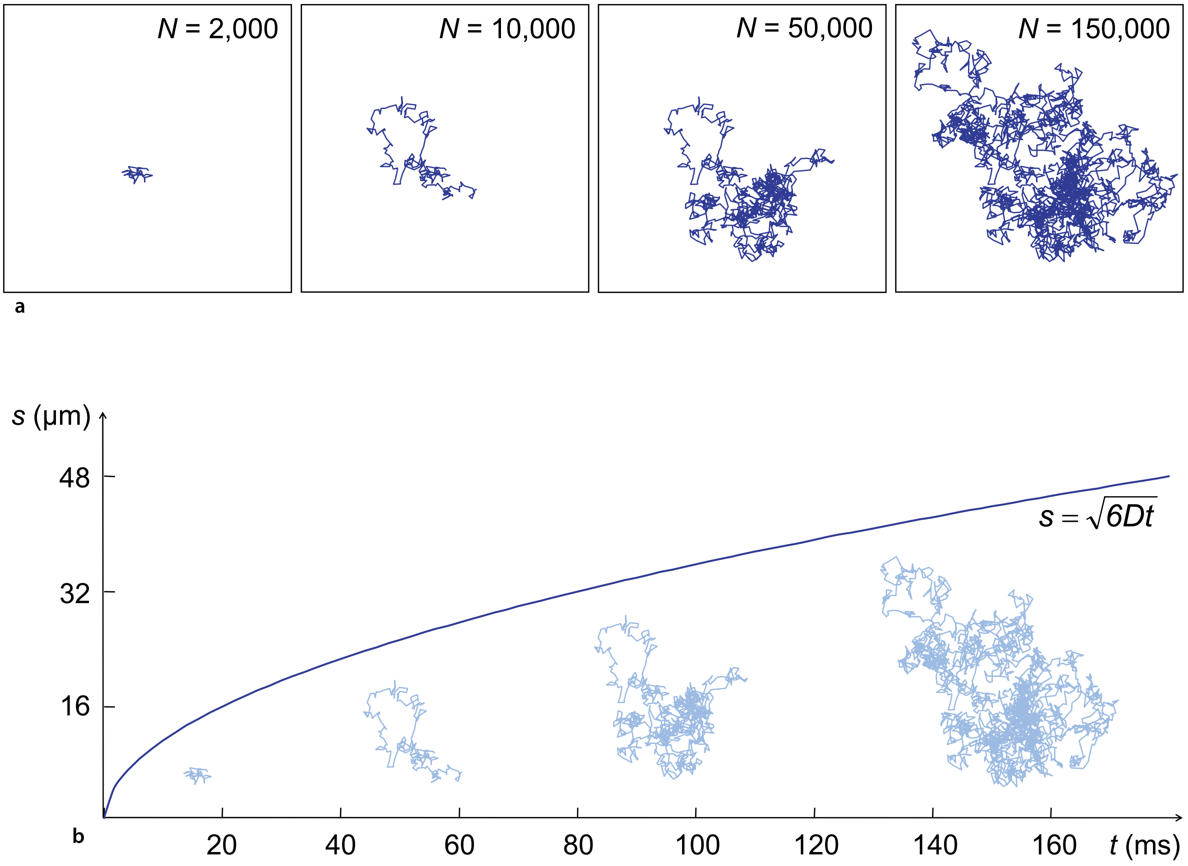

Fig. 2.8.1 Simulated diffusion path of a single molecule. **a** Random-walk simulation after $N = 2{,}000$, 10,000, 50,000, and 150,000 simulated steps. **b** Dependence of diffusion distance, *s*, on diffusion time, *t*

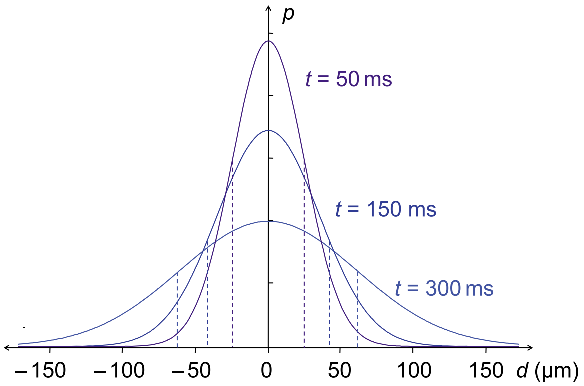

Fig. 2.8.2 Gaussian probability distribution of individual molecular diffusion distances, *d*, after diffusion times of $t = 50$ ms, 150 ms, and 300 ms; the distributions are based on the diffusion coefficient of water molecules at room temperature. The standard deviations of the Gaussian distributions are marked by *dashed lines* and indicate the mean diffusion distance, *s*

ecules do not move linearly in a certain direction but follow a random course that can be visualized in a random-walk simulation as shown in Fig. 2.8.1a. This figure also demonstrates that, macroscopically, the mean displacement or diffusion distance, *s*, after a time *t* is much more interesting than is the linear velocity of the molecule. The mean diffusion distance of a particle is proportional to the square root of the diffusion time *t* and is described by the diffusion coefficient *D*: $s = \sqrt{6Dt}$. This relation is shown in Fig. 2.8.1b for a water molecule with a diffusion coefficient of $D = 2.03 \times 10^{-3}$ mm²/s at a temperature of 20°C. Since diffusion is a stochastic process, the diffusion distance after the time *t* is not the same for all molecules but is described by a Gaussian probability distribution as illustrated in Fig. 2.8.2. As shown in this illustration, after a diffusion time *t* most molecules are still found at or close to their original position; the diffusion distance *s*, corresponds to the standard deviation of the shown distributions. Typical diffusion distances for free water molecules at room temperature are about 25 µm after a diffusion time of 50 ms and 110 µm after 1 s.

Table 2.8.1 Examples of diffusion coefficients of different fluids and tissues

	ADC (10^{-3} mm^2/s)	Reference
Water, 5°C	1.31	Mills 1973
Water, 20°C	2.02	Tofts et al. 2000
Water, 35°C	2.92	Mills 1973
Ethanol, 20°C	0.98	Tofts et al. 2000
Brain, white matter	0.70	Helenius et al. 2002
Brain, gray matter	0.89	Helenius et al. 2002
Liver	1.83	Boulanger et al. 2003
Kidney	2.19	Cova et al. 2004

In contrast to free diffusion in pure water (Fig. 2.8.3a), the water molecules in tissue cannot move freely, but are hindered by the cellular tissue structure, in particular by cell membranes, cell organelles, and large macromolecules as shown schematically in Fig. 2.8.3b. Due to additional collisions with these obstacles, the mean diffusion distance of water molecules in tissue is reduced compared to that of free water, and a decreased effective diffusion coefficient is found in tissue called the apparent diffusion coefficient (ADC). Obviously, the ADC depends on the number and size of obstacles and therefore on the cell types that compose the tissue. Hence, diffusion properties can be used to distinguish different types of tissue. Examples of diffusion coefficients in different tissues and in fluids at different temperatures are summarized in Table 2.8.1.

Not only does the number and size of organelles influence diffusion, but also the geometrical arrangement of the cell membranes. In particular, the diffusion of water molecules can reflect an anisotropic arrangement of cells as indicated in Fig. 2.8.3c. Since cell membranes are barriers for diffusing molecules, water diffuses more freely along the long axis of the cell than perpendicular to it (Beaulieu 2002). Hence, the ADC measured in the direction parallel to the cellular orientation will be greater than that measured in an orthogonal direction. This property, the dependence of a quantity on its orientation in space, is called anisotropy.

2.8.2.2 Diffusion Tensor

It has proven useful to illustrate the diffusion properties by spheres for isotropic diffusion and by three-dimensional ellipsoids for anisotropic diffusion as shown in Fig. 2.8.3d–f. These shapes visualize the probability density function of diffusion distances in space. Isotropic diffusion can be completely described by its (apparent) diffusion coefficient, D, which corresponds to the radius of the sphere (Fig. 2.8.3d,e). More quantities are required for a complete description of anisotropic diffusion, e.g., three angles that define the orientation of the ellipsoid in space, and the length of the three principal axes describing the magnitude of the diffusion coefficients. In physics or mathematics, a quantity that corresponds to such a three-dimensional ellipsoid is called a tensor.

The physical object called tensor can also be explained by comparing it to more commonly known objects such as scalars and vectors. A scalar is a quantity that can be measured or described as a single number; typical examples are the temperature, the mass, or the density of an object. In imaging, the image intensity, e.g., in a T_2-weighted image, is a scalar: a single number is required for each pixel to describe the intensity. As demonstrated in the last example, scalars can be spatially dependent and be visualized as intensity maps; another example is a temperature map of an object that describes the temperature as scalar quantity for each spatial position of an object.

Other physical quantities cannot be described by a single number, such as the velocity or acceleration of a particle in space or the flow of a liquid. These quantities are vectors and require both a direction in space and a magnitude to be fully described. A vector is typically visualized as an arrow. For example, in the case of velocity, the direction of the arrow describes the direction of motion and the length of the arrow represents the magnitude of the vector, e.g., as measured in meters/second. Such an arrow can be mathematically described by three independent numbers: either by its length and two angles defining its orientation or by three coordinates (x-, y-, and z-component of the vector). These coordinates are often presented as a column or row vector, e.g., $\boldsymbol{v} = (v_x\ v_y\ v_z)$. Vectors as well as scalars can depend on the spatial position; a flowing liquid can be described by a velocity vector at each position. A full data set consisting of a vector (i.e., an arrow) at each point in space is called a vector field.

Some quantities such as the molecular diffusion cannot be fully described as scalars or vectors; they are tensors. As mentioned above, the diffusion properties can be depicted by a three-dimensional ellipsoid and therefore require six independent numbers to define the direction and length of all axes. These six values are visualized in Fig. 2.8.4 as the three lengths of the axes defining the shape of the ellipsoid and the three angles describing its orientation. However, instead of using angles, tensors can equally well be described by six coordinates arranged in a symmetric 3 × 3-matrix in analogy to the three coordinates of a vector. These coordinates are called D_{xx}, D_{yy}, D_{zz}, D_{xy}, D_{xz}, and D_{yz} and form the matrix representation

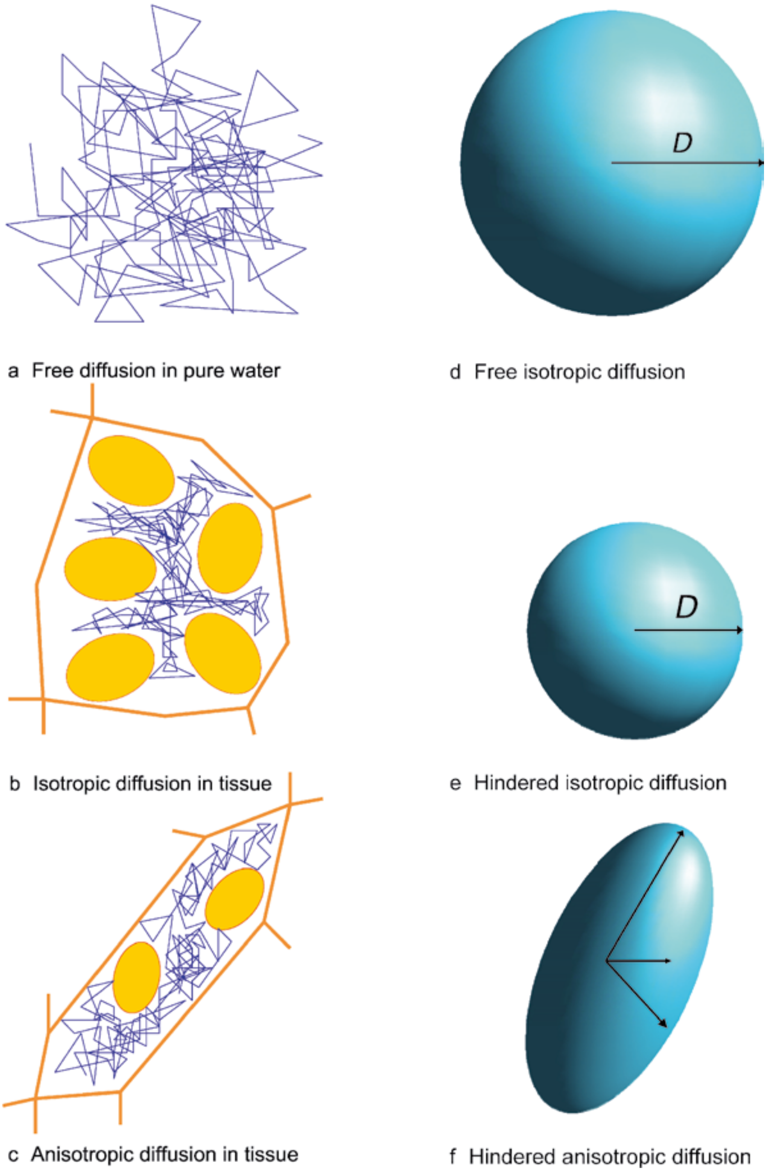

a Free diffusion in pure water

b Isotropic diffusion in tissue

c Anisotropic diffusion in tissue

d Free isotropic diffusion

e Hindered isotropic diffusion

f Hindered anisotropic diffusion

Fig. 2.8.3 Apparent diffusion coefficient and schematic depiction of diffusion properties: **a** Free diffusion in pure water **b** Hindered isotropic diffusion in tissue **c** Hindered anisotropic diffusion in tissue **d** schematic depiction of free isotropic diffusion as sphere with radius *D* **e** schematic depiction of hindered isotropic diffusion as sphere with radius *D* and **f** schematic depiction of anisotropic diffusion as ellipsoid with axes of different lengths

of the tensor D:

$$D = \begin{pmatrix} D_{xx} & D_{xy} & D_{xz} \\ D_{xy} & D_{yy} & D_{yz} \\ D_{xz} & D_{yz} & D_{zz} \end{pmatrix}.$$

This matrix is called symmetric because the elements are mirrored at the diagonal. Of these matrix elements, only the diagonal elements, D_{xx}, D_{yy}, D_{zz}, can be measured directly in MRI and correspond to the diffusion in the x-, y-, and z-directions; the off-diagonal elements must be determined indirectly from further measurements as described in Sect. 2.8.4.

In the case of isotropic diffusion, i.e., if the ellipsoid is a sphere, then this matrix has a very simple form, because a single diffusion coefficient suffices to describe the diffusion. This diffusion coefficient is found on the diagonal of the matrix, and all off-diagonal elements are zero:

$$D_{\text{isotropic}} = \begin{pmatrix} D & 0 & 0 \\ 0 & D & 0 \\ 0 & 0 & D \end{pmatrix}.$$

The diffusion tensor has some properties that are important to understand in order to measure and interpret diffusion imaging data. The mean diffusivity, i.e., the diffusion coefficient averaged over all spatial orientations, can be derived from the trace of the diffusion tensor, i.e., the sum of its diagonal elements:

$$\text{trace of } D = \operatorname{tr} D = \operatorname{tr}\begin{pmatrix} D_{xx} & D_{xy} & D_{xz} \\ D_{xy} & D_{yy} & D_{yz} \\ D_{xz} & D_{yz} & D_{zz} \end{pmatrix} = D_{xx} + D_{yy} + D_{zz}\,.$$

The mean diffusivity, $\langle D \rangle$, or ADC is a third of the trace of D: $\text{ADC} = \langle D \rangle = \frac{1}{3}\operatorname{tr} D$. An MRI measurement of the mean ADC is therefore also called trace imaging.

To analyze the non-isotropic properties of the diffusion tensor, a process called diagonalization of the tensor is used. The meaning of tensor diagonalization can be visualized as finding the three axes (i.e., their length and orientation) that define the ellipsoid in Fig. 2.8.4. Mathematically, the tensor matrix is transformed into a form where all off-diagonal elements are zero:

$$D = \begin{pmatrix} D_{xx} & D_{xy} & D_{xz} \\ D_{xy} & D_{yy} & D_{yz} \\ D_{xz} & D_{yz} & D_{zz} \end{pmatrix} \xrightarrow{\text{diagonalization}} \begin{pmatrix} D_1 & 0 & 0 \\ 0 & D_2 & 0 \\ 0 & 0 & D_3 \end{pmatrix}, \boldsymbol{v}_1\ \boldsymbol{v}_2\ \boldsymbol{v}_3\,.$$

The three new diagonal elements, D_1, D_2, D_3, are called eigenvalues of the tensor; they describe the length of the three axes of the ellipsoid in Fig. 2.8.4. (Some authors denote the eigenvalues as λ_1, λ_2, λ_3 instead of D_1, D_2, D_3.) Since six parameters are still required to fully describe the tensor, in addition to the three diagonal elements, three vectors, $\boldsymbol{v}_1$, $\boldsymbol{v}_2$, $\boldsymbol{v}_3$, are determined which are called eigenvectors. The eigenvectors, which are always orthogonal and have unit length, define the orientation of the ellipsoid and are shown as thick grey arrows in Fig. 2.8.4d.

2.8.2.3 Diffusion Anisotropy

The ratios of the diffusion eigenvalues describe the isotropy or anisotropy of diffusion. In the case of isotropic diffusion, all eigenvalues are the same, $D_1 = D_2 = D_3$, and diffusion is represented by a sphere; see Fig. 2.8.5a. If the largest eigenvalue is much greater than the two other eigenvalues, $D_1 >> D_2 \approx D_3$, then the tensor is represented by a cigar-like shape as in Fig. 2.8.5b. In this case, diffusion in one direction is much less hindered than in the other directions and is sometimes called linear diffusion; this is typically found in white matter fiber tracts, where the motion of water molecules is restricted by the cell membranes and the glial cells perpendicular to the fiber tract orientation. The orientation of the fiber tracts is described by the eigenvector $\boldsymbol{v}_1$ belonging to the large eigenvalue, D_1. If two large eigenvalues are much greater than the third one, $D_1 \approx D_2 >> D_3$, then the diffusion tensor is represented by a pancake-like shape; see Fig. 2.8.5c. This tensor corresponds to preferred diffusion within a two-dimensional plane, which can occur in layered structures and is referred to as planar diffusion.

In order to describe the diffusion anisotropy quantitatively, several anisotropy indices have been introduced to reduce the diffusion tensor to a single number, i.e., a scalar, measuring the anisotropy. Most frequently used is

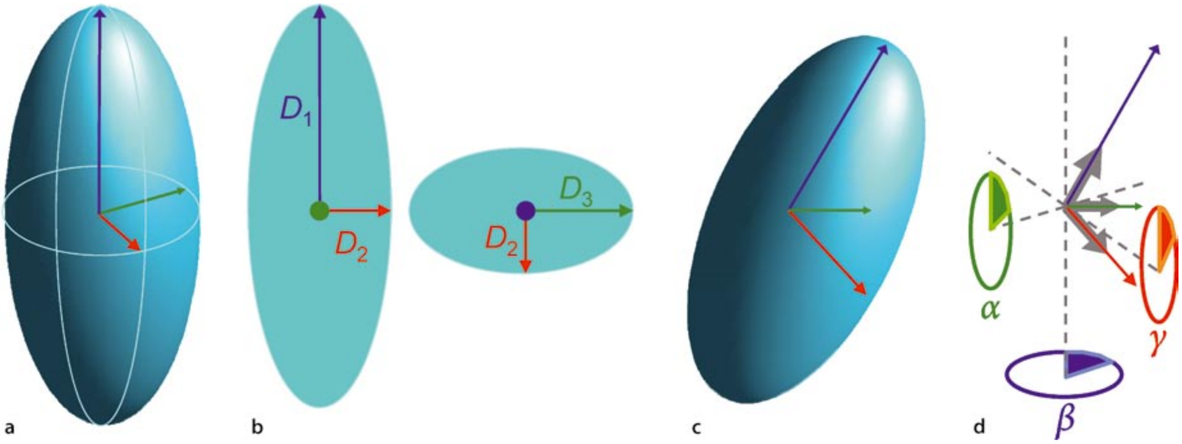

Fig. 2.8.4 Tensor visualized as three-dimensional ellipsoid: six independent numbers are required to define a tensor, three lengths (eigenvalues), D_1, D_2, D_3, corresponding to the length of the principal axes of the ellipsoid (shown three-dimensionally in **a** and in two-dimensional sections **b**), and three angles, α, β, γ, describing the spatial orientation of the axes (**c**,**d**). The eigenvectors of the tensor are shown as *thick gray arrows* in **d**

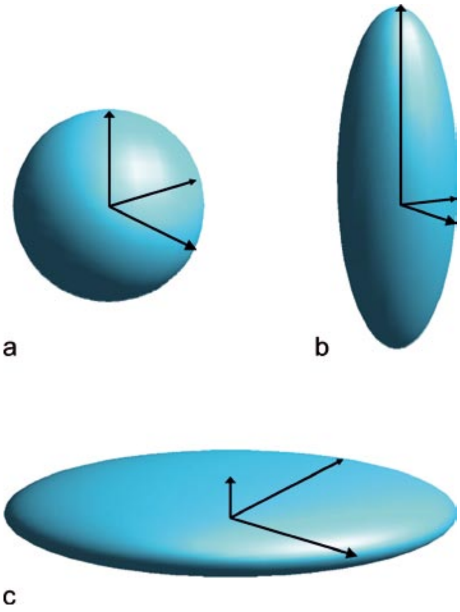

Fig. 2.8.5 Typical diffusion tensors in the case of **a** isotropic diffusion, **b** linear diffusion, and **c** planar diffusion

the fractional anisotropy (FA), defined as

$$\mathrm{FA} = \sqrt{\frac{3}{2}}\,\frac{\sqrt{(D_1 - D)^2 + (D_2 - D)^2 + (D_3 - D)^2}}{\sqrt{D_1^2 + D_2^2 + D_3^2}},$$

where $D = \frac{1}{3}(D_1 + D_2 + D_3)$ is the mean diffusivity. The fractional anisotropy ranges from 0 (isotropic diffusion) to 1 (maximum anisotropy) and can be interpreted as the fraction of the magnitude of the tensor that can be ascribed to anisotropic diffusion (Basser and Pierpaoli 1996). A similar index is the relative anisotropy (RA), defined as

$$\mathrm{RA} = \sqrt{\frac{1}{3}}\,\frac{\sqrt{(D_1 - D)^2 + (D_2 - D)^2 + (D_3 - D)^2}}{D}.$$

The relative anisotropy is the magnitude of the anisotropic part of the tensor divided by its isotropic part (Basser and Pierpaoli 1996) and ranges from 0 (isotropy) to $\sqrt{2} \approx 1.414$ (maximum anisotropy). In order to scale the maximum value of the RA to 1 as well, a normalized (or scaled) definition with an additional factor of $\sqrt{1/2}$ is sometimes used (and often called RA as well):

$$\mathrm{nRA} = \sqrt{\frac{1}{6}}\,\frac{\sqrt{(D_1 - D)^2 + (D_2 - D)^2 + (D_3 - D)^2}}{D}.$$

Less frequently used indices of anisotropy are the volume ratio (VR),

$$\mathrm{VR} = \frac{D_1 D_2 D_3}{D^3},$$

and the volume fraction (VF),

$$\mathrm{VF} = 1 - \mathrm{VR} = 1 - \frac{D_1 D_2 D_3}{D^3}.$$

All these anisotropy indices can be used to describe the diffusion anisotropy (Kingsley and Monahan 2005), but fractional anisotropy may be considered the preferred index that is currently most frequently used. Some typical values of these indices are compared in Table 2.8.2; FA, RA, nRA, and VF start with 0 for isotropic diffusion and increase with increasing anisotropy. The volume ratio is 1 in the case of isotropic diffusion and decreases with increasing anisotropy.

Table 2.8.2 Examples for different anisotropy indices

	(1, 1, 1)[a]	(1, 1, 0.5)	(1, 0.5, 0.5)	(1, 1, 0)	(1, 0.5, 0)	(1, 0, 0)
FA	0	0.33	0.41	0.71	0.77	1
RA	0	0.28	0.35	0.71	0.82	1.41
nRA	0	0.20	0.25	0.5	0.58	1
VF	0	0.14	0.16	1	1	1
VR	1	0.86	0.84	0	0	0

FA fractional anisotropy, *RA* relative anisotropy, *nRA* normalized (scaled) anisotropy, *VF* volume fraction, *VR* volume ratio

[a] Eigenvalues (D_1, D_2, D_3)

2.8.3 MR Measurement of Diffusion-Weighted Images

2.8.3.1 Diffusion Gradients and Diffusion Contrast

To introduce diffusion weighting in MRI pulse sequences, today almost exclusively a technique proposed by Stejskal and Tanner in 1965 (Stejskal and Tanner 1965) is used. The basic idea is to insert additional gradients (usually referred to as diffusion gradients) into the pulse sequence in order to measure the stochastic molecular motion as signal attenuation. Originally, these were two identical gradients on both sides of the refocusing 180° RF pulse of a spin-echo sequence: the so-called pulsed-gradient spin echo (PGSE) technique. However, to simplify the explanation, we will replace this scheme with two gradients with opposite signs that do not require a 180° pulse in between, as shown in Fig. 2.8.6. The contrast mechanism is the same for both gradient schemes.

As illustrated in Fig. 2.8.6, the diffusion gradients superpose a linear magnetic field gradient over the static field, B_0. Since the Larmor frequency of the spins is proportional to the magnetic field strength, spins at different positions now precess with different Larmor frequencies and, thus, become dephased. If the spins are stationary (no diffusion, i.e., diffusion coefficient $D = 0$) and remain at their position, the second diffusion gradient with opposite sign exactly compensates the effect of the first one and rephases the spins. Hence, without diffusion, the signal after the application of the pair of diffusion gradients is the same as before (neglecting relaxation effects).

In the case of diffusing spins, the second diffusion gradient cannot completely compensate the effect of the first one since spins have moved between the first and second gradient. The additional phase the spins gained during the first diffusion gradient is not reverted during the second one. Consequently, rephasing is incomplete after the second diffusion gradient, resulting in diffusion-dependent signal attenuation. As can be deduced from this explanation, the signal attenuation is larger if the diffusivity, i.e., the mobility of the spins, is larger. Quantitatively, the signal attenuation depends exponentially on the diffusion coefficient, D_g, in the direction defined by the diffusion gradient g_D:

$$S(D_g, b) = S_0 \times \exp(-b \times D_g),$$

where S_0 is the original (unattenuated) signal and $S(D_g, b)$ is the attenuated diffusion-weighted signal. The b-value, b, is the diffusion weighting that plays a similar role for diffusion-weighted imaging as the echo time for T_2-weighted imaging: the diffusion contrast, i.e., the signal difference between two tissues with different ADCs, is low at small b-values and can be maximized by choosing the optimal b-value as discussed below. The b-value is expressed in units of s/mm^2 and depends on the timing and the amplitude, g_D, of the diffusion gradients:

$$b = (\gamma \times g_D \times \delta)^2 \left(\Delta - \frac{\delta}{3} \right).$$

As illustrated in Fig. 2.8.6, δ is the duration of each diffusion gradient, and Δ is the interval between the onsets of the gradients; γ is the gyromagnetic ratio of the diffusing spins. A typical b-value used for diffusion-weighted imaging of the brain is 1,000 s/mm^2; for other applications b-values range between 50 s/mm^2 (dark blood liver imaging) and about 20,000 s/mm^2 (imaging of the diffusion q-space [Assaf et al. 2002; Wedeen et al. 2005]). To obtain b-values of about 1,000 s/mm^2, diffusion gradients are required to be much longer (e.g., $\delta = 25$ ms) and have larger amplitudes (e.g., $g_D = 25$ mT/m) than normal imaging gradients applied in MRI; hence, diffusion-weighted imaging can be demanding for the gradient amplifiers and is often acoustically noisy.

The formula for the b-value given above is valid only for a pair of Stejskal-Tanner diffusion gradients. The diffusion weighting of arbitrary time-dependent diffusion gradient shapes, $g_D(t)$, applied between $t = 0$ and $t = T$, can be calculated according to (Stejskal and Tanner 1965)

$$b = \gamma^2 \int_{t=0}^{T} \left(\int_{t'=0}^{t} g_D(t')\,\mathrm{d}t' \right)^2 \mathrm{d}t.$$

By applying diffusion gradients, diffusion-weighted images can be acquired in which the signal intensity depends on the ADC, e.g., structures with large ADC such as liquids appear hypointense. To quantify the ADC at least two diffusion-weighted measurements with different diffusion weightings (i.e., different b-values) are required as shown in Fig. 2.8.7. By determining the signal intensity at the lower b-value, $S(b_1)$, and the higher b-value, $S(b_2)$, the ADC can be calculated as

$$\mathrm{ADC} = \frac{\log(S(b_1) / \log S(b_2))}{b_2 - b_1}.$$

This can be done either for the mean signal intensities in a region of interest or pixel by pixel in order to calculate an ADC map as in Fig. 2.8.7. The ADC can also be calculated from more than two b-values by fitting an exponential to the measured signal intensities or by linear regression analysis applied to the logarithm of signal intensities.

It should be noted that diffusion-weighted images generally exhibit a mixture of different contrasts. Many diffusion-weighted pulse sequences require relatively long echo times between 60 and 120 ms because of the long duration of the diffusion preparation. Thus, diffusion-weighted images are often also T_2-weighted, and it can be difficult to differentiate image contrast due to diffusion and T_2 effects. This is a typical problem in diffusion-weighted MRI of the brain and known as T_2 shine-through effect (Burdette et al. 1999).

A further consequence of the long minimum echo times due to the diffusion preparation is the relatively

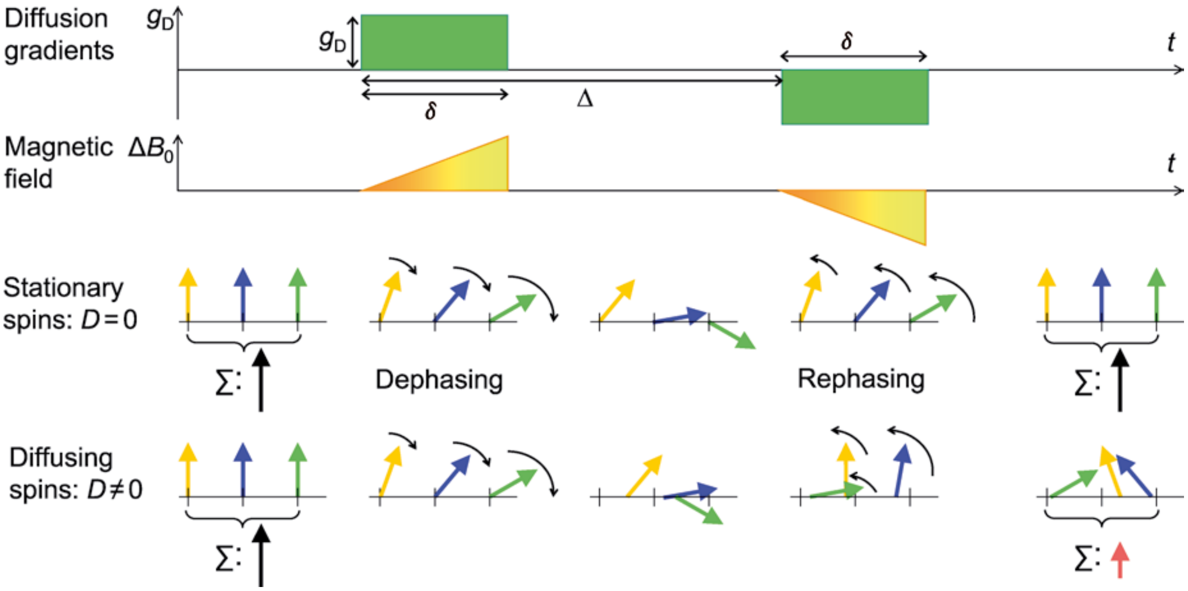

Fig. 2.8.6 Diffusion weighting using bipolar diffusion gradients. The diffusion gradients (*green*) cause a spatially varying magnetic field, ΔB_0 (*yellow*), and thus spatially varying Larmor frequencies. The first diffusion gradient dephases the spins (three spins at different spatial positions are shown as *yellow*, *blue*, and *green arrows*). If the spins are stationary (no diffusion), then the second diffusion gradient with opposite sign rephases the spins. In the case of diffusing spins, rephasing is incomplete since spins have moved between the first and second gradient; thus, diffusion-dependent signal attenuation is observed (*red arrow*)

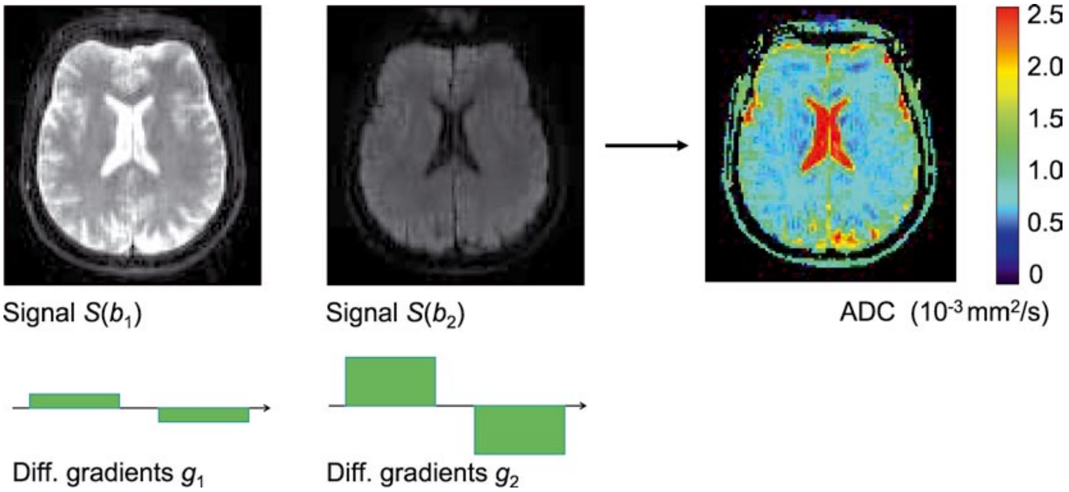

Fig. 2.8.7 Acquisition of two images with different diffusion weightings (*b*-values b_1 and b_2) in order to calculate an ADC map. Note the large signal attenuation in CSF at the higher *b*-value, b_2, and the correspondingly high diffusion coefficient in the ADC map

low signal-to-noise ratio of diffusion-weighted images. The combined effects of diffusion weighting, which particularly decreases the signal of fluids, and of T_2 weighting, which predominantly reduces the signal of other (non-fluid) tissue, results in globally low signal intensity on diffusion-weighted images. Therefore, signal-increasing techniques such as increasing the voxel volume or (magnitude) averaging are often required for diffusion-weighted MRI. In addition, ADC calculation can be corrected for the decreasing signal-to-noise ratio at higher *b*-values (Dietrich et al. 2001a).

The range of *b*-values chosen for a diffusion-weighted MRI experiment should depend on the typical diffusion coefficients that are measured and on the signal-to-noise ratio of the diffusion-weighted image data. As a rule of thumb, the signal attenuation should be at least about 60%, i.e., the product of diffusion coefficient and the *b*-value range, $b_{\max} - b_{\min}$, should be approximately 1 (Xing et al. 1997). This corresponds to a *b*-value difference of about 1,000–1,500 s/mm^2 in brain tissue with ADCs between 0.6×10^{-3} and 1.0×10^{-3} mm^2/s. However, the choice of the largest *b*-value is frequently limited by signal-to-noise considerations, and thus, the maximum diffusion weighting is often reduced in order to maintain sufficient signal-to-noise ratio. A second point to consider is the choice of the lowest *b*-value. Although a *b*-value of 0 is often chosen, a slightly higher value of, for example, 50 s/mm^2 can be advantageous in order to suppress the influence of perfusion effects (LeBihan et al. 1988; van Rijswijk et al. 2002).

2.8.3.2 Pulse Sequences for Diffusion MRI

Historically, the first MRI pulse sequences with inserted diffusion gradients were stimulated-echo (Taylor and Bushell 1985; Merboldt et al. 1985) and spin-echo sequences (LeBihan et al. 1986); a schematic spin-echo pulse sequence with diffusion gradients is shown in Fig. 2.8.8. In this diagram, diffusion gradients are added for all three spatial directions (readout, phase, and slice direction); however, they are usually switched on in only one or two of the three directions at a time. Since spins are refocused by a 180° pulse, both diffusion gradients have the same polarity. The main disadvantages of the diffusion-weighted spin-echo sequence are that it requires long acquisition times of many minutes per data set and is extremely sensitive to motion. Examples of images acquired with a diffusion-weighted spin-echo sequence are shown in Fig. 2.8.9a,b. The volunteers were asked to avoid any movements, but no head fixation was applied; severe motion artifacts degrade the images. These artifacts are caused by inconsistent phase information of the complex-valued raw data; stimulated-echo, and spin-echo sequences are particularly sensitive to these effects because the diffusion preparation must be repeated for each raw data line and different states of motion will occur during these diffusion preparations. More details about the motion sensitivity of diffusion-weighted sequences and about approaches to reduce these artifacts are described in the following section. With techniques such as cardiac gating and navigator-echo correction, image quality of diffusion-weighted spin-echo sequences can be dramatically improved (Fig. 2.8.9c,d).

Today, the most commonly used pulse sequence for diffusion-weighted MRI (particularly of the brain) is the single-shot echo planar imaging (EPI) sequence with spin-echo excitation. The diffusion preparation of this sequence is the same as in the conventional spin-echo sequence of Fig. 2.8.8, but instead of acquiring a single echo after each excitation, the full *k*-space can be read. The advantages of the diffusion-weighted EPI sequence are a very short acquisition time of less than 200 ms per slice and its insensitivity to motion. However, the image resolution is typically limited to 128 × 128 matrices and echo planar imaging is very sensitive to susceptibility variations as demonstrated in Fig. 2.8.10a,b—different susceptibilities of soft tissue, bone, and air, cause severe image distortion and signal cancellation close to interfaces between soft tissue and air or bone. These effects can be reduced with new imaging methods known as parallel imaging or parallel acquisition techniques (see Sect. 2.4). The underlying idea is to use several receiver coil elements with spatially different coil sensitivity profiles to acquire multiple data sets with reduced *k*-space sampling density in the phase-encode direction. These data sets are used to calculate a single image corresponding to a fully sampled *k*-space during post-processing. Reducing the number of phase-encode steps shortens the EPI echo train, decreases the minimum echo time as well as the total acquisition time, and increases the effective receiver bandwidth in the phase-encode direction. As a result, susceptibility-induced distortions are reduced as shown in Fig. 2.8.10c,d. Alternatively, the accelerated ac-

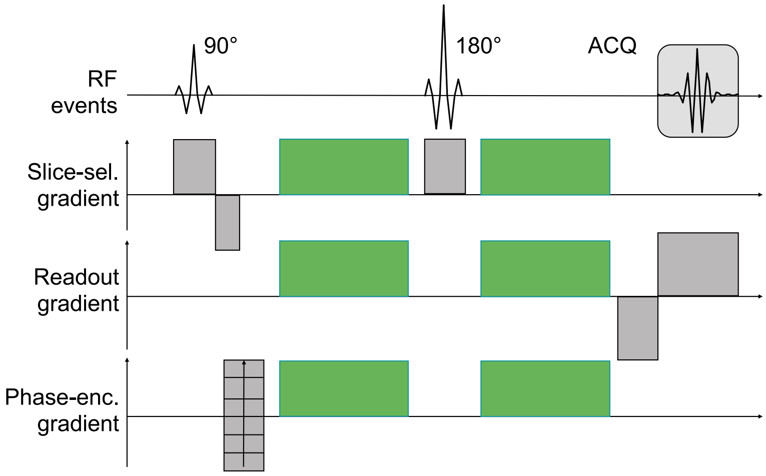

Fig. 2.8.8 Diffusion-weighted spin-echo pulse sequence. Diffusion gradients (shown in *green*) are inserted on both sides of the 180° pulse. Conventional imaging gradients are shown in *gray*

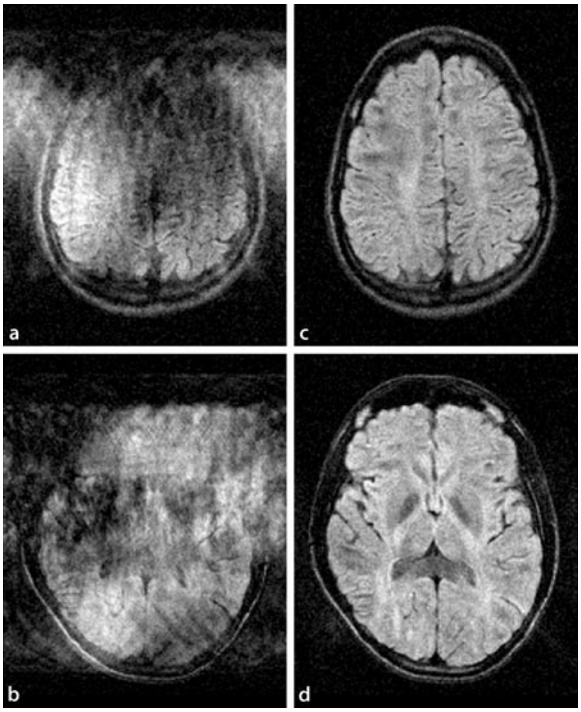

Fig. 2.8.9 Diffusion-weighted spin-echo acquisitions ($b = 550\ \mathrm{s/mm^2}$) of two healthy and cooperative volunteers. **a**,**b** Uncorrected images acquired without cardiac gating. **c**,**d** Images after navigator echo correction acquired with cardiac gating

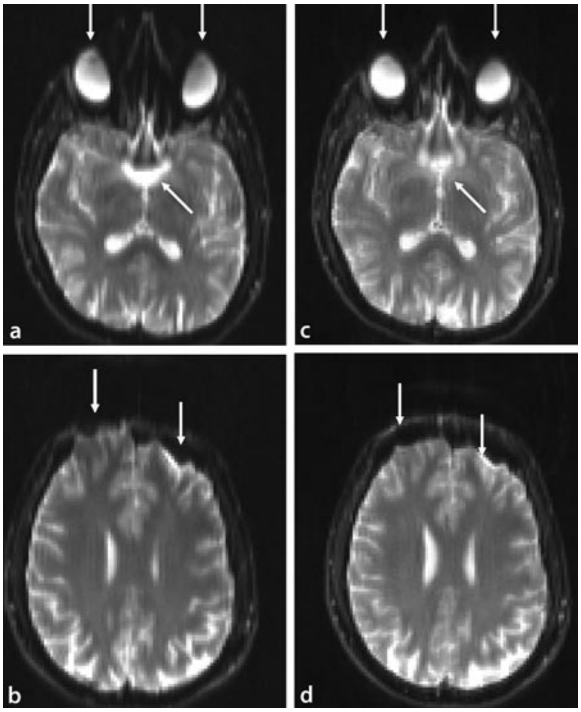

Fig. 2.8.10 Images acquired with a diffusion-weighted EPI sequence. **a**,**b** Conventional EPI sequence exhibiting severe distortions (*arrows*). **c**,**d** EPI sequence with parallel imaging (acceleration factor 2) showing reduced susceptibility artifacts. (For better visualization of artifacts, only images without diffusion weighting ($b = 0$) are shown)

quisition can be used to increase the matrix size and thus enables echo planar imaging with 192 × 192 or 256 × 256 matrices.

Diffusion-weighted imaging of the brain is almost exclusively performed with single-shot EPI sequences (with or without parallel imaging). Other organs or body areas, however, are less suited for echo-planar single-shot acquisitions because of much more severe susceptibility effects that often result in images of non-diagnostic quality. Depending on the slice orientation and receiver coil system, these distortions can be reduced either with parallel imaging as described above or with segmented (i.e., multi-shot) EPI sequences that assemble the raw data from multiple shorter echo trains (Holder et al. 2000; Ries et al. 2000; Einarsdottir et al. 2004). A disadvantage of this approach is the increased motion sensitivity since several excitations (and diffusion preparations) are required for a single data set, resulting in potentially inconsistent phase information; segmented EPI sequences are therefore often combined with additional motion correction techniques.

Several other pulse sequences have been proposed for diffusion-weighted imaging. Diffusion gradients can be added to single-shot fast spin-echo sequences with echo trains of multiple spin-echoes (see also Sect. 2.4) such as HASTE or RARE sequences (Norris et al. 1992). However, the additionally inserted diffusion gradients cause an irregular timing of the originally equidistant refocusing RF pulses. In combination with motion-dependent phase shifts, this violates the CPMG condition, which requires a certain phase relation between excitation and refocusing pulses. Thus, in order to avoid artifacts, various modifications to diffusion-weighted fast spin-echo sequences have been suggested such as additional gradients (Norris et al. 1992), a split acquisition of echoes of even and odd parity (Schick 1997), or modified RF pulse trains (Alsop 1997). These modified diffusion-weighted single-shot fast spin-echo sequences are fast and insensitive to motion; disadvantages are a relatively low signal-to-noise ratio, and a certain image blurring that is characteristic for all single-shot fast spin-echo techniques. They have been applied in the brain (Alsop 1997; Lovblad et al. 1998), the spine (Tsuchiya et al. 2003, Clark and Werring 2002), and in several non-neuro applications such as imaging of musculoskeletal (Dietrich et al. 2005) or breast (Kinoshita et al. 2002) tumors. In contrast to echo-planar imaging, these techniques are insensitive to susceptibility variations and, thus, particularly suited for applications outside the brain. Another, however only infrequently used alternative to echo-planar sequences are fast gradient-echo techniques (FLASH, MP-RAGE) with diffusion preparation (Lee and Price 1994; Thomas et al. 1998).

A special sequence type that has successfully been employed for diffusion-weighted imaging is based on steady-state free-precession (SSFP) sequences (see also Sect. 2.4). Pulse sequences known as CE-FAST or PSIF sequences (the acronym PSIF refers to a reverted fast imaging with steady precession, i.e., FISP, sequence) have been adopted to diffusion-weighted imaging by inserting a single diffusion gradient (LeBihan 1988; Merboldt et al. 1989). However, in contrast to all previously described sequences, the diffusion weighting of this technique cannot be easily determined quantitatively. The observed signal attenuation does not only depend on the diffusion coefficient and the diffusion weighting, but also on the relaxation times, T_1 and T_2, and the flip angle (Buxton 1993). Since these quantities are usually not exactly known, the ADC cannot be determined. Instead, these sequences have been used to acquire diffusion-weighted images that are evaluated based only on visible image contrast. A general advantage of diffusion-weighted PSIF sequences is the relatively short acquisition time due to short repetition times of about 50 ms. Thus, they exhibit only low motion sensitivity. The most important application of this sequence type is the differential diagnosis of osteoporotic and malignant vertebral compression fractures (Baur et al. 1998, 2003). Other applications include diffusion-weighted imaging of the brain (Miller and Pauly 2003) and the cartilage (Miller et al. 2004).

2.8.3.3 Artifacts in Diffusion MRI: Motion and Eddy Currents

As mentioned above, an unwanted side effect arising in virtually all diffusion-weighted pulse sequences is extreme motion sensitivity (Trouard et al. 1996; Norris 2001). By introducing diffusion gradients, the pulse sequence is made sensitive to molecular motion in the micrometer range, but it also becomes susceptible to very small macroscopic motions of the imaged object since the diffusion gradients do not distinguish between stochastic molecular motion and macroscopic bulk motion. Hence, even very small and involuntary movements of the patient, e.g., caused by cardiac motion, cerebrospinal fluid pulsation, breathing, swallowing, or peristalsis, can lead to severe image degradation due to gross motion artifacts. Typical appearances of these artifacts are signal voids and ghosting in phase-encode direction.

Several techniques and pulse-sequence modifications have been proposed to reduce the motion sensitivity of diffusion-weighted MRI. On the one hand, any kind of motion should be minimized. Depending on the body region being imaged, this can be achieved by improved fixation of the patient to the scanner, by imaging during breath hold, or by applying cardiac gating. Effects of motion can also be reduced by decreasing the acquisition time of a pulse sequence, i.e., by using fast acquisition techniques. This is particularly effective if single-shot sequences such as echo planar imaging techniques are applied. Most motion artifacts in diffusion-weighted imaging arise from inconsistent phase information in the complex-valued raw data set. This is caused by different states of motion in the repeated diffusion preparations of the acquisition. In single-shot sequences, only a single diffusion preparation is applied, and thus inconsistent phase information is avoided. It should be noted, however, that even single-shot sequences might be affected by inconsistent phase information if complex data of several measurements is averaged. Instead, only magnitude images should be averaged in diffusion-weighted MRI in order to improve the signal-to-noise ratio.

Another approach to reduce motion artifacts is to correct for motion-related phase errors in the acquired raw data. This can be done using navigator echo–correction techniques (Ordidge et al. 1994; Anderson and Gore 1994; Dietrich et al. 2000). The navigator echo is an additional echo without phase encoding acquired after each diffusion preparation. In the absence of motion, all navigator echoes should be identical. Thus, by comparing the acquired navigator echoes, bulk motion can be detected, and degraded image echoes can be discarded or a phase correction can be applied. More advanced navigator-echo techniques acquire several navigator echoes in different spatial directions (Butts et al. 1996) or use spiral navigator readouts (Miller and Pauly 2003). Certain pulse sequences are self-navigated, i.e., a subset of the acquired raw data can be used as navigator echo without the need for an extra navigator acquisition. Examples are pulse sequences with radial or spiral k-space trajectories that acquire the origin of k-space in every readout (Seifert et al. 2001; Dietrich et al. 2001b). An improved self-navigation is possible with the PROPELLER diffusion sequence, which repeatedly acquires a large area around the origin of k-space (Pipe et al. 2002).

Some image reconstruction techniques have been proposed that do not use the often-inconsistent phase information of raw data at all. In sequences with radial k-space trajectories, images can be reconstructed by filtered back projection of magnitude projection images (Gmitro and Alexander 1993). Another spin-echo–based approach known as line-scan diffusion imaging assembles the image from one-dimensional lines of magnitude data (Gudbjartsson et al. 1996). In addition to substantially reduced motion sensitivity, repetition times and thus image acquisition time can be considerably reduced since the one-dimensional lines are acquired independently of each other. On the other hand, the signal-to-noise ratio of line-scan sequences is substantially lower than that of conventional acquisition techniques and the spatial resolution of this approach is limited as well.

A second unwanted side effect of diffusion-weighted sequences is eddy current effects caused by the extraordinarily long and strong diffusion gradients. Eddy currents are induced electric currents in coils that occur after switching magnetic fields on or off. These currents then create unwanted additional gradient fields resulting in shifted or distorted images and in incorrect diffusion weightings. Whereas most MRI gradient systems compensate very well for eddy current effects after the switching of short gradients typically used for imaging, the longer diffusion gradients are often not well compensated. Hence, diffusion-weighted images are sometimes distorted depending on the diffusion weighting and the direction of the diffusion gradients, resulting in artifacts on ADC maps such as enhanced edges. To avoid these artifacts, several techniques have been suggested. Diffusion gradients can be shortened by using bipolar diffusion gradients (Alexander et al. 1997) or by adding additional 180° pulses during the diffusion preparation (Reese et al. 2003); eddy currents can be partially compensated for by an additional long gradient before the 90° excitation pulse (Alexander et al. 1997); or diffusion-weighted images can be acquired twice with diffusion gradients of opposite polarity (Bodammer et al. 2004). Other eddy-current correction schemes are based on the acquisition of diffusion gradient–dependent field maps and data correction in *k*-space (Horsfield 1999; Papdakis et al. 2005). In general, (automated) image registration as the first step of postprocessing is recommended to reduce influences from both patient motion and eddy-current effects.

2.8.4 MR Measurement of Diffusion Tensor Data

2.8.4.1 Diffusion Trace Imaging

Imaging with the Stejskal-Tanner diffusion preparation as described above in Sect. 2.8.3.1, is only sensitive for molecular diffusion parallel to the direction of the diffusion gradient. The diffusion preparation causes a dephasing of spins that move in the direction of the applied field gradient, i.e., between positions with different magnetic field strengths as illustrated in Fig. 2.8.6. Molecular motion perpendicular to this direction does not contribute to the signal attenuation. In general, the diffusion displacement of spins depends on the considered spatial direction; e.g., protons of water molecules in nerve fibers move more freely parallel to the fiber direction than they do in perpendicular directions. This dependence of the diffusion on spatial orientation can be measured by applying diffusion gradients in different spatial directions, e.g., separately in slice, readout, and phase direction as demonstrated in Fig. 2.8.11. The resulting diffusion-weighted images show substantial signal differences in areas with strong anisotropic diffusion such as the corpus callosum. The signal intensity of the corpus callosum is decreased if diffusion gradients in the left–right direction (readout direction in the example) are applied, but increased for diffusion gradients in the head–foot (slice) direction or the anterior–posterior (phase-encode) direction. This finding is explained by the fact that water molecules diffuse more freely in the left–right direction (parallel to the nerve fibers) than they do in perpendicular directions, i.e., the effective diffusion coefficient is greater in the left–right direction than it is in other directions, and thus the signal attenuation is increased. This orientation dependence is visible in the ADC maps as well: the ADC in the left–right direction of the corpus callosum is increased compared to the ADCs in perpendicular directions. Other areas such as gray matter or the CSF do not show significant differences depending on the diffusion gradient direction, indicating approximately isotropic diffusion.

If the mean (or average) diffusivity of molecules in tissue is to be measured, then diffusion coefficients for all spatial directions must be averaged as shown in Fig. 2.8.11d; the corresponding ADC map is given by the mean value of the three direction-dependent maps. Since the direction-independent or mean ADC of tissue is proportional to the trace of the diffusion tensor, this measurement is also referred to as diffusion trace imaging. The measurement of such a direction-independent diffusion-weighted image can be very important to avoid misinterpretation of hyperintense areas due to high anisotropy as tissue with generally reduced ADC such as areas of focal ischemia. Therefore, diffusion-weighted stroke MRI is generally based on isotropically diffusion-weighted images.

If only a single direction-independent diffusion-weighted image is required for diagnosis, it appears disadvantageous to perform three orthogonal diffusion measurements at the cost of three-times-increased acquisition duration. It should be noted that it is not possible to simply apply gradients in all three directions simultaneously for this purpose; this results in a single magnetic field gradient in diagonal direction, which is again only sensitive for diffusion parallel to this diagonal. However, the Stejskal-Tanner diffusion preparation can be extended by a more sophisticated series of gradient pulses in different directions to achieve an isotropic diffusion weighting within a single diffusion measurement (Wong et al. 1995; Mori and van Zilj 1995; Chun et al. 1998; Cercignani and Horsefield 1999).

2.8.4.2 Basic Diffusion Tensor Imaging

Isotropically diffusion-weighted images can thus be acquired by either a single or three orthogonal diffusion

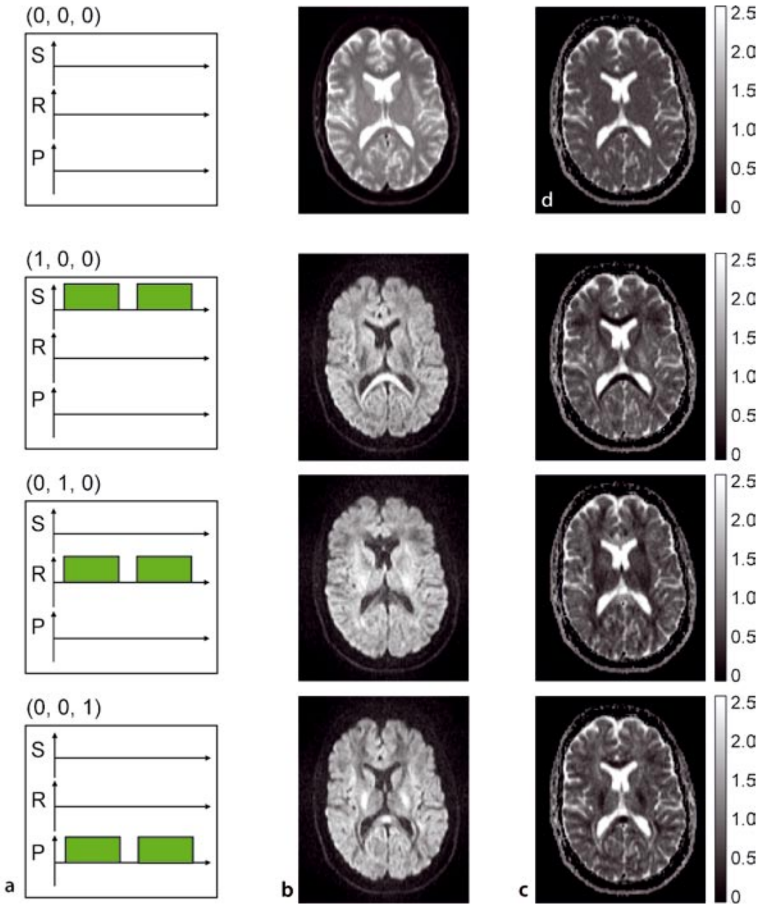

Fig. 2.8.11 Diffusion-weighted imaging in different spatial directions. **a** Diffusion gradients in slice (*S*), readout (*R*), and phase (*P*) direction; the row vectors (S, R, P) denote the selected gradients. **b** Corresponding diffusion-weighted images. **c** Calculated ADC maps corresponding to the diffusion directions in **a** and images in **b**. **d** Averaged ADC map; all ADCs are in units of 10^{-3} mm^2/s. Note the differing contrast in the diffusion-weighted images and ADC maps depending on the diffusion gradient direction (e.g., in the corpus callosum)

preparations. However, three measurements are not yet sufficient to determine the properties of diffusion anisotropy in all cases. For example, if a nerve fiber is oriented diagonally to all three coordinate axes, then the diffusion attenuation in this fiber will be the same for the three measurements and cannot be distinguished from isotropic diffusion. The measurement of the full diffusion tensor (cf. Sect. 2.8.2.2) is required to cope with these more general cases. In spite of this limitation, some studies have used the ratio of the largest and the smallest of three perpendicular diffusion coefficients as an estimation of the anisotropy (Holder et al. 2000). However, this approach should be regarded as an inferior method in comparison to diffusion tensor evaluation and is generally not recommended.

To determine the diffusion tensor, i.e., to fully measure anisotropic diffusion, more than three diffusion-sensitized measurements with diffusion gradients in different spatial directions are required. However, only the diagonal elements of the tensor, i.e., D_{xx}, D_{yy}, D_{zz}, can be measured directly; these elements are exactly the direction-dependent ADCs determined in the example above. The other three (off-diagonal) tensor components D_{xy}, D_{xz}, D_{yz} do not describe diffusion in a spatial direction but the correlation of diffusion in two different directions; they cannot be measured directly, but must be calculated as linear combinations of several measurements.

The minimum number of measurements required to determine the full diffusion tensor can be deduced from the form of the diffusion tensor matrix: The tensor has six independent components D_{xx}, D_{yy}, D_{zz}, D_{xy}, D_{xz}, D_{yz} and, thus, at least six independent diffusion measurements are required. Each of these measurements is based on images of at least two different *b*-values; in order to reduce the total number of measurements, usually a *b*-value of 0 is chosen as a direction-independent reference. Thus, this reference image has to be acquired only once instead of separately for each diffusion direction. A possible and frequently used choice of seven diffusion-weighted acquisitions that are sufficient to determine the diffusion tensor (Basser and Pierpaoli 1998) is shown in Fig. 2.8.12. None of the six tensor components D_{xx}, D_{yy}, D_{zz}, D_{xy}, D_{xz}, or D_{yz} is measured directly by this gradient scheme; instead, all components must be calculated as linear combinations of the diffusion coefficients in these six directions. This calculation is based on the so-called *b*-matrix (Basser and Pierpaoli 1998), a symmetric 3 × 3 matrix describing the diffusion weighting for an arbitrary diffusion gradient

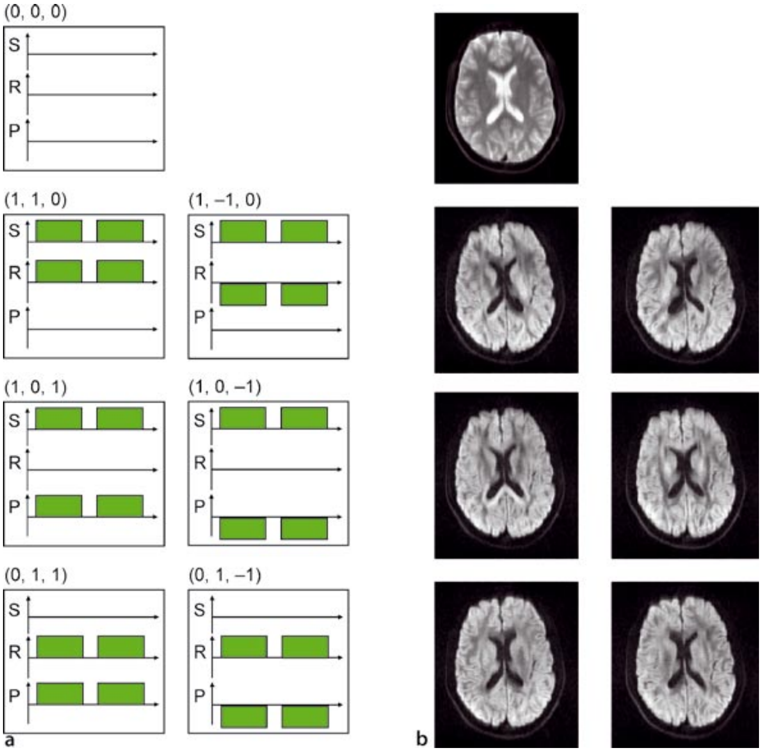

Fig. 2.8.12 Diffusion tensor imaging **a** Choice of diffusion gradients (*S* slice, *R* readout, *P* phase direction; the row vector denotes the selected gradients and their polarity) and **b** corresponding diffusion-weighted images for the determination of the diffusion tensor. Note the different contrast in the diffusion-weighted images depending on the diffusion gradient direction (e.g., in the corpus callosum)

$\boldsymbol{g} = (g_x\, g_y\, g_z)$:

$$b = (\gamma \times \delta)^2 \left(\Delta - \frac{\delta}{3}\right) \boldsymbol{gg}$$

$$= (\gamma \times \delta)^2 \left(\Delta - \frac{\delta}{3}\right) \begin{pmatrix} g_x g_x & g_x g_y & g_x g_z \\ g_x g_y & g_y g_y & g_y g_z \\ g_x g_z & g_y g_z & g_z g_z \end{pmatrix},$$

where $\boldsymbol{gg}$ denotes the dyadic product of these two vectors. This matrix is used to describe the signal attenuation due to the diffusion gradient as

$$S(D, b) = S_0 \times \exp(-\operatorname{tr}(bD))$$

$$= S_0 \times \exp\left(-\sum_{i=x,y,z} \sum_{j=x,y,z} b_{ij} \times D_{ij}\right),$$

where bD denotes the matrix product of the b-matrix and the diffusion tensor matrix. The elements of the diffusion tensor D_{ij} can be determined by solving a system of linear equations, since the b-matrix and the signal attenuation are known. The result of this calculation is shown in Fig. 2.8.13. The three calculated diagonal elements correspond to the direct ADC measurements of Fig. 2.8.11. The off-diagonal elements are generally much lower than the diagonal elements (note the differently scaled intensity maps) are and are close to zero in areas with predominantly isotropic diffusion (gray matter and CSF).

2.8.4.3 Optimizing Diffusion Tensor Imaging

A simple protocol for diffusion tensor imaging consists of one reference measurement without diffusion weighting (b-value is 0) and six diffusion-weighted measurements with different gradient directions. These gradient directions should be “as different as possible,” i.e., pointing isotropically in all spatial directions. A typical b-value for DTI measurements of the brain is 1,000 s/mm^2. Averaging of multiple acquisitions is frequently performed to increase the SNR especially of the images with diffusion weighting. However, all these parameters (b-values, diffusion directions, number of averages) have been evaluated in a number of studies with the aim of optimizing the accuracy of diffusion tensor data.

Several studies investigated the optimum choice of the b-values both for conventional diffusion-weighted imaging and for diffusion tensor imaging. Although the results of these studies vary to a certain extent, generally b-values in the range between about 900 and 1400 s/mm^2 have been found to provide the highest accuracy of diffusion measurements in the brain (Jones et al. 1999; Armitage and Bastin 2001; Kingsley and Monahan 2004). The optimum number of averages depends on the b-values, which influence the signal attenuation and, thus, the signal-to-noise ratio of the diffusion-weighted images. In general, a higher number of averages are recommended for the acquisition with the high b-value than for the reference image with low b-value or without

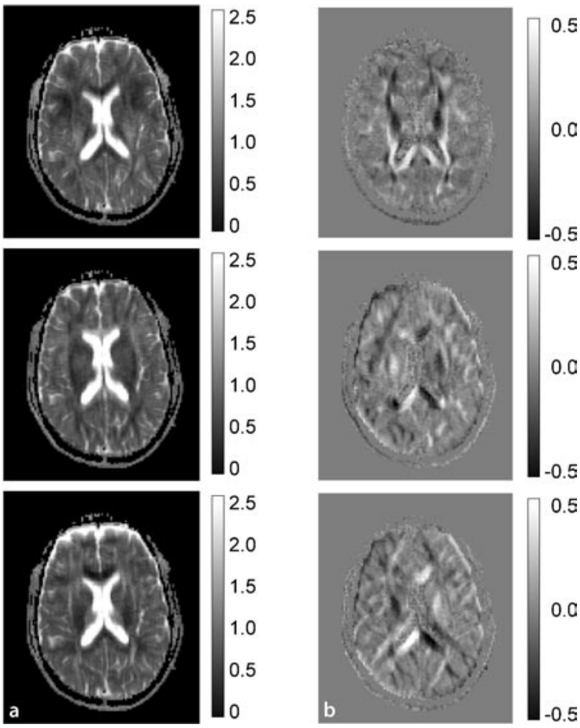

Fig. 2.8.13 Diffusion tensor data calculated from the measurements shown in Fig. 2.8.12; all diffusion coefficients are in units of 10^{-3} mm^2/s. **a** The three diagonal elements D_{xx}, D_{yy}, and D_{zz}, and **b** the off-diagonal elements D_{xy}, D_{xz}, and D_{yz} of the tensor matrix. Note the different intensity scales for diagonal and off-diagonal elements. Some remaining eddy-current artifacts can be seen as enhanced edges in the maps of the off-diagonal elements

any diffusion weighting. As shown by Jones et al. (1999) for their choice of *b*-values, the optimum ratio of the total number of acquisitions with high *b*-value and low *b*-value is about 8.4.

The number of diffusion gradients and their directions has also been investigated in several studies. Generally, the accuracy of diffusion tensor data, especially of the diffusion anisotropy and main diffusion direction, is improved when the number of different diffusion directions is increased (Jones et al. 1999; Papadakis et al. 2000; Skare et al. 2000; Jones 2004). If the number of different directions is fixed, then the accuracy of the measurements can be increased by choosing an optimized set of diffusion directions (Skare et al. 2000; Hasan et al. 2001). No final consensus about the optimum number and choice of directions of diffusion gradients has yet been established, but protocols with 20 or more diffusion directions are currently recommended by many research groups.

2.8.4.4 Beyond Diffusion Tensor Imaging

The diffusion tensor contains complex information about the tissue microstructure that is best visualized as a three-dimensional ellipsoid as discussed in Sect. 2.8.2.2. However, diffusion tensor data may be insufficient to describe tissue in certain geometrical situations. A well-known example is the crossing of white-matter fibers within a single voxel as illustrated in Fig. 2.8.14. Water diffusion in such voxels cannot be fully described by a single ellipsoid, i.e., by the diffusion tensor. To overcome this limitation, more complex measurement techniques such as high-angular resolution diffusion imaging (HARDI) (Frank 2001; Tuch et al. 2002) and q-ball imaging (Tuch 2004) have been proposed. All these techniques use a large number of different diffusion directions (e.g., between 43 [Frank 2001] and 253 [Tuch 2004]) distributed isotropically in space. Diffusion data is measured with high-angular resolution in order to determine the spatial distribution of diffusion in more detail as indicated in Fig. 2.8.14d.

A further generalization of diffusion tensor measurements loosens the assumption of Gaussian diffusion, which was illustrated in Fig. 2.8.2. If diffusion is severely restricted, e.g., by cell membranes, no or very few molecules will move through this border; the probability distribution of diffusion distances will be limited to distances within the cell volume and will no longer be Gaussian. The exact displacement probabilities in restricted diffusion can be measured with methods called *q*-space diffusion imaging (Assaf et al. 2002) or diffusion spectrum imaging (Wedeen et al. 2005). Both techniques require the acquisition of images with a large number of different *b*-values and, in the case of diffusion spectrum imaging, of different diffusion directions; e.g., the total number of diffusion measurements reported by Wedeen et al. (2005) is 515. Obviously, this large number of measurements severely limits the applicability of these new techniques in clinical studies; the studies should therefore be regarded as experimental work. Another approach to overcome the limitations of models based purely on Gaussian diffusion has been proposed by Jensen et al. as diffusional kurtosis imaging (Jensen et al. 2005). Diffusion data is acquired for several *b*-values over a large range between 0 and 2,500 s/mm^2 similarly to the way data is acquired in *q*-space imaging, but with a different mathematical model of the non-exponential decay. This method is related to several other studies that investigated diffusion properties in tissue at high *b*-values and found non-mono-exponential diffusion attenuation curves (Inglis et al. 2001; Clark et al. 2002). This observation has frequently been attributed to the simultaneous measurement of water molecules in different environments such as the intracellular and the extracellular space; however, no final agreement on the interpretation of these data has been established (Sehy et al. 2002).

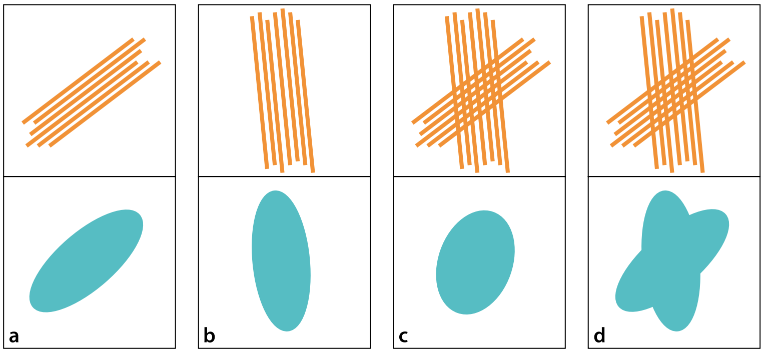

Fig. 2.8.14 The diffusion tensor cannot represent diffusion properties in voxels with crossing nerve fibers. Voxels with a single predominant fiber direction (**a**,**b**) show diffusion tensor ellipsoids whose longest axes correspond to the fiber orientation. Voxels with crossing fibers (**c**) result in a diffusion tensor ellipsoid with reduced anisotropy pointing in an averaged fiber direction. Advanced methods such as high angular resolution diffusion imaging (**d**) can resolve different fiber orientations within a single voxel

2.8.5 Visualization of Diffusion Tensor Data

Diffusion tensor imaging results in a large amount of data—a full diffusion tensor, i.e., a symmetric 3 × 3 matrix, is determined for each pixel of the image dataset. Due to this complex data structure, there is no simple way to visualize the complete diffusion tensor as a single intensity or color map. It would be straightforward to display the six independent elements of the tensor as separate maps as shown in Fig. 2.8.13; however, this would not be very helpful for the interpretation or quantitative evaluation of diffusion tensor data. Instead, several techniques are used to reduce the diffusion tensor information to simpler datasets that can as easily be displayed and interpreted as other imaging data.

2.8.5.1 Scalar Diffusion Quantities

Most results of imaging examinations are presented as either signal intensity images or scalar parameter maps. These images and maps have the advantage that they can easily be manipulated, e.g., the contrast can be interactively adjusted, and they can be quantitatively evaluated by statistics over regions of interest. In order to obtain similar parameter maps of diffusion tensor data, a single scalar reflecting a certain tensor property must be calculated. The most important examples of such scalars are the mean diffusivity or trace of the diffusion tensor and the anisotropy of the tensor. The mean diffusivity of a diffusion tensor measurement, i.e., the diffusion coefficient averaged over all spatial directions, is displayed as parameter maps in Fig. 2.8.15a,b. The same data can be displayed either as an intensity-coded map (Fig. 2.8.15a) or as a color-coded map (Fig. 2.8.15b). Both maps illustrate, e.g., the high diffusivity of CSF and the typical ADCs of about 0.7×10^{-3} mm^2/s in the white matter.

Many different scalar measures have been proposed to describe diffusion anisotropy, cf. Sect. 2.8.2.3. The two most important are the fractional anisotropy and the relative anisotropy shown in Fig. 2.8.15c,d. The maps are very similar; both show the high anisotropy of white matter as hyperintense areas in contrast to low anisotropy in gray matter or CSF.

These two scalars derived from the diffusion tensor are by far the most important quantities for the clinical evaluation of diffusion tensor data. The vast majority of clinical studies based on diffusion tensor imaging determine the mean diffusivity and the anisotropy in regions of interest in order, e.g., to statistically compare these data between certain patient groups or between patients and healthy controls.

2.8.5.2 Vector Diffusion Quantities

The mean diffusivity and the anisotropy contain certain important information about the diffusion tensor; if the diffusion tensor is visualized as ellipsoid, then the diffusivity reflects the volume of the ellipsoid and the anisotropy its deviation from a spherical shape. However, any information about the main diffusion direction, i.e., the orientation of the longest axis of the diffusion tensor ellipsoid, is missing. This direction corresponds to the microstructural orientation of tissue, e.g., the orientation of white-matter tracts, and is determined as the eigenvector of the largest eigenvalue of the tensor (c.f. Sect. 2.8.2.2). There are two common methods to visualize the direction of this eigenvector: color coding and direct vector display. The direction can be color-coded using the red–green–blue (RGB) color model. Each direction in space is defined by a three-component vector $\boldsymbol{v} = (v_x\ v_y\ v_z)$. If this three-component vector is interpreted as an RGB color specification, vectors in x-direction, $\boldsymbol{v} = (1\ 0\ 0)$, appear as red pixels, vectors in y-direction as green pixels, and vectors in z-direction as blue pixels. Eigenvectors in other directions are displayed as (additive) mixtures of different colors, e.g., the vector $\boldsymbol{v} = (1\ 0\ 1)$ as mixture of red and blue, yielding violet pixels. The resulting color map is finally scaled with the diffusion anisotropy, since the

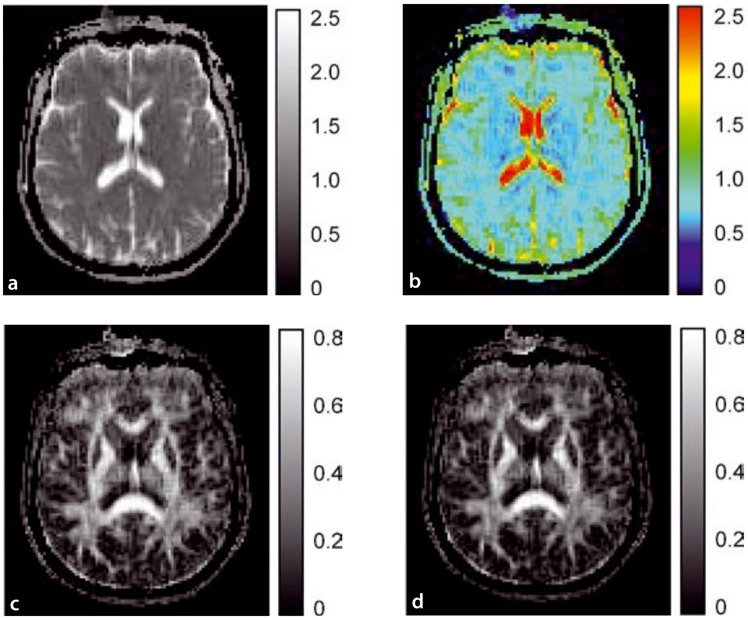

Fig. 2.8.15 Parameter maps displaying scalar quantities calculated from the diffusion tensor. Direction-independent mean diffusivity shown as gray-scaled map (**a**) and as color-coded map (**b**); the diffusion coefficients are given in units of 10^{-3} mm^2/s. (**c**) Fractional anisotropy and (**d**) relative anisotropy

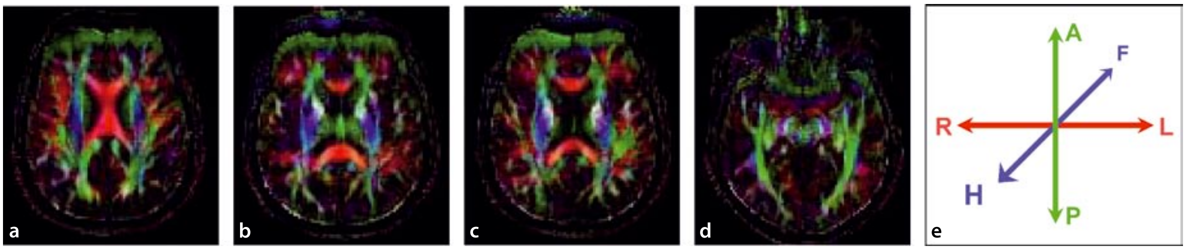

Fig. 2.8.16 Color-coded visualization of main diffusion orientation in four different slices (**a**–**d**). The main diffusion direction (orientation of the longest axes of the diffusion ellipsoid) is shown in *red*, *green*, and *blue* for left–right, anterior–posterior, and head–foot orientation, respectively, as indicated in **e**. The green rim at the frontal brain is caused by remaining eddy-current and susceptibility artifacts

main diffusion direction is of interest only in areas with high anisotropy. Some examples of these color-coded vector maps are shown in Fig. 2.8.16. The red color of the corpus callosum demonstrates that the nerve fibers are predominantly oriented in the left–right direction. White-matter areas in green and blue are oriented in the anterior–posterior direction and the head–foot direction, respectively.

Alternatively, the main diffusion direction can be directly displayed by a small line in each pixel; some authors refer to this technique as whisker plots. This visualization is on the one hand more intuitive than color coding, but on the other hand difficult to display for large areas because of the large number of pixels (and hence lines) of a complete image. An example is shown in Fig. 2.8.17; the magnified area shows again the corpus callosum, where the diffusion directions follow the anatomical orientation of the nerve fibers.

A general problem and limitation of the visualization of the main diffusion direction is that it is based on the assumption of linear diffusion, i.e., the diffusion ellipsoid is supposed to have a cigar-like shape. This is usually true in white matter tracts, but may lead to deceptive graphical depictions at crossing fibers or if diffusion is described by a planar tensor. Another disadvantage is that vector maps are difficult to compare or to evaluate statistically.

2.8.5.3 Full Tensor Visualization

It is also possible to visualize the full diffusion tensor using the diffusion ellipsoid introduced in Sect. 2.8.2.2. As in the vector plots, it is often difficult to visualize the entire amount of data belonging to a single image slice at once. Therefore, this 3D tensor visualization is usually combined with tools to zoom into the illustration and

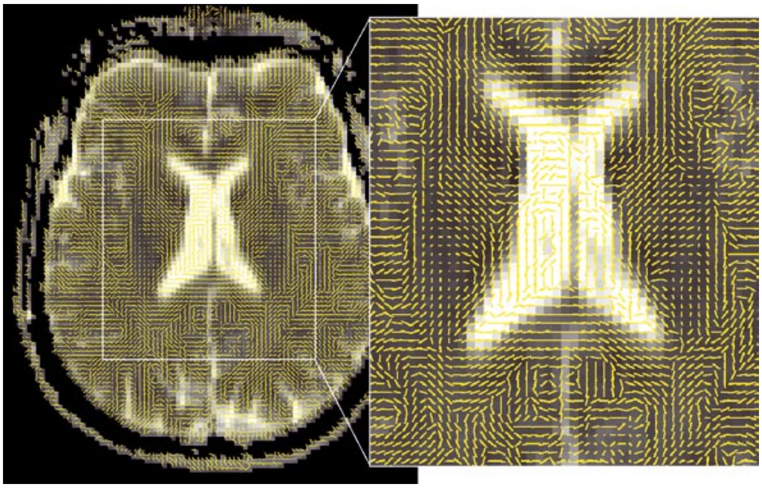

Fig. 2.8.17 Direct vector visualization of main diffusion orientation; the orientation of the longest axis of the diffusion ellipsoid is shown as a *yellow line* for each pixel

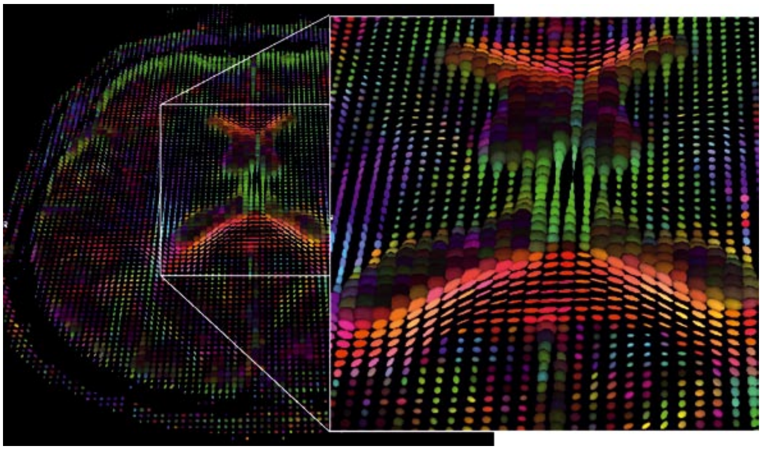

Fig. 2.8.18 Three-dimensional visualization of the full diffusion tensor as color-coded ellipsoid; the ellipsoids are colored as in Fig. 2.8.16. Visualization was performed with the "DTI Task Card" provided by the MGH/MIT/HMS Athinoula A. Martinos Center for Functional and Structural Biomedical Imaging (Ruopeng Wang)

to rotate the slice in order to view the tensors in specific areas of the brain, as demonstrated in Fig. 2.8.18. The ellipsoids are additionally color-coded to emphasize the direction of their longest axis (the main diffusion direction); their brightness is scaled by the anisotropy. Thus, the ellipsoid visualization combines features of the techniques described in the previous sections and, e.g., CSF is displayed as large but relatively dark spheres (denoting a high diffusion coefficient and low anisotropy), while the tensors in fiber tracts appear as bright elongated ellipsoids corresponding to linear diffusion in a single predominant orientation.

The exact depiction of the tensor information is not standardized but may look different depending on the tools used. An alternative visualization may substitute the ellipsoids by cuboids with equivalent dimensions as shown in Fig. 2.8.19. The presented information is the same as before, but the computational cost required to display cuboids is substantially lower than with smooth ellipsoids. Thus, interactive manipulation of the 3D datasets may be faster using the cuboid visualization.

2.8.5.4 Fiber Tracking

Close inspection of the main diffusion directions in Figs. 2.8.17 or 2.8.19 suggests that the shape of white matter tracts can be reconstructed by connecting several diffusion directions in an appropriate way. This process is illustrated in Fig. 2.8.20, based on a magnification of Fig. 2.8.17. By choosing a start point and following the main diffusion direction, trajectories can be constructed that visualize the fiber tracts of white matter. A typical example is shown in Fig. 2.8.21, where a seed region was placed within the corpus callosum, and all fibers through this seed region were reconstructed. The color of the fi-

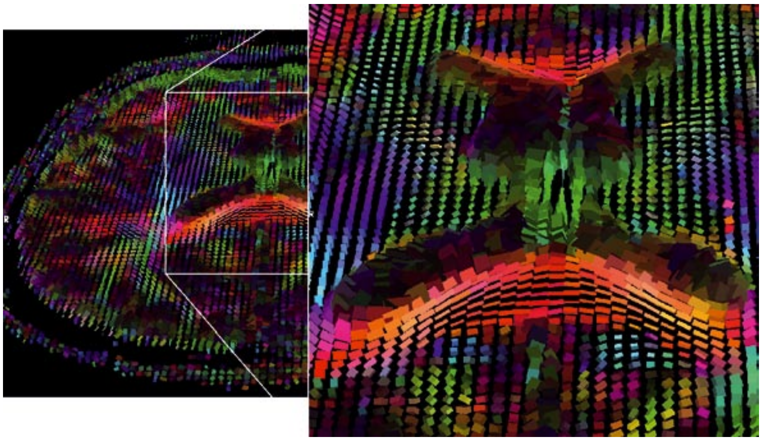

Fig. 2.8.19 Three-dimensional visualization of the full diffusion tensor as color-coded cuboids; the cuboids are colored as in Fig. 2.8.16. Visualization was performed with the "DTI Task Card" provided by the MGH/MIT/HMS Athinoula A. Martinos Center for Functional and Structural Biomedical Imaging (Ruopeng Wang)

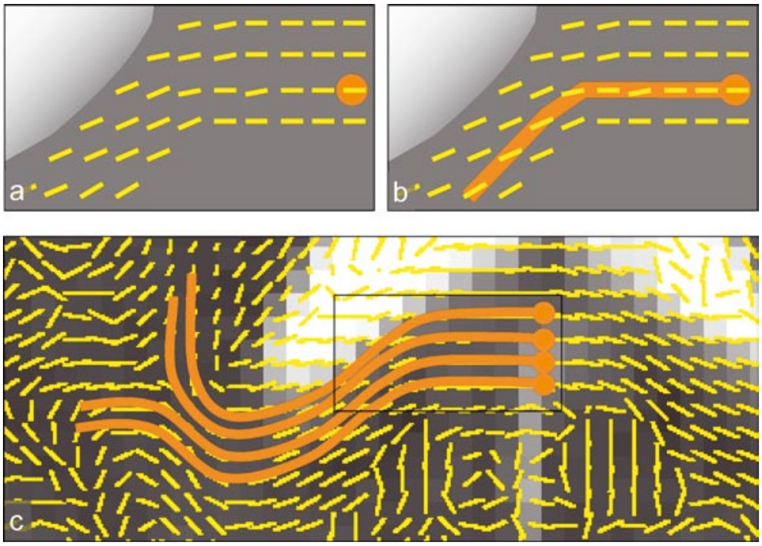

Fig. 2.8.20 Fiber tracking (white-matter tractography) is performed by connecting pixels along the main diffusion direction. **a** A start point (or seed region) is selected. **b** Pixels are connected following the main diffusion orientation. **c** Several reconstructed fiber tracts starting in the corpus callosum

bers reflects the local anisotropy in this case, but various other color schemes could be used instead.

Fiber tracking or diffusion tractography was developed in the late 1990s (Mori et al. 1999; Conturo et al. 1999; Mori and van Zijl 2002; Melhem et al. 2002), and a multitude of different algorithms to reconstruct fibers have been proposed since then. Most techniques include data interpolation to increase the spatial resolution, and all require certain criteria to decide when the tracking of a fiber should be stopped (e.g., at pixels with low anisotropy or at sudden changes of diffusion direction). Fiber tracking is usually based either on a single-region approach, in which all fibers are tracked that go through a user-defined region of interest, or on a two-region approach where connecting fibers between two regions are reconstructed.

Fiber tracking depends on good image quality, with sufficient signal-to-noise ratio and without substantial distortion artifacts. Increased noise can reduce the calculated anisotropy (Jones and Basser 2004) and, thus, the length of the reconstructed fibers. Image distortions cause a mismatch of anatomical fiber orientation and the measured diffusion direction and thus can lead to erroneous tractography results. Therefore, parallel imaging and eddy-current correction techniques can improve the results of white-matter tractography. It is generally assumed that isotropic spatial image resolution is preferable for fiber tracking applications. A typical protocol suggested by Jones et al. acquires data of the whole brain in isotropic $2.5 \times 2.5 \times 2.5$ mm^3 resolution (Jones et al. 2002b).

Fiber tracking is a valuable tool to visualize white matter structures of the brain. However, it is still very difficult to evaluate tractography results quantitatively, to assess the accuracy of reconstructed fibers, or to compare the results of different examinations. First approaches to these questions include the spatial normalization of ten-

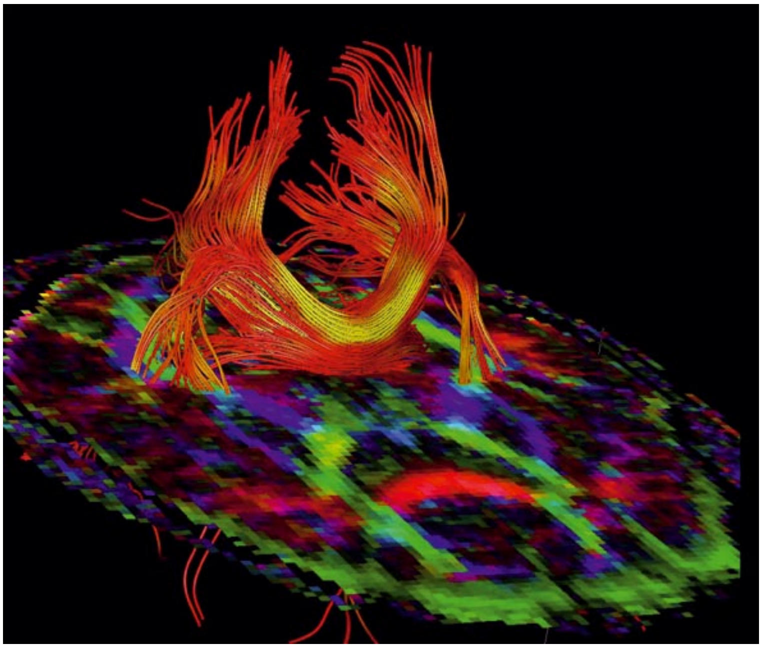

Fig. 2.8.21 Reconstruction of white matter tracts starting at a seed region in the corpus callosum. Visualization was performed with the "DTI Task Card" provided by the MGH/MIT/HMS Athinoula A. Martinos Center for Functional and Structural Biomedical Imaging (Ruopeng Wang)

sor data sets (Jones et al. 2002a) and the determination and visualization of uncertainties of diffusion tensor results (Jones 2003; Jones and Pierpaoli 2005).

References

1. Alexander AL, Tsuruda JS, Parker DL (1997) Elimination of eddy current artifacts in diffusion-weighted echo planar images: the use of bipolar gradients. Magn Reson Med 38:1016–1021
2. Alsop DC (1997) Phase insensitive preparation of single-shot RARE: application to diffusion imaging in humans. Magn Reson Med 38:527–533
3. Anderson AW, Gore JC (1994) Analysis and correction of motion artifacts in diffusion weighted imaging. Magn Reson Med 32:379–387
4. Armitage PA, Bastin ME (2001) Utilizing the diffusion-to-noise ratio to optimize magnetic resonance diffusion tensor acquisition strategies for improving measurements of diffusion anisotropy. Magn Reson Med 45:1056–1065
5. Assaf Y, Ben-Bashat D, Chapman J, Peled S, Biton IE, Kafri M, Segev Y, Hendler T, Korczyn AD, Graif M, Cohen Y (2002) High b-value q-space analyzed diffusion-weighted MRI: application to multiple sclerosis. Magn Reson Med 47:115–126
6. Basser PJ, Mattiello J, LeBihan D (1994) MR diffusion tensor spectroscopy and imaging. Biophys J 66:259–267
7. Basser PJ, Pierpaoli C (1996) Microstructural and physiological features of tissues elucidated by quantitative-diffusion-tensor MRI. J Magn Reson B 111:209–219
8. Basser PJ, Pierpaoli C (1998) A simplified method to measure the diffusion tensor from seven MR images. Magn Reson Med 39:928–934
9. Baur A, Stabler A, Bruning R, Bartl R, Krodel A, Reiser M, Deimling M (1998) Diffusion-weighted MR imaging of bone marrow: differentiation of benign versus pathologic compression fractures. Radiology 207:349–356
10. Baur A, Dietrich O, Reiser M (2003) Diffusion-weighted imaging of bone marrow: current status. Eur Radiol 13:1699–1708
11. Beaulieu C (2002) The basis of anisotropic water diffusion in the nervous system - a technical review. NMR Biomed 15:435–455
12. Bodammer N, Kaufmann J, Kanowski M, Tempelmann C (2004) Eddy current correction in diffusion-weighted imaging using pairs of images acquired with opposite diffusion gradient polarity. Magn Reson Med 51:188–193
13. Boulanger Y, Amara M, Lepanto L, Beaudoin G, Nguyen BN, Allaire G, Poliquin M, Nicolet V (2003) Diffusion-weighted MR imaging of the liver of hepatitis C patients. NMR Biomed 16:132–136
14. Brown R (1866) A brief account of microscopical observations made in the months of June, July and August, 1827, on the particles contained in the pollen of plants; and on the general existence of active molecules in organic and inorganic bodies. In: Bennett JJ (ed) The miscellaneous botanical works of Robert Brown, vol. 1. Hardwicke, London
15. Burdette JH, Elster AD, Ricci PE (1999) Acute cerebral infarction: quantification of spin-density and T2 shine-through phenomena on diffusion-weighted MR images. Radiology 212:333–339

16. Butts K, de Crespigny A, Pauly JM, Moseley M (1996) Diffusion-weighted interleaved echo planar imaging with a pair of orthogonal navigator echoes. Magn Reson Med 35:763–770
17. Buxton RB (1993) The diffusion sensitivity of fast steady-state free precession imaging. Magn Reson Med 29:235–243
18. Carr HY, Purcell EM (1954) Effects of diffusion on free precession in nuclear magnetic resonance experiments. Phys Rev 94:630–638
19. Cercignani M, Horsfield MA (1999) An optimized pulse sequence for isotropically weighted diffusion imaging. J Magn Reson 140:58–68
20. Cercignani M, Iannucci G, Rocca MA, Comi G, Horsfield MA, Filippi M (2000) Pathologic damage in MS assessed by diffusion-weighted and magnetization transfer MRI. Neurology 54:1139–1144
21. Chien D, Buxton RB, Kwong KK, Brady TJ, Rosen BR (1990) MR diffusion imaging of the human brain. J Comput Assist Tomogr 14:514–520
22. Chien D, Kwong KK, Gress DR, Buonanno FS, Buxton RB, Rosen BR (1992) MR diffusion imaging of cerebral infarction in humans. AJNR Am J Neuroradiol 13:1097–1102
23. Chun T, Ulug AM, van Zijl PC (1998) Single-shot diffusion-weighted trace imaging on a clinical scanner. Magn Reson Med 40:622–628
24. Clark CA, Werring DJ (2002a) Diffusion tensor imaging in spinal cord: methods and applications – a review. NMR Biomed 15:578-586
25. Clark CA, Hedehus M, Moseley ME (2002b) In vivo mapping of the fast and slow diffusion tensors in human brain. Magn Reson Med 47:623–628
26. Conturo TE, Lori NF, Cull TS, Akbudak E, Snyder AZ, Shimony JS, McKinstry RC, Burton H, Raichle ME (1999) Tracking neuronal fiber pathways in the living human brain. Proc Natl Acad Sci USA 96:10422–10427
27. Cova M, Squillaci E, Stacul F, Manenti G, Gava S, Simonetti G, Pozzi-Mucelli R (2004) Diffusion-weighted MRI in the evaluation of renal lesions: preliminary results. Br J Radiol 77:851–857
28. Dietrich O, Heiland S, Benner T, Sartor K (2000) Reducing motion artefacts in diffusion-weighted MRI of the brain: efficacy of navigator echo correction and pulse triggering. Neuroradiology 42:85–91
29. Dietrich O, Heiland S, Sartor K (2001a) Noise correction for the exact determination of apparent diffusion coefficients at low SNR. Magn Reson Med 45:448–453
30. Dietrich O, Herlihy A, Dannels WR, Fiebach J, Heiland S, Hajnal JV, Sartor K (2001b) Diffusion-weighted imaging of the spine using radial *k*-space trajectories. MAGMA 12:23–31
31. Dietrich O, Raya JG, Sommer J, Deimling M, Reiser MF, Baur-Melnyk A (2005) A comparative evaluation of a RARE-based single-shot pulse sequence for diffusion-weighted MRI of musculoskeletal soft-tissue tumors. Eur Radiol 15:772–783
32. Einarsdottir H, Karlsson M, Wejde J, Bauer HC (2004) Diffusion-weighted MRI of soft tissue tumours. Eur Radiol 14:959–963
33. Filippi M, Inglese M (2001) Overview of diffusion-weighted magnetic resonance studies in multiple sclerosis. J Neurol Sci 186:S37–S43
34. Frank LR (2001) Anisotropy in high angular resolution diffusion-weighted MRI. Magn Reson Med 45:935–939
35. Gmitro AF, Alexander AL (1993) Use of a projection reconstruction method to decrease motion sensitivity in diffusion-weighted MRI. Magn Reson Med 29:835–838
36. Gudbjartsson H, Maier SE, Mulkern RV, Morocz IA, Patz S, Jolesz FA (1996) Line scan diffusion imaging. Magn Reson Med 36:509–519
37. Hahn EL (1950) Spin-echoes. Phys Rev 80:580–594
38. Hasan KM, Parker DL, Alexander AL (2001) Comparison of gradient encoding schemes for diffusion-tensor MRI. J Magn Reson Imaging 13:769–780
39. Helenius J, Soinne L, Perkio J, Salonen O, Kangasmaki A, Kaste M, Carano RA, Aronen HJ, Tatlisumak T (2002) Diffusion-weighted MR imaging in normal human brains in various age groups. AJNR Am J Neuroradiol 23:194–199
40. Herneth AM, Philipp MO, Naude J, Funovics M, Beichel RR, Bammer R, Imhof H (2002) Vertebral metastases: assessment with apparent diffusion coefficient. Radiology 225:889–894
41. Holder CA, Muthupillai R, Mukundan S Jr, Eastwood JD, Hudgins PA (2000) Diffusion-weighted MR imaging of the normal human spinal cord in vivo. AJNR Am J Neuroradiol 21:1799–1806
42. Horsfield MA (1999) Mapping eddy current induced fields for the correction of diffusion-weighted echo planar images. Magn Reson Imaging 17:1335–1345
43. Inglis BA, Bossart EL, Buckley DL, Wirth ED III, Mareci TH (2001) Visualization of neural tissue water compartments using biexponential diffusion tensor MRI. Magn Reson Med 45:58–587
44. Jensen JH, Helpern JA, Ramani A, Lu H, Kaczynski K (2005) Diffusional kurtosis imaging: the quantification of non-gaussian water diffusion by means of magnetic resonance imaging. Magn Reson Med 53:1432–1440
45. Jones DK (2003) Determining and visualizing uncertainty in estimates of fiber orientation from diffusion tensor MRI. Magn Reson Med 49:7–12
46. Jones DK (2004a) The effect of gradient sampling schemes on measures derived from diffusion tensor MRI: a Monte Carlo study. Magn Reson Med 51:807–815
47. Jones DK, Basser PJ (2004b) "Squashing peanuts and smashing pumpkins": how noise distorts diffusion-weighted MR data. Magn Reson Med 52:979–993
48. Jones DK, Pierpaoli C (2005) Confidence mapping in diffusion tensor magnetic resonance imaging tractography using a bootstrap approach. Magn Reson Med 53:1143–1149
49. Jones DK, Horsfield MA, Simmons A (1999) Optimal strategies for measuring diffusion in anisotropic systems by magnetic resonance imaging. Magn Reson Med 42:515-525

50. Jones DK, Griffin LD, Alexander DC, Catani M, Horsfield MA, Howard R, Williams SC (2002a) Spatial normalization and averaging of diffusion tensor MRI data sets. Neuroimage 17:592–617
51. Jones DK, Williams SC, Gasston D, Horsfield MA, Simmons A, Howard R (2002b) Isotropic resolution diffusion tensor imaging with whole brain acquisition in a clinically acceptable time. Hum Brain Mapp 15:216–230
52. Kingsley PB, Monahan WG (2004) Selection of the optimum b factor for diffusion-weighted magnetic resonance imaging assessment of ischemic stroke. Magn Reson Med 51:996–1001
53. Kingsley PB, Monahan WG (2005) Contrast-to-noise ratios of diffusion anisotropy indices. Magn Reson Med 53:911–918
54. Kinoshita T, Yashiro N, Ihara N, Funatu H, Fukuma E, Narita M (2002) Diffusion-weighted half-Fourier single-shot turbo spin-echo imaging in breast tumors: differentiation of invasive ductal carcinoma from fibroadenoma. J Comput Assist Tomogr 26:1042–1046
55. Le Bihan D (1988) Intravoxel incoherent motion imaging using steady-state free precession. Magn Reson Med 7:346–351
56. Le Bihan D, Breton E, Lallemand D, Grenier P, Cabanis E, Laval-Jeantet M (1986) MR imaging of intravoxel incoherent motions: application to diffusion and perfusion in neurologic disorders. Radiology 161:401–407
57. Le Bihan D, Breton E, Lallemand D, Aubin ML, Vignaud J, Laval-Jeantet M (1988) Separation of diffusion and perfusion in intravoxel incoherent motion MR imaging. Radiology 168:497–505
58. Lee H, Price RR (1994) Diffusion imaging with the MP-RAGE sequence. J Magn Reson Imaging 4:837–842
59. Lovblad KO, Jakob PM, Chen Q, Baird AE, Schlaug G, Warach S, Edelman RR (1998) Turbo spin-echo diffusion-weighted MR of ischemic stroke. AJNR Am J Neuroradiol 19:201–208
60. Melhem ER, Mori S, Mukundan G, Kraut MA, Pomper MG, van Zijl PC (2002) Diffusion tensor MR imaging of the brain and white matter tractography. Am J Roentgenol 178:3–16
61. Merboldt KD, Hanicke W, Frahm J (1985) Self-diffusion NMR imaging using stimulated echoes. J Magn Reson 64:479–486
62. Merboldt KD, Bruhn H, Frahm J, Gyngell ML, Hanicke W, Deimling M (1989) MRI of "diffusion" in the human brain: new results using a modified CE-FAST sequence. Magn Reson Med 9:423–429
63. Miller KL, Pauly JM (2003) Nonlinear phase correction for navigated diffusion imaging. Magn Reson Med 50:343–353
64. Miller KL, Hargreaves BA, Gold GE, Pauly JM (2004) Steady-state diffusion-weighted imaging of in vivo knee cartilage. Magn Reson Med 51:394–398
65. Mills R (1973) Self-diffusion in normal and heavy water in the range 1–45°. J Phys Chem 77:685–688
66. Mori S, van Zijl PC (1995) Diffusion weighting by the trace of the diffusion tensor within a single scan. Magn Reson Med 33:41–52
67. Mori S, van Zijl PC (2002) Fiber tracking: principles and strategies - a technical review. NMR Biomed 15:468–480
68. Mori S, Crain BJ, Chacko VP, van Zijl PC (1999) Three-dimensional tracking of axonal projections in the brain by magnetic resonance imaging. Ann Neurol 45:265–269
69. Moseley M (2002) Diffusion tensor imaging and aging – a review. NMR Biomed 15:553–560
70. Moseley ME, Cohen Y, Mintorovitch J, Chileuitt L, Shimizu H, Kucharczyk J, Wendland MF, Weinstein PR (1990a) Early detection of regional cerebral ischemia in cats: comparison of diffusion- and T2-weighted MRI and spectroscopy. Magn Reson Med 14:330–346
71. Moseley ME, Kucharczyk J, Mintorovitch J, Cohen Y, Kurhanewicz J, Derugin N, Asgari H, Norman D (1990b) Diffusion-weighted MR imaging of acute stroke: correlation with T2-weighted and magnetic susceptibility-enhanced MR imaging in cats. AJNR Am J Neuroradiol 11:423–429
72. Moseley M, Bammer R, Illes J (2002) Diffusion-tensor imaging of cognitive performance. Brain Cogn 50:396–413
73. Moteki T, Horikoshi H, Oya N, Aoki J, Endo K (2002) Evaluation of hepatic lesions and hepatic parenchyma using diffusion-weighted reordered turboFLASH magnetic resonance images. J Magn Reson Imaging 15:564–572
74. Neil J, Miller J, Mukherjee P, Huppi PS (2002) Diffusion tensor imaging of normal and injured developing human brain – a technical review. NMR Biomed 15:543–552
75. Norris DG (2001) Implications of bulk motion for diffusion-weighted imaging experiments: effects, mechanisms, and solutions. J Magn Reson Imaging 13:486–495
76. Norris DG, Bornert P, Reese T, Leibfritz D (1992) On the application of ultra-fast RARE experiments. Magn Reson Med 27:142–164
77. Okamoto K, Ito J, Ishikawa K, Sakai K, Tokiguchi S (2000) Diffusion-weighted echo planar MR imaging in differential diagnosis of brain tumors and tumor-like conditions. Eur Radiol 10:1342–1350
78. Ordidge RJ, Helpern JA, Qing ZX, Knight RA, Nagesh V (1994) Correction of motional artifacts in diffusion-weighted MR images using navigator echoes. Magn Reson Imaging 12:455–460
79. Papadakis NG, Murrills CD, Hall LD, Huang CL, Adrian Carpenter T (2000) Minimal gradient encoding for robust estimation of diffusion anisotropy. Magn Reson Imaging 18:671–679
80. Papadakis NG, Smponias T, Berwick J, Mayhew JE (2005) *k*-space correction of eddy current-induced distortions in diffusion-weighted echo planar imaging. Magn Reson Med 53:1103–1111
81. Pierpaoli C, Jezzard P, Basser PJ, Barnett A, Di Chiro G (1996) Diffusion tensor MR imaging of the human brain. Radiology 201:637–648

82. Pipe JG, Farthing VG, Forbes KP (2002) Multishot diffusion-weighted FSE using PROPELLER MRI. Magn Reson Med 47:42–52
83. Reese TG, Heid O, Weisskoff RM, Wedeen VJ (2003) Reduction of eddy current-induced distortion in diffusion MRI using a twice-refocused spin-echo. Magn Reson Med 49:177–182
84. Ries M, Jones RA, Dousset V, Moonen CT (2000) Diffusion tensor MRI of the spinal cord. Magn Reson Med 44:884–892
85. Rijswijk CS van, Kunz P, Hogendoorn PC, Taminiau AH, Doornbos J, Bloem JL (2002) Diffusion-weighted MRI in the characterization of soft-tissue tumors. J Magn Reson Imaging 15:302–307
86. Schick F (1997) SPLICE: su*b*-second diffusion-sensitive MR imaging using a modified fast spin-echo acquisition mode. Magn Reson Med 38:638–644
87. Sehy JV, Ackerman JJ, Neil JJ (2002) Evidence that both fast and slow water ADC components arise from intracellular space. Magn Reson Med 48:765–770
88. Seifert MH, Jakob PM, Jellus V, Haase A, Hillenbrand C (2000) High-resolution diffusion imaging using a radial turbo-spin-echo sequence: implementation, eddy current compensation, and self-navigation. J Magn Reson 144:243–254
89. Skare S, Hedehus M, Moseley ME, Li TQ (2000) Condition number as a measure of noise performance of diffusion tensor data acquisition schemes with MRI. J Magn Reson 147:340–352
90. Snook L, Paulson LA, Roy D, Phillips L, Beaulieu C (2005) Diffusion tensor imaging of neurodevelopment in children and young adults. Neuroimage 26:1164–1173
91. Stejskal EO, Tanner JE (1965) Spin diffusion measurements: spin-echoes in the presence of a time-dependent field gradient. J Chem Phys 42:288–292
92. Sugahara T, Korogi Y, Kochi M, Ikushima I, Shigematu Y, Hirai T, Okuda T, Liang L, Ge Y, Komohara Y, Ushio Y, Takahashi M (1999) Usefulness of diffusion-weighted MRI with echo planar technique in the evaluation of cellularity in gliomas. J Magn Reson Imaging 9:53–60
93. Sullivan EV, Pfefferbaum A (2003) Diffusion tensor imaging in normal aging and neuropsychiatric disorders. Eur J Radiol 45:244–255
94. Sullivan EV, Adalsteinsson E, Pfefferbaum A (2006) Selective age-related degradation of anterior callosal fiber bundles quantified in vivo with fiber tracking. Cereb Cortex 16:1030–1039
95. Taber KH, Pierpaoli C, Rose SE, Rugg-Gunn FJ, Chalk JB, Jones DK, Hurley RA (2002) The future for diffusion tensor imaging in neuropsychiatry. J Neuropsychiatry Clin Neurosci 14:1–5
96. Taouli B, Vilgrain V, Dumont E, Daire JL, Fan B, Menu Y (2003) Evaluation of liver diffusion isotropy and characterization of focal hepatic lesions with two single-shot echo planar MR imaging sequences: prospective study in 66 patients. Radiology 226:71–78
97. Taylor DG, Bushell MC (1985) The spatial mapping of translational diffusion coefficients by the NMR imaging technique. Phys Med Biol 30:345–349
98. Thomas DL, Pell GS, Lythgoe MF, Gadian DG, Ordidge RJ (1998) A quantitative method for fast diffusion imaging using magnetization-prepared TurboFLASH. Magn Reson Med 39:950–960
99. Tien RD, Felsberg GJ, Friedman H, Brown M, MacFall J (1994) MR imaging of high-grade cerebral gliomas: value of diffusion-weighted echoplanar pulse sequences. Am J Roentgenol 162:671–677
100. Tofts PS, Lloyd D, Clark CA, Barker GJ, Parker GJ, McConville P, Baldock C, Pope JM (2000) Test liquids for quantitative MRI measurements of self-diffusion coefficient in vivo. Magn Reson Med 43:368–374
101. Torrey HC (1956) Bloch equations with diffusion terms. Phys Rev 104:563–565
102. Trouard TP, Sabharwal Y, Altbach MI, Gmitro AF (1996) Analysis and comparison of motion-correction techniques in diffusion-weighted imaging. J Magn Reson Imaging 6:925–935
103. Tsuchiya K, Katase S, Fujikawa A, Hachiya J, Kanazawa H, Yodo K (2003) Diffusion-weighted MRI of the cervical spinal cord using a single-shot fast spin-echo technique: findings in normal subjects and in myelomalacia. Neuroradiology 45:90–94
104. Tuch DS (2004) Q-ball imaging. Magn Reson Med 52:1358–1372
105. Tuch DS, Reese TG, Wiegell MR, Makris N, Belliveau JW, Wedeen VJ (2002) High angular resolution diffusion imaging reveals intravoxel white matter fiber heterogeneity. Magn Reson Med 48:577–582
106. Wedeen VJ, Hagmann P, Tseng WY, Reese TG, Weisskoff RM (2005) Mapping complex tissue architecture with diffusion spectrum magnetic resonance imaging. Magn Reson Med 54:1377–1386
107. Woessner DE (1961) Effects of diffusion in nuclear magnetic resonance spin-echo experiments. J Chem Phys 34:2057–2061
108. Wong EC, Cox RW, Song AW (1995) Optimized isotropic diffusion weighting. Magn Reson Med 34:139–143
109. Xing D, Papadakis NG, Huang CL, Lee VM, Carpenter TA, Hall LD (1997) Optimised diffusion-weighting for measurement of apparent diffusion coefficient (ADC) in human brain. Magn Reson Imaging 15:771–784

2.9 Risks and Safety Issues Related to MR Examinations

G. Brix

With the rapid development of MR technology and the significant level of growth in the number of patients examined with this versatile imaging modality, the consideration of possible risks and health effects associated with the use of MR procedures is gaining increasingly in importance. As described in detail in the previous chapters, three types of fields are employed:

- A high static magnetic field generating a macroscopic nuclear magnetization
- Rapidly alternating magnetic gradient fields for spatial encoding of the MR signal
- Radiofrequency (RF) electromagnetic fields for excitation and preparation of the spin system

In the following, the biophysical interaction mechanisms and biological effects of these fields are summarized as well as exposure limits and precautions to be taken to minimize health hazards and risks to patients and volunteers undergoing MR procedures. In the recent past, a number of excellent reviews and books related to this topic have been published. For details and supplementary information, the reader is referred to these publications quoted in the following and to the bibliographies given therein.

Because no ionizing radiation is used in MRI, it is generally deemed safer than diagnostic X-ray or nuclear medicine procedures in terms of health protection of patients. In this context, a fundamental difference between ionizing and non-ionizing radiation has to be noted: radiation exposure to ionizing radiation—at least at the relatively low doses occurring in medical imaging—results in stochastic effects, whereas biological effects of (electro)magnetic fields are deterministic. A stochastic process is one where the exposure determines the probability of the occurrence of an event but not the magnitude of the effect. In contrast, deterministic effects are those for which the magnitude is related to the level of exposure and a threshold may be defined (International Commission on Non-Ionizing Radiation Protection [ICNIRP] 2002). As a consequence, the probability of detrimental effects caused by diagnostic X-ray and nuclear medicine examinations performed over many years accumulate, whereas physiological stress induced by MR procedures is related to the acute exposure levels of a particular examination and does, to the present knowledge, not accumulate over years.

2.9.1 Safety Regulations and Operating Modes

In the recent past, regulations concerning MR safety have been largely harmonized. There are two comprehensive reviews by international commissions that form the basis for both national safety standards and the implementation of monitor systems by the manufacturers of MR devices:

1 The technical product standard IEC 60601-2-33 issued by the International Electrotechnical Commission (IEC) in 2002 (IEC 2002)
2 The safety recommendation issued by the ICNRIP in 2004 (ICNRIP 2004)

In order to reflect the existing uncertainty about deleterious effects of (electro)magnetic fields and to offer the necessary flexibility for the development and clinical evaluation of new MR technologies, both safety regulations give exposure limits for three different modes of operation:

1 ***Normal operating mode.*** Routine MR examinations that did not cause physiological stress to patients.
2 ***Controlled operating mode.*** Specific MR examinations outside the normal operating range where discomfort and/or physiological stress to some patients may occur. Therefore, a clinical decision must be taken to balance such effects against foreseen benefits and exposure must be carried out under medical supervision.
3 ***Experimental operating mode.*** Experimental MR procedures with exposure levels outside the controlled operating range. In view of the potential risks for patients and volunteers, special ethical approval and adequate medical supervision is required.

2.9.2 Static Magnetic Fields

2.9.2.1 Magnetic Properties of Matter

Magnetism in matter originates from the magnetic moments related to the movement and spin states of the electrons in atoms and molecules. The net magnetic moment per unit volume of the material considered is called magnetization $\boldsymbol{M}_e$. This quantity is related to the field strength $\boldsymbol{H}$ of the applied magnetic field by the magnetic susceptibility χ (cf. 2.2.8.1)

$$\boldsymbol{M}_e = \chi \boldsymbol{H}. \tag{2.9.1}$$

The "true" magnetic field in matter is given by the magnetic flux density $\boldsymbol{B}$ (cf. Sect. 2.2.8.1):

$$\boldsymbol{B} = \mu_0(\boldsymbol{H} + \boldsymbol{M}_e) = \mu_0(1 + \chi)\boldsymbol{H}, \tag{2.9.2}$$

with $\mu_0 = 1.257 \times 10^{-6}$ Vs/m the magnetic permeability in vacuum.

Due to the covalent binding of atoms, electron shells in most molecules are completely filled and thus all electron spins are paired. Nevertheless, these diamagnetic materials can be weakly magnetized in an external magnetic field. As described in Sect. 2.2.8.1, this universal effect is caused by changes in the orbital motion of electrons in an external magnetic field. The induced magnetization is very small and in a direction opposite to that of the applied field ($\chi < 0$). Paramagnetic materials, on the other hand, contain molecules with single, unpaired electrons. The intrinsic magnetic moments related with these electrons tend—comparable to the much weaker nuclear magnetic moment (cf. Sect. 2.2.3)—to align in an external magnetic field. This effect increases the magnetic field in paramagnetic materials ($0 < \chi < 0{,}01$). In ferromagnetic materials—such as iron, cobalt, or nickel—unpaired electron spins align spontaneously with each other in the absence of a magnetic field in a region called a domain. These materials are characterized by a large positive magnetic susceptibility ($\chi > 0{,}01$).

Biomolecules are in general diamagnetic and contain at most some paramagnetic centers. In almost all human tissues, the concentration of paramagnetic components is so low that they are characterized by susceptibilities differing by no more than 20% from that of water ($\chi = -9{,}05 \cdot 10^{-6}$) (Schenck 2000, 2005). As a consequence, there is virtually no effect of the human body on an applied magnetic field ($\boldsymbol{B} \cong \mu_0 \boldsymbol{H}$).

2.9.2.2 Biophysical Interaction Mechanisms

There are several established physical mechanisms through which static magnetic fields can interact with biological tissues and organisms. The most relevant mechanisms are discussed in the following.

Magneto-mechanical interactions. Even in a uniform magnetic field, molecules or structurally ordered molecule assemblies with either a field-induced (diamagnetic) or permanent (paramagnetic) magnetic moment $\boldsymbol{m}_{\text{mol}}$ experience a mechanical torque that tends to align their magnetic moment parallel (or antiparallel) to the external magnetic field and thus to minimize the potential energy (Fig. 2.9.1a). Orientation effects, however, can only occur when molecules or molecule clusters have a non-spherical structure and/or when the magnetic properties are anisotropically distributed. Moreover, the alignment must result in an appreciable reduction of the potential energy ($E_{\text{mag}} \propto -\boldsymbol{m}_{\text{mol}} \boldsymbol{B}$) of the molecules in the external field with respect to their thermal energy ($E_{\text{therm}} \propto kT$). At higher temperatures, as for example in the human body, the alignment of molecules with small magnetic moments is prevented by their thermal movement (Brownian movement).

In a non-uniform magnetic field, as for example in the periphery of an MR system, paramagnetic and ferromagnetic materials, moreover, are attracted and thus can quickly become dangerous projectiles (Fig. 2.9.1b).

Magneto-hydromechanical interactions. Static magnetic fields also exert forces (called Lorentz forces) on moving electrolytes (ionic charge carriers) giving rise to induced electric fields and currents. For an electrolyte with charge q, the Lorentz force, which acts perpendicular to the direction of the magnetic field, $\boldsymbol{B}$, and the velocity, $\boldsymbol{v}$, of the electrolyte is given by

$$\boldsymbol{F} = q \cdot (\boldsymbol{v} \times \boldsymbol{B}). \tag{2.9.3}$$

Since electrolytes with a positive or negative charge moving, for example, through a cylindrical blood vessel orientated perpendicular to a magnetic field are accelerated into opposite directions, this mechanism gives rise to an electrical voltage across the vessel, which is commonly referred to as blood flow potential (Fig. 2.9.2). Moreover, the induced transversal velocity component also interacts with the magnetic field according to Eq. 2.9.3, which results in a Lorentz force that is directed antiparallel to the longitudinal velocity component. At very high magnetic field strengths, this secondary effect can reduce the flow velocity and the flow profile of blood in large vessels (Tenforde 2005).

Theoretically modeling of magneto-hydromechanical interaction processes was performed by Tenforde (2005) based on the Navier-Stokes equation describing the flow of an electrically conductive fluid in the presence of a magnetic field using the finite element technique. Induced current densities in the region of the sinoatrial node are predicted to by greater than 100 mA/m^2 at field levels of more than 5 T in an adult human. Moreover, magneto-hydromechanical interactions were predicted to reduce the volume flow rate of blood in the human aorta by a maximum of 1.3, 4.9, and 10.4% at field levels of 5, 10, and 15 T, respectively.

Magnetic effects on chemical reactions. As shown by in vitro studies, several classes of organic chemical reactions can be influenced by static magnetic fields under

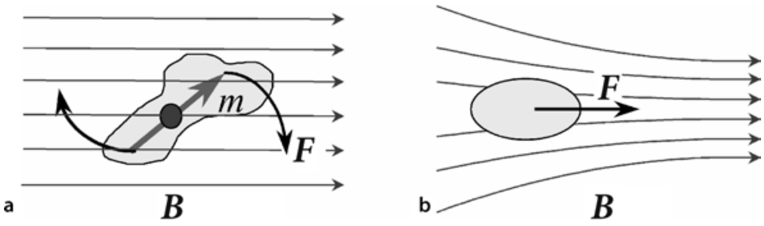

Fig. 2.9.1 Magneto-mechanical effects. **a** Orientation of a molecule with a magnetic moment $\boldsymbol{m}$ in a uniform magnetic field. **b** Attraction of a paramagnetic or ferromagnetic object in a non-uniform magnetic field. The direction of the acting forces $\boldsymbol{F}$ is indicated by *arrows*

appropriate, non-physiological conditions (Grissom 1995; World Health Organization [WHO] 2006). An established effect consists in the modification of the kinetics of chemical reactions with radicals as intermediate products, brought about by splitting and modification of electron spin states in the magnetic field. An example is the conversion of ethanolamine to acetaldehyde by the bacterial enzyme ethanolamine ammonia lyase. Radical pair magnetic field effects are thus used as a tool for in-vitro studies of enzyme reactions (WHO 2006).

2.9.2.3 Biological Effects

For individual macromolecules, the extent of orientation in strong magnetic fields is very small. For example, measurements on DNA in solution have been shown that a magnetic flux density of 12 T is required to produce orientation of about 1% of the molecules (Maret et al. 1975). In contrast, there are several examples of molecular aggregates that can be oriented to a large extend by static magnetic fields, such as outer segments of retinal rod cells, muscle fibers, and filamentous virus particles (ICNIRP 2003; WHO 2006). An example of an intact cell that can be oriented magnetically is the erythrocyte. It has been shown that both resting and flowing sickled erythrocytes align in fields of more than 0.35 T with their long axis perpendicular to the magnetic flux lines (Brody et al. 1985; Murayama 1965). Highashi et al. (1993) reported that normal erythrocytes could be oriented with their disk planes parallel to the magnetic field direction. This effect was detectable even at 1 T, and almost 100% of the cells were oriented when exposed to 4 T. On the other hand, calculations performed by Schenck (2005) yielded that all of these orientation effects observed in vitro are probably too small to affect the orientation of the equivalent structures in vivo. However, although biophysical models make it possible to roughly estimate the magnitude of static magnetic field effects, the reality is so complex that calculations can in principle not rule out physiological effects (Hore 2005).

Based on the evidence at present, there is no strong likelihood of major physiological consequences arising from radical-pair magnetic field effects on enzymatic reactions. Reasons against are the efficacy of homeostatic buffering and the fact that the contrived conditions needed to observe a magnetic field response in the laboratory are unlikely to occur under physiological conditions (Hore 2005).

There have been only a few studies on the effects of static magnetic fields at the cellular level. They reveal that exposure to static magnetic fields alone has no or extremely small effects on cell growth, cell cycle distribution, and the frequency of genetic damage, regardless of the magnetic flux density. However, in combination with other external factors such as ionizing radiation or some chemicals, there is evidence to suggest that a static magnetic field modifies their effects (Miyakoshi 2005).

With regard to possible effects on reproduction and development, no adverse effects of static magnetic fields have been consistently demonstrated; few good studies however have been carried out, especially to fields in excess of 1 T (ICNIRP 2003; Saunders 2005; WHO 2006). Several studies indicate that implantation as well as prenatal and postnatal development of the embryo and fetus is not affected by exposure for varying periods during gestation to magnetic fields of flux densities between 1 and 9.4 T (Konermann and Mönig 1986; Murakami et al. 1992; Okazaki et al. 2001; Sikov et al. 1979). On the other hand, Mevissen et al. (1994) reported that continuous exposure of rats to a 30-mT field slightly decreased the numbers of viable fetuses per litter.

Electric flow potentials generated across the aorta and other major arteries by the flow of blood in a static magnetic field can routinely seen in the ECG of animals and humans, exposed to fields in excess of 100 mT. In humans, the largest potentials occur across the aorta after ventricular contraction and appear superimposed on the T-wave amplitude of the ECG. Different animal studies demonstrated effects of static magnetic fields on blood flow, arterial pressure, and other parameters of the cardiovascular system, often at fields with flux densities much less than 1 T (Saunders 2005). The results of these studies, however, have to be interpreted with caution because it is difficult to reach any firm conclusion from cardiovascular responses observed in anaesthetized animals (Saunders 2005; WHO 2006). On the other hand, two recent studies on humans exposed to a maximum flux density of 8 T (Chakeres et al. 2003; Kangarlu et al. 1999) did not yield clinically relevant changes in the heart rate, respiratory

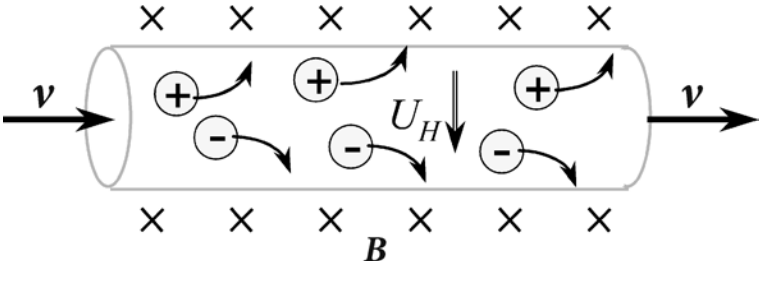

Fig. 2.9.2 Magneto-hydrodynamic effect. Positively and negatively charged electrolytes moving with a velocity $\boldsymbol{v}$ through a blood vessel oriented perpendicular to a magnetic field are accelerated into opposite directions and thus induce an electric voltage U_H across the vessel (blood flow potential). *Cross-hatches* indicate the direction of the magnetic field into the paper plane

rate, diastolic blood pressures, finger pulse oxygenation levels, and core body temperature The only physiologic parameter that was found to be altered significantly by high-field exposure was a change in measured systolic blood pressure. This is consistent with a hemodynamic compensatory mechanism to counteract the drag on blood flow exerted by magneto-hydrodynamic forces as described in Sect. 2.9.2.2 (Chakeres and de Vocht 2005).

Various behavioral studies yielded that the movement of laboratory rodents in static magnetic fields above 4 T may be unpleasant, inducing aversive responses and conditioned avoidance (WHO 2006). Such effects are thought to be consistent with magneto-hydrodynamic effects on the endolymph of the vestibular apparatus (WHO 2006). This is in line with reports that some volunteers and patients exposed in static magnetic fields with flux densities above 1.5 T experienced sensations of vertigo, nausea, and a metallic taste in the mouth (Chakeres et al. 2003; Kangarlu et al. 1999; Schenck 2000, 2005). Moreover, some of them reported on magnetophosphenes occurring during rapid eye movement in a field of at least 2 T, which may be attributable to weak electric fields induced by movements of the eye, resulting in an excitation of structures in the retina (Reilly 1998; Schenck 2000).

Two recent studies evaluated neurobehavioral effects among subjects exposed to static magnetic fields of 1.5 and 8 T, respectively, using a neurobehavioral test battery. Performance in an eye–hand coordination test and a near-visual contrast sensitivity task slightly declined at 1.5 T (de Vocht et al. 2003), whereas a small negative effect on short-term memory was noted at 8 T (Chakeres et al. 2003). Taking also into account the results of other neurobehavioral studies, it can be concluded that there is at present no evidence of any clinically relevant modification in human cognitive function related to static magnetic field exposure (Chakeres and de Vocht 2005).

There are only a few epidemiological studies available that were specifically designed to study health effects of static magnetic fields. The majority of these have been focused on cancer risks. In 2002, the International Agency for Research on Cancer (IARC) (2002) reviewed epidemiological studies focused on cancer risks. Generally, these studies have not pointed to higher risks, although the number of studies was small, the numbers of cancer cases were limited, and the information on individual exposure levels was poor. Therefore, the available evidence from epidemiological studies is at present not sufficient to draw any conclusions about potential health effects of static magnetic field exposure (Feychting 2005; WHO 2006).

Some epidemiological studies have investigated reproductive outcome for workers involved in aluminum industry or in MRI. Kanal et al. (1999), for example, evaluated 1,421 pregnancies of women working at clinical MR facilities. Comparing these pregnancies with those occurring in employees at other jobs, they did not find significant increased risks for spontaneous abortions, delivery before 39 weeks, reduced birth weight, and male gender of the offspring. However, no studies of high quality have been carried out of workers occupationally exposed to fields greater than 1 T.

Table 2.9.1 Limits for the magnetic flux density B_0 for volunteers and patients undergoing MR procedures (ICNIRP 2004; IEC 2002)

Operating mode		
Normal	Controlled	Experimental
$B_0 \leq 2$ T	2 T $< B_0 \leq 4$ T	$B_0 > 4$ T

2.9.2.4 Exposure Limits

Although there are initial experiences concerning the examination of volunteers and patients in ultra-high MR systems with magnetic flux densities of up to 8 T, most clinical MR procedures have been performed so far at static magnetic fields below 3 T. As summarized in Sect. 2.9.2.3, the literature does not indicate any serious adverse health effects from the exposure of healthy human subjects up to a flux density of 8 T (ICNIRP 2004). However, because movements in static magnetic fields above 2 T can produce nausea and vertigo, both the IEC standard and the ICNIRP recommendation (Table 2.9.1) regulate that MR examinations above this static magnetic flux density should be performed in the controlled operating mode under medical supervision. The recommended upper limit for the operating mode is 4 T, due to the limited information concerning possible effects above this magnetic flux density. For MR examinations performed in the experimental operating mode, there is no upper limit for the magnetic flux density. In a safety document issued in 2003, the US Food and Drug Administration (FDA) (2003) deemed MR devices significant risk only when a static magnetic field of more than 8 T is used.

2.9.3 Time-Varying Magnetic Gradient Fields

2.9.3.1 Electric Fields and Currents Induced by Time-Varying Magnetic Fields

According to Faraday's law, a time-varying magnetic field $\boldsymbol{B}(t)$ induces an electric field $\boldsymbol{E}(t)$, which has two important characteristics: the field strength is proportional to the time rate of change of the magnetic flux density, $\mathrm{d}\boldsymbol{B}(t)/\mathrm{d}t$, and the field lines form closed loops around the direction of the magnetic field.

Time-varying magnetic fields are used in MRI—among others—to spatially encode MR signals arising from the different volume elements within the human body. To this end, three independent gradient coils are

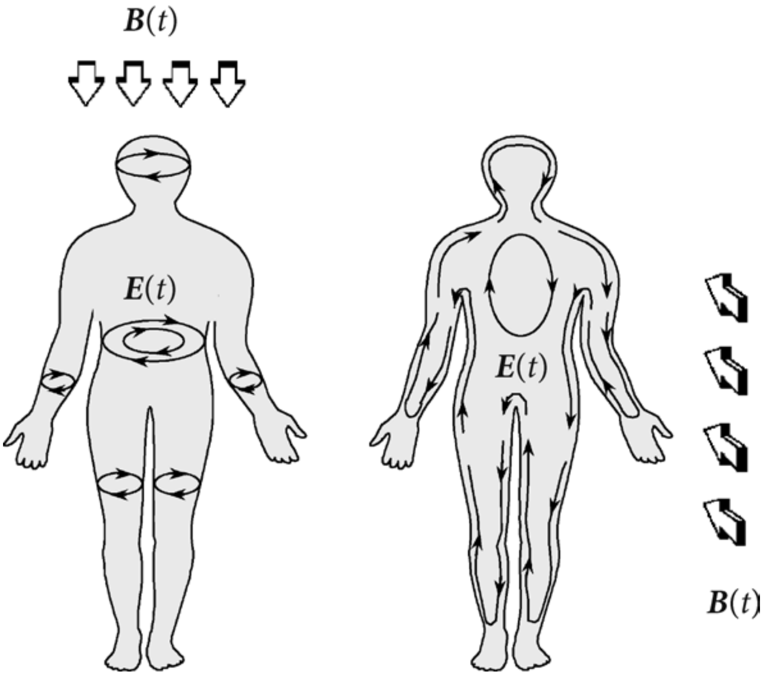

Fig. 2.9.3 Schematic representation of the electric field induced by time-varying magnetic fields $\boldsymbol{B}(t)$ that are directed parallel (*left*) and perpendicular (*right*) to the long axis of the human body. The electric field lines form closed loops around the direction of the magnetic field

used to produce magnetic fields directed parallel to the static magnetic field $\boldsymbol{B}_0 = (0, 0, B_0)$ with a field strength varying in a linear manner along the x-, y- and z-direction as shown in Fig. 2.3.1.

For the special case of a spatially uniform magnetic field directed in the z-direction, $B_z(t)$, the electric field strength along a circular (conductive) loop of radius r in the x–y-plane is given by

$$E(r) = -\frac{r}{2} \cdot \frac{\mathrm{d}B_z(t)}{\mathrm{d}t}\,. \tag{2.9.4}$$

This equation reveals that the electric field strength in the considered circular loop increases linearly with its radius as well as with the rate of change, $\mathrm{d}B(t)/\mathrm{d}t$. This model gives, for example, the electric field induced by the magnetic gradient field $\boldsymbol{B} = (0, 0, G^z \cdot z)$ of the z-gradient coil.

In contrast, the distribution of the electric fields induced by the time-varying magnetic gradient fields $\boldsymbol{B} = (0, 0, G^x \cdot x)$ and $\boldsymbol{B} = (0, 0, G^y \cdot y)$ is much more complex, since the magnetic flux density of these fields is not uniform over the x–y-plane. Moreover, the generation of these gradient fields is inevitable connected – due to fundamental principles of electrodynamics – with the occurrence of magnetic fields directed in the x- and y-direction, i.e., $\boldsymbol{B} = (B_x, 0, 0)$ and $\boldsymbol{B} = (0, B_y, 0)$, respectively. Although these “Maxwell terms” are of no relevance for the acquisition of MR images, they have to be considered carefully with respect to biological effects.

The distribution of electric fields induced by time-varying magnetic fields directed parallel and perpendicular to the long axis of the human body is schematically shown in Fig. 2.9.3. The precise spatial and temporal distribution of the electric fields in the human body, of course, strongly depends on both the technical characteristics of the gradient coils implemented at a specific MR system and the morphology of the body region exposed, and thus cannot be described by a simple mathematical expression. For worst-case estimations, however, it can be assumed that the electric field induced by a non-uniform magnetic field is equal or smaller than the electric field produced by a uniform magnetic field with field strength equal to the maximum magnetic flux density of the non-uniform field (Schmitt et al. 1998). For a uniform magnetic field, the electric field strength reaches, in general, a maximum when the magnetic field is orientated perpendicular to the coronal plane of the body (see Fig. 2.9.3, right) since the extension of conductive loops is largest in this direction (Reilly 1998).

In conductive media, such as biological tissues, the internally induced electric field $\boldsymbol{E}(t)$, results in circulating eddy currents, $\boldsymbol{j}(t)$. Both quantities are related by the electric conductivity of the medium, σ,

$$\boldsymbol{j}(t) = \sigma\,\boldsymbol{E}(t). \tag{2.9.5}$$

Calculation of the current distribution in the human body is complicated due to widely differing conductivities of various tissue components. For rough estimations, however, the body can be treated as a homogeneous medium with an average conductivity of $\sigma = 0.2$ S/m (Reilly 1998). According to Eqs. 2.9.4 and 2.9.5, for example, a current density of 20 mA/m^2 is induced at a radius of 20 cm by a rate of change in the magnetic flux density of $\mathrm{d}B_z/\mathrm{d}t = 1$ T/s.

2.9.3.2 Biophysical Interaction Mechanisms

The magnetic flux density of gradient fields used in MRI is about two orders of magnitude lower than that of the static magnetic field B_0. Therefore, time-varying magnetic fields produced by gradient coils in MRI can be neglected compared to the strong static magnetic field as far as interactions of magnetic fields with biological tissues and organisms are concerned (cf. Sect. 2.9.2.2). In contrast, however, biophysical effects related to the electric fields and currents induced by the magnetic fields have to be considered carefully.

In general, rise times of magnetic gradients in MRI are longer than 100 µs, resulting in time-varying electric fields and currents with frequencies below 100 kHz. In this frequency range, the conductivity of cell membranes is several orders of magnitude lower than that of the extra- and intracellular fluid (Foster and Schwan 1995). As illustrated in Fig. 2.9.4, this has two important consequences. First, the cell membrane tends to shield the interior of cells very effectively from current flow, which is thus restricted to the extracellular fluid. Second, voltages are induced across the membrane of cells. When the electric voltages are above a tissue-specific threshold level, they can stimulate nerve and muscle cells (Foster and Schwan 1995).

Theoretical models describing cardiac and peripheral nerve stimulation have been presented by various scientists (i.e., by Irnich, Mansfield, and Reilly). A detailed discussion of the underlying assumptions of the different models and the differences between them can be found, among others, in (Schaefer et al. 2000; Schmitt et al. 1998). The best approximation to experimental data is given by a hyperbolic strength-duration expression

$$\frac{\mathrm{d}B(t)}{\mathrm{d}t} = \dot{B}_{\infty} \cdot \left(1 + \frac{\tau_c}{t}\right), \qquad (2.9.6)$$

which relates the stimulation threshold, expressed as rate of change dB/dt of the magnetic flux density, with the stimulus duration t, i.e., the ramp time of the magnetic gradient field (Schaefer et al. 2000; Schmitt et al. 1998). A hyperbolic model comparable to Eq. 2.9.6 was first established by G. Weiss in 1901 for an electric current pulse and the corresponding electric charge. This "fundamental law of electrostimulation" has been confirmed meanwhile in numerous studies for neural and cardiac excitation as well as for defibrillation (Schaefer et al. 2000). As shown in Fig. 2.9.5, the threshold for the strength of a stimulus decreases with its duration. The asymptotic stimulus strength, $\dot{B}_{\infty}$, for an infinite duration is denoted as "rheobase"; the characteristic response time constant, τ_c, as "chronaxie". It should be mentioned that according to a model presented by Irnich et al. stimulation depends on mean (rather than peak) dB/dt changes and is thus independent on the special shape of the gradient pulse (Schaefer et al. 2000). In current safety regulations, however, exposure limits are unanimously expressed as maximum dB/dt values.

2.9.3.3 Biological Effects

In accordance with the biophysical mechanisms described in the previous section, there is now a strong body of evidence suggesting that the transduction processes through which induced electric fields and currents can influence cellular properties involve interactions at the level of the cell membrane (ICNIRP 2003). In addition to the stimulation of electrically excitable tissues, changes in membrane properties—such as ion-binding to membrane macromolecules, ion transport across the membrane, or ligand–receptor interactions—may trigger transmembrane signaling events.

Cardiac and peripheral nerve stimulation. Experimental studies with magnetic stimulation of the heart have been carried out since about 1991, with the introduction of improved gradient hardware for EPI. Experiments

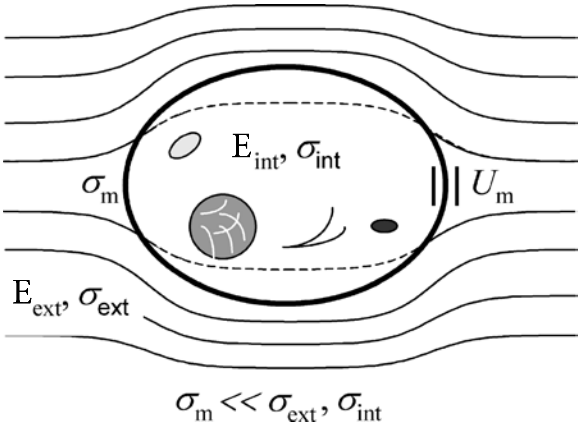

Fig. 2.9.4 In the frequency range below 100 kHz, the conductivity of cell membranes (σ_m) is several orders of magnitude lower than that of the extra- and intracellular fluid (σ_{ext} and σ_{int}, respectively) so that the induced electric fields (and also the resulting electric currents) are mainly restricted to the extracellular fluid ($E_{ext} > E_{int}$). As a result, electric voltages are generated across the membrane of cells that can stimulate nerve and muscle cells

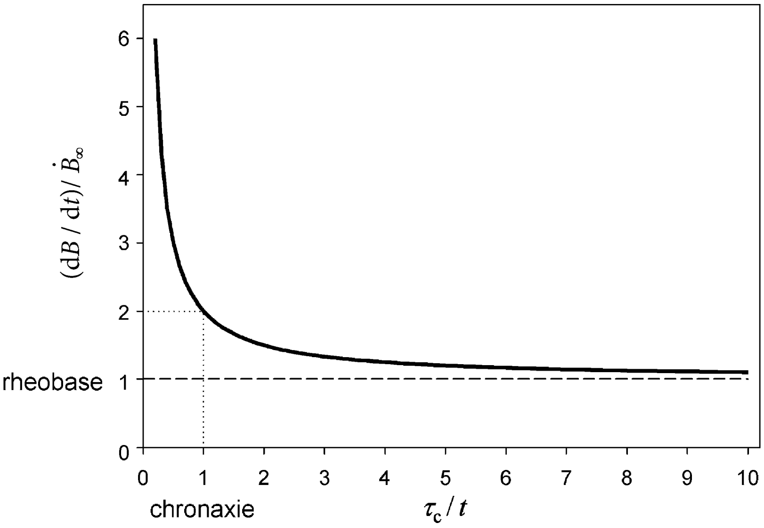

Fig. 2.9.5 Hyperbolic strength-duration expression that relates the stimulation threshold, expressed as rate of change d*B*/d*t* of the magnetic flux density, with the stimulus duration *t*, i.e., the ramp time of the magnetic gradient field. The asymptotic stimulus strength, $\dot{B}_\infty$, for an infinite duration is denoted as *rheobase*; the characteristic response time constant, τ_c, as *chronaxie*

were not performed of course with humans, but rather with dogs. The data, which are listed and reviewed by Reilly (1998), reveal that magnetic stimulation is most effective, when it is delivered during the T wave of the cardiac cycle. Moreover, excitation thresholds for the heart are substantially greater than that for nerve as long as the pulse duration is sufficiently less than the chronaxie time of the heart of about 3 ms. Therefore, the avoidance of peripheral sensations in a patient provides a conservative safety margin with respect to cardiac stimulation. Bourland et al. (1991) determined a mean value of 14.1 ± 6.7 for the ratio of cardiac (the induction of ectopic beats) to muscle stimulation in dogs for a pulse duration of 530 µs, which is quite close to the theoretical heart/nerve ratio of 14.0 estimated by Reilly (1998). Various studies yielded that the cardiac threshold variability of healthy persons is surprisingly low, which is confirmed by experimental and clinical experience that pacing thresholds are rather uniform (Schmitt et al. 1998). Drugs and changes in electrolyte concentrations can lower thresholds, but not below about 80% of the normal value (Schmitt et al. 1998).

Peripheral nerve stimulation has been investigated in various volunteer studies. A systematic evaluation of the available data was presented by Schaefer et al. in 2000. They recalculated published threshold levels—often reported for different gradient coils and shapes in different terms—to the maximum d*B*/d*t* occurring during the maximum switch rate of the gradient coil at a radius of 20 cm from the central axis of the MR system, i.e., at the border of the volume normally accessible to patients. In Fig. 2.9.6, the recalculated threshold levels are plotted for the *y*- (anterior/posterior) and *z*-gradient coils (superior/inferior) as compared to model estimates by Reilly. As expected, *y*-gradient coils have lower stimulation threshold for a given ramp time than *x*-gradient coils since the *x*–*z* cross-sections of the body are usually larger than are *x*–*y* cross-sections. By fitting the hyperbolic strength-duration relationship defined in Eq. 2.9.6 to mean peripheral nerve stimulation thresholds measured by Bourland et al. (1999) in 84 human subjects, Schaefer et al. estimated the following values for the rheobase/chronaxie: 22.1 T/s/0.365 ms for the *y*-gradient and 31.7 T/s /0.378 ms for the *z*-gradient. As shown in Fig. 2.9.6, the d*B*/d*t* intensity to induce a sensation that the subject described as uncomfortable or even painful was significantly above the sensation threshold. Bourland et al. (1999) also analyzed their stimulation data in the form of cumulative frequency distributions, that gives for a d*B*/d*t* level the number of subjects that had already reported on perceptible, uncomfortable, or even intolerable sensations. They found that the d*B*/d*t* level needed for the lowest percentile for uncomfortable stimulation is approximately equal to the median threshold for perception. The lowest percentile for intolerable stimulation occurs at a d*B*/d*t* level approximately 20% above the median perception threshold.

Time-varying magnetic fields can also result in the perception of magnetophosphenes due to the induction of electrical currents, presumably in the retina (cf. Sect. 2.9.2.3). A unique feature of phosphenes, which are not considered to be hazardous to humans, is their low excitation threshold and sharply defined excitation frequency of about 20 Hz as compared to other forms of neural stimulation (Reilly 1998).

In general, a combination of magnetic gradient fields from all three gradient coils is used in MRI. In this case, the biological relevant time-varying magnetic field is approximately given by the vector sum of the magnetic field components. A detailed discussion of the effect of stimulus shape, number of stimuli, and other experimental set-

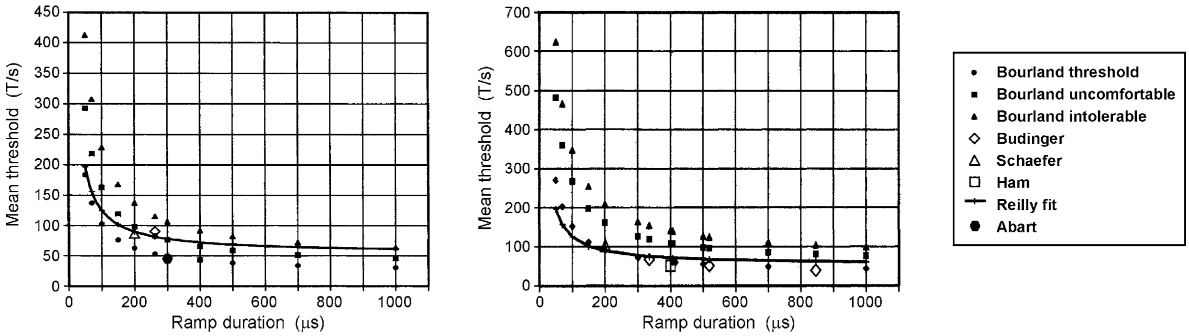

Fig. 2.9.6 Mean human nerve stimulation thresholds determined in different volunteer studies for *y*-gradient coils (anterior–posterior; *left*) and *z*-gradient coils (superior–inferior; *right*) as compared to model estimates by Reilly. For details see text. (From Schaefer et al. 2000; reprinted by permission of John Wiley & Sons, Ltd. All Rights Reserved)

tings on stimulation thresholds can be found in (Reilly 1998; Schmitt et al. 1998).

Other biological endpoints. A comprehensive review of the current scientific evidence on biological effects of low-frequency electromagnetic fields in the frequency range up to 100 kHz has been published by ICNIRP in 2003. The majority of the reviewed studies focus on extremely low–frequency (ELF) magnetic fields associated with the use of electricity at power frequencies of 50 or 60 Hz. According to the ICNRIP review, cellular studies do not provide convincing evidence that low-frequency magnetic fields alter cell division, calcium homeostasis, and signaling pathways. Furthermore, no consistent effects were found in animals and humans with respect to genotoxicity, reproduction, development, immune system function, as well as endocrine and hematological parameters. On the other hand, a number of laboratory and field studies on humans demonstrated an effect of low-frequency magnetic fields at higher exposure levels on the power spectrum of different EEG frequency bands and on sleep structure. In the light of cognitive and performance studies yielding a number of biological effects, further studies are necessary to clarify the significance of the observed effects for human health.

Over the last two decades, a large number of high quality epidemiological investigations of long-term disease endpoints such as cancer, cardiovascular and neurodegenerative disorders have been performed in relation to time-varying—mainly ELF—magnetic fields. Following the mentioned ICNIRP review (2003), the results can be summarized as follows. Among all the outcomes evaluated, childhood leukemia in relation to postnatal exposures to 50 or 60 Hz magnetic fields at flux densities above 0.4 μT is the one for which there is most evidence of an association. However, the results are difficult to interpret in the absence of evidence from cellular and animal studies. There is also evidence for an association of amyotrophic lateral sclerosis (ALS) with occupational EMF exposure although confounding is a potential explanation. Whether there are associations with breast cancer and cardiovascular disease remains unsolved.

2.9.3.4 Exposure Limits

From a safety standpoint, the primary concern with regard to rapid switching of magnetic gradients is cardiac fibrillation, because it is a life-threatening condition. In contrast, peripheral nerve stimulation is of practical concern because uncomfortable or intolerable stimulations would interfere with the examination (e.g., patient movements) or would even result in a termination of the examination.

In the current safety recommendations issued by IEC (2002) and and ICNRIP (2004), maximum $\mathrm{d}B/\mathrm{d}t$ values for time-varying magnetic fields created by gradient coils is limited for patient and volunteer examinations performed in the normal and the controlled operating mode by the $\mathrm{d}B/\mathrm{d}t$ level of 80% and 100% of the mean perception threshold for peripheral nerve stimulation, respectively. To this end, mean perception threshold levels have to be determined by the manufacturers for any given type of gradient system by means of experimental studies on human volunteers. As an alternative, the following empirical hyperbolic strength-duration expression for the mean threshold for peripheral nerve stimulation (expressed as maximum change of the magnetic flux density in T/s) can be used:

$$\frac{\mathrm{d}B}{\mathrm{d}t} < 20 \cdot \left(1 + \frac{0.36}{t_{\mathrm{eff}}}\right). \tag{2.9.7}$$

In this equation, t_{eff} is the effective stimulation duration (in milliseconds), i.e., the duration of the period of monotonic increasing or decreasing gradient. A mathematical definition for arbitrary gradient shapes can be found in the IEC standard (2002).

2.9.4 Radiofrequency Electromagnetic Fields

2.9.4.1 Biophysical Interaction Mechanisms

Time-varying magnetic fields used for the excitation and preparation of the spin system in MRI (B_1 fields, cf. Sect. 2.2.4) have typically frequencies above 10 MHz. In this RF range, the conductivity of cell membranes is comparable to that of the extra- and intracellular fluid, which means that no substantial voltages are induced across the membranes (Foster and Schwan 1995). Due to this reason, stimulation of nerve and muscle cells is no longer a matter of concern. Instead, thermal effects due to tissue heating are of importance.

Energy dissipation of RF fields in tissues is described by the frequency-dependent conductivity $\sigma(\omega)$, which characterizes energy losses due to the induction and orientation of electrical dipoles as well as the drift of free charge carriers in the induced time-varying electric field (Foster and Schwan 1995). The energy absorbed per unit of tissue mass and time, the so-called specific absorption rate (*SAR*, in W/kg), is approximately given by

$$SAR = \frac{\boldsymbol{j} \cdot \boldsymbol{E}}{\rho} = \frac{\sigma \cdot E^2}{\rho}, \tag{2.9.8}$$

where $\boldsymbol{E}$ is the induced electric field, $\boldsymbol{j}$ the corresponding current density, and ρ the tissue density (cf., 2.9.3.1).

Absorption of energy in the human body strongly depends on the size and orientation of the body with respect to the RF field as well as on the frequency and polarization of the field. Theoretical and experimental considerations reveal that RF absorption in the body approaches a maximum when the wavelength of the field is in the order of the body size. Unfortunately, the wavelength of the RF fields used in MRI falls into this "resonance range."

In order to discuss the effect of various measurement parameters on RF absorption, let us consider a simple MR sequence with only one RF pulse—such as a 2D or 3D FLASH sequence. In this case, the time-averaged *SAR* can approximately be described by the expression

$$SAR \propto B_0^2 \cdot a^2 \cdot \frac{t_\mathrm{P}}{T_\mathrm{R}} \cdot N_\mathrm{S}. \tag{2.9.9}$$

According to this equation, the time-averaged *SAR* is proportional

- To the square of the static magnetic field, B_0, which means that energy absorption is markedly higher at high-field as compared to low-field MR systems
- To the square of the pulse angle, α, so that a sequence with a 90° or even a 180° pulse will result in a much higher *SAR* value than a sequence with a low-angle excitation pulse
- To the duty cycle, $t_\mathrm{P} / T_\mathrm{R}$, of the sequence, e.g., the ratio of the pulse duration t_p and the repetition time T_R of the pulse or sequence
- To the number of slices, N_S, subsequently excited within the repetition time of a 2D sequence (multi-slice technique, cf. Sect. 2.3.5; $N_\mathrm{S} = 1$ for 3D sequences)

In case of a more complex MRI sequence with various RF pulses, e.g., a spin-echo or a turbo spin-echo sequence, the contribution of the different RF pulses to patient exposure has to be summed up.

The most relevant quantity for the characterization of physiological effects related to RF exposure is the temperature rise in the various body tissues, which is not only dependent on the localized *SAR* and the duration of exposure, but also on the thermal conductivity and microvascular blood flow (perfusion). In case of a partial-body RF exposure, the latter two factors lead to fast temperature equalization within the body (Adair 1996). Based on the bioheat equation, it can be shown (Brix et al. 2002) that for this particular exposure scenario the temperature response in the center of a homogenous tissue region, which is larger in each direction than the so-called thermal equilibration length, λ, is given by a convolution of the exposure-time course, $SAR(t)$, with a tissue-specific system function, exp $(-t/\tau)$,

$$\Delta T(t) = T(t) - T_a = \frac{1}{c} \int_0^t \mathrm{d}t' \, SAR(t') \exp\left(-\frac{t-t'}{\tau}\right), \tag{2.9.10}$$

where τ is the thermal equilibration time, T_a the constant temperature of arterial blood, and c the specific heat capacity of the tissue. For representative tissues, equilibration lengths and times are between 1.5 and 12 mm and 0.2 and 25 min, respectively (Brix et al. 2002). Both parameters are inversely related to tissue perfusion and thus vary considerably. In case of a continuous RF exposure, the temperature rise even in poorly perfused tissues is less than 0.5°C for each W/kg of power dissipated.

Using a simple model of power deposition in the head, Athey (1989) showed that continuous RF exposure over 1 h is unlikely to raise the temperature of the eye by more than 1.6°C when the average *SAR* to the head is less than 3.2 W/kg. More complex computations were performed by Gandhi and Chen (1999) for a high-resolution model of the human body using the finite-difference time domain in order to assess *SAR* distributions in the body for different RF coils. Their calculations indicate that the maximum *SAR* averaged over 100 g of tissue can be ten times greater than the whole-body average *SAR* ("hot spots").

2.9.4.2 Biological Effects

Established biological effects of RF fields used for MR examinations are primarily caused by tissue heating. Therefore, it is important to critically evaluate the numerous number of studies focused on temperature effects, from the cellular and tissue level to the whole-body level, including potential effects on vulnerable persons. In contrast, non-thermal (or athermal) effects are not well understood but seem—as far as this can be assessed at moment—to have no relevance with respect to the assessment of adverse effects associated with MR examinations. Non-thermal effects are those which can only be explained in terms of mechanisms other than increased random molecular motion (i.e., heating) or which occur at *SAR* levels so low that a thermal mechanism seems unlikely (ICNIRP 1997).

As summarized in a review by Lepock (2003), relative short exposures of mammalian cells to temperatures in excess of 40–41°C result in a variety of effects, such as inhibition of cell growth, cytotoxic changes, alteration of signal transduction pathways, and an increased sensitivity to other stresses such as ionizing radiation and chemical agents. This suggests that damage is not localized to a single target, but that multiple heat-labile targets are damaged. Extensive protein denaturation has been observed at temperatures of 40–45°C for moderate periods.

The most sensitive animal responses to heat loads are thermoregulatory adjustments, such as reduced metabolic heat production, vasodilatation, and increased heart rate. The corresponding *SAR* thresholds are between about 0.5 and 5 W/kg (ICNIRP 1998). The observed cardiovascular changes reflect normal thermoregulatory responses that facilitate the conduction of heat to the body surface in order to maintain normal body temperatures. Direct quantitative extrapolation of the animal (including primate) data to humans, however, is difficult given the marked species differences in the basal metabolism and thermoregulatory ability (WHO 1993).

At levels of RF exposure that cause body temperature rises of 1°C or more, a large number of additional, in most cases reversible, physiological effects have been observed in animals, such as alterations in neural and neuromuscular functions, increased blood-brain barrier permeability, stress-associated changes in the immune system, and hematological changes (ICNIRP 1998; Michaelson and Swicord 1996; WHO 1993). Thermal sensitivities and thresholds for irreversible tissue damage from hyperthermia have been summarized by Dewhirst et al. (2003). The most sensitive organs to acute damage are the testes and brain as well as portions of the eye (lens opacities and corneal abnormalities). The *SAR* threshold for irreversible effects even in the most sensitive tissues caused by RF exposure, however, is greater than 4 W/kg under normal environmental conditions (ICNIRP 1998).

Effects of heat on embryo and fetus have been thoroughly reviewed by Edwards et al. (2003). Processes critical to embryonic development, such as cell proliferation, migration, differentiation, and apoptosis are adversely affected by elevated maternal temperatures. Therefore, hyperthermia of animals during pregnancy can cause embryonic death, abortion, growth retardation, and developmental defects. Especially the development of the central nervous system is susceptible to heat. However, most animal data indicate that implantation and the development of the embryo and fetus are unlikely to be affected by RF exposures that increase maternal body temperature by less than 1°C (WHO 1993). In humans, epidemiological studies suggest that an elevation of maternal body temperature by 2°C for at least 24 h during fever can cause a range of developmental defects, but there is little information on temperature thresholds for shorter exposures (Edwards et al. 2003).

Humans possess comparatively effective heat loss mechanisms. In addition to a well-developed ability to sweat, the dynamic range of blood flow rates in the skin is much higher than it is in other species. Studies focused on RF-induced heating of patients during MR procedures have been summarized and evaluated in a review by Shellock (2000). They indicate that exposure of resting humans for 20–30 min to RF fields producing a whole-body *SAR* of up to 4 W/kg results in a body temperature increase between 0.1 and 0.6°C (WHO 1993). Of special interest is an extensive MR study reported by Shellock et al. (1994). In this study, thermal and physiologic responses of healthy volunteers undergoing an MR examination over 16 min at a whole-body averaged *SAR* of 6.0 W/kg were investigated in a cool (22°C) and a warm (33°C) environment. In both cases, significant variations of various physiologic parameters were observed, such as an increase in the heart rate, systolic blood pressure, or skin temperature. However, all variations were in a range that can be physiologically tolerated by an individual with normal thermoregulatory function (Shellock et al. 1994). Generally, these studies are supported by mathematical modeling of human thermoregulatory responses to MR exposure (Adair 1996; Adair and Berglund 1986, 1989). It should be noted, however, that heat tolerance or thermoregulation may be compromised in some individuals undergoing an MR examination, such as the elderly, the very young and people with certain medical conditions (e.g., obesity, hypertension, impaired cardiovascular functions, diabetes, fever, etc.) and/or taking certain medications (e.g., beta-blockers, calcium channel blockers, sedatives, etc.) (Donaldson et al. 2003; Goldstein et al. 2003; ICNIRP 2004; Shellock 2000).

Some regions of the human body, in particular the brain, are particularly vulnerable to raised temperatures. Mild-to-moderate hyperthermia (body temperature less than 40°C) induced thermal stress. For example, it affects cognitive performance (Sharma and Hoopes 2003) and can produce specific alterations in the CNS that may have long-term physiological and neuropathological consequences (Hancock and Vasmatzidis 2003).

There have been a large number of epidemiological studies over several decades, particularly on cancer, cardiovascular disease, and cataract, in relation to occupational, residential, and mobile-phone RF exposure. As summarized in a review published by the ICNIRP Standing Committee on Epidemiology (Ahlbom et al. 2004), results of these studies give no consistent or convincing evidence of a causal relation between RF exposure and adverse health effect. It has to be noted, however, that the studies considered not only have too many deficiencies to rule out an association but also focus on chronic exposures at relatively low levels—an exposure scenario that is not comparable to MR examinations of patients.

2.9.4.3 Exposure Limits

As reviewed in the previous section, no adverse health effects are expected if the RF-induced increase in body core temperature does not exceed 1°C. In case of infants, pregnant women, or persons with cardiocirculatory impairment, it is desirable to limit body core temperature increases to 0.5°C. As indicated in Table 2.9.2, these values have been laid down in the current safety recommendations (IEC, ICNIRP) to limit the body core temperature for the normal and controlled operating mode. Additionally, local temperatures under exposure to the head, trunk, and extremities are limited for each of the two operating modes to the values given in Table 2.9.2.

However, temperature changes in the different parts of the body are difficult to control during an MR procedure in clinical routine. Therefore, *SAR* limits have been derived on the basis of experimental and theoretical studies, which should not be exceeded in order to limit the temperature rise to the values given in Table 2.9.2. As only parts of the body—at least in the case of adult patients—are exposed simultaneously during an MR procedure, not only the whole-body *SAR* but also partial-body

Table 2.9.2 Basic restrictions for body temperature rise and partial-body temperatures for volunteers and patients undergoing MR procedures (ICNIRP 2004; IEC 2002)

Operating mode	Rise of body core temperature (°C)	Spatially localized temperature limits		
		Head (°C)	Trunk (°C)	Extremities (°C)
Normal	0.5	38	39	40
Controlled	1	38	39	40
Experimental	> 1	> 38	> 39	> 40

Table 2.9.3 *SAR* limits for volunteers and patients undergoing MR procedures (ICNIRP 2004; IEC 2002), which holds at environmental temperatures below 24°C

Body region → Operating mode ↓	Averaging time: 6 min					
	Whole-body *SAR* (W/kg)	Partial-body *SAR* (W/kg)		Local *SAR* (averaged over 10 g tissue) (W/kg)		
	Whole-body	Any region, except head	Head[a]	Head	Trunk	Extremities
Normal	2	2–10[b]	3.2	10[c]	10	20
Controlled	4	4–10[b]	3.2	10[c]	10	20
Experimental	> 4	> (4–10)[b]	> 3.2	10[c]	> 10	> 20
Short-term *SAR*	The *SAR* limit over any 10-s period shall not exceed 3 times the corresponding average *SAR* limit					

[a] Partial-volume *SAR*s given by IEC; ICNIRP limits *SAR* exposure to the head to 3 W/kg

[b] Partial-body *SAR*s scale dynamically with the ratio *r* between the patient mass exposed and the total patient mass: normal operating mode, $SAR = (10-8 \cdot r)$ W/kg; controlled operating mode, $SAR = (10-6 \cdot r)$ W/kg

[c] In cases where the eye is in the field of a small local coil used for RF transmission, care should be taken to ensure that the temperature rise is limited to 1°C

*SAR*s for the head, the trunk, and the extremities have to be estimated by means of suitable patient models (e.g., Brix et al. 2001) and limited to the values given in Table 2.9.3 for the normal and controlled operating mode.

With respect to the application of the *SAR* levels defined in Table 2.9.3, the following points should be taken into account:

- When a volume coil is used to excite a greater field-of view homogeneously, the partial-body and the whole-body *SAR*s have to be controlled: in the case of a local RF transmit coil (e.g., a surface coils), the local and the whole-body *SAR* (IEC 2002).
- Partial-body *SAR*s scale dynamically with the ratio r between the patient mass exposed and the total patient mass. For $r \rightarrow 1$ they converge against the corresponding whole-body values, for $r \rightarrow 0$ against the localized *SAR* level of 10 W/kg established by ICNIRP for occupational exposure of head and trunk (ICNIRP 1998).
- The recommended *SAR* limits do not relate to an individual MR sequence, but rather to running *SAR* averages computed over each 6-min-period, which is assumed a typical thermal equilibration time of smaller masses of tissue.

But even if MR examinations are performed within the established *SAR* limits, severe burns can occur under unfavorable conditions at small focal skin-to-skin contact zones. The potential danger is illustrated in Fig 2.9.7 by the case of a patient who developed third-degree burns at the calves after conventional MR imaging. In this case, the contact between the calves resulted in the formation of a closed conducting loop and high current densities near the small contact zone. Therefore, patients should always be positioned in such a way that focal skin-to-skin contacts are avoided (e.g., by foam pads) (Knopp et al. 1998).

Fig. 2.9.7 Current-induced third-degree burns due to a small focal skin-to-skin contact between the calves during the MR examination. (From Knopp et al. 1998, with permission by Springer-Verlag)

2.9.5 Special Safety Issues, Contraindications

To protect volunteers, patients, accompanying persons, and uninformed healthcare workers from possible hazards and accidents associated with the MR environment, it is indispensable to perform a proper control of access to the MR environment. The greatest potential hazard comes from metallic, in particular ferromagnetic materials (such as coins, pins, hair clips, pocketknives, scissors, nail clippers, etc.), that are accelerated in the inhomogeneous magnetic field (cf. Sect. 2.9.2.2) in the periphery of an MR system and quickly become dangerous projectiles (missile effect). This risk can only be minimized by a strict and careful screening of all individuals entering the MR environment for metallic objects.

Every patient or volunteer should complete a detailed questionnaire prior to the MR examination to ensure that every item posing a potential safety issue is considered. An example of such a form can be found, for example, in Shellock and Crues (2004), or can be downloaded from http://www.MRIsafety.com. Next, an oral interview should be conducted to verify the information of the form and to allow discussion of any question or concern that the patient may have before undergoing the MR procedure. An in-depth discussion of the various aspects of screening patients for MR procedures and individuals for the MR environment can be found in various publications by Shellock (e.g., Shellock 2005; Shellock and Crues 2004) and the webpage mentioned above. Here only a condensed summary of the most important risks and contraindications can be given.

All patients (and volunteers) undergoing MR procedures should—at the very least—be visually (e.g., by using a camera system) and/or acoustically (using an intercom system) monitored. Moreover, physiologic monitoring is indicated whenever a patient requires observation of vital functions due to a health problem or whenever the patient is unable to communicate with the MR technologist regarding pain, respiratory problems, cardiac stress, or other difficulty that might arise during the examination (Shellock 2001). This holds especially in the case of sedated or anesthetized patients. For patient monitoring, special MR-compatible devices are available (Shellock 2001).

Pregnant patients undergoing MR examinations are exposed to the static magnetic field, time-varying gradient fields and RF fields. The few studies concerning the combined effects of these fields on pregnancy outcome in humans following MR examinations have not revealed any adverse effects, but are very limited due to the small numbers of patients involved and difficulties in the interpretation of the results (Colletti 2001; ICNIRP 2004). It is thus advised that MR procedures may be performed in pregnant patients, in particular in the first trimester, only after critical risk/benefit analysis and with verbal and written informed consent of the mother or parents (Colletti 2001). The standard of care is that MR imaging may be used in pregnant woman, if other non-ionizing forms of diagnostic imaging (e.g., sonography) are inadequate or if the examination provides important information that would otherwise require exposure to ionizing radiation (e.g., fluoroscopy or CT) (Colletti 2001; Shellock and Crues 2004). In any case, however, exposure levels of the normal operating mode should not be exceeded and the duration of exposure should be reduced as far as possible (ICNIRP 2003).

MR examinations of patients with implants or metallic objects (such as bullets, pellets) are always associated with a serious risk, even if all procedures are performed within the established exposure limits summarized in the previous sections. This risk can only be minimized by a careful interview of the patient, evaluation of the patient's file and contacting the implanting clinician and/or the manufacturer for advice on MR safety and compatibility of the implant (Medical Devices Agency 2002). In any case, MR procedures should be performed only after critical risk/benefit analysis. It should be noted that having undergone a previous MR procedure without incident does not guarantee a safe subsequent MR examination, since various factors (type of MR system, orientation of the patients, etc.) can substantially change the scenario (Shellock and Crues 2004).

In the case of passive implants—e.g., vascular clips and clamps, intravascular stents and filters, vascular access ports and catheters, heart valve prostheses, orthopedic prostheses, sheets and screws, intrauterine contraceptive devices, etc.—it has to be clarified if they are made of or contain ferromagnetic materials. As already mentioned, strong forces act on ferromagnetic objects in a static magnetic field. These forces (ASTM 2005a) may result in a movement and dislodgment of ferromagnetic objects that could injure vessels, nerves or other critical tissue structures. Comprehensive information on the MR compatibility (ASTM 2005b) of more than 1,200 implants and other metallic objects is available in a reference manual published by Shellock (2005) and online at http://www.MRIsafety.com. MR examinations are deemed relatively safe for patients with implants or objects that have been shown to be non-ferromagnetic or weakly ferromagnetic (Shellock and Sawyer-Glover 2001). Furthermore, patients with certain implants that have relatively strong ferromagnetic qualities may safely undergo MR procedures when the object is held in place by sufficient retentive forces, is not located near vital structures, and will not heat excessively (Shellock and Sawyer-Glover 2001). However, such examinations should be restricted to essential cases and should be performed at MR systems with a low magnetic field strength.

Examinations of patients with active implants or life-support systems are strictly contraindicated at conventional MR systems, if the patient implant card does not explicitly state their safety in the MR environment. In addition to the risks already mentioned above, there is the possibility that the function of the active implant is changed or perturbed, which may result in a health hazard for the patient. Clinically important examples are cardiac pacemakers, implantable cardioverter defibrillators, infusion pumps, programmable hydrocephalus shunts, neurostimulators, and cochlear implants, etc. (Medical Devices Agency 2002; Shellock and Sawyer-Glover 2001).

The induction of electric currents by RF fields during imaging in implants made from conducting materials can result in excessive heating and thus may pose risks to patients. Excessive heating is typically associated with implants that have elongated configurations and/or are electronically activated, as for example the leads of cardiac pacemakers or neurostimulation systems (Shellock and Crues 2004). The same holds for electrically conductive objects (e.g., ECG leads, cables, wires, etc.), in particular when they form conductive loops in the bore of the MR system. To avoid severe burns, the instructions for proper operation of the equipment provided by the manufacturer of the implant or device have strictly to be followed. Practical recommendations concerning this issue can be found in (Shellock and Sawyer-Glover 2001).

In various reports, transient skin irritations, cutaneous swellings or heating sensations were described in relation to the presence of both permanent (cosmetic) and decorative tattoos. These findings seem to be associated with the use of iron oxide or other metal-based pigments that are prone to magnetic field–related interactions and/or RF-induced heating, in particular when the pigments are organized as loops or rings. According to a survey performed by Tope and Shellock (2002), however, this side effect has an extremely low rate of occurrence in a population of subjects with tattoos and should not prevent patients—after informed consent—from undergoing a clinically indicated MR procedures (Shellock and Crues 2004). As a precautionary measure, a cold compress may be applied to the tattoo site during the MR examination (Tope and Shellock 2002).

References

1. Adair ER (1996) Thermoregulation in the presence of microwave fields. In: Polk C, Postow E (eds) Handbook of biological effects of electromagnetic fields. CRC, Boca Raton, pp 403–433
2. Adair ER, Berglund LG (1986) On the thermoregulatory consequences of NMR imaging. Magn Reson Imaging 4:321–333

3. Adair ER, Berglund LG (1989) Thermoregulatory consequences of cardiovascular impairment during NMR imaging in warm/humid environments. Magn Res Imaging 7:25–37
4. Ahlbom A, Green A, Kheifets L, Savitz D, Swerdlow A, ICNIRP Standing Committee on Epidemiology (2004) Epidemiology of health effects of radiofrequency exposure. Environ Health Perspect 112:1741–1754
5. ASTM International Standard F2052-02 (2005a) Standard test method for measurement of magnetically induced displacement force on medical devices in the magnetic resonance environment
6. ASTM International Standard F2503-05 (2005b) Standard practice for marking medical devices and other items for safety in the magnetic resonance environment
7. Athey TW (1989) A model of the temperature rise in the head due to magnetic resonance imaging procedures. Magn Reson Med 9:177–184
8. Bourland JD, Nyenhuis JA, Mouchawar GA, Geddes LA, Schaefer DJ, Riehl ME (1991) *Z*-gradient coil and eddy-current stimulation of skeletal and cardiac muscle in the dog. Society for Magnetic Resonance in Medicine, Proc. 10th Annual Meeting, San Francisco
9. Bourland JD, Nyenhuis JA, Schaefer DJ (1999) Physiologic effects of intense MR imaging gradient fields. Neuroimaging Clin N Am 9:363–377
10. Brix G, Reinl M, Brinker G (2001) Sampling and evaluation of specific absorption rates during patient examinations performed on 1.5-Tesla MR systems. Magn Reson Imaging 19:769–779
11. Brix G, Seebass M, Hellwig G, Griebel J (2002) Estimation of heat transfer and temperature rise in partial-body regions during MR procedures: an analytical approach with respect to safety considerations. Magn Reson Imaging 20:65–76
12. Brody AS, Sorette MP, Gooding CA et al (1985) Induced alignment of flowing sickle erythrocytes in a magnetic field: a preliminary report. Invest Radiol 20:560–566
13. Chakeres DW, de Vocht F (2005) Static magnetic field effects on human subjects related to magnetic resonance imaging systems. Prog Biophys Molec Biol 87:255–265
14. Chakeres DW, Kangarlu A, Boudoulas H, Young DC (2003) Effect of static magnetic field exposure of up to 8 Tesla on sequential human vital sign measurements. J Magn Reson Imaging 18:346–352
15. Colletti PM (2001) Magnetic resonance procedures and pregnancy. In: Shellock FG (ed) Magnetic resonance procedures: health effects and safety. Boca Raton: CRC, Boca Raton, pp 149–182
16. Dewhirst MW, Viglianti BL, Lora-Michiels M, Hanson M, Hoopes PJ (2003) Basic principles of thermal dosimetry and thermal thresholds for tissue damage from hyperthermia. Int J Hyperthermia 19:267–294
17. Donaldson GC, Keatinge WR, Saunders RD (2003) Cardiovascular responses to heat stress and their adverse consequences in healthy and vulnerable human polulations. Int J Hyperthermia 19:225–235
18. Edwards MJ, Saunders RD, Shiota K (2003) Effects of heat on embryos and foetuses. Int J Hyperthermia 19:295–324
19. Feychting M (2005) Health effects of static magnetic fields – a review of the epidemiological evidence. Prog Biophys Molec Biol 87:241–246
20. Foster KR, Schwan HP (1995).Dielectrical properties of tissues. In: Polk C, Postow E (eds) Handbook of biological effects of electromagnetic fields. CRC, Boca Raton, pp 25–102
21. Gandhi OP, Chen XB (1999) Specific absorption rates and induced current densities for an anatom*y*-based model of the human for exposure to time-varying magnetic fields of MRI. Magn Reson Med 41:816–823
22. Goldstein LS, Dewhirst MW, Repacholi M, Kheifets L (2003) Summary, conclusions and recommendations: adverse temperature levels in the human body. Int J Hyperthermia 19:373–384
23. Grissom CB (1995) Magnetic field effects in biology – a survey of possible mechanisms with emphasis on radical-pair recombination. Chemical Reviews 95:3–24
24. Hancock PA, Vasmatzidis I (2003) Effects of heat stress on cognitive performance: the current state of knowledge. Int J Hyperthermia 19:355–372
25. Higashi T, Yamagishi A, Takeuchi T et al (1993) Orientation of erythrocytes in a strong static magnetic field. Blood 82:1328–1334
26. Hore PJ (2005) Rapporteur's report: sources and interactions mechanisms. Prog Biophys Molec Biol 87:205–212
27. International Agency for Research on Cancer (IARC) (2002) Static and extremely low frequency electric and magnetic fields. IARC Monographs on the evaluation of carcinogenic risks to humans, vol. 80
28. International Commission on Non-Ionizing Radiation Protection (ICNIRP) (1997) Non-thermal effects of rf electromagnetic fields. ICNIRP Report 3/97
29. ICNIRP (1998). Guidelines for limiting exposure to time-varying electrical, magnetic, and electromagnetic fields (up to 300 GHz). Health Physics 74:494–522
30. ICNIRP (2002) General approach to protection against non-ionizing radiation. Health Physics 74:494–522
31. ICNIRP (2003). Matthes R, Vecchia P, McKinlay AF, Veyret B, Bernhardt JH (eds) Review of the scientific evidence on dosimetry, biological effects, epidemiological observations, and health consequences concerning exposure to static and low frequency electromagnetic fields (0–100 kHz). Märkl, Munich
32. ICNIRP (2004) Medical magnetic resonance (MR) procedures: protection of patients. Health Physics 87:197–216
33. International Electrotechnical Commission (IEC) (2002) Particular requirements for the safety of magnetic resonance equipment for medical diagnosis. IEC 60601-2-33 (2nd edn.)
34. Kanal E, Evans JA, Savitz DA, Shellock FG (1993) Survey of reproductive health among female MR workers. Radiology 187:395–399

35. Kangarlu A, Burgess RE, Zhu H et al (1999) Cognitive, cardiac, and physiological safety studies in ultra high field magnetic resonance imaging. Magn Reson Imaging 17:1407–1416
36. Knopp MV, Metzner R, Brix G, van Kaick G (1998) Sicherheitsaspekte zur Vermeidung strominduzierter Hautverbrennungen in der MRT. Radiologe 38:759–763
37. Konermann G, Mönig H (1986) Untersuchungen über den Einfluß statischer Magnetfelder auf die pränatale Entwicklung der Maus. Radiologe 26:490–497
38. Lepock JR (2003) Cellular effects of hyperthermia: relevance to the minimum dose for thermal damage. Int J Hyperthermia 19:252–266
39. Maret G, von Schlickfus M, Mayer A, Dransfeld K (1975) Orientation of nucleic acids in high magnetic fields. Phys Rev Lett 35:397–400
40. Medical Devices Agency (2002) Guidelines for magnetic resonance equipment in clinical use. http://www.mhra.gov.uk
41. Mevissen M, Buntenkötter S, Löscher W (1994) Effects of static and time-varying (50 Hz) magnetic fields on reproduction and fetal development in rats. Teratology 50:229–237
42. Michaelson SM, Swicord ML (1996) Interaction of nonmodulated and pulse modulated radio frequency fields with living matter: experimental results. In: Polk C, Postow E (eds) Handbook of biological effects of electromagnetic fields. CRC, Boca Raton, pp 435–533
43. Miyakoshi J (2005) Effects of static magnetic fields at the cellular level. Prog Biophys Molec Biol 87:213–223
44. Murakami J, Torii Y and Masuda K (1992) Fetal development of mice following intrauterine exposure to a static magnetic field of 6.3 T. Magn Reson Imaging 10:433–437
45. Murayama M (1965) Orientation of sickled erythrocytes in a magnetic field. Nature 206:420–422
46. Okazaki R, Ootsuyama A, Uchida S, Norimura T (2001) Effects of a 4.7 static magnetic field on fetal development in ICR mice. J Radiat Res 42:273–283
47. Reilly JP (1998) Applied bioelectricity. From electrical stimulation to electropathology. Springer, Berlin, Heidelberg, New York
48. Saunders R (2005) Static magnetic fields: animal studies. Prog Biophys Molec Biol 87:225–239
49. Schaefer DJ, Bourland JD, Nyenhuis JA (2000) Review of patient safety in time-varying gradient fields. J Magn Reson Imaging 12:20–29
50. Schenck JF (2000) Safety of strong, static magnetic fields. J Magn Reson Imaging 12:2–19
51. Schenck JF (2005) Physical interactions of static magnetic fields with living tissues. Prog Biophys Molec Biol 87:185–204
52. Schmitt F, Irnich W, Fischer H (1998) Physiological side effects of fast gradient switching. In: Schmitt F, Stehling ML, Turner R (eds) Echo planar imaging. Springer, Berlin Heidelberg New York
53. Sharma HS, Hoopes PJ (2003) Hyperthermia-induced pathophysiology of the central nervous system. Int J Hyperthermia 19:325–354
54. Shellock FG (2000) Radiofrequency energy-induced heating during MR procedures: a review. J Magn Reson Med 12:30–36
55. Shellock FG (2001) Patient monitoring in the magntic resonance environment. In: Shellock FG (ed) Magnetic resonance procedures: health effects and safety. CRC, Boca Raton pp 217–240
56. Shellock FG (2005) Reference manual for magnetic resonance safety, implants, and devices: 2005 edn. Biomedical Researc, Los Angeles
57. Shellock FG, Crues JV (2004) MR procedures: biologic effects, safety, and patient care. Radiology 232:635–652
58. Shellock FG, Sawyer-Glover AM (2001) The magnetic resonance environment and implants, devices, and materials. In: Shellock FG (ed) Magnetic resonance procedures: health effects and safety. CRC, Boca Raton, pp 271–326
59. Shellock FG, Schaefer DJ, Kanal E (1994) Physiological responses to MR imaging at an *SAR* Level of 6.0 W/kg. Radiology 192:865–868
60. Sikov MR, Mahlum DD, Montgomery LD, Decker JR (1979) Development of mice after intrauterine exposure to direct-current magnetic fields. In: Phillips RD, Gillis MF, Kaune WT, Mahlum DD (eds) Biological effects of extremely low frequency electromagnetic fields. 18th Hanford Life Sciences Symposium, Richland, Washington, October 1978. Springfield, Virginia, US Department of Energy, National Technical Information Service, pp 462–473, 1979
61. Tenforde TS (2005) Magnetically induced electric fields and currents in the circulatory system. Prog Biophys Molec Biol 87:279–288
62. Tope WD, Shellock FG (2002) Magnetic resonance imaging and permanent cosmetics (tattoos): survey of complications and adverse events. J Magn Reson Imging 15:180–184
63. US Food and Drug Administration (2003) Center for Devices and Radiological Health. Criteria for significant risk investigations of magnetic resonance diagnostic devices. http://www.fda.gov/cdrh/ode/guidance/793.pfd
64. Vocht F de, van-Wendel-de-Joode B, Engels H, Kromhout H (2003).Neurobehavioral effects among subjects exposed to high static and gradient magnetic fields from a 1.5 Tesla magnetic resonance imaging system: case-crossover pilot study. Magn Reson Med 50:670–674
65. World Health Organization (WHO) (1993) United Nations Environment Programme/Word Health Organisation/International Radiation Protection Association: environmental health criteria 137, electromagnetic fields (300Hz to 300 GHz). WHO Press, Brussells
66. WHO (2006) Environmental health criteria 232, static fields. WHO Press, Brussells